AN INNOVATIVE APPROACH TO FABRICATION WITH PHOTO-CURED RESINS BY SHELL-PRINTED-CORE-CASTING

Emil SZYMCZYK* , **Maciej REĆKO*** , **Kazimierz DZIERŻEK*** , **Karol SAPIOŁKO***

*Faculty of Mechanical Engineering, Bialystok University of Technology, ul. Wiejska 45C, 15-351 Bialystok, Poland

emil-szymczyk3@wp.pl, m.recko@pb.edu.pl, k.dzierzek@pb.edu.pl, karol@sapiolko.com

Abstract: Modified LCD-based method was used to print three-dimensional (3D) elements. This innovative method combines printing the external shell and filling, thus obtaining mould by casting resin. In order to compare the properties of prints obtained with this method with the ones fabricated in a standard procedure, we conducted bending tests of vertically/horizontally printed and shell-printed cast specimens. The shell-cast samples showed higher flexural strength and larger values of apparent Young's modulus. The presented results also concern the kinetics of curing samples obtained with different fabrication routes.

Key words: stereolithography, resin, printing, casting, curing, tensile test, bending

1. INTRODUCTION

Stereolithography (SLA) is one of the methods of three-dimensional (3D) printing that is based on a process of photopolymerisation (1). This method involves the use of a laser beam to cure a photopolymer liquid, layer by layer, into a solid object. The dimensional accuracy of elements printed with SLA is the main advantage of this method, and it is often used to create precise, intricate designs. However, a significant disadvantage of SLA is the poor mechanical properties of the product (2), which can be a major limitation in certain applications. SLA products have properties (3) that depend strongly on several factors such as the layer thickness, curing time during and post-curing time, printing temperature and fabrication orientation (4, 5). These factors can significantly affect the mechanical properties of the final product, such as its strength and durability. 3D printed elements, by definition, have layered structures and anisotropic properties along and across the layers, which means that the properties of the material vary in different directions.

On one hand, cast elements have isotropic properties (6), which means that the properties of the material are consistent in all directions. In some applications, this makes casting an attractive alternative to 3D printing. However, comparing the two methods, one should also consider the required processing time. Printing with laser technology can take up to several dozen hours. In contrast, the use of LCD printers significantly reduces this time, but cannot be viewed as a fast fabrication route, especially in comparison with casting. On the other hand, casting needs to be proceeded by building the moulds, which might be time-consuming and require additional fabrication capacity.

Because of the above-given comments, we have put forward a hypothesis that an attractive alternative to 3D printing and casting can be a method combining these two. More precisely, we propose a two-step procedure: (a) printing of external shell of the element of interest and (b) casting resin to the thus printed shell/mould. This method allows for the creation of complex designs with high dimensional accuracy while also providing good

mechanical properties. The results of experiments described in the following sections demonstrate this method's advantages.

2. MATERIALS AND EXPERIMENTAL DETAILS

Elegoo Mars 2 desktop LCD-SLA printer was used as the primary equipment to fabricate the printed specimens in this study. This particular piece of equipment is quite popular among enthusiast-level customers, due to its ease of use and accessibility. LCD-SLA printers work by curing the resin layer using an LCD light source, illuminating the specimen cross-section (7). In this specific study, the layers in the prints were set at a thickness of 0.05 mm, with a curing time of 2.5 s for each layer.

The models for the specimens were designed using SolidWorks 2022® (Dassault Systèmes SolidWorks Corporation, USA) and then exported to a .stl file. Additional supports were added to the models using Formware 3D (Formware B.V. Amsterdam, Netherlands) to ensure the structural integrity of the printed specimens. The final step in the printing process involved slicing the files into G-code using CHITUBOX Software (CBD-Tech, China).

In this study, a transparent resin was used as it allows for the complete hardening of the resin. However, in order to conduct a thorough investigation, pigmented resins were also considered by incorporating black-coloured resin samples fabricated using the same printing parameters for comparison. The samples were cured for varying amounts of time, including 0 min, 2 min, 4 min, 8 min and 16 min (8). The resin supplier's data indicate that the tensile strength of the resin should be 23.4 MPa, with a Shore D hardness of 79. The recommended wavelength of curing light for this type of resin is 405 nm.

The geometry of the samples used in this study is shown in Figs. 1–3. The specimens were also printed in both horizontal and vertical orientations in order to further evaluate the impact of the printing orientation on the final specimens.
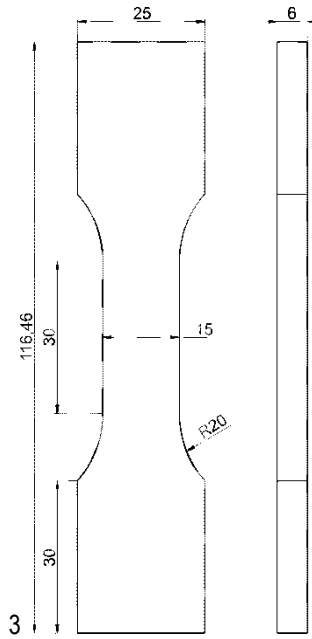
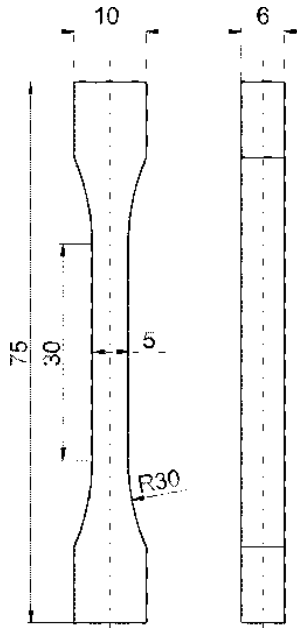**Fig. 1.** Geometry of samples used in a uniaxial tensile test

Fig. 2. Specimens used for testing flexural strengthz

In the case of print-cast samples, the resin was introduced into shells with a syringe. Special measures were taken to reduce the density of trapped air bubbles within the resin to mitigate their impact.

In order to conduct the three-point bend test, the samples were fabricated by being cast into an intricately designed mould. This mould, constructed out of plexiglass material, was explicitly created to expose the resin to the curing machine's light. In addition, the forms were tightly sealed using screw fastenings and plexiglass plates that were coated with multi-hydrocarbon sealant, ensuring a secure and reliable seal. A visual depiction of the casting sample preparation process is shown in Fig. 4.

During the production of cast samples, we encountered a significant obstacle in the form of air bubbles in the resin. We had to devise a method to overcome this issue (9), and after much

experimentation, we discovered that by reducing the pressure, we could effectively eliminate any air from the resin. To achieve this, we placed the moulds in a vacuum chamber (Fig. 5) during the pouring and hardening process, ensuring that the final product was free from any defects caused by air bubbles.
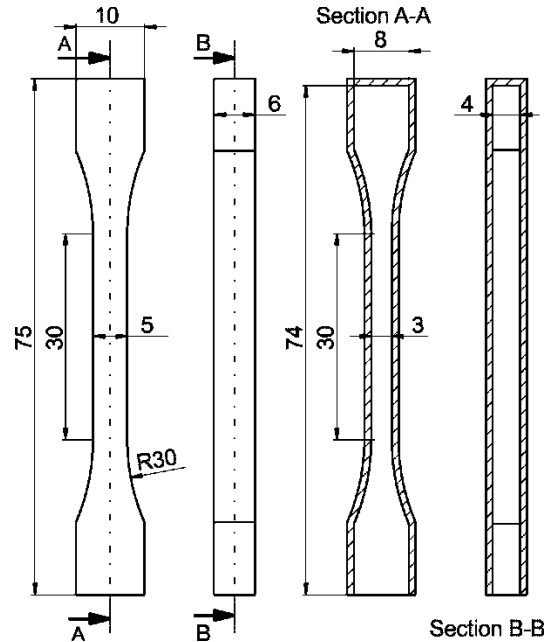

Fig. 3. Shells for shell-cast specimens

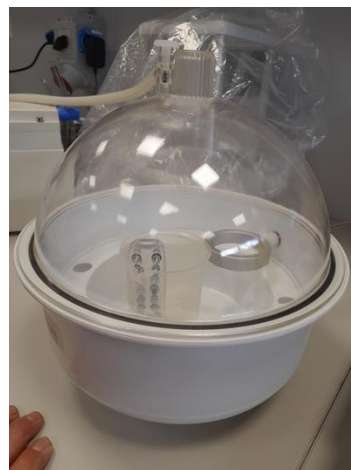**Fig. 4.** Mould used for casting

Fig. 5. Moulds with resin in a vacuum (de-gassed) chamber

Final curing was accomplished using Elegoo Mercury Plus Curing Station. The machine is equipped with sets of UV emitters. The light emitted by the light source is tuned to the wavelength required to cure this resin – 405 nm, and in addition, it has a set of UV-A emitting LEDs. The power of the light source, measured at the centre of the curing plate, was 220 W/m^2. Since the light was obstructed during our studies by plexiglass and pre-cured resin, we measured the power provided to the resin at 180 W/m^2 and 23 W/m^2, respectively. Based on the thermal imaging camera recordings, we obtained a temperature–time graph during the curing process, as shown in Fig. 6.
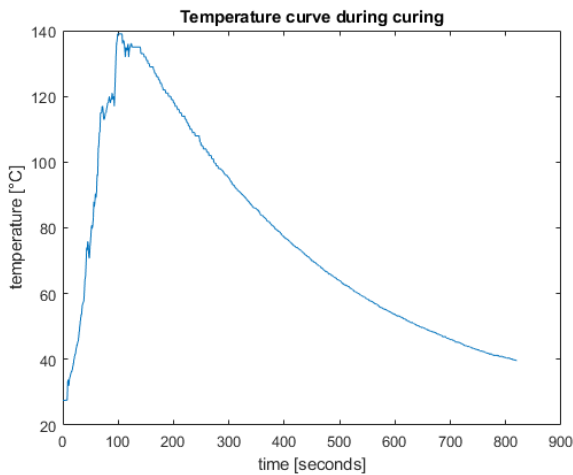

Fig. 6. Temperature profile of the tested sample

It can be noted that after 100 s, the sample reaches the maximum temperature of 140°C. It is much less than 180°C reported in "Mechanical property modelling of photosensitive liquid resin in SLA additive manufacturing: Bridging degree of cure with tensile strength and hardness. Materials & Design" (10). Nevertheless, the curing employed proved to provide sufficient strength to all samples. It should be noted that the temperature measurements in our case were performed on the surface of the specimen. This meant a 1 mm layer of pre-cured resin between the "heat source" and the sample's surface.

The tensile tests were performed on a Zwick/Roell Z010 (11) testing machine, following the procedure described by (12). Engineering stress–strain curves were analysed to determine maximum engineering stress, elastic limit and apparent Young's modulus based on the trend of linear parts of the curves. Aramis 3D 4M system was used to determine strain distributions along the gauge length of the specimens. The bending tests were carried out on the MTS Insight.

3. RESULTS

Results of the tensile tests are shown in Figs. 7 and 8 using the following description of the specimens:
- FVS – vertical,
- FHS – horizontal,
- FHSS – horizontal supports,
- FHBS – horizontal black.

The results of the bending tests are presented in Fig. 9 in the form of a bar plot of maximum bending forces. As determined from the bending test, apparent Young's modulus values are

given in Fig. 10. As a test, we added two more cast samples with 60 min- and 90-min curing times to see if further curing would affect performance.

Results of the bending tests shown in Figs. 9 and 10 are using the following description of the specimens:
- FVS – vertical,
- FHS – horizontal,
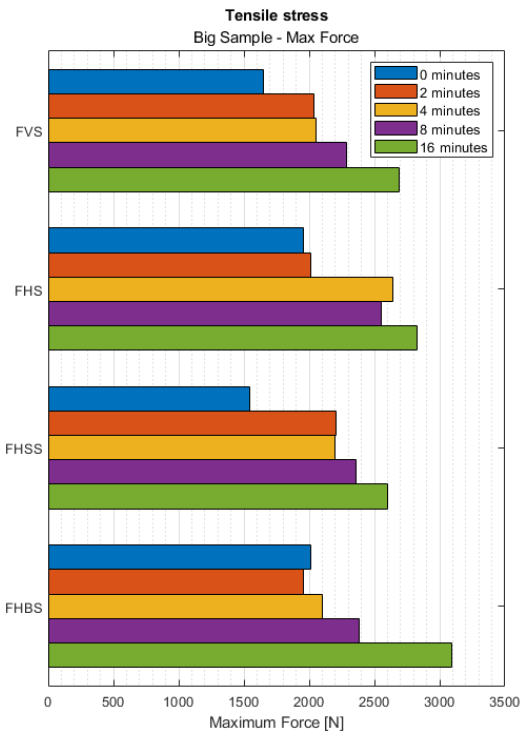- SHELL – printed shell filled with resin,
- CS – casted specimen.

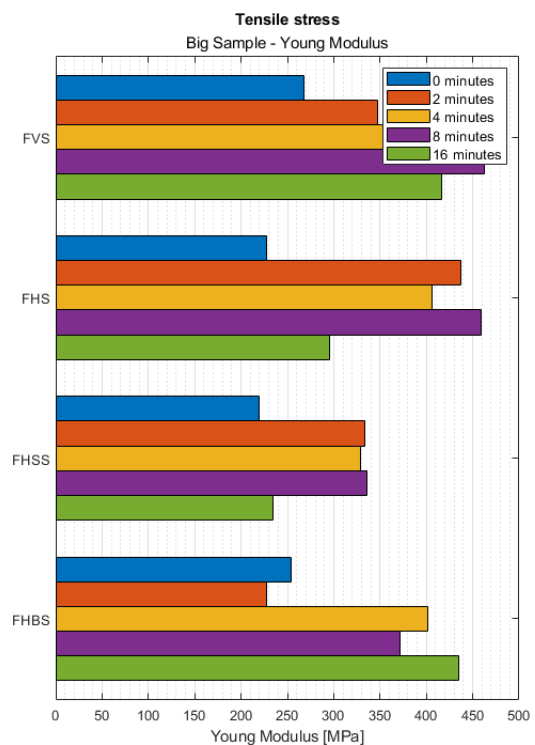

Fig. 7. Maximum engineering stress of the specimens

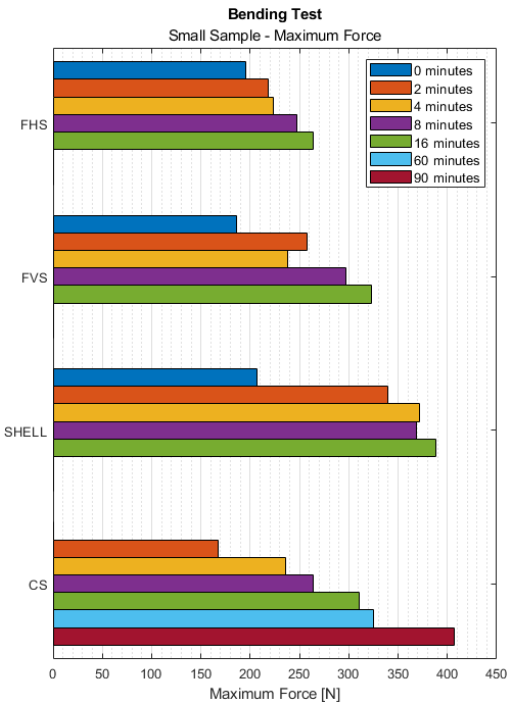
Fig. 8. Apparent Young's modulus

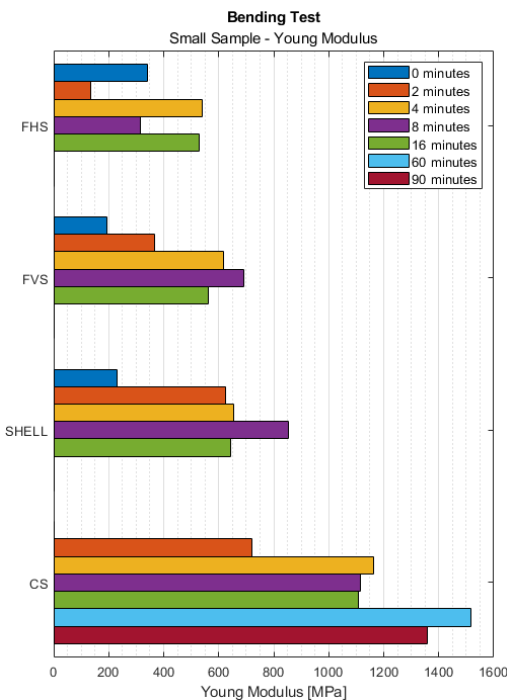**Fig. 9.** Maximum bending forces of the studied specimens

Fig. 10. Young's modulus determined based on a bending test

4. DISCUSSION

The results obtained in this study provide useful insight into the properties of print-outs prepared with SLA LCD technology. However, we intend to focus the discussion on the properties of print-cast specimens, benchmarking them against the properties of the one obtained by printing/casting alone. In this context, bending tests have shown that the shell-cast samples have the highest flexural strength, 20% higher than the second-best result in our sample (vertical printed and cured for 16 min).

However, tensile tests have shown that horizontally printed samples without supports have the highest tensile strength. For example, after curing it for 16 min, the FHBS sample increased its tensile strength by 53.7%.

The results of our study indicate that cast specimens demonstrate the highest values of apparent Young's modulus. In contrast, shell-cast specimens exhibit a 26.77% lower Young's modulus in comparison to cast specimens. However, shell-cast specimens still display a 23.70% higher Young's modulus than the next best result, which is a sample printed vertically and cured for 8 min. Given that shell samples are easier to obtain than cast samples.

For SLA printers using a laser to print, this shell method can significantly reduce the time to receive the print. Comparing the time of obtaining the best samples, i.e. cast and shell, for the exemplary curing time of 16 min, the shell sample looks much better. Obtaining a cast sample consists of the following process: cutting the mould from plexiglass, tightening the mould screws, pouring, and curing the resin, and removing the sample from the mould. The entire process of obtaining one sample takes an average of 90 min. When removing the sample, we had to be careful not to damage the sample because the resin was sticking to the mould. However, making a shell sample involves printing the shell, pouring it and curing it. The entire process for one sample takes an average of 45 min.

A study conducted by Son et al. (12) explored a concept similar to our own, utilising ABS material for 3D-printed shells filled with epoxy resin. However, the study employed a different printing technique, FDM, and used a second material as a core cast. The scientists provided a detailed explanation of their multi-step procedure, which encompassed printing, shell treatment to enhance optimal casting and specimen curing. Their findings revealed that their samples exhibited an increase in mechanical properties in comparison to regular prints obtained with FDM printers, and at a higher manufacturing rate. In our opinion, their findings further indicate the viability of our manufacturing method.

Based on our observations, we have discovered a notable difference in the curing process for resin between moulds at the curing station and printed shell-cast samples. The reason for this discrepancy is likely due to the amount of energy delivered to the resin in each scenario. Specifically, while the energy delivered to print-cast samples is comparable to that of printed samples at 23 W/m^2 received from printer during manufacturing, cast samples inside a mould receive a significantly higher amount of energy, approximately eight times more. This ultimately leads to the entrapment of air bubbles within the resin. As part of our visual inspection process, we have rejected samples that exhibit excessive bubbles.

It should be noted that samples printed in black resin had similar mechanical parameters to those fabricated with transparent resin. UV curing time impacts the mechanical properties of the samples made of the resin used in this study, in agreement with the findings of (2, 13, 14). Furthermore, our results show that the curing time should be optimised for various fabrication methods and considering the elements' physical dimensions.

5. CONCLUSIONS

The findings of the study indicate that the combination of printing and casting presents a viable alternative to employing

either technique in isolation. The mechanical characteristics of shell-printed-core-cast elements are akin to those of conventional castings, and in some instances, even surpass those of SLA prints. This approach holds the potential to reduce printing duration, as well as eliminate the requirement for casting moulds, while additionally providing superior polymerisation conditions that are congruent with the designated curing parameters.

However, it is important to note that to fully exploit this technology's potential, the curing conditions need to be optimised, depending on the shape and size of the product. This is because the size and shape of the product can greatly impact the curing process and ultimately affect the mechanical properties of the final product. Additionally, it is worth noting that the curing time plays an important role in the mechanical properties of the samples and should be considered when choosing the appropriate curing conditions.

In this research, we have gained valuable insights into the use of SLA LCD technology for printing purposes and the potential benefits of combining printing and casting techniques. This approach has demonstrated the ability to improve the mechanical properties of SLA prints while also reducing printing time, rendering it a suitable option for a range of applications. However, in order to optimise this approach, specific curing conditions must be tailored to the size and shape of the intended product.

REFERENCES

1. Dizon JRC, Espera AH, Chen Q, Advincula RC. Mechanical characterisation of 3D-printed polymers. Addit Manuf. 2018 Mar 1;20:44–67.
2. Kazemi M, Rahimi A. Stereolithography process optimisation for tensile strength improvement of products. Rapid Prototyp J. 2018 Jan 1;24(4):688–97.
3. Formlabs. Inc. Validating Isotropy in SLA 3D Printing [Internet]. FORMLABS WHITE PAPER Validating Isotropy in SLA 3D Printing. [cited 2022 Dec 19]. Available from: https://3d.formlabs.com/validating-isotropy-in-sla-3d-printing/
4. Dulieu-Barton J m., Fulton M c. Mechanical Properties of a Typical Stereolithography Resin. Strain. 2000;36(2):81–7.
5. Wang S, Ma Y, Deng Z, Zhang K, Dai S. Implementation of an elastoplastic constitutive model for 3D-printed materials fabricated by stereolithography. Addit Manuf. 2020 May 1;33:101104.
6. Chacón JM, Caminero MA, García-Plaza E, Núñez PJ. Additive manufacturing of PLA structures using fused deposition modelling: Effect of process parameters on mechanical properties and their optimal selection. Mater Des. 2017 Jun 15;124:143–57.
7. Schmidleithner C, Kalaskar D. Chapter 1 Stereolithography. In 2019 [cited 2023 Jan 19]. Available from: https://www.semanticscholar.org/paper/Chapter-1-Stereolithography-Schmidleithner-Kalaskar/0af4e17637d487d284f9f15330572d555634fe81
8. Guttridge C, Shannon A, O'Sullivan A, O'Sullivan KJ, O'Sullivan LW. Impact of increased UV curing time on the curing depth of photosensitive resins for 3D Printing [Internet]. In Review; 2022 May [cited 2023 Jan 19]. Available from: https://www.researchsquare.com/article/rs-1626243/v1
9. Tek-Tip: Reduce Bubbles in Clear Casting Resin [Internet]. Polytek Development Corp. [cited 2023 Jan 19]. Available from: https://polytek.com/tutorial/tek-tip-reduce-bubbles-clear-casting-resin
10. Yang Y, Li L, Zhao J. Mechanical property modeling of photosensitive liquid resin in stereolithography additive manufacturing: Bridging degree of cure with tensile strength and hardness. Mater Des. 2019 Jan 15;162:418–28.
11. ProLine universal testing machine [Internet]. ProLine universal testing machine. Available from: https://www.zwickroell.com/products/static-materials-testing-machines/universal-testing-machines-for-static-applications/proline/
12. Petraşcu OL, Manole R, Pascu AM. The behavior of composite materials based on polyurethan resin subjected to uniaxial tensile test. Mater Today Proc. 2022 Jan 1;62:2673–8.
13. Son J, Yun S, Park K, Ryu S, Kim S. Isotropic 3D printing using material extrusion of thin shell and post-casting of reinforcement core. Addit Manuf. 2022 Oct;58:102974.
14. Dzadz Ł, Pszczółkowski B. Analysis of the influence of UV light exposure time on hardness and density properties of SLA models. Tech Sci [Internet]. 2020 Dec 9 [cited 2023 Jan 19];(2020). Available from: https://czasopisma.uwm.edu.pl/index.php/ts/article/view/6119
15. Miedzińska D, Gieleta R, Popławski A. Experimental Study on Influence of Curing Time on Strength Behavior of SLA-Printed Samples Loaded with Different Strain Rates. Materials. 2020 Dec 21;13(24):5825.

Emil Szymczyk: https://orcid.org/0009-0001-7242-2611

Maciej Rećko: https://orcid.org/0000-0001-8768-3753

Kazimierz Dzierżek: https://orcid.org/0000-0001-9184-1806

Karol Sapiołko: https://orcid.org/0009-0000-8490-8582

EFFECTIVENESS OF FRICTION FORCE REDUCTION IN SLIDING MOTION DEPENDING ON THE FREQUENCY OF LONGITUDINAL TANGENTIAL VIBRATIONS, SLIDING VELOCITY AND NORMAL PRESSURE

Mariusz LEUS* , **Paweł GUTOWSKI*** , **Marta RYBKIEWICZ***

*Faculty of Mechanical Engineering and Mechatronics, West Pomeranian University of Technology in Szczecin,
al. Piastów 19, 70-310 Szczecin, Poland

mariusz.leus@zut.edu.pl, pawel.gutowski@zut.edu.pl, marta.rybkiewicz@zut.edu.pl

Abstract: The article presents the results of experimental research and simulation analyses of the influence of slip velocity, normal pressures and vibration frequency on the effectiveness of friction force reduction carried out in sliding motion in the presence of forced tangential vibrations. In experimental studies, changes in the driving force were measured during the slip of the upper body over the vibrating lower body. The direction of these vibrations was parallel both to the contact plane and to the direction of movement of the shifted body. The simulation tests were carried out in the Matlab/Simulink environment through the use of numerical procedures that were specially created for this purpose. Dynamic friction models considering the tangential compliance of contact and the phenomenon of pre-sliding displacement were used for calculations. The paper presents the designated values of the so-called coefficient of average friction force reduction in sliding motion for the following friction pairs: steel C45–steel C45, steel C45–cast iron GGG40 and steel C45–polytetrafluoroethy-lene PTFE (Teflon). The results of numerical analyses were in good agreement with those of experimental tests. A significant dependence of the level of average friction force reduction on the frequency of forced vibrations, sliding velocity as well as the kind of sliding pair material, and normal pressures was shown.

Key words: reduction of friction force, vibrations, experimental verification

1. INTRODUCTION

Due to the frequent need to minimise the force necessary to introduce a body into sliding motion and maintain this movement, the phenomenon of reducing the friction force has been and still is the subject of interest among scientists in many research centres around the world. The authors' own studies [1–8] and the works of other authors [9–24] indicate that introducing the shifted body or the substrate on which the slip takes place into a vibrating motion in a direction tangential to the track can significantly reduce the driving force, F_d. This phenomenon is identified with the reduction of the average friction force, $\bar{F}_f$ [19]. The level of this reduction depends on many factors related to the vibration parameters, sliding velocity and magnitude of surface pressures, as well as the kind of material and the microgeometry of contact surfaces of elements forming the sliding pair.

The direction of these vibrations in relation to the direction of slip is also an important factor, responsible for influencing to a large extent the effectiveness of the friction force reduction in the presence of forced vibrations. Different mechanisms of friction force reduction occur for vibrations normal to the contact plane [20, 24–31], and the ones occurring for tangential vibrations are different [1–24]. There are also two different friction force reduction mechanisms within tangential vibrations. Different for longitudinal vibrations – consistent with the direction of slip [2, 4–24], and different for transverse vibrations – perpendicular to this direction [1–3, 12, 19–24].

A condensed review of experimental works and model analyses related to the impact of tangential vibrations on friction processes in sliding motion is presented in the work of Shao et al. [25], as well as in several previous works of the authors of the present study [1–8]. This review shows that the greatest effectiveness of friction force reduction in tangential vibrations is possible when the direction of these vibrations is consistent with the direction of the macroscopic movement of the body being moved, i.e. in the case of longitudinal tangential vibrations. However, for the reduction of the friction force during longitudinal vibrations to occur, the amplitude of the vibration velocity v_a must be greater than the sliding velocity v_d. If this condition is not met, the reduction of the friction force will not occur during longitudinal vibrations.

It should be emphasised that, according to the results of the analyses presented in the study of Gutowski and Leus [4], reduction of the driving force in the sliding motion in the presence of tangential longitudinal vibrations, identified with the reduction of the average friction force, may occur both with temporary changes in the sign of the friction force and without such changes.

The fulfilment of the condition $v_a > v_d$ and the knowledge of the ratio v_a/v_d are not, however, tantamount to determining the level of friction force reduction under the influence of vibrations. In harmonic motion, the amplitude v_a of vibration velocity is a function of two independent vibration parameters, which determine the level of friction force reduction. It is a function of both the frequency f of the vibrations and the amplitude u_o of their displacements.

Thus, the reduction level cannot be unequivocally determined only on the basis of the value of vibration velocity amplitude since the same value of this parameter can be obtained at different values of frequency and amplitude of vibrations. Hence, an important information in the studies of sliding motion in the presence of forced longitudinal tangential vibrations is not only the knowledge of the individual influence that each of these vibration parameters exert on the level of friction force reduction but also the knowledge of their cumulative influence on this reduction. It shows that, in all analyses of the impact of vibrations on the friction force in sliding motion and in particular when using these vibrations to control the friction force on the contact surfaces of the friction pair, both vibration parameters u_o and f must be considered. Maintaining the amplitude v_a of vibration velocity at a constant level does not mean the maintenance of a constant level of friction force reduction.

The available literature lacks both model and experimental analyses illustrating this very important, especially due to the possibility of practical use, impact of the simultaneous change of both vibration parameters, i.e. their frequency f and displacement amplitude u_o, on the level of friction force reduction in sliding motion. Hence, the purpose of this work was to fill this prevalent gap in the existing literature.

This work considers the experimental and numerical analyses of the influence of the sliding velocity, normal pressures and the frequency of forced vibrations on the effectiveness of friction force reduction in sliding motion performed in the presence of longitudinal tangential vibrations. Simulation studies of the friction force reduction as a function of these parameters were carried out in the Matlab/Simulink environment, using the computational model described in detail in the study of Gutowski and Leus [4]. Two relatively simple, dynamic friction models were used there to describe the friction force: the Dahl model [32, 33] and the elasto-plastic model [34, 35]. In the Dahl model, it is assumed that the contact deformations in the tangential direction are elastoplastic already from the initial load phase. In the second of these adopted friction models, there is a pure-elastic phase before the elasto-plastic deformation phase. In these models, the friction force F_f is a function of contact tangential stiffness, the measure of which is the coefficient k_t, and depends on the magnitude of the elastic deformation s of the contact area ($F_f = k_t \cdot s$) [32–35]. It is evident that assuming the wrong value of the coefficient k_t will lead to incorrect determination of the level of friction force reduction. The values of this coefficient, for a given set of contact joints of sliding pairs tested in this paper, were determined experimentally from the compliance characteristics of these joints plotted in

the tangential direction. The appropriate tests were carried out on the tests stand described in the study of Leus and Gutowski [36].

The experimental tests of the friction force reduction as a function of the frequency of forced vibrations, sliding velocity and normal pressures presented in this article were carried out, in turn, on the test stand described in work [2].

The present study provides the experimentally and numerically determined values of the coefficient of average friction force reduction at a fixed amplitude u_o of vibrations (u_o = const) and changing values of the frequency f of these vibrations, for different drive velocities v_d and strictly defined normal pressures p. Experimental and simulation tests were carried out for three sliding pairs, namely steel C45–steel C45, steel C45–cast iron GGG40 and steel C45–polytetrafluoroethylene PTFE (Teflon).

Introducing vibrations of a set amplitude and frequency into the contact area of the shifted body and the ground is not always possible due to hardware limitations, such as limited power of the vibration exciter, and often, it may even be unacceptable because of the resonance phenomenon. Hence, the paper also presents the results of model and experimental analyses of changes in the level of friction force reduction under the influence of vibrations, with simultaneous modification of both the frequency f and the amplitude u_o of vibrations. These changes in the values of vibration parameters were made in such a way that the ability to reduce the friction force by means of introduced longitudinal vibrations is maintained, resulting from the necessary fulfilment of the condition $v_a > v_d$. These tests were carried out at a fixed value of the velocity amplitude v_a = const, meeting this condition.

2. EXPERIMENTAL INVESTIGATIONS

The experimental tests were carried out on the test stand that is shown in Fig. 1. A complete description of this test stand is included in the study of Gutowski and Leus [2]. Its main part is a sliding pair consisting of specially designed specimens: upper *A* and lower *B*. During tests, the upper specimen is shifted with a set velocity over the lower specimen by means of a drive system consisting of a stepper motor with a gear, a linear guide and a driver. In the initial stage of this shift, the lower specimen is fixed, and then, while the upper specimen is moving, it is set into vibration motion generated by a piezoelectric vibration actuator. At the final stage of the test, the vibration generator is turned off, and the upper sample is moved again over the stationary lower specimen. Each experimental test at each measurement point was repeated thrice.
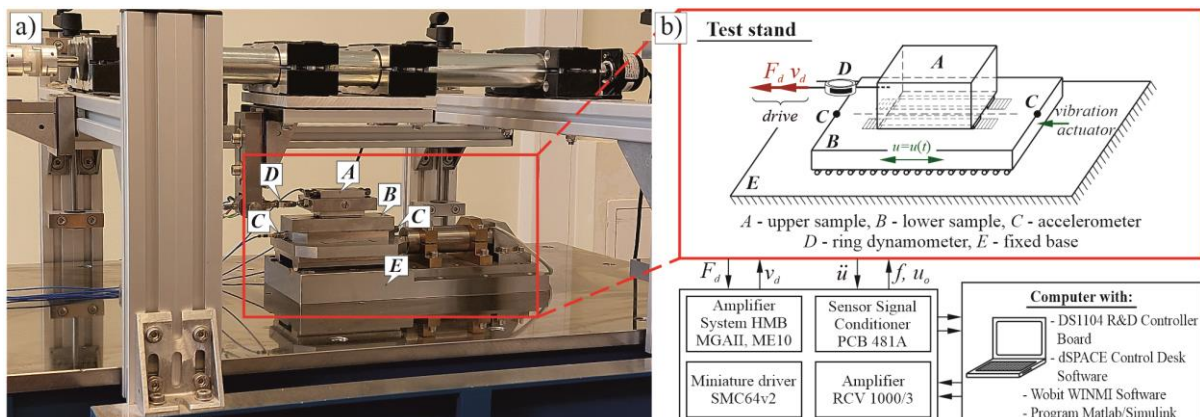

Fig. 1. Test stand: (a) photo of the mechanical part of the stand prepared for testing and (b) block diagram of the measurement and data handling system

The tests were carried out with harmonic forcing of the lower specimen. Its displacement was described by the relationship:

$$u = u_o \sin(\omega t) \qquad (1)$$

where u_o is vibration amplitude, ω is angular frequency of vibrations ($\omega = 2\pi f$) and f is vibration frequency.

The vibration velocity of the lower specimen was given by the following expression:

$$\dot{u} = v_a \cos(\omega t) \qquad (2)$$

where v_a is an amplitude of vibration velocity. It is a function of both the frequency f and the amplitude u_o of the vibrations:

$$v_a = u_o \omega = 2\pi f u_o \qquad (3)$$

During the tests, throughout the shift of the upper specimen, the drive force necessary at first to set this specimen into sliding motion, and then to maintain this motion, was measured. This force was measured with a special ring dynamometer D (Fig. 1) placed between the upper specimen and the driver. The values set during the measurement were drive velocity v_d, frequency f and amplitude u_o of forced vibrations and surface pressures p. For control purposes, during each measurement, the acceleration of the lower specimen was also registered with the use of miniature acceleration sensors such as M352C65 type ICP (manufactured by PCB).

The contact pressure p, normal to the contact surface, is the result of the self-weight of the upper sample with an additional load of $m_1 = 1$ kg attached to it and the external force F_z applied to this sample centrally in the vertical direction, in concomitance with the use of a lever containing sliding weights for string loading [6]. Such a system allows us to obtain normal pressures on the contact surface of the friction pair starting from $p_{min} = 0.00544$ N/mm² up to $p_{max} = 0.120$ N/mm². The contact pressure, during the sliding/vibration interactions, was controlled continuously by means of a force gauge placed on the vertical string, connecting the sliding sample with the lever with sliding weights.

The surface roughness of the specimens, forming the tested contact joints (Fig. 2a–c), was measured with a profilometer (Mitutoyo Surftest SJ-210) (Fig. 2d). Tab. 1 shows the measured R_a values of the upper and lower specimens. Each of the values given in this table is an average of six surface roughness measurements carried out in different places of the contact surface. All measurements were performed in the direction of the slip.

Tab. 1. R_a parameters of sliding pair samples

Sample	Material	R_a [μm]	
		Mean	Stand. dev.
Upper	Steel C45	0.44	0.038
Lower	Steel C45	1.35	0.095
	Cast iron GGG40	1.14	0.099
	PTFE	2.05	0.246

PTFE, polytetrafluoroethylene

Experimental tests were carried out in normal room conditions at temperatures ranging from 22° to 26°C. Ambient humidity was not measured.
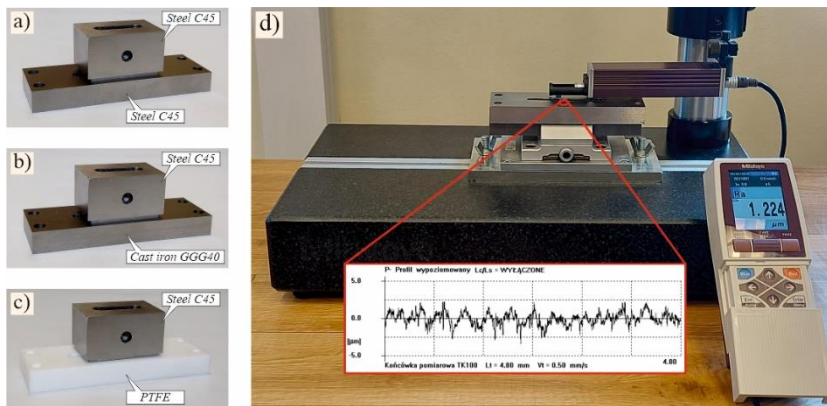

Fig. 2. Photos of specimens prepared for testing and roughness measurement stand: (a) steel–steel, (b) steel–cast iron, (c) steel–PTFE and (d) profilometer Mitutoyo Surftest SJ-210

For each sliding pair, during the measurements, the change in the driving force F_d was measured as a function of the vibration frequency f at the determined amplitude $u_o = 0.1$ μm. The tests were carried out at five different frequencies f of forced vibrations, namely 1 kHz, 2 kHz, 3 kHz, 4 kHz and 5 kHz, with vibration velocity amplitudes of $v_a = 0.628$ mm/s, 1.256 mm/s, 1.884 mm/s, 2.513 mm/s and 3.141 mm/s, respectively; and for four drive velocities, $v_d = 0.2$ mm/s, 0.5 mm/s, 1 mm/s and 2 mm/s. These measurements were performed for three selected values of normal pressures: $p = 0.022$ N/mm², 0.063 N/mm² and 0.104 N/mm². Examples of test results in the form of drive force plots for the analysed friction pairs at $v_d = 0.5$ mm/s and $p = 0.063$ N/mm² are shown in Fig. 3.

The comparison of the driving force runs shown in Figure 3 indicates that, in all the presented cases, the introduction of longitudinal vibrations into the contact area of the friction pair resulted in a decrease in the driving force necessary to maintain the sliding movement of the upper sample. The higher the frequency f of the forced vibrations, the greater was the magnitude of this reduction, which means that it increased with the increase of the amplitude of the vibration velocity v_a, because with a fixed displacement amplitude u_o, the increase in the frequency of vibrations causes a corresponding increase in the amplitude of the vibration velocity. From the runs shown in Fig. 3, it can also be seen that the level of this reduction depends on the type of friction pair, and it was the lowest in the case of the steel C45–PTFE pair.

It should be emphasised that in any tests carried out with forced vibrations of the ground with amplitudes of velocity v_a lower than the drive velocity v_d, there was no reduction of the driving force.
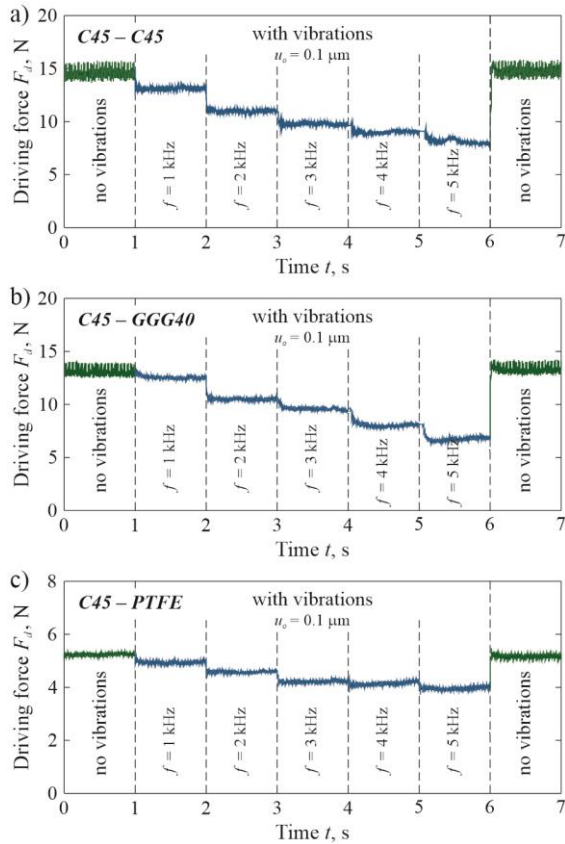

Fig. 3. Variability of the driving force F_d in relation to frequency f at fixed amplitude u_o of vibration: (a) steel–steel, (b) steel–cast iron and (c) steel–PTFE; p = 0.063 N/mm², v_d = 0.5 mm/s, u_o = 0.1 μm

3. SIMULATION ANALYSES AND THEIR EXPERIMENTAL VERIFICATION

Numerical studies were carried out using the model developed to analyse the effect of longitudinal tangential vibrations on the friction force in sliding motion, as described in detail in the study of Gutowski and Leus [4]. This model is based on the dynamic equation of motion of a body sliding over the ground, which is introduced into vibrations in a strictly defined direction, i.e. a direction parallel to both the contact plane and the direction of the sliding body motion. To describe the friction force, dynamic friction mo-

dels such as the Dahl model [32, 33] and the elastoplastic [34, 35] model were adopted. The simulation tests were carried out in the Matlab/Simulink environment in accordance with the calculation algorithm presented in Fig. 4.

The main purpose of the model simulation analyses was, as in the experimental studies, to examine the impact of the frequency of tangential longitudinal vibrations, as well as the sliding speed and surface pressures, on the level of friction force reduction in sliding motion. The comparison of the obtained results of model analyses with the results of experimental tests also allowed us to assess the correctness of the developed calculation procedures.

The analyses were carried out at the forced vibration frequencies f of the lower specimen ranging from 0 kHz to 6 kHz. The drive velocity v_d and normal pressures p in the contact area of the upper and lower specimens were identical to those in the experimental tests. The value of the contact stiffness coefficient k_t of the analysed sliding pair contact, at given pressure p, was determined based on curves $k_t = f(p)$ described by equations given in Tab. 2. These relationships were determined experimentally for the tested sliding pairs in the range of normal pressures from p = 0.014 N/mm² to p = 0.112 N/mm², in accordance with the procedures presented in the study of Leus and Gutowski [36].

Tab. 2. Regression equations and the values of curves $k_t = f(p)$ correlation coefficient R^2 for given sliding pairs

Sliding pair	Regression equation, $k_t = f(p)$	Correlation coefficient R^2
C45–C45	$k_t = 917.36p^2 + 289.22p + 55.663$	0.9899
C45–GGG40	$k_t = 4089.9p^2 + 186.42p + 44.116$	0.9955
C45–PTFE	$k_t = -57.381p^2 + 46.7p + 2.1792$	0.9891

Values of contact stiffness coefficients k_t of tested sliding pairs at normal pressures at which the simulation analyses have been performed are given in Table 3.

Tab. 3. Values of contact stiffness coefficients k_t of sliding pair contact at normal pressures p assumed in performed tests

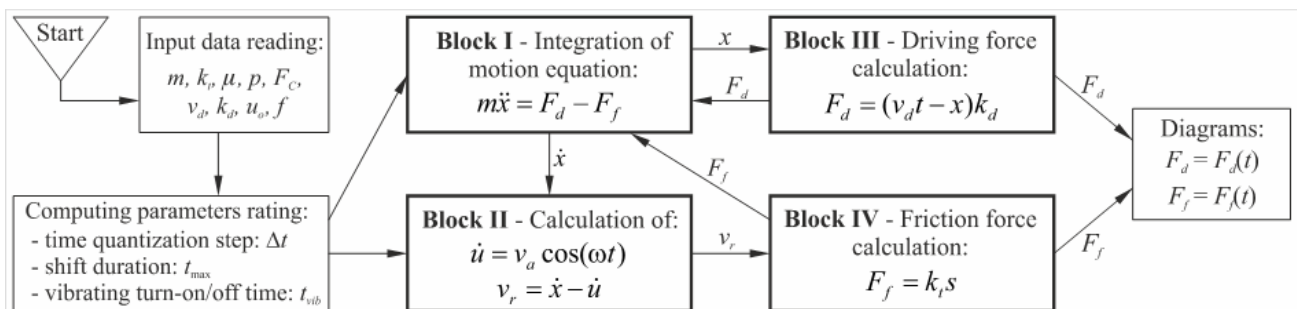| Sliding pair | k_t [N/μm] | | |
	p = 0.022 [N/mm²]	p = 0.063 [N/mm²]	p = 0.112 [N/mm²]
C45–C45	62.47	77.52	95.66
C45–GGG40	50.20	72.15	107.74
C45–PTFE	3.18	4.89	6.42

Fig. 4. Algorithm for calculating the friction force in sliding motion at longitudinal vibrations

In the simulation analyses, it was assumed that the stiffness of the drive system was $k_d = 0.92$ N/μm. This value was determined experimentally on the test stand as described in the study of Leus [5]. Moreover, it was assumed that the damping of the drive was negligible. Such an assumption was made because there were no sliding joints between the driver and the movable upper sample, in which the vibration energy could be dissipated, and all drive elements between the driver and this sample were steel elements with very low material damping. It was therefore assumed that the drive damping coefficient was $h_d = 0$.

It was also assumed that the mass of the sliding upper steel sample together with the additional weight attached to it was $m = 1.665$ kg and that the coefficients of friction of the tested sliding pairs were $\mu_1 = 0.193$, $\mu_2 = 0.176$ and $\mu_3 = 0.071$, for the steel–steel pair, steel–cast iron pair and steel–PTFE pair, respectively. These values were determined on the same test stand on which the experimental tests of friction force reduction under the influence of vibrations, described in this paper, were carried out.

In the conducted simulation analyses, at each measurement point, the calculations were started with the upper sample immobile and the ground immobilised. Therefore, it was assumed that at the initial moment for the sliding sample, $x_o = 0$ and $\dot{x} = 0$, and the amplitude of the ground vibrations at the initial moment was $u_o = 0$. The vibrations of the ground were excited for some time after the start of the sliding movement of the upper sample. In the simulation analyses described in the paper, this time was $t = 0.04$ s. The friction pair materials used in the experimental tests and adopted in the numerical analyses, such as C45 steel, GGG40 cast iron and PTFE, can be classified as ductile materials. Therefore, the shape factor α in the Dahl model and in the elastoplastic model for these materials, according to the data contained in the study of Dahl [33], must meet the condition $\alpha \geq 1$. In this paper, in simulation analyses, the value $\alpha = 1$ was assumed.

To evaluate the effectiveness of the friction force reduction, the dimensionless value of parameter ρ was adopted and described by the following relationship:

$$\rho = \frac{\bar{F}_f}{F_C} \tag{4}$$

where $\bar{F}_f$ is an average friction force in the contact of a given friction pair during one period of vibrations, corresponding to the value of drive force F_d necessary to introduce the body into sliding motion and maintain this motion, with set vibration parameters f and u_o, drive velocity v_d and normal pressures p, while F_C is the Coulomb friction force, i.e. the friction force without vibrations.

The average value $\bar{F}_f$ of the friction force during one vibrations period T can be determined in numerical analyses from the following relationship:

$$\bar{F}_f = \frac{1}{n} \sum_{i=1}^{n} F_f(t + i\Delta t) \tag{5}$$

where n is the number of time steps Δt into which one period T of vibrations was divided.

The value $\rho = 1$ means no reduction of friction force, while when $\rho < 1$, the reduction takes place. The smaller the value of parameter ρ, the greater the reduction of friction force.

Figs. 5 and 6 summarise the results of simulation studies and the corresponding results of experimental tests in the form of collective diagrams. These figures present plots of variations of the parameter ρ as a function of forced vibrations frequency f for four fixed drive velocities, namely 0.2 mm/s, 0.5 mm/s, 1 mm/s

and 2 mm/s. Numerical waveforms are marked with lines, while the results of experimental tests are marked with points. Fig. 5 presents the results obtained for the sliding steel–steel pair for three values of normal pressures, namely $p = 0.022$ N/mm^2, 0.063 N/mm^2 and 0.104 N/mm^2, while the results presented in Fig. 6 pertain to the analyses carried out for the sliding steel–cast iron pair (Fig. 6a) and the steel–PTFE pair (Fig. 6b). These analyses were performed at normal pressures, $p = 0.063$ N/mm^2.

The graphs presented in Figs. 5 and 6 show the average values of three measurement results together with marked standard deviations. It should be emphasised that very good repeatability of the results was obtained in subsequent repetitions. This is evidenced by the value of standard deviations, which for the most part did not exceed the level of 4% of the average value determined at a given measurement point. The very good repeatability of the results proves that the number of repetitions has no significant effect on the quality of conclusions regarding the nature of the studied phenomenon.
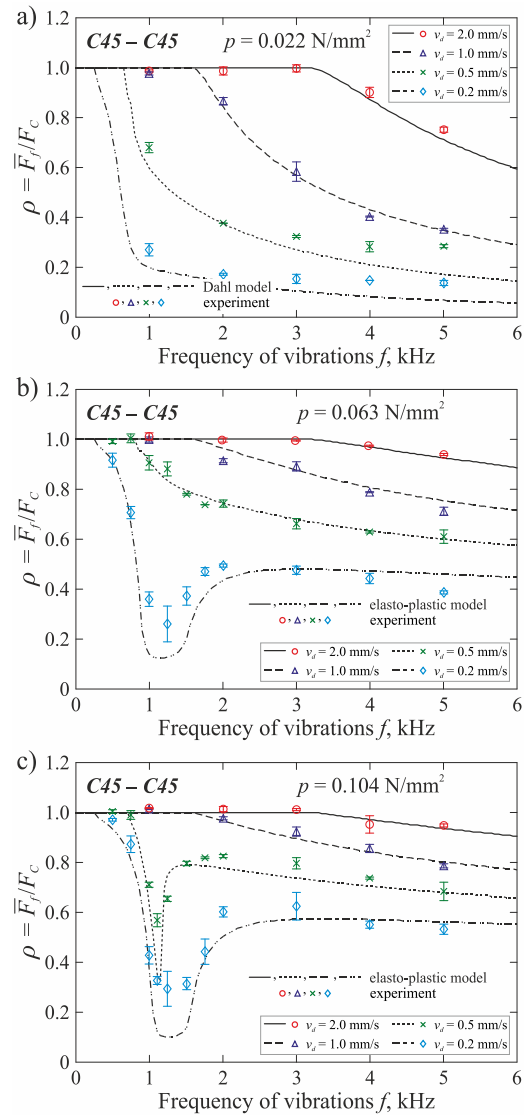

Fig. 5. Effectiveness of friction force reduction for joint steel–steel as a function of vibrations frequency f at their fixed amplitude $u_o = 0.1$ μm and different normal pressures: (a) $p = 0.022$ N/mm^2, (b) $p = 0.063$ N/mm^2 and (c) $p = 0.104$ N/mm^2

The results of experimental tests and numerical analyses presented in Figs. 5 and 6 clearly indicate that, when the condition $v_a > v_d$ was not fulfilled, introducing longitudinal tangential vibrations into the contact area of the sliding body and the ground did not change the friction force. For the drive velocities adopted in the tests v_d = 2 mm/s, 1 mm/s, 0.5 mm/s and 0.2 mm/s, the boundary frequencies at the beginning of the friction force reduction at longitudinal vibrations with the amplitude u_o = 0.1 µm, according to Eq. (3), are 3183 Hz, 1591.5 Hz, 795.75 Hz and 318.3 Hz, respectively. The reduction occurred only in the case where $v_a > v_d$ and it was the higher, the higher was the frequency of forced vibrations f and the lower was the drive velocity v_d.

The comparison of the plots in Fig. 5 for the friction steel–steel pair indicates that the level of friction force reduction depends on the normal pressures p. These plots clearly show that with the increase in normal pressures on the contact surface, the value of the parameter ρ visibly increased, which means that the increase in normal pressures caused a lowering of the level of friction force reduction.
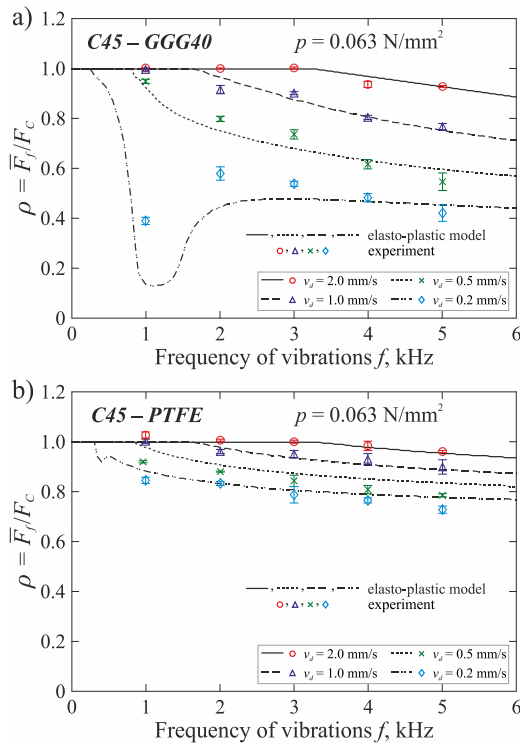

Fig. 6. Effectiveness of friction force reduction as a function of vibrations frequency f at their fixed amplitude u_o = 0.1 µm for joints: (a) steel–cast iron and (b) steel–PTFE; p = 0.063 N/mm²

In turn, when comparing the friction force reduction curves for different materials of friction pairs as presented in Figs. 5b, 6a and 6b, determined with the same vibration parameters u_o and f, the same pressures p and the same drive velocities v_d, it can be noticed that definitely the smallest of friction force reduction under the influence of longitudinal tangential vibrations occurs in the joint steel–PTFE pair. However, in the case of the two remaining friction pairs, i.e. steel–steel and steel–cast iron, the level of friction force reduction was definitely higher – the highest was for the steel–steel contact, while that for the steel–cast iron contact was only slightly less. In all three presented cases, the vibrations parameters, such as amplitude u_o and frequency f as well as drive velocity v_d and surface pressures p, were the same in tests. The

frictional pairs differed in the kind of material of the lower specimen and the roughness of this sample's surface. Therefore, the tangential compliance of contact of these pairs was also different. At the pressure p = 0.063 N/mm², the stiffness coefficients k_t of the tested contacts, in accordance with the equations given in Tab. 3, were derived as k_t = 77.5 N/µm, k_t = 72.09 N/µm and k_t = 4.89 N/µm for steel–steel pair, steel–cast iron pair and steel–PTFE pair, respectively. It can be noticed that the tangential stiffness of the steel–PTFE contact was definitely lower than that of the other two contacts. Hence, a significantly lower level of friction force reduction was obtained in this contact as compared with the other two friction pairs. This result is consistent with the results of the study of Gutowski and Leus [4].

The results of friction force reduction obtained at low frequencies of 0.5–1.5 kHz and higher pressures p = 0.063 N/mm² (Fig. 5b and Fig. 6a) and p = 0.104 N/mm² (Fig. 5c) for steel – steel and steel – cast iron pairs that deviate from the clear trend require a separate comment. The reason for this happening was probably the fact that at these frequencies and these surface pressures, the phenomenon of resonance occurs for the shifted specimen.

To prove the appearance of this resonance from the numerical model developed in Matlab/Simulink, for the analysis of the impact of vibrations on the friction force, displacement diagrams of the upper sample being moved during the ground vibrations were generated. They were generated at various normal pressures p. These diagrams are shown in Fig. 7. They clearly indicate that at the assumed normal pressures, in the excitation frequency range of f = 500–1500 Hz, the system is subject to the phenomenon of resonance.
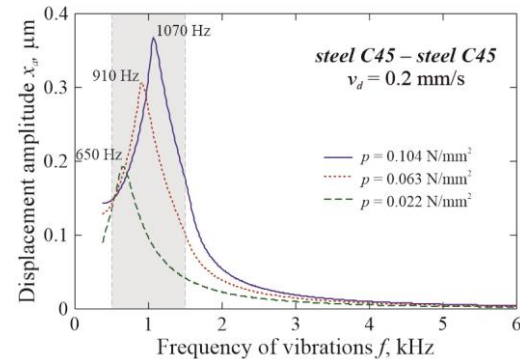

Fig. 7. Diagrams of the displacement of the upper sample on a vibrating ground, illustrating the occurrence of resonance in the frequency range f = 500–1500 Hz

4. REDUCTION OF FRICTION FORCE AT A FIXED AMPLITUDE OF VIBRATIONS VELOCITY

When analysing the influence of longitudinal tangential vibrations on the friction force in sliding motion, the most important parameter is the amplitude of the vibration velocity v_a, because its value determines the upper limit of the sliding velocity – the drive velocity – above which the reduction of the friction force does not occur. In harmonic motion, the value of this amplitude is determined based on dependence (3), which means that in real systems, it can be controlled by two vibration parameters: amplitude u_o and frequency f, which are changed simultaneously; or, one of them is at a fixed value with respect to the other parameter.

In this paper, this problem is illustrated by presenting the results of experimental and numerical tests of changes in the level

of friction force reduction at the amplitude of vibration velocity v_a fixed at the level that guarantees the occurrence of the friction force reduction, i.e. $v_a > v_d$, but with a different set of the vibration parameters u_o and f, while maintaining a constant value of vibration velocity amplitude, v_a = const. Here, v_a = 1.256 mm/s was assumed.

The tests were carried out for the same friction pairs as in the previous case, with five frequencies of forced vibrations f, namely 1 kHz, 2 kHz, 3 kHz, 4 kHz and 5 kHz, and for four drive velocities: v_d = 0.2 mm/s, 0.5 mm/s, 1 mm/s and 2 mm/s. In order to maintain a constant value of the vibration velocity amplitude, v_a = const, with each change of frequency f, the value of the amplitude u_o was changed suitably in accordance with the dependence (3). As before, these measurements were made at three selected values of normal pressure: p = 0.022 N/mm², 0.063 N/mm² and 0.104 N/mm². Examples of test results in the form of drive velocity plots for the analysed friction pairs at v_d = 0.5 mm/s and p = 0.063 N/mm² are presented in Fig. 8.
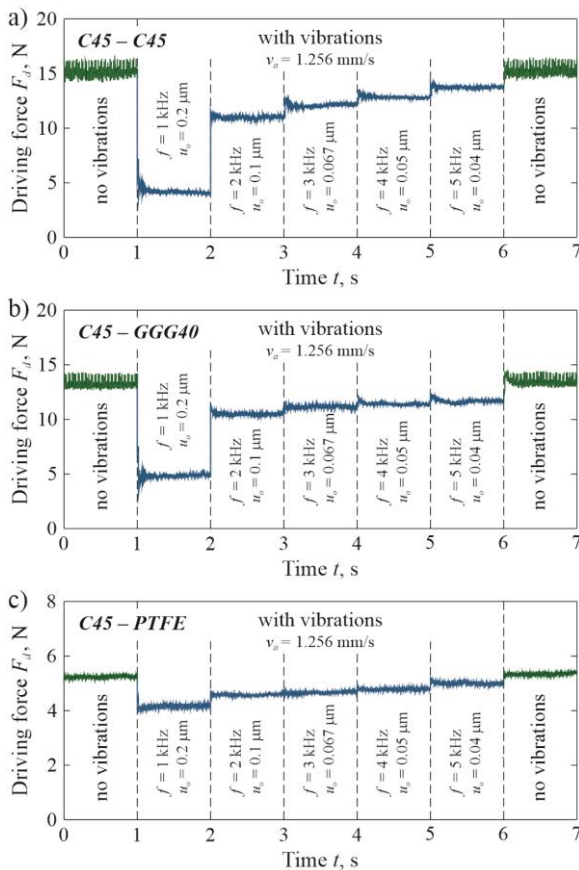

Fig. 8. Variability of the driving force F_d in relation to frequency f and amplitude u_o at fixed amplitude of vibration velocity v_a = const: (a) steel–steel, (b) steel–cast iron and (c) steel–PTFE; p = 0.063 N/mm², v_d = 0.5 mm/s, v_a = 1.256 mm/s

Figs. 9 and 10 present the results of simulation studies and the corresponding results of experimental tests in the form of collective plots. These figures show plots of changes of the parameter ρ as a function of increasing frequency f and correspondingly decreasing vibrations amplitude u_o at a fixed value of vibration velocity amplitude v_a = const for four drive velocities v_d, namely 0.2 mm/s, 0.5 mm/s, 1 mm/s and 2 mm/s. Numerical results are marked with lines, while the results of experimental tests are

marked with points. Fig. 8 presents the results obtained for the sliding steel–steel pair for three values of normal pressures: p = 0.022 N/mm², 0.063 N/mm² and 0.104 N/mm². The results presented in Fig. 10 pertain to the analyses carried out for the sliding steel–cast iron pair (Fig. 10a) and for the steel–PTFE pair (Fig. 10b).
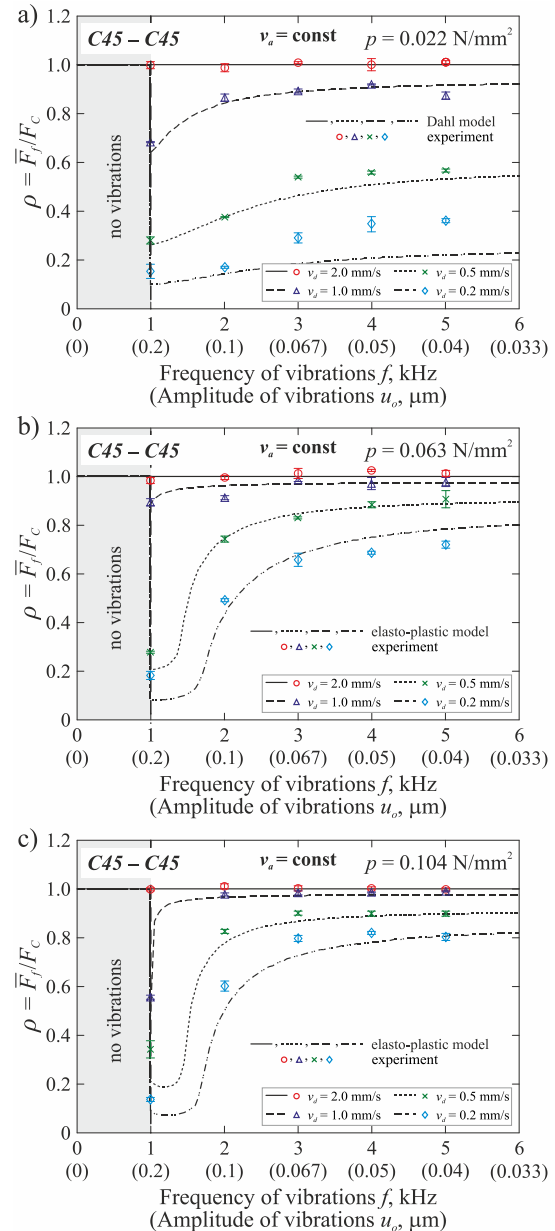
Fig. 9. Change of the reduction coefficient ρ at different pressures p and fixed vibrations velocity amplitude v_a = const caused by increasing the frequency f with a simultaneous reduction of vibrations amplitude u_o for the pair steel–steel: (a) p = 0.022 N/mm², (b) p = 0.063 N/mm², (c) p = 0.104 N/mm²; v_a = 1.256 mm/s

From the obtained results of the experimental tests and numerical analyses presented in Figs. 9 and 10, it can be noticed that when v_d = 2 mm/s, i.e. when the condition that $v_a > v_d$ was not fulfilled, the reduction of friction force did not occur in any of the considered cases. For the three remaining values of v_d = 1 mm/s, v_d = 0.5 mm/s and v_d = 0.2 mm/s, the excitation of vibrations caused a reduction of the friction force, which resulted in the

reduction of the parameter ρ to a value lower than 1. The effectiveness of this reduction is significantly influenced by the ratio of drive velocity v_d to vibration velocity amplitude v_a and excitation frequency f, the kind of material of the sliding pair and the value of normal pressures p in the plane of contact between the shifted body and the ground. The lower the drive velocity v_d relative to the amplitude v_a, the higher the reduction level.

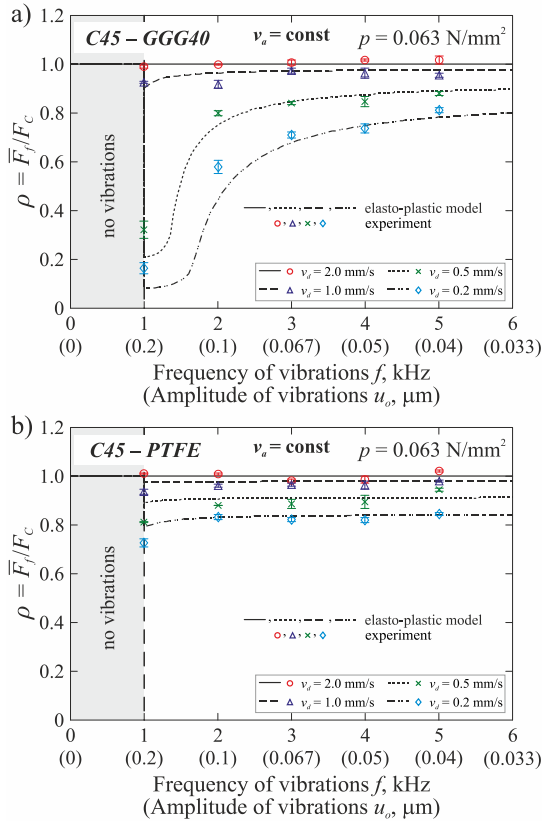**Fig. 10.** Change of the reduction coefficient ρ at fixed vibration velocity amplitude v_a = const, caused by increasing the frequency f with a simultaneous reduction of vibrations amplitude u_o for the pair: (a) steel–cast iron and (b) steel–PTFE; p = 0.104 N/mm²; v_a = 1.256 mm/s

Increasing the frequency of vibrations with a simultaneous reduction of their amplitude, in order to maintain a constant value of the vibrations velocity amplitude, resulted in an increase in the value of the parameter ρ in each of the analysed cases. This means that such a treatment reduces the level of friction force reduction under the influence of longitudinal vibrations introduced into the contact area. As in the previous test variant, the test results from this variant, presented in Figs. 9 and 10, clearly indicate that both the increase in normal pressures on the contact surface of friction pair and the increase in sliding velocity reduce the effectiveness of the friction force reduction.

5. CONCLUSIONS

The conducted simulation analyses and experimental tests demonstrate that the influence of the forced longitudinal tangential vibrations on the friction force in sliding motion is highly complex. These vibrations can cause an explicit reduction of the drive force necessary to start and maintain the slip of one body over another,

but the necessary condition for this reduction to occur is that the vibration velocity amplitude v_a be higher than the drive velocity v_d. However, the value of the parameter v_a cannot be treated as a determinant of the reduction level, because, as shown by the conducted tests, with a constant vibration velocity amplitude v_a, different values of the frequency f and the amplitude u_o of these vibrations, as well as different reduction effectiveness values of the average friction force, can be obtained. The reason is that the amplitude of the vibration velocity is a function of both of the above-mentioned vibration parameters, i.e. their frequency and amplitude of displacement.

The conducted research clearly indicates that the increase in the vibrations frequency with their constant amplitude increases the effectiveness of the friction force reduction under the influence of longitudinal tangential vibrations, while the increase in surface pressure and the increase in drive velocity cause the opposite effect – lowering the level of reduction of this force. In an extreme case, a slip at a velocity higher than the vibration velocity amplitude eliminates the possibility of using longitudinal vibrations to achieve a reduction in friction force.

An important conclusion resulting from the conducted research is that with low contact stiffness, related to the kind of material of the elements forming the friction pair and higher roughness of the contact surfaces, the effect of friction force reduction under the influence of vibrations is visible lower than that obtained in case of contact with high stiffness, and furthermore, the level of this reduction depends to a much lesser extent on the frequency of the vibrations.

There is a very good agreement between the results of numerical calculations and experimental tests, even at resonant frequencies of the sliding pair, which proves the correctness of the developed procedures for the analyses of the effect of longitudinal tangential vibrations on the friction force in sliding motion and proves the possibility of using these procedures to control the friction force in the sliding motion of real objects by means of vibrations.

REFERENCES

1. Gutowski P, Leus M. Computational model for friction force estimation in sliding motion at transverse tangential vibrations of elastic contact support. Tribology International. 2015;90:455-462. https://doi.org/10.1016/j.triboint.2015.04.044
2. Gutowski P, Leus M. Computational model of friction force reduction at arbitrary direction of tangential vibrations and its experimental verification. Tribology International. 2020;143:106065. https://doi.org/10.1016/j.triboint.2019.106065
3. Gutowski P, Leus M. Estimation of the tangential transverse vibrations effect on the friction force with the use of LuGre model. Acta Mechanica. 2021;232(10):3849-3861. https://doi.org/10.1007/s00707-021-03033-1
4. Gutowski P, Leus M. The effect of longitudinal tangential vibrations on friction and driving forces in sliding motion. Tribology International. 2012;55:108-118. https://doi.org/10.1016/j.triboint.2012.05.023
5. Leus M. Investigation of the longitudinal tangential contact vibrations influence on the friction force. Doctoral thesis. 2010.
6. Leus M, Gutowski P. Practical possibilities of utilization of tangential longitudinal vibrations for controlling the friction force and reduction of drive force in sliding motion. Mechanics and Mechanical Engineering. 2011;15(4):103-113.
7. Rybkiewicz M, Gutowski P, Leus M. Experimental and numerical analysis of stick-slip suppression with the use of longitudinal tangential vibration. Journal of Theoretical and Applied Mechanics. 2020;58(3):637-648. https://doi.org/10.15632/jtam-pl/116594

Mariusz Leus, Paweł Gutowski, Marta Rybkiewicz

DOI 10.2478/ama-2023-0057

Effectiveness of Friction Force Reduction in Sliding Motion Depending on the Frequency of Longitudinal Tangential Vibrations, Sliding Velocity and Normal Pressure

8. Rybkiewicz M, Leus M. Selection of the friction model for numerical analyses of the impact of longitudinal vibration on stick-slip movement. Advances in Science and Technology Research Journal. 2021;15(3):277-287. https://doi.org/10.12913/22998624/141184

9. Gao H, De Volder M, Cheng T, Bao G, Reynaerts D. A pneumatic actuator based on vibration friction reduction with bending longitudinal vibration mode. Sensors and Actuators A: Physical. 2016;252:112-119. https://doi.org/10.1016/j.sna.2016.10.039

10. Kapelke S, Seemann W. On the effect of longitudinal vibrations on dry friction: Modelling aspects and experimental investigations. Tribology Letters. 2018;66(3):1-11.
    https://doi.org/10.1007/s11249-018-1031-0

11. Kapelke S, Seemann W, Hetzler H. The effect of longitudinal high-frequency in-plane vibrations on a 1-DoF friction oscillator with compliant contact. Nonlinear Dynamics. 2017;88:3003-3015.
    https://doi.org/10.1007/s11071-017-3428-y

12. Kumar VC, Hutchings IM. Reduction of sliding friction of metals by the application of longitudinal or transverse ultrasonic vibration. Tribology International. 2004;37(10):833-40.
    https://doi.org/10.1016/j.triboint.2004.05.003

13. Kutomi H, Sase N, Fujii H. Development of friction controller. Proceedings of the International Conf AMPT'99. 1999;I:605-612.

14. Littmann W, Stork H, Wallaschek J. Reduction of friction using piezoelectrically excited ultrasonic vibrations. Proceedings of the SPIE's 8th Annual International Symposium on Smart Structures and Material, Billingham, Washington 2001. 2001;302-311.
    https://doi.org/10.1117/12.432714

15. Littmann W, Stork H, Wallaschek J. Sliding friction in the presence of ultrasonic oscillations: superposition of longitudinal oscillations. Archive of Applied Mechanics. 2001;71:549-54.
    https://doi.org/10.1007/s004190100160

16. Liu W, Ni H, Wang P, Zhao B. Analytical investigation of the friction reduction performance of longitudinal vibration based on the modified elastoplastic contact model. Tribology International. 2020;146:106237. https://doi.org/10.1016/j.triboint.2020.106237

17. Qu H, Zhou N, Guo W, Qu J. A model of friction reduction with in-plane high-frequency vibration. Proceedings of the Institution of Mechanical Engineers. Part J: Journal of Engineering Tribology. 2016;230(8):962-967. https://doi.org/10.1177/135065011562101

18. Sase N, Kurahashi T, Fujii M, Kutomi H, Fujii H. Control of friction coefficient between metal surfaces. Proceedings of the International Conference AMPT'97. 1997;2:609-615.

19. Storck H, Littmann W, Wallaschek J, Mracek M. The effect of friction reduction in presence of ultrasonic vibrations and its relevance to traveling wave ultrasonic motors. Ultrasonic. 2002;40:379-383.
    http://dx.doi.org/10.1016/S0041-624X(02)00126-9

20. Teidelt E, Starcevic J, Popov VL. Influence of ultrasonic oscillation on static and sliding friction. Tribology Letters. 2012;48:51-62.
    https://doi.org//10.1007/s11249-012-9937-4

21. Tsai CC, Tseng CH. The effect of friction reduction in presence of in-plane vibrations. Archive of Applied Mechanics. 2006;75:164-76.
    https://doi.org/10.1007/s00419-005-0427-0

22. Wang P, Ni H, Wang R, Li Z, Wang Y. Experimental investigation of the effect of in-plane vibrations on friction for different materials. Tribology International. 2016;99:237-247.
    https://doi.org/10.1016/j.triboint.2016.03.021

23. Wang P, Ni H, Wang R, Liu W, Lu S. Research on the mechanism of in-plane vibration on friction reduction. Materials. 2017;10(9):1-21.
    https://doi.org/10.3390/ma10091015

24. Yang CL, Wu CS, Shi L. Analysis of friction reduction effect due to ultrasonic vibration exerted in friction stir welding. Journal of Manufacturing Processes. 2018;35:118-126.
    https://doi.org/10.1016/j.jmapro.2018.07.025

25. Shao G, Li H, Zhan M. A Review on Ultrasonic-Assisted Forming: Mechanism, Model, and Process. Chinese Journal of Mechanical Engineering. 2021;34(1):99.
    https://doi.org/10.1186/s10033-021-00612-0

26. Chovdhury MA, Helali MM. The effect of frequency of vibration and humidity on the coefficient of friction. Tribology International. 2006;39(9):958-962. https://doi.org/10.1016/j.triboint.2005.10.002

27. Chovdhury MA, Helali MM. The effect of amplitude of vibration on the coefficient of friction for different materials. Tribology International. 2008;41(4):307-314. https://doi.org/10.1016/j.triboint.2007.08.005

28. Hess DP, Soom A. Normal vibrations and friction under harmonic loads: part I – Hertzian contacts. Journal of Tribology. 1991;113(1):80-86. https://doi.org/10.1115/1.2920607

29. Popov M, Popov VL, Popov NV. Reduction of friction by normal oscillations. I. Influence of contact stiffness. Friction. 2017;5(1):45-55.
    https://doi.org/10.1007/s40544-016-0136-4

30. Xinyu M, Popov VL, Stracevic J, Popov M. Reduction of friction by normal oscillations. II. In-plane system dynamics. Friction. 2017;5(2):194-206. https://doi.org/10.1007/s40544-017-0146-x

31. Cheng Y, Zhu PZ, Li R. The influence of vertical vibration on nanoscale friction: a molecular dynamics simulation study. Crystals. 2018;8(3):129. https://doi.org/10.3390/cryst8030129

32. Dahl PR. A solid friction model. Technical Report TOR-158(3107-18), The Aerospace Corporation, El Segundo, CA. 1968.

33. Dahl PR. Solid friction damping of mechanical vibrations. AIAA Journal. 1976;14(12):1675-1682. https://doi.org/10.2514/3.61511

34. Dupont P, Armstrong B, Hayward V. Elasto-plastic friction model: contact compliance and stiction. Proceedings of the American Control Conference, Chicago, Illinois 2000. 2000:1072-1077.
    https://doi.org/10.1109/ACC.2000.876665

35. Dupont P, Hayward V, Armstrong B, Altpeter F. Single state elasto-plastic friction models. IEEE Transactions on Automatic Control. 2002;47(5):787-792. https://doi.org/10.1109/TAC.2002.1000274

36. Leus M, Gutowski P. The experimental analysis of the tangential stiffness of the flat contact joints. Modelling in Engineering. 2009;6(37):185-192 [in Polish].

Mariusz Leus: https://orcid.org/0000-0002-1073-1734

Paweł Gutowski: https://orcid.org/0000-0002-0618-2357

Marta Rybkiewicz: https://orcid.org/0000-0002-6584-033X

EXPERIMENTAL INVESTIGATION OF A UNIAXIAL DIELECTRIC ELASTOMER GENERATOR

Wojciech SIKORA*

*Faculty of Mechanical Engineering and Robotics, Department of Machine Design and Maintenance,
AGH University of Krakow, al. Mickiewicza 30, 30-059 Kraków, Poland*

wosikora@agh.edu.pl

Abstract: The widespread use of battery-powered electronic devices creates the need to develop methods to extend their maximum operating time. This can be achieved by using ambient energy, which would otherwise be dissipated. The conversion of energy, usually mechanical energy, into electric energy takes place in energy harvesters. Energy harvester systems based on a dielectric elastomer (DE) are a relatively new field that is being constantly developed. Due to their features, dielectric elastomer generators (DEGs) may complement the currently dominant piezoelectric harvesters. The major feature of employing a hyperelastic material is that it allows relatively large displacements to be utilised for generating energy, which is impossible in the case of piezoceramics. This article presents a DEG designed to operate under uniaxial tensile loads and which has a multilayer structure, describes the general operating principles of a DEG, explains the construction and assembly process of the investigated design and shows the electric circuit necessary to properly direct current flow during the DEG operation. The experimental part consists of two series of tests based on a central composite design (CCD). The objective of the first part was to map a capacitance response surface of the DEG in the selected range of the cyclic mechanical load. The second part concerned the amount of generated energy for the specific load case as a function of operating voltages. The result of the work is the formulation of regression models that allow the characteristics of the presented DEG design to be identified.

Key words: dielectric elastomer, energy harvester, DEG, uniaxial tension

1. INTRODUCTION

The utilisation of ambient energy, by harvesting it using dedicated devices and converting it into electric energy, allows the extension of the operating time of small electronics or even the design of self-powered systems. The use of the energy that would otherwise be dissipated also corresponds to the trend of sustainability and ensures that available resources are used in the best way currently possible.

The most common harvester systems are based on piezoelectricity [1,2] or electromagnetics [3,4]. Another group are dielectric elastomer generators (DEGs), which utilise changing capacitance to convert mechanical energy into electric energy. As piezoelectric devices are a well-known and popular solution for harvesting ambient energy, it is convenient to consider dielectric elastomer (DE) features compared with them. The major characteristic of DE devices is the utilisation of a hyperelastic material with stiffness several orders lower than that of piezoelectric materials (especially ceramics). In combination with the fact that DEGs, for proper operation, usually require quite large deformations, it can be concluded that piezoelectric generators cannot be directly replaced by DEGs, and vice versa. Piezoceramics undergo small strains and are highly vulnerable to tensile loads. Thus, DEGs can fulfil the role of a complementary solution to piezoceramics in the field of energy harvesting.

Similarly to piezoelectric devices, systems utilising DEs can function not only as generators but also as actuators (DEA, dielectric elastomer generator). Design challenges are common for both types of devices, especially regarding assembly, electric breakdown or mechanical stability. DE actuators are an important seg-ment of soft robotics, where they are used in biomimetic robots and manipulators [5,6].

The majority of studies concerning DEGs describe the laboratory tests of various prototypes, with generated energy in the range of micro- or milliwatts [7,8]. Nonetheless, there are a few examples of large-scale projects that provide more power and are mainly designed for the conversion of kinetic energy of sea waves [9,10].
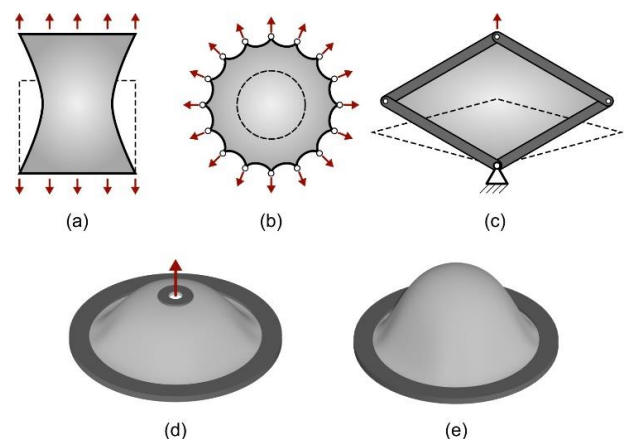

Fig. 1. DEG common types: (a) uniaxial, (b) equibiaxial, (c) diamond, (d) conical, (e) diaphragm

From the mechanical standpoint and based on how they are physically loaded during operation, DEGs can be divided into the following major types [11], as shown in Fig. 1:

- uniaxial,
- equibiaxial,
- diamond,
- conical,
- circular diaphragm.

Each of these designs has benefits and drawbacks, but cone and diaphragm types are most commonly used due to their relatively easy assembly and application. To ensure mechanical stability and avoid buckling during the DEG operation, it is necessary for the elastomer layer to be pretensioned. For a single layer, this is easily achieved in the designs from Fig. 1c–e; it is not required in the equibiaxial variant (Fig. 1b) and is problematic in the case of uniaxial designs (Fig. 1a). For a uniaxial DEG, there is no axial symmetry, especially in a boundary fixture, like in circular designs. Nonetheless, the pretension has to be applied in both axial and transverse directions to maintain the mechanical stability of the layer during cyclic operation.

This article presents an experimental investigation of a DEG operating in a uniaxial mode. It has a multilayer structure with compliant electrodes enclosed between external, elastomer layers. The performed analysis considers a capacitance change and the amount of generated energy of the given DEG design. The observations are further presented in the form of linear regression models, enabling interpolation and, to an extent, extrapolation of the registered data.

2. PRINCIPLE OF OPERATION

The most important trait of a DEG is the requirement to connect it to a DC voltage supply. Initially, this seems counter-intuitive as a DEG aim is to generate electric energy. However, its function does not depend on directly generating potential difference as a response to a physical deformation. A typical elastomer material does not have any inherent piezoelectric properties that would allow such behaviour. Instead, a DEG's actual task is to boost the electric potential of the fixed amount of electric charge.

In general, elastomers are dielectric materials and, therefore, can function as a core material in a plate capacitor. By covering opposite sides of an elastomeric sheet with a conductive layer that performs the role of a compliant electrode, such a capacitor can be created. It is, in fact, a non-polarised variable capacitor as, by applying physical deformation to it, its capacitance will change. This is crucial to the operating principle of DEGs.
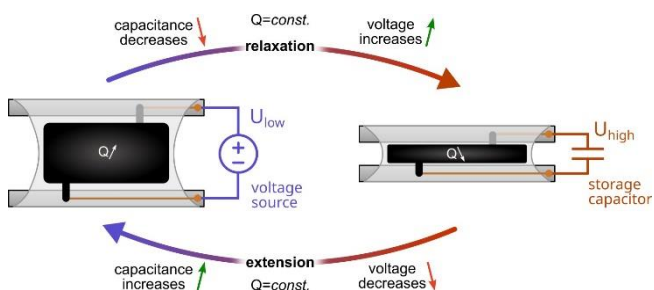

Fig. 2. Operating principle of a uniaxial DEG

Fig. 2 presents the working principle diagram of a DEG based on an elastomer membrane undergoing a uniaxial load. The left side shows a stretched (physically loaded) membrane with a conductive (black) area, which performs the role of an electrode. It

also has to be mirrored on the underside of the membrane to obtain the opposite electrode of the same shape and area. At this stage, the DEG has to be connected, through terminals, to a DC supply which provides a constant voltage (U_{low}). This may be a battery or a laboratory supply. Charge flows to the electrodes till the voltage reaches U_{low}. The final amount of accumulated charge is adequate to U_{low} and the actual capacitance of the system. Capacitance is maximum at this stage as the elastomer is deformed and has an increased area. During the transition to the relaxed state (on the right), system capacitance decreases due to membrane area reduction. To ensure that the charge remains constant, the connection with the voltage source U_{low} has to be separated to prevent the charge flowing out. For the separated system to maintain equilibrium, voltage between the electrodes has to increase with decreasing capacitance. This phenomenon occurs due to the conversion of mechanical energy (elastic return of the elastomer) into electric energy (increased potential of the charge), which is caused by mechanical forces overcoming electrostatic forces between elastomeric capacitor electrodes. At that point, to receive the uplifted charge, another circuit has to be connected to the system. This is usually some storage capacitor which has to be already initially charged up to the high voltage U_{high}. It is assumed that the system's voltage after membrane relaxation is $U > U_{high} > U_{low}$. Therefore, the excess charge flows from the system to the storage capacitor, which corresponds to the amount of generated electric energy. After stretching the membrane again, the whole cycle repeats. The DEG function can be best described as similar to that of a "charge pump" that moves the electric charge from U_{low} to U_{high}.

It is important to note that, in an actual system, the periods of charging and discharging the elastomeric capacitor take place not at specific points but during fragments of, appropriately, loading and relaxing half cycles. This will be shown later in Fig. 13 on the registered voltage and charge signals.

3. PREPARATION OF SAMPLES

A thin membrane stretched between two bars subject to a uniaxial load, as a general concept, is often referenced in the literature. However, practical tests of such a DEG are seldom presented. More often DE systems of similar construction, but operating as actuators, can be found [12].

Fig. 3 shows consecutive assembly steps of a DEG. It starts with preparation of a small strip (50 mm × 30 mm × 1 mm) of VHB4910 acrylic foam, which is next stretched ca. 3.6 times in both, perpendicular, directions. As the stretch is applied only along two opposite edges, the silhouette of the expanded layer resembles an hourglass. The first practical problem arises with the practical realisation of a simultaneous expanding layer in two directions. This was performed with the help of a scissor mechanism that can be used for this purpose [13]. The prepared layer was next transferred to the surface of two, parallelly aligned, bars fixed in place at a constant distance of 36 mm from each other. In the physical sample, this constant distance was ensured by two extra L-shaped profiles screwed to the sides of bars, which were removed after the DEG was mounted in the test rig. Excessive parts of the layer were cut (red hatching in Fig. 3). Next, a thin layer of conductive grease (MG Chemicals 846-80G) was applied in the middle and strips of metallic tape that serve as connection terminals were placed. It is crucial that metallic paths have to be

located in the part of the layer that does not deform during operation, otherwise it would lead to an imminent rupture of the layer during operation. The exact same procedure was carried out for the second and the third layers, but in the case of the third one, no conductive grease nor metallic paths were placed. Fig. 3 shows a DEG section of a fully assembled sample.
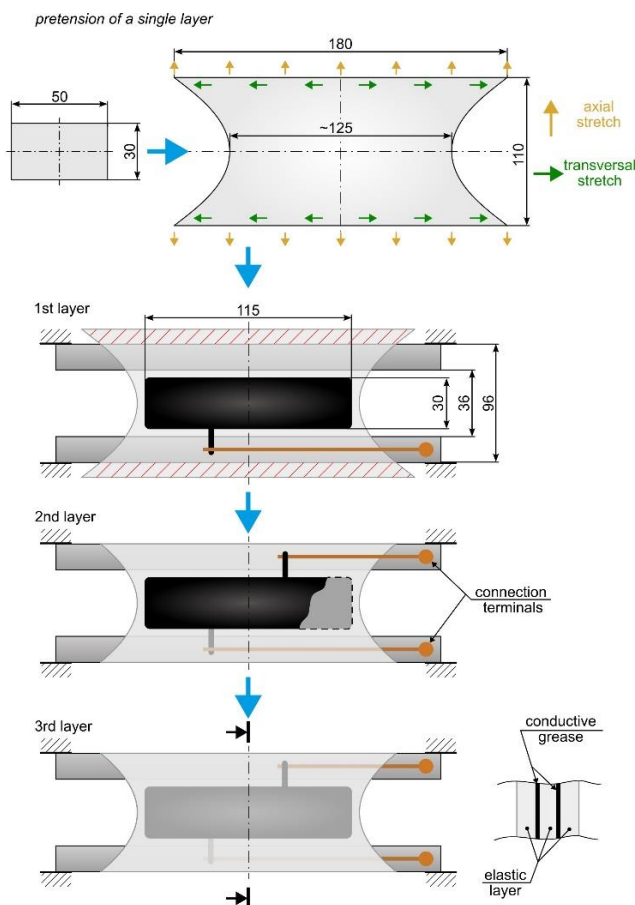

Fig. 3. Assembly stages of the DEG

Fig. 4. Mounted DEG sample on the test rig

The conductive layer has significant internal resistance. For a given area of ca. 115×30, resistance measured diagonally is around $20 \div 30 \ \mathrm{k\Omega}$. To minimise the distance along the conductive layer that the electric charge has to travel, four, instead of one (in Fig. 3), connections between the metallic paths and the active area were placed for both electrodes. This can be seen in Fig. 4 and it allowed the effective resistance of the conductive layer to be reduced to ca. $5 \ \mathrm{k\Omega}$.
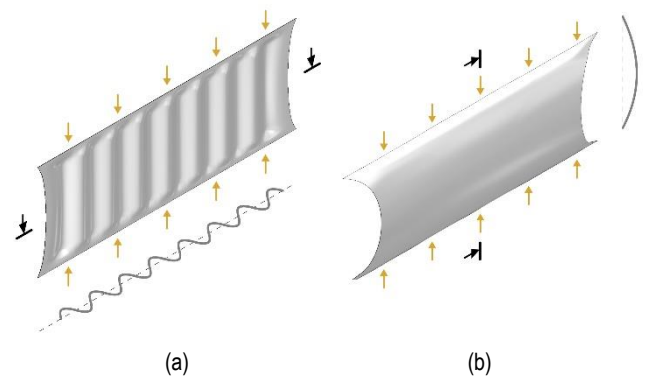

(a)   (b)

Fig. 5. Possible mechanical instabilities (buckling) appearing in an elastomeric membrane during unloading due to insufficient pretension in the (a) transverse, (b) axial direction

The importance of a preliminary stretch of elastic layers can be illustrated through Fig. 5. Due to the viscoelastic properties of the utilised elastomeric material, during cyclic loading of a sample, in an unloading half-cycle when the displacement speed is too great, the layer can temporarily lose its tension causing mechanical instability. When the relaxation is too fast in the transverse direction, it generates wrinkles similar to those in Fig. 5a; when it happens in the axial direction, the layer forms a bulge (Fig. 5b). While the second case can be easily dealt with by applying higher mean displacement during cyclic loading, the first one can only be diminished through applying the proper transverse pretension of a layer during sample assembly.

The multilayer structure in the presented construction is dictated by improved handling of the sample. Such a DEG could be assembled using only one elastic layer, however, active conductive areas would be exposed and more prone to accidental damage. Moreover, using three layers makes connection of the underside electrode easier. The current design is more durable and simpler to handle. It can also be a foundation for future designs utilising additional electrode layers.

4. ELECTRIC CIRCUIT

The generation of electric energy by a DE undergoing cyclic deformation can be conducted only while properly directing the electric current in the whole system. This can be realised with a dedicated circuit (Fig. 6). In general, the most important elements of the circuit are two diodes (2, 3) that function as check valves and prevent reverse current flow. Operational voltage levels are dictated by the lower voltage source (1) and initially charged storage capacitor (4). The DEG itself is, in fact, a non-polarised variable capacitor (5). Voltage U_{low} (1) can be provided by a laboratory power supply with a step-up converter.

Unlike in a laboratory, in field applications of DEGs, providing a constant supply of voltage in the range of hundreds or thousands of volts as U_{low}, can be a practical obstacle. Therefore, a different solution can be found in the literature, for instance, in Ref [14], a classic circuit is expanded by adding a self-priming circuit. When supplied with a 6 V battery, such circuit can prime up the U_{low} voltage level to a given value before transferring the accumulated electric charge further.

The described circuit (Fig. 6) is well known in the field, yet there are some variations of it. The role of a high voltage source is performed by the capacitor (4). However, it is often replaced by a

series of Zener diodes [15], through which current starts to flow after the DEG voltage reaches its equivalent breakdown voltage. Characteristics of such a design are the fixed value of U_{high} and smoother transition between the stages, as described in Fig. 2.
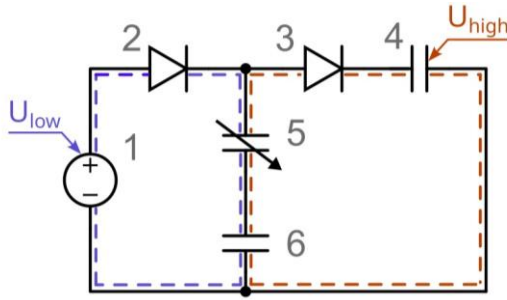

Fig. 6. Electric circuit used for converting energy using a DEG. 1 - low voltage source, 2,3 - diodes, 4 – high-voltage storage capacitor, 5 - variable capacitor (DEG), 6 - capacitor for measuring charge

Another version of the circuit differs by the method of measuring charge flowing in and out of the DEG (5). Here, the measurement is made using an additional capacitor (6) [7] connected in series with the DEG (5). Its capacity (ca. $2.2\,\mu\text{F}$ in this work) should be a few orders higher than that of the DEG (ca. $3.5\,\text{nF}$) so that the voltage drop on it does not significantly affect voltage directly on the DEG. An alternative is to replace the capacitor (6) with a resistor and estimate charge flow through integration of the registered current [15].

As diodes (2, 3) manage the electric current flow, and while charging the DEG, only the left part (violet) of the circuit functions, as shown in Fig. 6,. When the DEG discharges at minimum capacitance, the right part (orange) is active. In between, when the DEG is stretched or relaxed, theoretically, the circuit is inactive as diodes block any current flow. Actually, none of the electronic components are ideal, and leakage currents appear during each of these phases.

5. DESIGN OF EXPERIMENT

The experiment was divided into two parts. One of the major traits influencing the amount of converted energy by the DEG is its capacitance change under a physical load. For the given voltage levels, it determines how much charge can be boosted. Therefore, the first part of the experiment concentrates on the peak-to-peak amplitude ΔC of capacitance during cyclic loading of the sample. Capacitance of the sample was continuously measured using a circuit based on the design described in Ref [16]. The sample was axially loaded with sinusoidally (similar to that in Fig. 7) changing displacement $s(t)$ and at constant frequency f. The remaining parameters, amplitude A and mean displacement m, were changed between test runs. The experiment was performed on an MTS Acumen 3 electrodynamic testing machine.

$$s(t) = m + A \cdot \sin(2\pi f \cdot t) \tag{1}$$

where s is the displacement [mm], m is the mean displacement [mm], A is the amplitude [mm] and $f = 1\,\text{Hz}$ is the frequency.
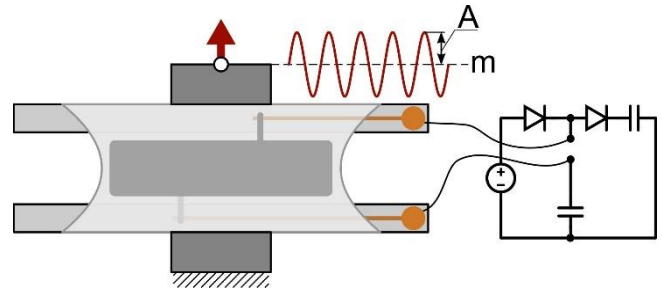
$$\Delta C = g(m, A) \tag{2}$$

Fig. 7. Sample mounted in the test rig connected with an electric circuit during energy generation measurements

For the sample design and dimensions from Fig. 3, in the course of initial runs, limits of selected factors were determined as follows: amplitude $A = 2 \div 8\,\text{mm}$ and mean displacement $m = -2 \div 2\,\text{mm}$. Too small amplitude can reduce DEG performance to immeasurable levels, while too high amplitude can cause membrane buckling during unloading (as in Fig. 5b). Mean amplitude influences average tension in a membrane as it can encourage buckling if it is too low or, in combination with the amplitude, negatively affects the DEG durability if is too high.
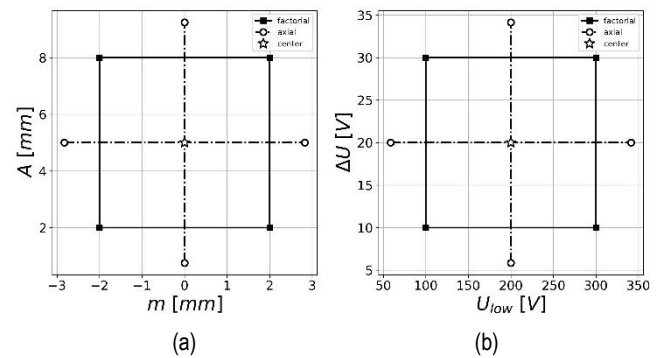
Fig. 8. Design of experiments for investigating (a) capacitance change ΔC (b) generated energy ΔE

These limit values constitute factor points that were next used to plan an experiment based on a central composite design (CCD) [17]. To obtain more general information on the system behaviour, additional points, called central and axial points, were also selected and are presented in Fig. 8a. With three identical samples, three measurements were performed for each of these nine points, giving three replications. Afterwards, the registered data were utilised to fit a linear regression model.

The second part of the experiment was an investigation of the amount of generated energy for the selected point ($A = 8\,\text{mm}$ and $m = 2\,\text{mm}$) from the first part, as a function of U_{low} and ΔU:

$$\Delta U = U_{\text{high}} - U_{\text{low}} \tag{3}$$

$$\Delta E = g(U_{\text{low}}, \Delta U) \tag{4}$$

Apart from the capacitance change, the most important parameters for energy generation in a DEG are voltage levels U_{low} and U_{high}. Lower voltage U_{low} decides on the minimum charge density that is observed in a stretched state (maximum capacitance) of the DEG and, therefore, on the amount of charge that will be later boosted. Instead of directly taking U_{high} into account,

it is more convenient to use the difference ΔU, which determines the level of boost. Extreme values of both U_{low} and U_{high} are limited in theory, from below, by the feasibility of observing phenomena occurring in the DEG, and from the top, by an electric breakdown of the elastomeric layer. Lower voltage levels were assumed as $U_{\text{low}} = 100 \div 300 \, \text{V}$ and the difference as $\Delta U = 10 \div 30 \, \text{V}$, and these values are presented in Fig. 8b. Similarly to the previous part, a total of 27 test runs were performed, and the results were used to fit a linear regression model.

6. RESULTS AND DISCUSSION

The empirical results acquired during the experiments are grouped in Tabs. 1 and 2. The values are sorted in the following order: rows 1–4 correspond to the factor points, row 5 correspond to the central point, and rows 6–9 correspond to the axial points. Before commencing experiments, there was a doubt concerning whether the manufactured multilayer samples would be identical in terms of their electric properties. Presentation of the data in the form of bar plots shows that in both cases, measured capacitance ΔC (Fig. 9) and generated energy ΔE (Fig. 10) differences between samples are very small. Therefore, measurements performed for each sample can be treated as a replication of the same experimental case. Amplitude and mean value of displacement were converted to strains in Tab. 1, using initial DEG length equal to 36 mm (Fig. 3).

Tab. 1. Capacitance ΔC [nF] measurement results

No.	m [mm]	A [mm]	ε_m [-]	ε_A [-]	Sample 1	Sample 2	Sample 3
1	−2	2	−0.056	0.056	0.56	0.53	0.58
2	−2	8	−0.056	0.222	2.17	2.09	2.14
3	2	2	0.056	0.056	0.62	0.6	0.62
4	2	8	0.056	0.222	2.5	2.32	2.44
5	0	5	0	0.139	1.48	1.4	1.48
6	−2.5	5	−0.07	0.139	1.4	1.31	1.38
7	0	1.2	0	0.033	0.35	0.34	0.35
8	0	8.8	0	0.244	2.55	2.43	2.49
9	2.5	5	0.07	0.139	1.58	1.47	1.38

Tab. 2. Energy ΔE [µJ] measurement results

No.	U_{low} [V]	ΔU [V]	Sample 1	Sample 2	Sample 3
1	100	10	2.39	2.22	2.44
2	100	30	5.46	4.75	5.44
3	300	10	7.65	7.33	7.74
4	300	30	21.25	19.5	21.61
5	200	20	9.48	8.94	9.37
6	73.5	20	2.73	2.51	2.82
7	200	7.4	3.24	3.74	3.93
8	200	32.6	14.55	12.42	14.35
9	326.5	20	16.39	15.68	16.16

The first set of data concerns capacity change as a function of displacement mean and amplitude value. From time series, similar to Fig. 13a, a peak-to-peak amplitude of capacitance ΔC was read. Based on these data and with the help of the Python *Stats-*

Models package [18], a regression model was fitted in the following form (capacitance in [nF]):
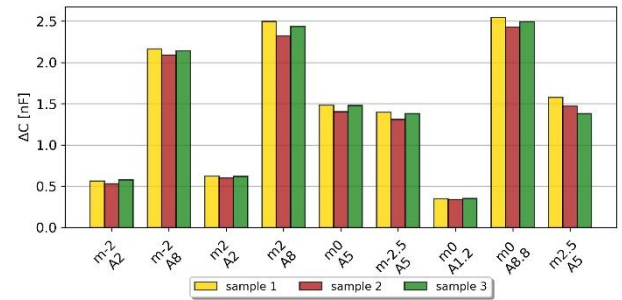
$$\Delta C(m, A) = 0.0339 \, m + 0.2848 \, A \qquad (5)$$

Fig. 9. Comparison of capacitance ∆C experimental results between samples
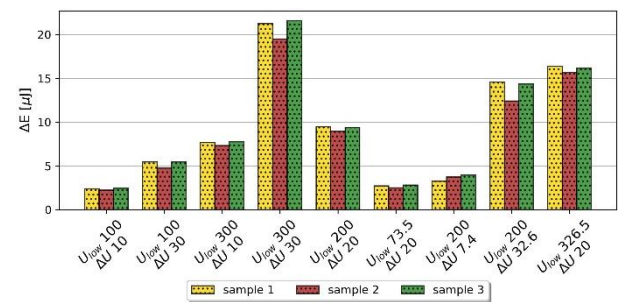
Fig. 10. Comparison of energy ∆E experimental results between samples

Fig. 11. Comparison of experimental and model results for capacitance change estimation. The surface represents the fitted model within the area designated by the factor points

The obtained coefficient of determination $R^2 = 0.998$ and root mean square error $\text{RMSE} = 0.065$ show that the proposed model very well approximates the ∆C parameter in the investigated range. Visualisation of the data in Fig. 11 contains a comparison between mean experimental values and approximations through the model. Additionally, the response surface corresponding to Eq. (5) for the area designated by four factor points is shown there. The surface is practically flat and inclined only in a single dimension. This implies that mean displacement does not have a significant influence on capacitance change. This is because within the investigated range of *m*, a significant change in

the transverse dimension of the elastomer layer did not occur. When mean displacement, also in conjunction with amplitude (which would also further imply an interaction effect between these two factors), is large enough, an increase in the DEG area caused by a uniaxial load would be, in part, diminished by a contraction, due to Poisson's effect, in a transverse direction. This can be observed in the so-called strips [19], which are of a slender shape along the load axis. However, this did not occur in the investigated range of load parameters and should be avoided in practice as it lowers DEG performance.
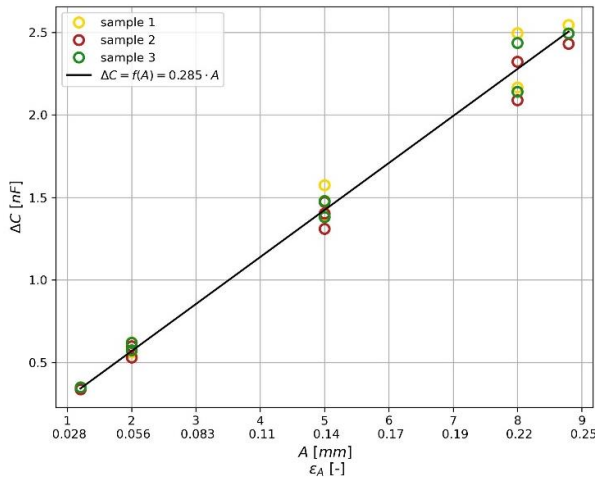
Fig. 12. Comparison between a single-variable regression model and experimental results for capacitance change

Removal of the mean displacement component from Eq. (5) results in a simpler model:

$$\Delta C(A) = 0.2848\, A \tag{6}$$

with a similar value of $R^2 = 0.997$ and comparable RMSE = 0.089. Fig. 12 presents a trend of increasing disparity between the model and experiment with increasing amplitude. This is probably caused by an increasing effect of, omitted here, mean displacement, which, if it has a positive value, can improve minimum tension of the DEG membrane at higher amplitudes. Without the aid of the m part at larger amplitudes (>5 mm), the membrane starts to slightly buckle in the relaxation half-cycle, which only slightly affects the effective capacitance change.

The second part of the experiment consists of the measurement of energy generated by the DEG. This was performed for the sinusoidal displacement of $A = 8\,\mathrm{mm}$ and $m = 2\,\mathrm{mm}$. An example of signals registered during measurements, for the central point (Fig. 8b), where $U_{\mathrm{low}} = 200\,\mathrm{V}$ and $\Delta U = 20\,\mathrm{V}$, is presented in Fig. 13. The first plot (Fig. 13a) shows capacitance variability that follows the external physical load in the form of displacement. The second plot (Fig. 13b) is the voltage between positive and negative electrodes of the DEG, which follows stages described in Fig. 2. Fragments where voltage rises or drops are related to relaxation and stretching of the membrane. Boundaries are determined by low and high voltage, and the signal takes a constant value when the DEG is charged or discharged. Fig. 13c, which presents the amount of electric charge accumulated in the DEG, is a kind of negative of Fig. 13b. When voltage is constant, the charge changes, and vice versa. These two signals, voltage and charge in the DEG, are used to estimate energy generated by the DEG.
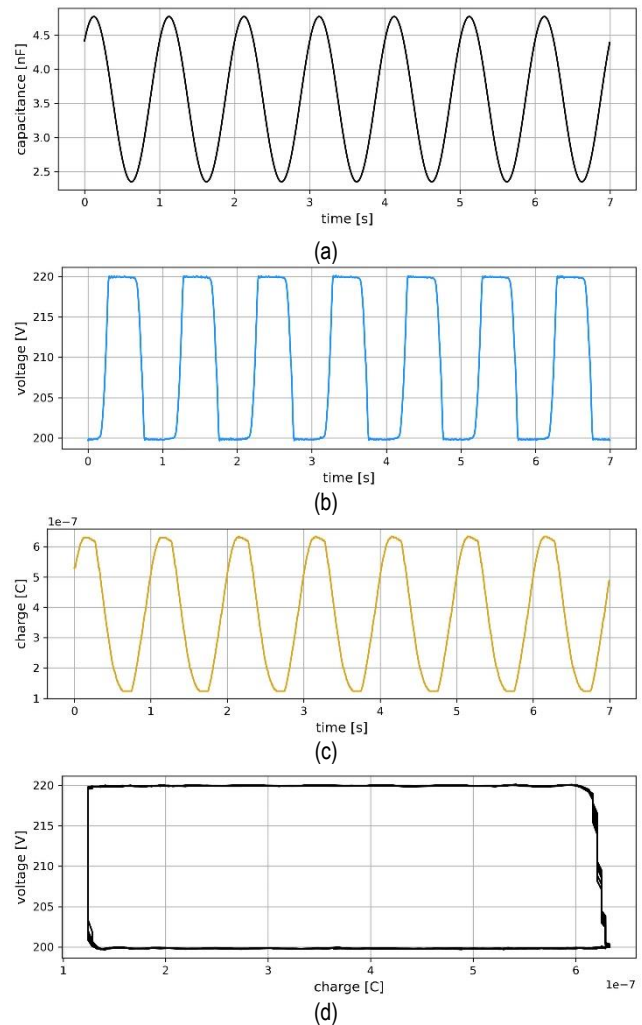
Fig. 13. Signals registered during DEG energy measurement for U_{low} = 200 V and ΔU = 20 V: (a) capacitance, (b) DEG voltage, (c) charge accumulated on the electrodes, (d) U(Q) curve used to estimate energy converted during one full cycle

Fig. 13d sums up the DEG operation and presents voltage as a function of charge. For an ideal system (e.g., in the case of simulation [20]), it should take a rectangular shape. Its area should be equivalent to the amount of energy generated in a single cycle. In the presented case, where curves come from the actual DEG, there are some small leakages, due to which the right side of the rectangle in Fig. 13d is slightly inclined. This can also be seen in Fig. 13c, where charge does not stay perfectly constant at the maximum value. However, in the presented work, it does not significantly influence the amount of generated energy. An example of a similar, but more significant in scale, case can be found in Ref [7], where the mentioned curve has a trapezoidal shape, instead of a rectangular one. Among the sources of such observed behaviour are the diodes (Fig. 6) used in a circuit, through which a very small current flows even when they are in a non-conducting state.

Similarly to the case of measured capacitance, the obtained results of generated energy for the given combinations of U_{low} and ΔU are presented in Fig. 14. The range of generated electric energy is between ca. 2 μJ and 21 μJ, which further equals 2 μW and 21 μW of power as the load frequency was 1 Hz. The relationship between the accounted factors and output energy is more

complex. The regression model based on the experimental data is as follows (energy in [µJ]):

$$\Delta E(U_{\text{low}}, \Delta U) = 0.0045\, U_{\text{low}} + 0.0024\, U_{\text{low}}\Delta U - 0.0774 \Delta U \tag{7}$$
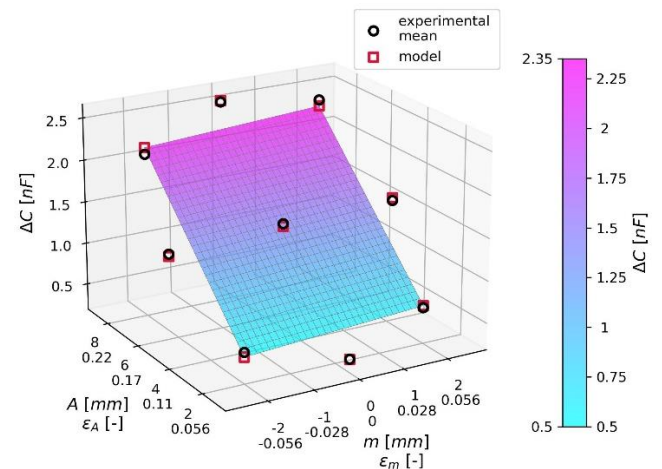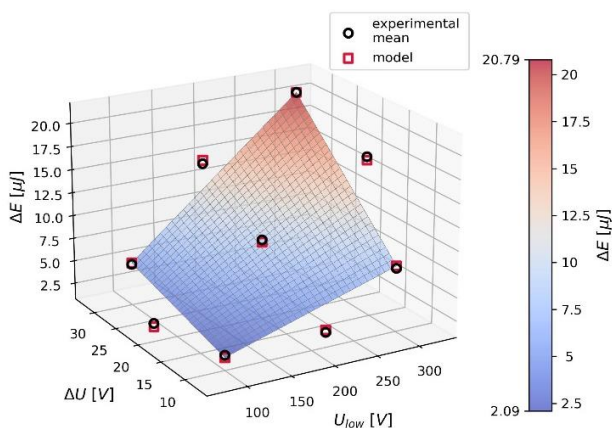

Fig. 14. Comparison of experimental and model results for generated energy estimation. The surface represents the fitted model within the area designated by the factor points

It includes the effects of both factors U_{low} and ΔU and their interaction. The model (Eq. [7]) fits the experimental data very well as it is described by $R^2 = 0.997$ and RMSE = 0.597, as shown in Fig. 14 as a surface plot. Low voltage U_{low} is responsible for the amount of charge accumulated in the DEG at the highest stretch (the highest capacitance); therefore, its significance is clear. The increase in voltage ΔU during DEG relaxation defines how much energy is necessary to boost the deposited charge. An excessively high value of ΔU can result in an interruption of the energy conversion process as the DEG will not be able to boost voltage sufficiently. Thus, no charge flow from the DEG to a storage capacitor will take place. The more the initial charge is deposited as a result of U_{low}, the more energy will be converted at a given level of ΔU, and for that reason, an interaction part was added to Eq. (7).

7. CONCLUSIONS

In the scope of this work, three identical DEG samples were designed and assembled to operate under a uniaxial tensile load. Next, the samples were investigated for capacitance alteration in a given range of physical load parameters. For a selected point from the capacitance experiment, another analysis was performed for the estimation of generated energy. For both cases, linear regression models were fitted to generalise the observations made.

The multilayer structure of the presented DEG allows active layers made of conductive grease to be enclosed between elastomeric layers, improving the handling and durability of the system. The presented design is the final one of several designs considered initially in the course of this work. During the conducted tests, each of the three samples underwent more than 10,000 load cycles without any significant change in their parameters and without any damage to membranes. The high similarity of the obtained results observed between all three samples also shows that using the described design, it is possible to manufacture repeatable samples.

DEGs intended to work in a uniaxial tensile mode are often mentioned in the literature, but examples of working prototypes are sparse. They are often referenced as pure-shear generators [21,22] due to the fact that plane tension can also be interpreted just as pure shear. This is correct, however, under the condition that the membrane width-to-length ratio is >10 and occurring strains are small [23]. In the presented design, this ratio is ca. 3.5; therefore, it should be classified as a uniaxial DEG. The main reason behind utilising wide membranes is to minimise transverse shrinkage during axial extension (Poisson's effect) as it can diminish the capacitance change during loading.

Systems based on DEs can be influenced by a viscoelastic creep [24]. However, in the presented case, registered signals were stable and did not exhibit any long time trends that could be associated with a creep. Most probably it is due to the fact that physical loads during tests were applied with a relatively large rate, that is, a frequency of 1 Hz.

One of the limiting factors in the operation of DEGs is an electrical breakdown of the elastomer membrane. According to Ref [24], a minimum value of electric field that can cause a VHB4910 membrane failure is E≈20 MV/m. This suggests that presented uniaxial DEG was not at risk of breakdown as, in any of tested cases, electric field did not exceed c.a. 2.4 MV/m. DE membrane parameters such as dielectric breakdown strength or electric permittivity can depend on material stretch or temperature [25]. However, working stretches in the performed experiments were relatively small and did not exceed 1.3; therefore, aforementioned effects were not included in the analysis.

Investigation of the capacitance change of the DEG in the selected range of load parameters showed that it is stable and, practically, a linear relation. Mean displacement in $s(t)$ sinusoidal loading has a huge impact on the mechanical stability of the membrane but can be omitted when considering capacitance alone. Initially, there were some doubts whether interaction between layers during cyclic loading can affect DEG parameters as the presence of a conductive grease allows relative slip. However, no such effect was observed in relation to both mean displacement and amplitude. This opens a way to further investigate multilayer structures with additional electrodes.

The amount of energy generated in the researched scope of voltage was between ca. 2 µJ and 21 µJ. Regarding absolute values, it is a small quantity but comparable to those being reported in other works. However, it is worth noting that voltage levels used in the presented DEG are below 350 V, while typical values found in the literature are of a few kilovolts. This is possible due to the quite large capacitance change ΔC that reached almost 2.5 nF.

In the case of both parts of the experiment, linear regression models fitted the empirical data well. Using the further model of Eq. (7) to extrapolate, the presented DEG design has the potential to generate even up to ca. $0.12\, mJ$ if $U_{\text{low}} = 1000$ V and $\Delta U = 50$ V. Increasing frequency over 1 Hz can also increase the amount of generated power.

REFERENCES

1. Grzybek D, Kata D, Sikora W, Sapiński B, Micek P, Pamuła H, Huebner J, Rutkowski P. Piezoelectric particulate composite for energy harvesting from mechanical vibration. Materials. 2020; 21 (13): 1-14. doi: 10.3390/en15176254
2. Micek P, Grzybek D. Impact of a connection structure of Macro Fiber Composite patches on energy storage in piezoelectric energy har-

vesting from a rotating shaft. Energies. 2022; 17 (15): 1-15. doi: 10.3390/en15176254

3. Sapiński B, Jastrzębski Ł, Kozieł A. Ideal Rectifier Bridge Converting the Harvested Energy of Vibrations into Electric Energy to Power an MR Damper. Acta Mechanica et Automatica. 2020; 14 (4): 198 - 205. doi: 10.2478/ama-2020-0028

4. Rosół M, Sapiński B. Ability of Energy Harvesting Mr Damper to Act as a Velocity Sensor in Vibration Control Systems. Acta Mechanica et Automatica. 2019; 13 (2): 135 - 145. doi: 10.2478/ama-2019-0019

5. Liu L, Zhang J, Luo M, Li B, Tang C, Chen H, Yang Z, Li P, Li D. Electro-pneumatic dielectric elastomer actuator incorporating tunable bending stiffness. Physical Review Research. 2020: 2 (2): 023202. doi: 10.1103/PhysRevResearch.2.023202

6. Berlinger F, Duduta M, Gloria H, Clarke D, Nagpal R, Wood R. A Modular Dielectric Elastomer Actuator to Drive Miniature Autonomous Underwater Vehicles. 2018 IEEE International Conference on Robotics and Automation (ICRA). 2018.

7. McKay T, Rosset S, Anderson I, Shea H. Dielectric elastomer generators that stack up. Smart Materials and Structures. 2014; 24: 015014. doi: 10.1088/0964-1726/24/1/015014

8. Zhang C, Lai Z, Zhang G, Yurchenko D. Energy harvesting from a dynamic vibro-impact dielectric elastomer generator subjected to rotational excitations. Nonlinear Dynamics. 2020; 102: 1271–1284. doi: 10.1007/s11071-020-05988-7

9. Moretti G, Malara G, Scialò A, Daniele L, Romolo A, Vertechy R, Fontana M, Arena F. Modelling and field testing of a breakwater-integrated U-OWC wave energy converter with dielectric elastomer generator. Renewable Energy. 2020; (146): 628-642. doi: 10.1016/j.renene.2019.06.077

10. Jean P, Wattez A, Ardoise G, Melis C, van Kessel R, Fourmon A, Barrabino E, Heemskerk J, Queau J. Standing Wave Tube Electro Active Polymer Wave Energy Converter. Proceedings of SPIE - The International Society for Optical Engineering. 2012. doi: 10.1117/12.934222

11. Moretti G, Rosset S, Vertechy R, Anderson I, Fontana M. A Review of Dielectric Elastomer Generator Systems. Advanced Intelligent Systems. 2020;2(10): 2000125. doi: 10.1002/aisy.202000125

12. Goh Y, Akbari S, Vo T, Koh S. Electrically-Induced Actuation of Acrylic-Based Dielectric Elastomers in Excess of 500% Strain. Soft Robotics. 2018; 6 (5): 675-684. doi: 10.1089/soro.2017.0078

13. Araromi O, Gavrilovich I, Shintake J, Rosset S, Shea H. Towards a deployable satellite gripper based on multisegment dielectric elastomer minimum energy structures. Electroactive Polymer Actuators and Devices (EAPAD) 2014. 2014. doi: 10.1117/12.2044667

14. Panigrahi R., Mishra SK. An Electrical Model of a Dielectric Elastomer Generator. IEEE Transactions on Power Electronics. 2018; 33 (4). doi: 10.1109/TPEL.2017.2749329

15. Huang J, Shian S, Suo Z, Clarke D. Maximizing the Energy Density of Dielectric Elastomer Generators Using Equi-Biaxial Loading. Advanced Functional Materials. 2013; 40 (23): 5056-5061. doi: 10.1002/adfm.201300402

16. Gasosoth T, Lianghiranthaworn T, Unai S. A period-based measurement for grounding capacitance meter with Arduino using a relaxation oscillator. Journal of Physics Conference Series. 2020;(1380), doi: 10.1088/1742-6596/1380/1/012074

17. Montgomery DC. Design and Analysis of Experiments. EMEA edition, 9th ed. Hoboken, NJ: John Wiley & Sons; 2017.

18. Seabold S, Perktold J. Statsmodels: Econometric and statistical modeling with Python. Proceedings of the 9th Python in Science Conference. 2010.

19. Lau G, Chen F, Ren Z. Axial force transmission in flexible bowtie dielectric elastomer actuators. Applied Physics Letters. 2022; 120: 012903. doi: 10.1063/5.0072852

20. Sikora W. Adaptation of an energy harvester working in the bending mode to utilize dielectric elastomers. Proceedings of the 22nd International Carpathian Control Conference. 2021. doi: 10.1007/s00707-021-03046-w

21. Chen Y, Kang G, Yuan J, Li T. Experimental study on pure-shear-like cyclic deformation of VHB 4910 dielectric elastomer. Journal of Polymer Research. 2019; 26: 186. doi: 10.1007/s10965-019-1858-6

22. Chen Y, Kang G, Hu Y, Yuan J, Li T., Qu S. Low-cycle electromechanical fatigue of dielectric elastomers: Pure-shear experiments and life-prediction model. International Journal of Fatigue. 2021; 148: 106220. doi: 10.1016/j.ijfatigue.2021.106220

23. Bergström J. Mechanics of solid polymers: theory and computational modeling, San Diego, USA: William Andrew; 2015.

24. Srivastava AK, Basu S. Modelling the performance of devices based on thin dielectric elastomer membranes. Mechanics of Materials. 2019; 137. doi: 10.1016/j.mechmat.2019.103136

25. Khajehsaeid H., Baghshomal Azar H. Influence of stretch and temperature on the energy density of dielectric elastomer generators. Applied Mathematics and Mechanics. 2019; 40: 1547–1560. doi:10.1007/s10483-019-2539-7

Wojciech Sikora: https://orcid.org/0000-0002-2953-5653

SEMI-ANALYTICAL ANALYSIS OF A RIGID ROTOR
MOUNTED ON FOUR-PAD HYDROSTATIC SQUEEZE FILM DAMPER
WITH SINGLE-ACTION MEMBRANE-TYPE RESTRICTORS

Ahmed KECHRA* , **Ahmed BOUZIDAINE***

*Research Laboratory of Industrial Technologies, Department of Mechanical Engineering,
Ibn Khaldun's University of Tiaret, BP 78 City, Tiaret, Algeria

ahmedkechra@yahoo.fr, ahmed.bouzidane@gmail.com

Abstract: The current study is a semi-analytical analysis of the vibratory behaviour of a rigid vertical rotor, supported by a new hydrostatic squeeze film damper (HSFD), consisting of four hydrostatic pads fed through four single-action membrane-type variable-flow restrictors. The Reynolds equation based on the Newtonian theory of lubrication is used and then adapted to our work, which is solved semi-analytically. In this paper, we study the effect of different parameters, the eccentricity, membrane geometry coefficient, pressure ratio and rotational speed, on the main characteristics of a four-pad HSFD. From the simulation results, we observed that at the critical speed, the rigid rotor fed by membrane restrictor shows a decrease in transmitted forces, a decrease in vibration response and good system stability as compared with a similar rotor fed by capillary restrictor. From the results reported in this work, we observed good agreement between our study and other works.

Key words: linear vibration, unbalance, hydrostatic squeeze film damper, Reynolds equation, Newtonian fluids, membrane restrictor, squeeze film lubrication

1. INTRODUCTION

The main and most common problem in the industry is the phenomenon of harmful vibrations resulting from imbalances in rotating machines, such as industrial turbo machinery, aircraft gas turbine engines and machining spindles. This has prompted many researchers to study the use of hydrostatic squeeze film dampers (HSFDs) as one of the effective solutions to control these vibrations. The latter has received increasing attention recently, due to its very low cost, durability and simplicity, with high efficiency in reducing the transmitted forces and increasing system stability.

Bouzidane et al. [1] investigated the effects of geometry, recess pressure and film thickness on the equivalent stiffness and damping of a four-pad hydrostatic journal bearing. In another work, Bouzidane et al. [2] studied the effect of rotational speed, supply pressure, pressure ratio, and viscosity on the transmitted force and unbalance response of a rigid rotor supported by a four-pad HSFD. In their work, a non-linear model was developed and the results obtained were compared with the simulation data of a linear model of HSFDs.

Many researchers have worked on the same topic. Abed et al. [3] analyzed three-pad HSFDs compensated with new electrorheological valve restrictors. Nemchi et al. [4] present a theoretical study of the effects of eccentricity ratio and Poiseuille Reynolds number on the performance of four-pad HSFDs. The results obtained indicate that the flow systems have a very significant impact on the performance of an HSFD loaded between pads. Benariba et al. [5] indicate that the micropolar effect is also mostly influenced by the stress ratio, on bearing performance. In another work [6], they deal with an analytical resolution of the modified Reynolds equation in order to study the effects of the coupling

number and the characteristic length of the micro-fluidic fluid on the transmitted forces, the vibratory response, the pressure profile and the flow.

Generally, there are two types of compensation: passive compensation, such as orifice and capillary restrictors, and active compensation [7–10]. In passively compensated bearings, the geometry of the compensating element never changes. However, in actively compensated bearings, the internal geometry is adjusted automatically by a pressure sensor.

In several works, contributions to the study of the behaviour of these externally pressed bearings with variable flow constraints have been made by Digast et al. [7], Mayer and Shaw [8], O'Donoghue and Rowe [9] and Cusano et al. [10]. The double diaphragm valve (membrane) was developed for grinding machine slide ways and spindle supports. It is a form of pressure sensing valve designed to control equal area opposed pad bearings. For high-performance practical purposes, this type of valve can be used to obtain infinite hardness as well as negative stiffness. The main advantage of the double diaphragm valve over the other systems is its manufacturing simplicity. Mohsin et al. [11] showed that the use of a membrane restrictor to compensate for the hydrostatic bearings enhances the static and dynamic stiffness of a bearing and reduces the power requirement. Morsi [12] discussed the performance of a hydrostatic thrust bearings compensated by passive and active restrictors from the point of view of fluid film stiffness and power requirement. Mohsin and Morsi [13] conducted both theoretical and experimental studies on the dynamic performance of a hydrostatic thrust pad bearing system compensated by variable resistance restrictors. Other important investigations which advocated the use of membrane restrictors as compensating elements in hydrostatic bearing systems to obtain better

performance characteristics are the studies of Degast [14] and Wang et al. [15], with diaphragm variable flow compensation, who studied the dynamic properties of externally pressurized, doubled pad, circular thrust bearings; they used Reynolds equation in cylindrical coordinates to simulate the pressure distribution and flow continuity. Sharma et al. and Singh et al. [16, 17] studied the influences of bearing flexibility and recess shape on the performance characteristics of multi-recess journal bearings, to determine the flow rate of membrane-type restrictor; they used the third-order polynomial of pressure difference.

Kang et al. [18, 19] used the coupled field to determine the flow rate between a rigid sill and elastic membrane. However, their simulation results do not provide a simple relationship between the flow rates or restriction coefficients and the pressure differences, which they used by using both analytical and experimental methods to study the membrane-type restrictor. Kang et al. [20, 21] used the identification method of restriction parameter, and deformation parameter for membrane-type restrictors obtained directly from the experimental results.
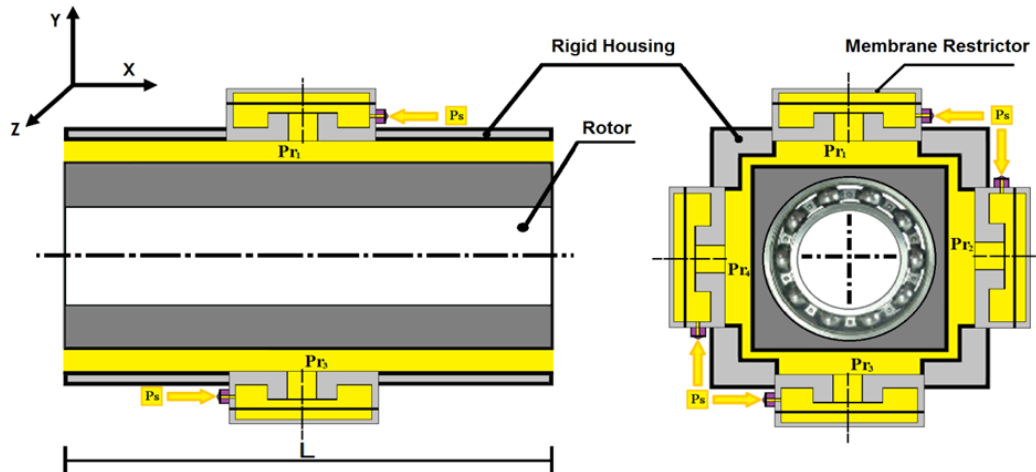

Fig.1. Schematic of a membrane-compensated four-pad hydrostatic squeeze film damper

As shown in Fig. 1, the fluid enters the membrane flow valve restrictor at a supply pressure (P_s), then escapes through the membrane clearance (x_0) and is then conducted through a line into a recess (Pr_0). From the recess or pocket, the fluid escapes out of the bearing through the bearing clearances (Pa). If an external load (W) is applied, the pressure difference between the two opposite recess forces the membrane to move in such a way that the external resistance increases. If all the dimensions are properly chosen, the bearing may yield a much larger value of fluid film stiffness than that of fixed external restrictors. The membrane flow valve restrictor uses the gap height (x_0) as the variable. Because the flow resistance varies with the gap height, the diaphragm flow valve restrictor is a load sensing resistance that varies with the load; that is to say, the required change in resistance can be obtained through a precise diaphragm deflection.

In order to reach special results, we chose in the present work a semi-analytical analysis of the modified Reynolds equation to study the effects of pressure ratio, eccentricity, membrane geometry coefficient and rotational speed on the vibration response, transmitted forces and flow rate. For the selected operating conditions, quantitative changes in the performance characteristics of a four-pad, membrane-compensated HSFD are compared with the previous results obtained for capillary compensation.

Certainly, the presented results obtained in this study are very useful for designers' tolerance.

2. PROBLEM FORMULATION

In this analysis, we adopt the assumptions given below:
– The bearing system is modelled as a two degree of freedom system.

– The pressure in the annular region is governed by the Reynolds equation, while that in the recess region it is assumed to be constant.
– The lubricant has a constant density and viscosity and is definitely incompressible.
– The flow is laminar in the membrane and in the bearing compensator.
– The relative ambient pressure is taken as zero.
– The inertia force of the lubricant is neglected.

3. FOUR-PAD HSFD DESCRIPTION

Fig. 2(a) shows a rigid rotor supported by an HSFD in the eccentric case composed of four identical plane pads fed through four single-action membrane restrictor-type hydraulic resistances. All pad geometries are equally spaced around the journal and are identical. The indices 1, 2, 3 and 4 refer to the characteristics of the lower, left and right hydrostatic flat pad, respectively. Each pad is fed by a membrane restrictor through a recess, which is supplied with an external pressure (Ps). Fig. 2(b) shows a longitudinal section of an HSFD with four identical pads, and Fig. 2(c) shows the geometrical details of one of the four identical hydrostatic pads.

In our study, we will use the commonly used semi-analytical method. On one hand, it allows to reduce the size of the calculation programmes, while on the other hand, it requires the knowledge of the pressure in the cavity and the pressure at the free ends at each pad. The calculation of the characteristics of the HSFD can be obtained through the juxtaposition of four hydrostatic flat pads.
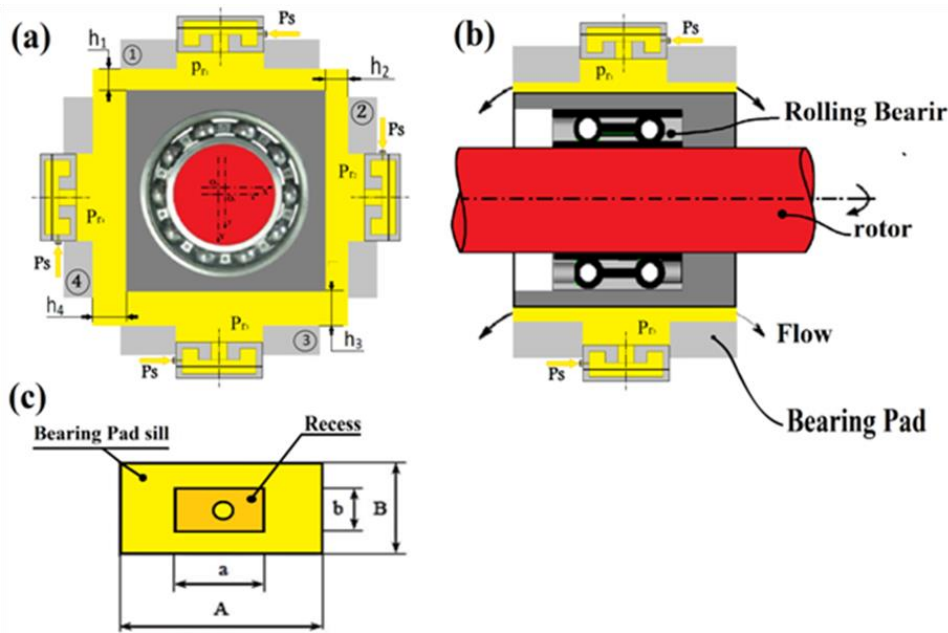
Fig. 2. (a) Four-pad HSFD; (b) longitudinal section of a four-pad HSFD; (c) geometric details of the hydrostatic pad

3.1 Reynolds equation

The Reynolds equation governs the pressure tion$P_i(x_i, z_i)$. In some cases, the equation can be solved semi-analytically by applying the infinitely short or long pad. If we assume that between the sheaths and the fluid there is no slip, the boundary conditions (Fig. 3.) associated with the field speed will be as follows:

− On pad (y=0) : $U_{1i} = 0$; $V_{1i} = 0$ et $W_{1i} = 0$

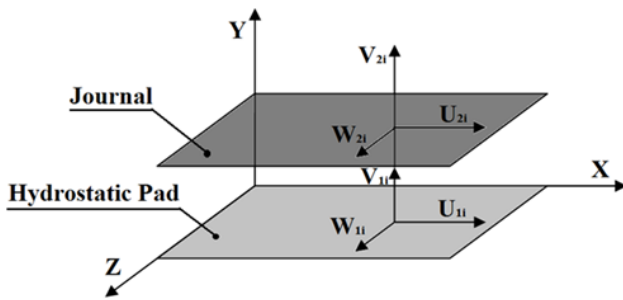− On journal (y=hi) : $U_{2i} = 0$; $V_{2i} = h_i$ et $W_{2i} = 0$

Fig. 3. Conditions for hydrostatic pad limits

The ith hydrostatic pad:U_{2i} , V_{2i} and $W_{2i}$are the speeds surface of the runner and h_i is the squeeze velocity of the ith hydrostatic pad (i = 1,2,3 and 4).

It is assumed that the recess is sufficiently deep to justify the assumption of the constant pressure. The housing of the rolling ball bearing is driven by a linear velocity (squeeze velocity) noted as V_{pi}.

We bind the centre of the Bering of the fixed ence$(O_1, \vec{X}, \vec{Y}, \vec{Z})$, where$O_1$: represents the centre of the bearing (Fig. 2a). The position and velocity of the housing relative to the centre are, respectively, defined in the Cartesian coordinates, whereO_2 is the centre of the housing as:

$$\overrightarrow{O_1 O_2} = x_1 \vec{X} = y_1 \vec{Y} \text{and} \vec{V}(O_2) = V_a \vec{X} = V_b \vec{Y}.$$

The geometric characteristics of four-pad HSFDs are defined as follows:
− The number of pads n (n = 4)
− The size of the pad (Fig. 2c)
  − Outside dimension of the pad: A, B
  − The size of the races: a, b
− The dimension of the housing (Fig. 2b)

The knowledge of the film thickness and housing speed in each pad are given, respectively, in Fig. 2(a):

− Pad n°1:
$$h_1 = h_0 + x_1$$
$$V_{p1} = \frac{\partial h_1}{\partial t} = V_a \tag{1}$$

− Pad n°2:
$$h_2 = h_0$$
$$V_{p2} = \frac{\partial h_2}{\partial t} = 0 \tag{2}$$

− Pad n°3:
$$h_3 = h_0 - x_1$$
$$V_{p3} = \frac{\partial h_3}{\partial t} = -V_a \tag{3}$$

− Pad n°4:
$$h_4 = h_0$$
$$V_{p4} = \frac{\partial h_4}{\partial t} = 0 \tag{4}$$

Note that

$$\begin{cases} B' + h_1 + h_3 = \text{Cte} \Rightarrow h_1 + h_3 = \text{Cte} \\ A' + h_2 + h_4 = \text{Cte} \Longrightarrow 2h_0 = h_2 + h_4 = \text{Cte} \end{cases} \tag{5}$$

where h_0 represents the film thickness with the housing in a centered position and x_1, V_a respectively, represent the linear displacement and squeezing velocity of the housing along the *X*-axis (Fig. 2a).

3.1.1 Calculations

In this study, we choose the semi-analytical method as it allows reduction in the programmes size. However, it requires knowledge of the pressure in the recess and the pressure at the free ends of each pad. Calculating the characteristics of four-pad HSFDs therefore, it returns to calculate the characteristics of the four hydrostatic pads separately.

sciendo

Ahmed Kechra, Ahmed Bouzidaine   DOI 10.2478/ama-2023-0059
Semi-Analytical Analysis of a Rigid Rotor Mounted on Four-Pad Hydrostatic Squeeze Film Damper with Single-Action Membrane-Type Restrictors

3.1.2 Infinitely long hydrostatic flat pad

The semi-analytical method is used to calculate the four-pad HSFD characteristics, under the assumption of the infinitely long pad.

3.1.3 Calculation of pressure field

When A/B ratio (the length $A (A = L)$ to the width B) is big, the outflow in the Z direction is negligible compared with that in the X direction (Fig. 4b).

$$Q_{xi} <<< Q_{zi} \Rightarrow \frac{\partial P_i}{\partial x} = 0 \tag{6}$$

with

$$\begin{cases} Q_{xi} = Q_{xi}^+ + Q_{xi}^- \\ Q_{zi} = Q_{zi}^+ + Q_{zi}^- \end{cases} \tag{7}$$

where Q_{xi} is the flow rate along the X axis relative to the single-acting pad $n°1$ and Q_{zi} flow rate along the Z axis relative to the same pad.
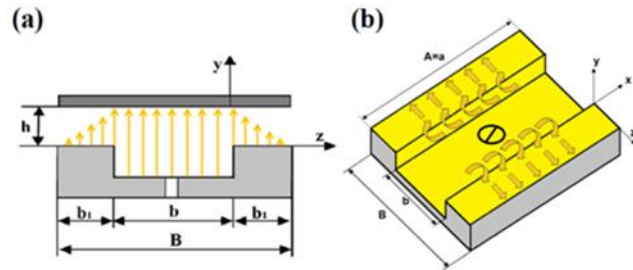

Fig. 4. Hydrostatic pad with infinite length. (a) Geometric details and longitudinal section and of hydrostatic pad with infinite length; (b) hydrostatic pad with infinite length

From Eq. (6), the pressure does not vary along the X axis, therefore the Reynolds equation for a single pad in direction n°1 is given as:

$$\frac{\partial}{\partial X} \left[\frac{h_i^3}{\mu} \left(\frac{\partial P_i}{\partial X} \right) \right] + \frac{\partial}{\partial Z} \left[\frac{h_i^3}{\mu} \left(\frac{\partial P_i}{\partial Z} \right) \right] = 12 \, V_{P_i} \tag{8}$$

which simplifies to:

$$\frac{\partial}{\partial Z} \left(h_i^3 \frac{\partial P_i}{\partial Z} \right) = 12 \, \mu \dot{h}_i \tag{9a}$$

with

$$\dot{h}_i = V_{P_i} = \frac{\partial h_i}{\partial t} \tag{9b}$$

The integration of Eq. (9) and the application of the boundary conditions in terms of pressure are:

$P_i = P_{ai}$ for $Z = 0$

$P_i = 0$ for $Z = b_1$

The atmospheric pressure is taken as the reference pressure which allows us to have:

$$P_i = \frac{6 \, \mu \, \dot{h}_i}{h_i^3} Z^2 - \left(\frac{P_{ai}}{b_1} + \frac{6 \, \mu \, \dot{h}_i}{h_i^3} b_1 \right) Z + P_{ai} \tag{10}$$

This is valid for: $(b_1 + b) \le Z \le -b$

Particular case: for $\dot{h}_i = 0$ (static case)

$$P_i = P_{ai} \left(1 - \frac{Z}{b_1} \right) \tag{11}$$

$0 \le Z \le b_1$

$$P_i = \left(\frac{P_{ai}}{b_1} \right) (Z + b + b_1) \tag{12}$$

$-(b + b_1) \le Z \le -b$

3.2. Recess pressure

By resolving the following flow continuity equation, the recess pressure is determined for each hydrostatic pad as:

$$Q_{ri} = Q_{oi} \tag{13}$$

where

$$Q_{oi} = Q_{vi} + Q_{si} \tag{14}$$

Here Q_{vi} represents the squeeze flow of the ith hydrostatic pad where:

$$Q_{vi} = S_i \dot{h}_i \tag{15}$$

Q_{ri} is the flow through the hydraulic resistance and Q_{si} the flow rate requirement of the ith hydrostatic pad.

$$Q_{si} = Q_{sxi} + Q_{szi} \tag{16}$$

$$Q_{Sxi} = \int_0^A dz \int_0^{h_i} u_{xi} dy \tag{17}$$

$$Q_{Szi} = \int_0^B dx \int_0^{h_i} u_{zi} dy \tag{18}$$

$$u_{xi} = \frac{1}{2\mu} \frac{dP_i}{dZ} \, y(y - h_i) \tag{19}$$

$$u_{zi} = \frac{1}{2\mu} \frac{dP_i}{dZ} \, y(y - h_i) \tag{20}$$

where u_{xi} and u_{zi} are the flow velocities in directions x and z, respectively, of the ith hydrostatics pads.

3.2.1. The total volumetric flow rate

The equation of the total volumetric flow rate is as follows:

$$Q_T = \sum_{i=1}^4 Q_{oi} = Q_{o1} + Q_{o2} + Q_{o3} + Q_{o4} \tag{21}$$

3.2.2. Flow equilibrium

3.2.2.1. Constant restriction of capillary

The equation of flow through the capillary to a recess can be determined as:

$$Q_{ci} = \frac{\pi d_c^4}{128 \mu l_c} (P_s - P_{ri}) \tag{22}$$

3.2.2.2 Single-action membrane-type variable restrictor

The external fluid is supplied by a hydraulic pump, which passes through the membrane restrictor and is fed into the recesses on the inner surface of the pad to form a fluid film, for

separating between the solid sliding surfaces in order to avoid contact of both solids.
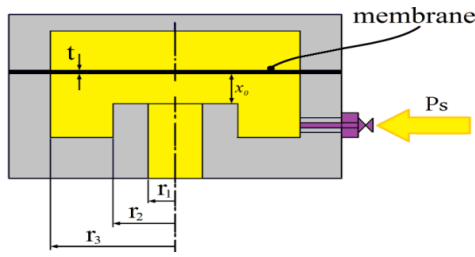

Fig. 5. Single action membrane-type restrictor [20]

In the membrane restrictor, as shown in of four-pad (Fig. 5), we find membrane thickness (t), Poisson's ratio (m), elastic modulus (E), membrane radius (r_3), radius of cylindrical sill (r_2) and radius of outlet from sill to recess (r_1); (x_0) is the initial opening when the membrane is subjected to only (P_s), and ($p_{ri} = 0$), and (x) is the equivalent opening as both pressures (P_s) and ($p_{ri} \neq 0$) act on the membrane.The flow rate through a single-acting membrane-type restrictor, to be obtained from the equation governing the viscous laminar flow between two parallel circular plates [20], can be determined by:

$$Q_{mi} = \frac{x_{mi}^3 \pi}{6\mu \ln(r_2/r_1)} (P_s - P_{ri}) = \frac{P_s - P_{ri}}{R_{mi}} \qquad (23)$$

where (μ) is fluid viscosity, $x_{mi} = \delta + x_0$ is the gap between the sill and the membrane, (δ) is the membrane deflection, (x_0) is the initial gap after assembling and (R_{mi}) is defined as the flow resistance of this membrane-type restrictor as:

$$R_{mi} = 6\mu \ln(r_2/r_1)/\pi x_{mi}^3 \qquad (24)$$

The membrane deflections vary with the radial position. In order to simplify the calculation of membrane deflection, the membrane deflections are assumed to be constant and equal to the membrane deflection at location (r_1), and so the membrane deflection can be expressed as:

$$\delta = K(P_s - P_{ri}) \qquad (25)$$

where K is the deformation coefficient [13] of the membrane:

$$K = 12(r_3^2 - r_1^2)^2(1 - m^2)/64Et^3 \qquad (26)$$

3.3. Flow rate requirement

The total volumetric flow rate that must be supplied to the hydrostatic pad according to the x and y axes are given by the following equation:

$$\begin{cases} Q_{tx} = Q_{S2} + Q_{S4} \\ Q_{ty} = Q_{S1} + Q_{S3} \end{cases} \qquad (27)$$

3.4. Carrying load capacity

The pad load for a length L relative to the pad n°1 is:

$$W_{Pi} = \int_S P_i ds = \int_{S_1} P_{ai} ds + 2 \int_{S_2} P_i ds \qquad (28)$$

where S are the contact surface, ds is an element of the surface, S_1 is the surface of the recess and S_2 is the surface pad sill.

After integration, we obtain:

$$W_{Pi} = P_{ai} L (b_1 + b) - \frac{2 \mu \dot{h}_i}{h_i^3} b^3{}_1 L \qquad (29)$$

We can write this relationship in a more general form as:

$$W_{Pi} = P_{ai} S K_w - \frac{2 \mu \dot{h}_i}{h_i^3} b^3{}_1 L \qquad (30)$$

where K_w is the coefficient of load, ranging from 0 to 1, as $K_w = 1 - (b_1/B)$ The relation (27) may also be written as:

$$W_{Pi} = \beta_i P_S S K_w - \frac{2 \mu \dot{h}_i}{h_i^3} b^3{}_1 L \qquad (31)$$

where $\beta_i = P_{ai}/P_S$ is the ratio of the recess over the supply pressures.

The forces of the liquid film on the journal can be written as:

$$\begin{cases} W_X = W_{P2} - W_{P4} \\ W_Y = W_{P1} - W_{P3} \end{cases} \qquad (32)$$

where W_X and W_Y are the load capacities in directions X and Y, respectively.

4. ROTOR DYNAMICS BEHAVIOUR

The rotor motion equation is given as:

$$\begin{cases} M\ddot{X} = (F_x + M\varepsilon_b \omega^2 h_0 \cos(\omega t)) \\ M\ddot{Y} = (F_y + M\varepsilon_b \omega^2 h_0 \sin(\omega t)) \end{cases} \qquad (33)$$

The fluid film forces on the four-pad HSFD are

$$\begin{cases} F_x = F_{p3} - F_{p1} \\ F_y = F_{p4} - F_{p2} \end{cases} \qquad (34)$$

where (e) is eccentricity, ($\varepsilon = e/h_0$) is eccentricity ratio and (h_0) is film thickness, (m) is mass of the rotor, ω is the excitation frequency, F_x and F_y are hydrostatic forces in the x and y directions, respectively, and F_{pi} ($i = 1,2,3$ and 4) is hydrostatic force of the ith hydrostatic ad.

5. SOLUTION PROCEDURE

In order to study the non-linear dynamic behaviour of assembling a vertically rigid rotor, supported by HSFD fed by a membrane restrictor and using a Newtonian lubricant, we adopted the Newmark method, which is briefly discussed as follows.

Assuming that the assembly is rigid, the hydrostatic forces, which vary according to the change in velocity and eccentricity, are determined by applying the boundary and pressure field integral conditions, which is determined by solving Reynolds Eq. (8) in a semi-analytical method.

By solving the rotor motion Eq. (33) using non-linear methods, the flow rates, dimensionless vibration amplitude and transmitted force amplitudes are calculated.

The computed amplitudes are determined from direct numerical integration of the equations of motion by using a step-by-step method. For each frequency of excitation, the temporal responses are determined through the Newmark method.

The amplitude calculations for the first five periods yielded very adequate results. The negative pressure is set to zero during the interactive process of caring for the oil film cavities, and at each step the hydrostatic forces are determined. Film thickness and pressure are determined by solving the continuity of flow Eq. (13) of a given pressure ratio.

6. RESULTS AND DISCUSSION

6.1. Effects of pressure ratio

Fig. 6 shows the effects of the pressure ratio (β) and the speed of rotation on the dimensionless amplitude, transmitted force and flow; for supply pressure 10 [bar], a viscosity of 0.0025 [Pa.s] and 0.2 of dynamic eccentricity unbalance.
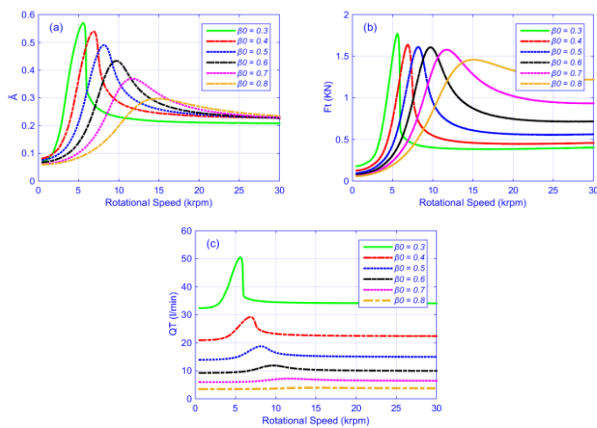

Fig. 6. Effects of pressure ratio on (a) variation of dimensionless vibratory amplitude, (b) variation of transmitted force amplitude and (c) variation of flow rate amplitude as a function of rotational speed

Panel (a) shows that, when the pressure ratio increases, the dimensionless vibration amplitude decreases due to the increase in film stiffness. We also record from panel (c) a decrease in the flow and in the transmitted forces (see (b)) as well.
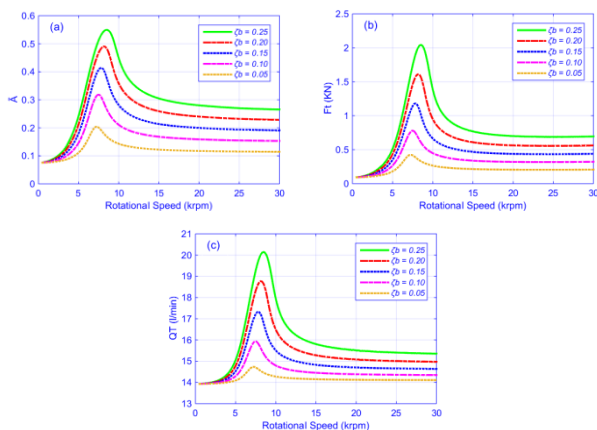
6.2. Effects of the imbalance eccentricity

Fig. 7. Effects of imbalance eccentricity on (a) variation of dimensionless vibratory amplitude, (b) variation of transmitted force amplitude and (c) variation of flow rate amplitude as a function of rotational speed

Fig. 7 shows the effect of unbalance eccentricity (ζ_b) and the rotational speed on the dimensionless amplitude of vibration, the transmitted force and the flow rate for a supply pressure of 10 [bar], a pressure ratio $\beta = 0.5$ and a viscosity $\mu = 0.0025$ [Pa.s].

We can notice that in panel (a), when the eccentricity increases the vibration amplitudes also increase. The same can be noticed for transmitted force in panel (b), which can be explained by the increase in dynamic load. Panel (c) shows that the increase in flow is directly proportional to the speed of rotation and eccentricity.

6.3. Effects of membrane geometry coefficient

Fig. 8 shows the effect of the membrane geometry coefficient (α) and the rotational speed on the dimensionless amplitude of vibration, the transmitted force and the flow rate for a supply pressure of 10 [bar], a pressure ratio $\beta = 0.5$ with a viscosity $\mu=0.0025$ [Pa.s] and $r_2=\alpha r_1$, $r_3=\alpha r_2$. It can be seen from panels (b) and (c) that the membrane geometry modulus is directly proportional to the flow rate and inversely proportional to the change in the transmitted force with very slightly reduced vibration amplitudes (a).
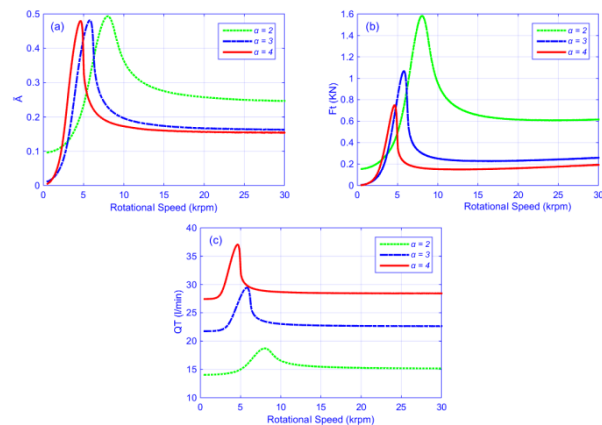
Fig. 8. Effects of membrane geometry coefficient on (a) variation of dimensionless vibratory amplitude, (b) variation of transmitted force amplitude and (c) variation of flow rate amplitude as a function of rotational speed

7. COMPARISON BETWEEN THE CAPILLARY MEMBRANE AND FLOW RESISTANCES

Let us represent, on the same graph, the analytical variance of dimensional vibration amplitude, transmission force and flow rate as a function of rotational speed, as shown in Fig. 9. It is clear from panels (a) and (b) that we obtained greater amplitude of vibrations and transmitted force thanks to the results presented in the curve obtained by the analytical code for capillary-type resistance as compared with the results of the semi-analytical code for a set with membrane-type resistance, and vice versa for flow (c). This leads us to state that the system supported by a membrane resistance is more stable.

Fig. 9. (a) Dimensional vibration amplitude, (b) amplitude of the transmission force and (c) flow amplitude as a function of rotational speed for both capillary flow and membrane resistances
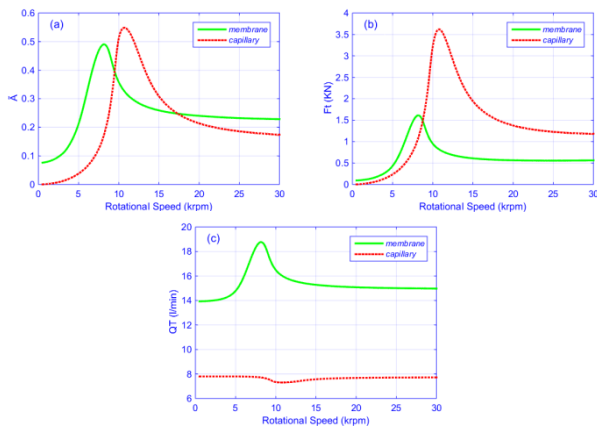
8. CONCLUSIONS

The aim of this research is to assess semi-analytically the performance of four-pad HSFDs with membrane-type variable flow restrictors as compensating elements.

The study focuses on the effects of the pressure ratio, membrane geometry coefficient, unbalance eccentricity and rotational speed on key parameters of the rotor dynamic behaviour. The role of HSFD is to control the vibration amplitudes, and to reduce the forces transmitted to the base, caused by the rotor imbalance. The conclusions can be summarized as follows:

- Effect of pressure ratio: due to the increase in compression ratio, we record a decrease in response amplitude, transmitted force and flow. When the rotational speed moves away from the critical speeds, changes in the compression ratio do not affect the amplitude of the response and stability is achieved.
- Effect of unbalance eccentricity: as expected, the amplitude of the response, transmitted forces and flux increase with increasing the unbalance eccentricity.
- Effect of membrane geometry coefficient: a lower membrane geometry modulus increases the transmitted forces with a lower flow rate, whatever the velocity. On the contrary, it leads to a very slight decrease in response amplitude when working near critical speed, due to increased damping.

From the analysis of the results and comparison of the two resistance properties of four-pad HSFD membranes and capillaries, we conclude that the membrane flow value is greater than capillary flow with a lower load and lower response amplitude, which allow good stability of the system.

Notation:

A	pad length	$[m]$
a	recess length	$[m]$
B	pad width	$[m]$
b	recess pad width	$[m]$
$F_X; F_Y$	represent the hydrostatic forces, in the X and Y directions	$[N]$
h_0	film thickness at the center position of the hydrostatic squeeze film damper	$[m]$
h_i	film thickness of the ith hydrostatic pad	$[m]$
M	mass of the rotor	$[Kg]$
N	The speed of rotation	$[tr/min]$

O_1	Center of the bearing	$[\ ]$
O_2	shaft center	$[\ ]$
P_{ri}	recess pressure of the ith hydrostatic pad	$[Pa]$
P_{r0}	recess pressure at the center position of the hydrostatic squeeze film damper	$[Pa]$
P_S	supply pressure	$[Pa]$
$Q_{xi}; Q_{zi}$	flow in the x ,y and z direction respectively of the ith hydrostatic pad	$[m^3/S]$
Q_{Si}	lubricant outlet flow rate of the pad	$[m^3/S]$
Q_{mi}	lubricant inlet flow rate of the membrane	$[m^3/S]$
Q_T	total flow rate	$[m^3/S]$
S_b	area of hydrostatic pad	$[m2]$
S_r	area of hydrostatic recess	$[m2]$
S	cross-section area	$[m2]$
$\dot{h}_i$	squeeze velocity of the ith hydrostatic pad	$[m/S]$
$(u_{xi}; u_{zi})$	flow velocities in the x and y directions, respectively of the ith hydrostatic pad	$[m/S]$
(x_i, z_i, y_i)	coordinate system used in the Reynolds equation	$[m/S]$
(x, y)	coordinate system used to describe the rotor motion	
β_0	ratio of recess pressure over supply pressure at the center position of hydrostatic squeeze film damper	$[\ ]$
β_i	pressure ratio of the ith hydrostatic pad	$[\ ]$
ε	Unbalance eccentricity.(e_b/h_0)	$[\ ]$
e_b	Eccentricity	$[m]$
μ	Viscosity	$[Pa.s]$
ω	excitation frequency	$[rad/s]$
E	elastic modulus	(N/mm)
x, x_0	gap and initial gap between sill and membrane	$[m]$
K_m	deformation coefficient of the membrane	(N/mm)
R_m	flow resistance of membrane restrictor	
r_1	exit radius	$[m]$
r_2	radius of restriction ring	$[m]$
r_3	Radius of the membrane	$[m]$
t	Thickness of the membrane	$[m]$
δ	membrane deflection	$[m]$
m	Poisson's ratio	$[\ ]$

REFERENCES

1. Bouzidane A, Thomas M. Equivalent Stiffness and damping investigation of a hydrostatic journal bearing. Tribology transactions. 2007; 50 (2), 257-267. https://doi.org/10.1080/10402000701309745
2. Bouzidane A, Thomas M, Lakis A. Non linear dynamic behaviour of a rigid rotor supported by hydrostatic squeeze film dampers. Journal of tribology transactions of the ASME,2008; 130 (4), 041102-041102-9. https://doi.org/10.1080/10402000701309745
3. Abed A, Bouzidane A, Thomas M, Zahloul H. Performance characteristics of a three-pad hydrostatic squeeze film damper compensated with new electrorheological valve restrictors. Proc imeche, part j: j engineering tribology. 2017; 231, 889–899. https://doi.org/10.1177/1350650116683622
4. Nemchi A, Bouzidane A, Thomas M, Abed A. Performance analysis of four-pad hydrostatic squeeze film dampers loaded between pads under laminar and turbulent flow conditions. Tribol mater. 2018; surf inter, 12, 59-70. https://doi.org/10.1080/17515831.2018.1441789
5. Benariba A, Bouzidane A, Thomas M, Raynald G. Numerical analysis of a rigid rotor mounted on four-pad hydrostatic squeeze film damper lubricated with micropolar lubricant. Proc imeche, part j: journal of engineering tribology. 2018 ; 232, 513–524. https://doi.org/10.1177/1350650117721119

6. Benariba A, Bouzidane A, Thomas A. Analytical analysis of a rigid rotor mounted on three hydrostatic pads lubricated with micropolar fluids. Proceedings of the institution of mechanical engineers, part j: journal of engineering tribology. 2018; 0(0),1-11. https://doi.org/10.1177/135065011880637

7. Mayer JE, Shaw MC. Characteristics of externally pressurized bearing having variable external flow restrictors. ASME journal of basic engineering.1963; 85, 291. https://doi.org/10.1115/1.365657

8. DeGast JGC. A new type of controlled restrictor (M.D.R.) for double film hydrostatic bearings and its application to high-precision machine tools. Advances in machine tool design and research, In: Proceedings of the 7th international M.T.D.R. conference, Birmingham. 1966 ; 12–16, 273–298. https://doi.org/10.1115/1.2920582

9. Rowe WB, O'donoghue JP. Diaphragm valves for controlling opposed pad hydrostatic bearings. Engineer's Digest.1969; 30(4), 49.

10. Cusano C. Characteristics of externally pressurized journal bearing with membrane-type variable-flow restrictors as compensating elements. Inst, of Mechanical Engineers, London. 1974;188(52),527. https://doi.org/10.1243/PIME_PROC_1974_188_064_02

11. Mohsin ME. The use of controlled restrictors for compensating hydrostatic bearings. Proceedings of the third international machine tool design research conference University of Birmingham. 1963 ; 429–42.

12. Morsi SA. Passively and actively controlled externally pressurized oil-film bearings. Trans ASME. 1972; 56–63. https://doi.org/10.1115/1.3451635

13. Mohsin ME, Morsi SA. The dynamic stiffness of controlled hydrostatic bearings. Trans ASME J Lub Tech.1969; 597–608. https://doi.org/10.1115/1.3555006

14. Degast JGC. A new type of controlled restrictor M.D.R for double film hydrostatic bearings and its application to high-precision machine tools. In: Advances in machine tool design and research, Oxford:Pergamon Press. 1966; 273–98.

15. Wang C, Cusano C. Dynamic characteristics of externally pressurized, double-pad, circular thrust bearings with membrane restrictors, ASME J Trib.1991; 113,158–65. https://doi.org/10.1115/1.2920582

16. Sharma SC, Sinhasan R, Jain SC. Performance characteristics of multirecess hydrostatic hybrid flexible journal bearing with membrane type variable-flow restrictor as compensating elements. Wear. 1992; 152,279–300. https://doi.org/10.1016/0043-1648(92)90126-S

17. Singh N, Sharma S C, Jain S C, Reddy S S. Performance of membrane compensated multirecess hydrostatic/hybrid flexible journal bearing system considering various recesses shapes. Tribol Int. 2004; 37, 11–24. https://doi.org/10.1016/S0301-679X(03)00110-5

18. Kang Y, Shen PC, Chang YP, Lee HH. Modified determination of fluid resistance for membrane-type restrictor. Industrial Lubrication and Tribology. 2007; 59(3),123-31. https://doi.org/10.1108/00368790710746084

19. Kang Y, Shen PC, Chang YP, Chiang CP. Modified predictions of restriction coefficient and flow resistance for membrane-type restrictors in hydrostatic bearing by using regression. Tribology International. 2007 ; 40(9),1369-80. https://doi.org/10.1016/j.triboint.2007.03.002

20. Kang Y, Chen CH, Lee HH, Hung YH, Hsiao ST. Design for static stiffness of hydrostatic bearings: single-action variable compensations. Industrial Lubrication and Tribology. 2011 ; 63 (2),103-18. https://doi.org/10.1108/00368791111112225

21. Kang Y, Chen CH, Chen YC, Chang C. Hsiao ST. Parameter identification for single-action membrane-type restrictors of hydrostatic bearings, Industrial Lubrication and Tribology. 2012;64(1),39-53. https://doi.org/10.1108/00368791211196880

Ahmed Kechra: [iD] https://orcid.org/0000-0002-1463-5600

Ahmed Bouzidaine: [iD] https://orcid.org/0009-0001-9731-1870

INFLUENCE OF THE MANIPULATOR CONFIGURATION ON VIBRATION EFFECTS

Paulina PIETRUŚ*, **Piotr GIERLAK***

**Rzeszów University of Technology, Faculty of Mechanical Engineering and Aeronautics,
Department of Applied Mechanics and Robotics,
al. Powstańców Warszawy 12, 35-959 Rzeszów, Poland*

p.pietrus@prz.edu.pl, pgierlak@prz.edu.pl

Abstract: Vibration analysis of industrial robots is one of the key issues in the context of robotisation of machining processes. Low-frequency vibrations result from flexibility in manipulator joints. Within the scope of the article, a model of a two-link robot manipulator was built. Dynamic equations of motion were formulated to study the influence of the robot arm configuration on vibration effects. Based on numerical simulations, the frequency spectrum of vibrations of the robot's links was determined, and tests were carried out in a number of configurations, obtaining a map of resonant frequencies depending on the configuration of the manipulator. Experimental studies were then carried out, which confirmed the conclusions from the simulation studies. The results obtained confirm that the positioning of the manipulator's links has a significant effect on vibration effects. Tests conducted using a vision system with a motion amplification application made it easier to interpret the results. The formulated mathematical model of the manipulator generates results that coincide with the results of experimental studies.

Key words: industrial manipulator, manipulator model, robot vibration

1. INTRODUCTION

Nowadays, industrial robots are increasingly used in many sectors of industry, such as machining, assembly and welding processes. For machining operations, industrial robots provide an economical and flexible alternative to standard CNC machine tools [1]. Machining operations performed by CNC machine tools provide greater accuracy and process stability. However, their maintenance costs are higher, and their movement capabilities are lower than those of robots. Therefore, CNC machines are often replaced by industrial robots [2]. The studies in Ref [2, 3] present general technical limitations of robots that occur during robotic machining processes, that is, accuracy, flexibility and possibility of excitation of robot resonant frequencies. The stability of operation during robotic machining is related to the stiffness of the robot and the vibrations that occur during machining. Therefore, research is being conducted to reduce the impact of negative effects occurring during robotic machining processes, among others vibrations. The most common applications of robots in machining processes include grinding, deburring and milling in soft materials [4, 5]. Proper planning of these processes requires the knowledge of the dynamic properties of the robot, so as not to excite, for example, its resonant vibrations. Identification of a mathematical model of the robot's mechanical structure is possible in the following experiments: modal analysis, measurement of the stiffness of the robot's structural elements and measurement of the stiffness in the manipulator's workspace [1]. Based on a review of existing solutions, examples of the application of the modal analysis of ABB and KUKA robots were found. In the studies in Ref [1, 6, 7, 8], modal analysis of KUKA manipulators was carried out to determine the frequencies of resonant vibrations.

Impulse excitation generated using an impact hammer was used to excite the vibration, and the frequency response function was determined. The presented studies showed the dependence of the effect of the position of the robot arm on the excited natural frequencies. The studies in Ref [2, 8] presented an experimental modal analysis for an ABB manipulator. The study in Ref [9] extends the frequency determination problem to include an uncertainty analysis of the determination of resonance zones. The study in Ref [10] allows the determination of modal parameters of robots under static conditions. The study in Ref [8] presents a position-dependent control methodology to actively damp end effector vibration during robotic machining processes. The study in Ref [11] presents a hybrid vibration control of an industrial composite robotic manipulator based on a reduced order model. In the study in Ref [12], a method using machine intelligence was used to control the open-loop vibration of manipulators.

There are three main approaches to modelling the dynamics of industrial robots: modelling the robot as a system of rigid bodies with no flexibility and no joint backlash [13, 14], modelling with flexibility and backlash in joints [15, 16, 17, 18] and modelling with link flexibility [19, 20, 21]. The study in Ref [22] presents a modified method of modelling flexible robotic manipulators for use in dynamic analysis.

Models of manipulators, taking into account the flexibility of the joints [23], created for control purposes include a model of the drives, and then an underactuated system is obtained. The study of such a model is complex because, in addition to the movement of the arm, there are vibration phenomena and a complex problem of motion control. Modal models are also built based on the results of the experiments [24]. The aim of this study is to create the simplest possible analytical model of a robot that takes into account the vibration phenomena at selected positions of the robot

arm, without taking into account the influence of the arm movement on the vibration.

The article presents a model of a two-link robot manipulator, taking into account the flexibility of joints. The dynamic equations of motion of the manipulator were formulated using the Lagrangian approach. The purpose of the modelling was to determine the effect of the robot arm configuration on vibration effects. Due to the complexity of the equations of motion, properties were studied using numerical methods. The frequency spectrum of vibrations of the robot's links was determined. The study was carried out in many configurations, obtaining a map of resonant frequencies depending on the configuration of the robot. The results of theoretical analysis were confirmed by the results of a number of experimental tests. The main contribution of the research is the determination of the frequencies and modes of resonant vibrations using the experimental method and the formulation of a mathematical model of the dynamics of the robot arm, taking into account the flexibility of the joints.

The purpose of the modal analysis presented in this article is to determine the value of the resonant frequency and its dependence on the current position of the robot. The variability of the values of the resonant frequencies can lead to their activation in certain configurations, although the parameters of the processes to be carried out remain constant. The knowledge of the dynamic properties of the robot, which are of a vibrational nature, makes it possible to avoid resonances by correctly designing the robotic processes. This applies, for example, to robotic machining.

In the case of a typical industrial robot with six degrees of freedom, there will be no new phenomena, but there will be an accumulation of those that are present in a two-part robot. Hence, the model will be qualitatively the same. This article, however, draws attention to the occurring phenomena and presents the possibilities of their analysis. The simplification of modelling only two degrees of freedom of the robot makes it easier to present the results and understand the analysed phenomena.

2. MODEL OF MANIPULATOR

To analyse the influence of the manipulator configuration on vibration effects, a model of a two-link planar manipulator was adopted, the schematic diagram of which is shown in Fig. 1. It consists of two articulated links that have the ability to move in the xy plane. The model takes into account the flexibility in joints A and B, which is the cause of low-frequency vibration of the manipulator. Point C is the end point of the arm, while points S1 and S2 are the centres of mass of links 1 and 2, respectively.

Low-frequency vibrations of robots result from flexibility in the joints, that is, at points A and B. They involve the rotational oscillatory motion of the links relative to the joints. To account for them, it can be assumed that each configuration coordinate, that is, q_1 and q_2, can be expressed as the sum of two angular values:

$$\begin{cases} q_1 = \beta_1 + \alpha_1 \\ q_2 = \beta_2 + \alpha_2 \end{cases} \tag{1}$$

where β_1 and β_2 are the values describing the positions of the manipulator's links, relative to which the oscillations of these links occur, expressed by the variables α_1 and α_2. In the ideal case, when no oscillations occur, β_1 and β_2 are simply the same as the configuration coordinates q_1 and q_2. When the flexibility in the joints is taken into account, the angles α_1 and α_2 are fast-variable

values related to the vibration effects of the robotic arm, while β_1 and β_2 are slow-variable values whose changes result from the realisation of the motion trajectory, or alternatively, they are constant values if the robotic arm is in a fixed position.
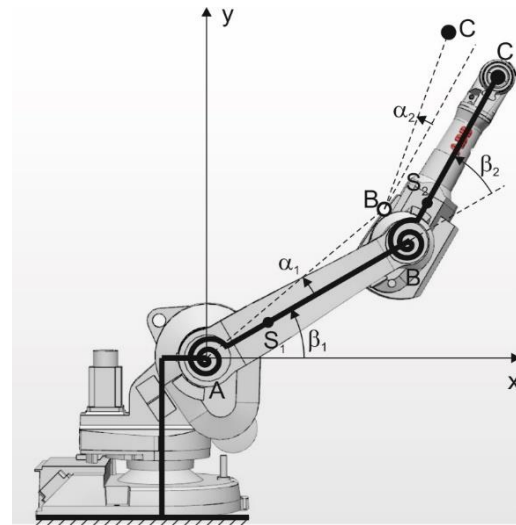

Fig. 1. A two-link planar manipulator with flexible joints

The equations of motion of the manipulator were formulated using the Lagrangian approach. For this purpose, the potential energy was determined first, followed by the kinetic energy of the manipulator.

The potential energy of the system is the sum of the potential energies of the masses in the earth's gravitational field and the potential energies of the elastic elements at the joints:

$$V = V_{k1} + V_{k2} + V_{g1} + V_{g2} \tag{2}$$

where V_{k1} and V_{k2} are the potential energies of the elastic joints of links 1 and 2, and V_{g1} and V_{g2} are the potential energies of the masses of links 1 and 2 in the gravitational field. They are described by the following equations:

$$V_{k1} = \frac{1}{2}k_1(\alpha_1 + \alpha_{1st})^2 \tag{3}$$

$$V_{k2} = \frac{1}{2}k_2(\alpha_2 + \alpha_{2st})^2 \tag{4}$$

$$V_{g1} = m_1 g l_{c1} sin(\beta_1 + \alpha_1) \tag{5}$$

$$V_{g2} = m_2 g[l_1 sin(\beta_1 + \alpha_1) + l_{c2} sin(\beta_1 + \beta_2 + \alpha_1 + \alpha_2)] \tag{6}$$

in which k_1 and k_2 are the elastic coefficients of the joints 1 and 2 (at points A and B), respectively; α_{1st} and α_{2st} are the static deformations of the joints under the influence of moments from the gravity forces of the links, m_1 and m_2 are the masses of links 1 and 2, respectively; l_1 is the length of link 1; and l_{c1} and l_{c2} are the distances of the centres of mass of the links from the joints (distances AS1 and BS2). The trigonometric functions appearing in Eqs. (5) and (6) can be decomposed as follows:

$$sin(\beta_1 + \alpha_1) = sin\beta_1 cos\alpha_1 + cos\beta_1 sin\alpha_1 = sin\beta_1 + \alpha_1 cos\beta_1 \tag{7}$$

$$sin(\beta_1 + \beta_2 + \alpha_1 + \alpha_2) = sin(\beta_1 + \beta_2)cos(\alpha_1 + \alpha_2) + cos(\beta_1 + \beta_2)sin(\alpha_1 + \alpha_2) = sin(\beta_1 + \beta_2) + (\alpha_1 + \alpha_2)cos(\beta_1 + \beta_2) \tag{8}$$

where the following approximations are considered in the second step of the transformation: $\sin \alpha_1 = \alpha_1$, $\cos \alpha_1 = 1$, $\sin(\alpha_1 + \alpha_2) = \alpha_1 + \alpha_2$, $\cos(\alpha_1 + \alpha_2) = 1$. These are due to the fact that the angular coordinates α_1 and α_2 describing the vibration have small values. The total potential energy, taking into account the linearisation performed, is given as follows:

$$V = \frac{1}{2} k_1 (\alpha_1^2 + 2\alpha_1 \alpha_{1st} + \alpha_{1st}^2) + \frac{1}{2} k_2 (\alpha_2^2 + 2\alpha_2 \alpha_{2st} + \alpha_{2st}^2) + m_1 g l_{c1} (\sin \beta_1 + \alpha_1 \cos \beta_1) + m_2 g l_1 (\sin \beta_1 + \alpha_1 \cos \beta_1) + m_2 g l_{c2} \sin(\beta_1 + \beta_2) + m_2 g l_{c2} (\alpha_1 + \alpha_2) \cos(\beta_1 + \beta_2) \tag{9}$$

The static deformations of the joints were determined using the Dirichlet criterion. For this purpose, the derivatives of the potential energy (9) were determined after the coordinates α_1 and α_1, which are equal to zero at the static equilibrium position defined by the values $\alpha_1 = \alpha_2 = 0$, that is, they satisfy the following conditions:

$$\left.\frac{\partial V}{\partial \alpha_1}\right|_{\alpha_1=0, \alpha_2=0} = k_1(\alpha_1 + \alpha_{1st}) + (m_1 g l_{c1} + m_2 g l_1) \cos \beta_1 + m_2 g l_{c2} \cos(\beta_1 + \beta_2) = 0 \tag{10}$$

$$\left.\frac{\partial V}{\partial \alpha_2}\right|_{\alpha_1=0, \alpha_2=0} = k_2(\alpha_2 + \alpha_{2st}) + m_2 g l_{c2} \cos(\beta_1 + \beta_2) = 0 \tag{11}$$

From Eqs. (10) and (11), static deformations were calculated as follows:

$$\alpha_{1st} = -\frac{(m_1 g l_{c1} + m_2 g l_1)}{k_1} \cos \beta_1 - \frac{m_2 g l_{c2}}{k_1} \cos(\beta_1 + \beta_2) \tag{12}$$

$$\alpha_{2st} = -\frac{m_2 g l_{c2}}{k_2} \cos(\beta_1 + \beta_2) \tag{13}$$

Taking into account the static deformations (12) and (13) in Eq. (9), and omitting α_{1st}^2 and α_{2st}^2 as small values of higher order than α_{1st} and α_{2st}, the potential energy can be written in the following form:

$$V = \frac{1}{2} k_1 \alpha_1^2 + \frac{1}{2} k_2 \alpha_2^2 + m_1 g l_{c1} \sin \beta_1 + m_2 g l_1 \sin \beta_1 + m_2 g l_{c2} \sin(\beta_1 + \beta_2) \tag{14}$$

The kinetic energy of the system is the sum of the kinetic energies of all links:

$$E = E_1 + E_2 \tag{15}$$

where the kinetic energy of link 1 is the energy of the solid in rotation relative to point A:

$$E_1 = \frac{1}{2} I_A^{(1)} \dot{q}_1^2 \tag{16}$$

and the kinetic energy of link 2 is the energy of plane motion understood as the sum of the progressive motion of the link's centre of mass (point S2) and rotational motion relative to the link's centre of mass:

$$E_2 = \frac{1}{2} m_2 v_{S2}^2 + \frac{1}{2} I_{S2}^{(2)} (\dot{q}_1 + \dot{q}_2)^2 \tag{17}$$

Thus, the kinetic energy is as follows:

$$E = \frac{1}{2} I_A^{(1)} \dot{q}_1^2 + \frac{1}{2} m_2 v_{S2}^2 + \frac{1}{2} I_{S2}^{(2)} (\dot{q}_1 + \dot{q}_2)^2 \tag{18}$$

where $I_A^{(1)}$ is the mass moment of inertia of link 1 defined relative to point A and $I_{S2}^{(2)}$ is the mass moment of inertia of link 2 defined relative to the centre of mass of link 2.

A quasi-static case was further considered, in which the motions of the links described by the variables α_1 and α_2 were considered relative to the position of the links described by the coordinates β_1 and β_2. The coordinates β_1 and β_2 are treated as constants because their changes during movement are many times slower than those of α_1 and α_2. Therefore, based on these assumptions and Eq. (1), the angular velocities of the links are expressed as follows:

$$\begin{cases} \dot{q}_1 = \dot{\beta}_1 + \dot{\alpha}_1 = \dot{\alpha}_1 \\ \dot{q}_2 = \dot{\beta}_2 + \dot{\alpha}_2 = \dot{\alpha}_2 \end{cases} \tag{19}$$

where it is assumed that β_1 and β_2 are constants. This assumption leads to the analysis of the vibration of the manipulator at the positions defined by the angles β_1 and β_2.

The coordinates of the centre of mass of link 2 are defined by the following formula:

$$\begin{cases} x_{S2} = l_1 \cos(q_1) + l_{c2} \cos(q_1 + q_2) \\ y_{S2} = l_1 \sin(q_1) + l_{c2} \sin(q_1 + q_2) \end{cases} \tag{20}$$

which, after taking into account Eq. (1), is written in the following form:

$$\begin{cases} x_{S2} = l_1 \cos(\beta_1 + \alpha_1) + l_{c2} \cos(\beta_1 + \beta_2 + \alpha_1 + \alpha_2) \\ y_{S2} = l_1 \sin(\beta_1 + \alpha_1) + l_{c2} \sin(\beta_1 + \beta_2 + \alpha_1 + \alpha_2) \end{cases} \tag{21}$$

After differentiating these equations with respect to time, the components of the velocity of the centre of mass of link 2 can be obtained:

$$\begin{cases} \dot{x}_{S2} = -l_1 \dot{\alpha}_1 \sin(\beta_1 + \alpha_1) - l_{c2}(\dot{\alpha}_1 + \dot{\alpha}_2) \sin(\beta_1 + \beta_2 + \alpha_1 + \alpha_2) \\ \dot{y}_{S2} = l_1 \dot{\alpha}_1 \cos(\beta_1 + \alpha_1) + l_{c2}(\dot{\alpha}_1 + \dot{\alpha}_2) \cos(\beta_1 + \beta_2 + \alpha_1 + \alpha_2) \end{cases} \tag{22}$$

while the square of the velocity value of point S2 is as follows:

$$v_{S2}^2 = \dot{x}_{S2}^2 + \dot{y}_{S2}^2 = l_1^2 \dot{\alpha}_1^2 + l_{c2}^2 (\dot{\alpha}_1 + \dot{\alpha}_2)^2 + 2 l_1 l_{c2} \dot{\alpha}_1 (\dot{\alpha}_1 + \dot{\alpha}_2) \cos(\beta_2 + \alpha_2) \tag{23}$$

Taking into account the kinematic relations, the kinetic energy can be written in the following form:

$$E = \frac{1}{2} \left[I_A^{(1)} + I_{S2}^{(2)} + m_2 l_1^2 + m_2 l_{c2}^2 + m_2 l_1 l_{c2} \cos(\beta_2 + \alpha_2) \right] \dot{\alpha}_1^2 + \left[m_2 l_{c2}^2 + m_2 l_1 l_{c2} \cos(\beta_2 + \alpha_2) + I_{S2}^{(2)} \right] \dot{\alpha}_1 \dot{\alpha}_2 + \frac{1}{2} (m_2 l_{c2}^2 + I_{S2}^{(2)}) \dot{\alpha}_2^2 \tag{24}$$

The Lagrange function is introduced as follows:

$$L = E - V = \frac{1}{2} \left[I_A^{(1)} + I_{S2}^{(2)} + m_2 l_1^2 + m_2 l_{c2}^2 + m_2 l_1 l_{c2} \cos(\beta_2 + \alpha_2) \right] \dot{\alpha}_1^2 + \frac{1}{2} (m_2 l_{c2}^2 + I_{S2}^{(2)}) \dot{\alpha}_2^2 + \left[I_{S2}^{(2)} + m_2 l_{c2}^2 + m_2 l_1 l_{c2} \cos(\beta_2 + \alpha_2) \right] \dot{\alpha}_1 \dot{\alpha}_2 - \frac{1}{2} k_1 \alpha_1^2 - \frac{1}{2} k_2 \alpha_2^2 - m_1 g l_{c1} \sin \beta_1 - m_2 g l_1 \sin \beta_1 - m_2 g l_{c2} \sin(\beta_1 + \beta_2) \tag{25}$$

and then the Lagrange equations are formulated:

$$\begin{cases} \frac{d}{dt}\left(\frac{\partial L}{\partial \dot{\alpha}_1}\right) - \frac{\partial L}{\partial \alpha_1} = 0 \\ \frac{d}{dt}\left(\frac{\partial L}{\partial \dot{\alpha}_2}\right) - \frac{\partial L}{\partial \alpha_2} = 0 \end{cases} \tag{26}$$

which describe the free vibration of the robot arm. Their detailed form is as follows:

$$\left[I_A^{(1)} + I_{S2}^{(2)} + m_2 l_1^2 + m_2 l_{c2}^2 + 2 m_2 l_1 l_{c2} \cos(\beta_2 + \alpha_2) \right] \ddot{\alpha}_1 + \left[I_{S2}^{(2)} + m_2 l_{c2}^2 + m_2 l_1 l_{c2} \cos(\beta_2 + \alpha_2) \right] \ddot{\alpha}_2 -$$

$$2m_2 l_1 l_{c2}\, sin(\beta_2 + \alpha_2)\ddot{\alpha}_2\, \dot{\alpha}_1 - m_2 l_1 l_{c2}\, sin(\beta_2 + \alpha_2)\, \dot{\alpha}_2^2 + k_1 \alpha_1 = 0$$

$$\left(I_{S2}^{(2)} + m_2 l_{c2}^2\right)\ddot{\alpha}_2 + \left[I_{S2}^{(2)} + m_2 l_{c2}^2 + m_2 l_1 l_{c2}\, cos(\beta_2 + \alpha_2)\right]\ddot{\alpha}_1 + m_2 l_1 l_{c2}\, sin(\beta_2 + \alpha_2)\, \dot{\alpha}_1^2 + k_2 \alpha_2 = 0 \qquad (27)$$

By grouping the individual expressions into matrices, the equation of motion was obtained in the general form given by the following equation:

$$M\ddot{\alpha} + C\dot{\alpha} + K\alpha = 0 \qquad (28)$$

in which matrices have the following form:

$$\alpha = \begin{bmatrix} \alpha_1 \\ \alpha_2 \end{bmatrix} \qquad (29)$$

$$M = \begin{bmatrix} a_1 + 2a_2\, cos(\beta_2 + \alpha_2) & a_3 + a_2\, cos(\beta_2 + \alpha_2) \\ a_3 + a_2\, cos(\beta_2 + \alpha_2) & a_3 \end{bmatrix} \qquad (30)$$

$$C = \begin{bmatrix} -a_2\, sin(\beta_2 + \alpha_2)\dot{\alpha}_2 & -a_2\, sin(\beta_2 + \alpha_2)\, (\dot{\alpha}_1 + \dot{\alpha}_2) \\ a_2\, sin(\beta_2 + \alpha_2)\, \dot{\alpha}_1 & 0 \end{bmatrix} \qquad (31)$$

$$K = \begin{bmatrix} k_1 & 0 \\ 0 & k_2 \end{bmatrix} \qquad (32)$$

while parameters a_i result from the following grouping of coefficients:

$$\begin{cases} a_1 = I_A^{(1)} + I_{S2}^{(2)} + m_2 l_1^2 + m_2 l_{c2}^2 \\ a_2 = m_2 l_1 l_{c2} \\ a_3 = I_{S2}^{(2)} + m_2 l_{c2}^2 \end{cases} \qquad (33)$$

The trigonometric functions occurring in the model can be decomposed as follows:

$$cos(\beta_2 + \alpha_2) = cos\,\beta_2\, cos\,\alpha_2 - sin\,\beta_2\, sin\,\alpha_2 \qquad (34)$$

$$sin(\beta_2 + \alpha_2) = sin\,\beta_2\, cos\,\alpha_2 + cos\,\beta_2\, sin\,\alpha_2 \qquad (35)$$

For the purpose of research involving vibration analysis in selected robot configurations defined by angular coordinates β_1 and β_2, it can be assumed that the values of $sin\,\beta_2$ and $cos\,\beta_2$ are constant in each analysed configuration. Thus, the designations $b_1 = sin\,\beta_2$, $b_2 = cos\,\beta_2$ were introduced. From the fact that the angular coordinates α_1 and α_2 describing the oscillations are small angles, it follows that the following approximations can be used: $sin\,\alpha_2 = \alpha_2$, $cos\,\alpha_2 = 1$. Then the expressions described by Eqs. (34) and (35) can be written in the linearised form:

$$cos(\beta_2 + \alpha_2) = b_2 - b_1 \alpha_2 \qquad (36)$$

$$sin(\beta_2 + \alpha_2) = b_1 + b_2 \alpha_2 \qquad (37)$$

Introducing these designations into the dynamic equations of motion, the M and C matrices are written as follows:

$$M = \begin{bmatrix} a_1 + 2a_2 b_2 - 2a_2 b_1 \alpha_2 & a_3 + a_2 b_2 - a_2 b_1 \alpha_2 \\ a_3 + a_2 b_2 - a_2 b_1 \alpha_2 & a_3 \end{bmatrix} \qquad (38)$$

$$C = \begin{bmatrix} -(a_2 b_1 + a_2 b_2 \alpha_2)\dot{\alpha}_2 & -(a_2 b_1 + a_2 b_2 \alpha_2)(\dot{\alpha}_1 + \dot{\alpha}_2) \\ (a_2 b_1 + a_2 b_2 \alpha_2)\dot{\alpha}_1 & 0 \end{bmatrix} \qquad (39)$$

An important fact is that the angular coordinate β_1 does not appear in the obtained equations of motion, from which it follows that the angular position of link 1 does not affect the vibrations of the robot arm. However, they depend on the angular coordinate β_2.

Since the authors had a second manipulator, identical to the one studied in this article, and used it for detailed analyses of its structure, the masses and mass moments of inertia were determined experimentally. The lengths of the links were obtained from geometric measurements. The joint stiffness coefficients k_1 and k_2 were determined experimentally. The manipulator arm was loaded with known, successively increasing loads (from the weights suspended at the end of the arm), and the displacements of each manipulator joint were measured using a Leica AT 960 Laser Tracker (Fig. 2). This was used to determine the characteristics of the moments as a function of the angular displacements of the links. The characteristics were approximated by linear functions, which allowed the assumption of constant values for the stiffness coefficients given in Tab. 1.

Fig. 2. Measurement of displacements of links under the loads

Tab. 1. Coefficient values used in robot model

Coefficient	Unit	Value
$I_A^{(1)}$	kgm²	0.55
$I_{S2}^{(2)}$	kgm²	0.0009
m_2	kg	50.58
l_1	m	0.63
l_{c2}	m	0.1
k_1	Nm/rad	555,000
k_2	Nm/rad	138.000
β_1	rad	2π/3

3. ANALYTICAL SOLUTION

To analytically determine the resonant frequencies of the robot, simplifications were introduced into the equations of motion (28) to obtain linear equations. Firstly, the terms of the equations containing the angular velocities $\dot{\alpha}_i$ were omitted to eliminate the quadratic forms of the velocities. This is equivalent to omitting the C matrix. Furthermore, the influence of the angles α_i on the matrix M was omitted, justified by the relatively small influence of the angles α_i on the phenomena related to the inertia of the links compared to the influence of these angles on the phenomena related to the elasticity expressed by the $K\alpha$ term. The equation of

motion was thus obtained in the following form:

$$M_0\ddot{\alpha} + K\alpha = 0 \tag{40}$$

where $M_0 = M(\alpha = 0, \beta)$ was adopted. The matrix M_0 is constant in a given configuration defined by the coordinate vector β. The solution to the equation of motion (40) has the following form:

$$\alpha_i = A_i cos(\omega t + \varphi) \tag{41}$$

Substituting this solution and its second derivative into the equation of motion (40) gives the following algebraic equation:

$$(-\omega_0^2 M_0 + K)A = 0 \tag{42}$$

where A is the displacement amplitude vector of the form $A = [A_1 \quad ... \quad A_n]^T$. Eq. (42) is satisfied if

$$det(-\omega_0^2 M_0 + K) = 0 \tag{43}$$

This is the equation for the natural frequencies of the system, which, in the case of the considered manipulator, has the following form:

$$(a_1 a_3 - a_3^2 - a_2^2 \cos^2 \beta_2)\omega_0^4 - (a_1 k_2 + 2a_2 k_2 \cos \beta_2 + a_3 k_1)\omega_0^2 + k_1 k_2 = 0 \tag{44}$$

The positive solutions of Eq. (44) are follows:

$$\omega_{0\{1,2\}} = \sqrt{\frac{d_1}{2d_2} \mp \sqrt{\frac{d_1^2}{4d_2^2} - \frac{k_1 k_2}{d_2}}} \tag{45}$$

where $d_1 = a_1 k_2 + 2a_2 k_2 \cos \beta_2 + a_3 k_1$ and $d_2 = a_1 a_3 - a_3^2 - a_2^2 \cos^2 \beta_2$ were adopted. Taking into account the values of the parameters a_1, a_2 and a_3 and the elasticity coefficients k_1 and k_2 (Tab. 1), the values of the natural frequencies $f_1 = \omega_{0\,1}/(2\pi)$ and $f_2 = \omega_{0\,2}/(2\pi)$ have been calculated as a function of the configuration determined by the β_2 coordinate for $\beta_2 \in \langle -2{,}269 \div 2{,}619 \rangle$ rad. The results of the calculations are shown in Fig. 3.
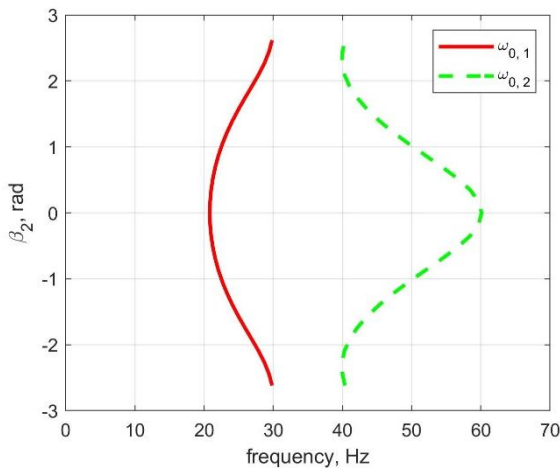

Fig. 3. Robot natural frequencies as a function of the β_2 angle, obtained from the analytical solution

Fig. 3 shows that the natural frequencies of the robot arm depend significantly on its positioning. As the absolute value of the angle β_2 increases, the value of the first natural frequency increases, while the value of the second natural frequency decreases. Changes in the frequencies of the natural vibrations in differ-

ent positions of the robot result from changes in the inertia of the system since the M and C matrices depend on the position of link 2 with respect to link 1. The stiffness matrix, on the other hand, is constant regardless of the configuration. The first frequency increases and the second frequency decreases as the absolute value of the angle β_2 increases because the term $\frac{d_1^2}{4d_2^2} - \frac{k_1 k_2}{d_2}$ in Eq. (45) decreases as the angle β_2 increases.
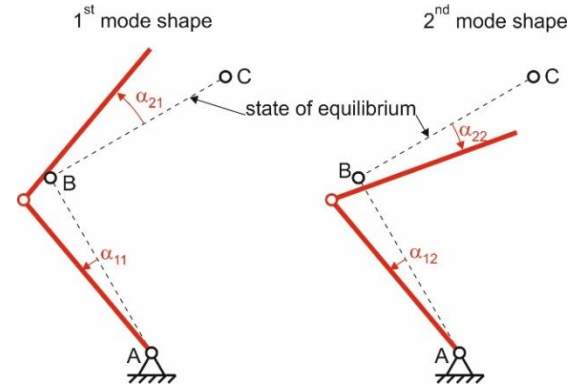

Fig. 4. Vibration mode shapes

The mode shapes of the robot arm vibrations are shown in Fig. 4. The first mode of vibration consists of the links rotating in the same direction, whereas the second mode consists of the links rotating in opposite directions.

4. NUMERICAL ANALYSIS

Due to the complexity of the equations of motion, it is not possible to obtain analytical forms of solutions without simplification. Therefore, the study of properties of Equ. (28) was carried out using numerical methods. Eq. (28) was transformed to the following form:

$$\ddot{\alpha} = -M^{-1}[C\dot{\alpha} + K\alpha] \tag{46}$$

Eq. (46) was solved numerically, assuming non-zero initial conditions causing vibrations with resonant frequencies. Then, the frequency spectrum of the vibrations of the robot's links, that is, the solutions of Eq. (46), was determined. Tests were carried out in many configurations obtaining a map of resonant frequencies depending on the robot's configuration. In the simulation studies (Tab. 1), the data corresponding to a section of the ABB IRB 1600 robot arm were adopted. The first link in the model corresponds to the second link of the IRB 1600 robot arm, and the second link in the model corresponds to the third link of the IRB 1600 robot.

Fig. 5 shows resonant frequency maps showing the vibration spectra of the robot's links as a function of the arm configuration defined by the angular coordinate β_2. This coordinate describes the angular position of link 2 relative to link 1. The characteristics show two resonant frequencies as the model takes into account the two degrees of freedom of the manipulator associated with vibration movements. The characteristics further show that the resonant frequencies of the robotic arm's vibration significantly depend on its positioning. As the absolute value of the angle β_2 increases, the value of the first resonant frequency increases, while the value of the second resonant frequency decreases, and significantly so.
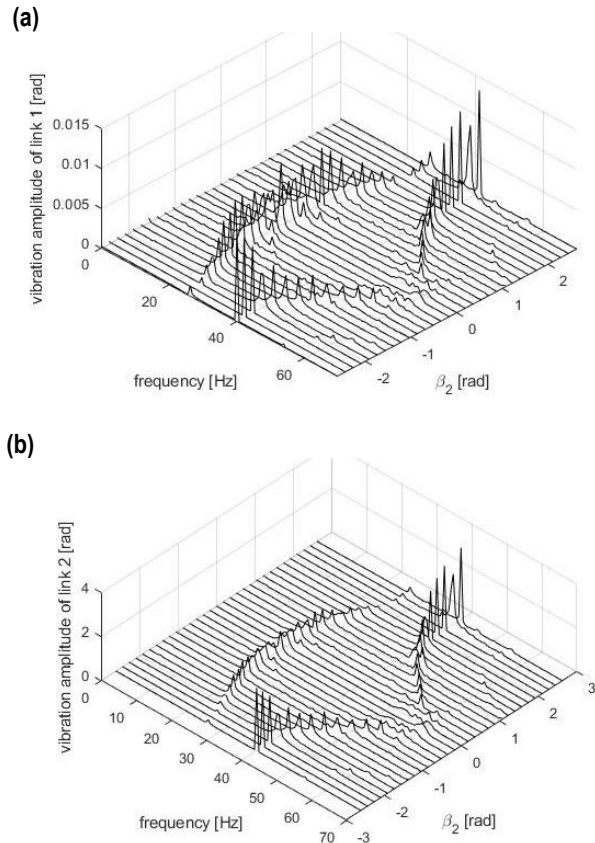
(a)

(b)

Fig. 5. Resonant frequency maps of the manipulator depending on the configuration: (a) vibration spectrum of link 1, (b) vibration spectrum of link 2

4. EXPERIMENTAL STUDIES

An ABB IRB 1600 robot (Fig. 6) was used in the experimental studies to verify the analytical modelling and simulation results. A PCB 086C03 soft-tipped impact hammer was used to excite the vibrations since the subject of the analysis was low-frequency vibrations of the manipulator related to flexibility in the joints. The point of application of the forcing was the robot's flange. The Iris M system, which includes a high-resolution camera and a computer with RDI Motion Amplification software, was used to record and analyse the robot's vibrations. The functionality of the system allows image acquisition and further processing, including amplification of the recorded motion and vibration analysis of selected regions (points) in the time and frequency domains.

The motion amplification function allows observation of displacements with amplitudes of several micrometres at multiple magnifications. On the other hand, vibration analysis of selected regions marked on the recorded image allows determining the motion parameters (displacement, velocity) at a given point and performing Fourier transformation of the motion parameters. In addition, the available filters allow separating each vibration frequency present and filtering the image in such a way as to observe each form of vibration of the robot separately. This functionality is particularly useful in the context of robot vibration analysis as it makes it possible to determine the direction of vibration at a given frequency and the form of deformation of the robot arm. In addition, the advantage of this technique is the ability to select any number of points for analysis after image acquisition, even without

prior use of markers. Disadvantages include the sensitivity of the method to lighting, as is the case with most vision techniques.
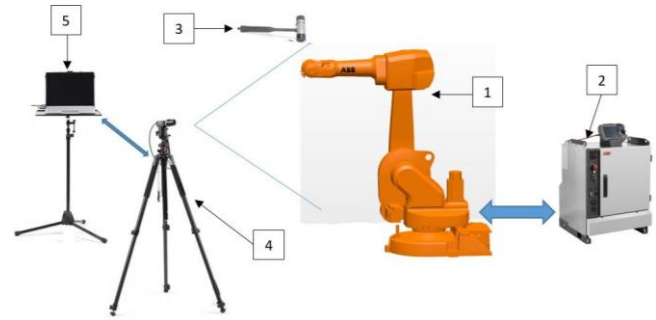

Fig. 6. Schematic diagram of the test stand: 1 – IRB 1600 robot, 2 – IRC5 controller, 3 – Impact hammer, 4 – camera, 5 – computer with RDI Motion Amplification software

The duration of a single image acquisition was 5 s at 140 frames per second and 1920 x 1200 resolution. Accordingly, the spectral analysis of vibrations was conducted in the frequency range of 0–70 Hz, and the frequency resolution of the spectral analysis was 0.2 Hz.

Fig. 7 shows selected configurations of the robot. The tests were carried out in configurations falling within the range of angle $\beta_2 \in -2{,}269 \div 2{,}619$ rad for $\beta_1 = 2\pi/3$.
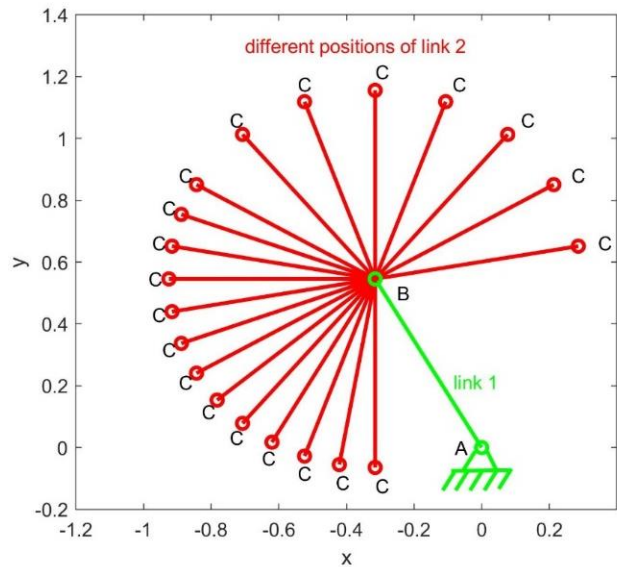

Fig. 7. Tested robot configurations

Based on the conducted tests, the characteristics of the excited vibration frequencies on the real object were obtained. The results of simulation and experimental studies are presented in Tab. 2. Fig. 8 presents a comparison of the results obtained from simulation studies (Fig. 5) and experimental studies. Since the vibration amplitudes of the links during the experiments and simulations have different values, and they are not significant in the presented studies, the results are presented in a two-dimensional graph. The values of the resonant frequencies obtained from the simulation (corresponding to the graphs in Fig. 5) are marked with the symbols "•" and "*", while the data from experimental studies are marked with the symbols "○" and "□".

The graphs shown in Fig. 8 confirm that the obtained results of simulation studies were confirmed by experimental studies. The obtained characteristics of the resonant frequencies in the studied range differ slightly from each other.

Tab. 2. Values of resonance frequencies obtained in simulation and experimental studies

β_2 [rad]	Simulation		Experiment	
	Frequency f_1 [Hz]	Frequency f_2 [Hz]	Frequency f_1 [Hz]	Frequency f_2 [Hz]
2.618	26.58	41.14	25.31	39.30
2.443	26.39	40.84	24.99	39.11
2.269	26.39	40.21	24.51	37.78
2.094	25.63	40.00	24.22	39.25
1.920	25.07	40.12	23.53	38.94
1.745	24.16	40.27	23.58	39.97
1.571	23.33	41.60	23.195	39.40
1.396	23.05	42.89	22.67	41.51
1.222	22.73	43.45	22.40	45.46
1.047	21.62	45.93	22.12	48.41
0.873	20.72	47.66	21.47	48.90
0.698	20.54	50.28	20.20	49.72
0.523	20.36	52.36	20.97	49.74
0.174	19.84	58.77	20.79	58.81
−0.174	20.23	60.67	19.26	60.02
−0.524	19.87	58.84	21.83	58.22
−0.873	20.40	52.44	20.11	52.15
−1.222	20.83	47.90	20.51	47.78
−1.571	22.10	44.22	22.14	44.06
−1.920	23.33	41.60	21.79	41.20
−2.269	25.07	40.12	-	-

An additional advantage of using a vision system with image filtering software is that it can generate movies containing extracted modes of resonance vibrations. There are two modes of resonance vibrations in the tested system. Fig. 9 presents one video frame, which shows the robot arm in a selected position defined by the angles $\beta_1 = 2\pi/3$ i $\beta_2 = -5\pi/9$. In addition, displacements of selected points are marked, which are proportional to the

length of the arrows. Fig. 9a shows the total vibrations of the arm in a selected position, Fig. 9b shows the first mode of vibrations and Fig. 9c shows the second mode of vibrations. For better visibility, for the purposes of motion analysis, the displacements in Figs. 9b and 9c are shown on a larger scale than shown in Fig. 9a.

For the first and second modes of vibration, a plan of displacements was made. The displacement vector of point A for the i-th mode of vibration is $\bar{r}_{Ai} = 0$. The displacement $\bar{r}_{Bi}$ of point B is determined based on image analysis and is different from zero for each mode of vibration. From the displacement distribution of link 1, the angle α_{1i} was determined, describing the angular vibrations of link 1 relative to point A. The displacement of point C in the i-th mode of vibration is equal to $\bar{r}_{Ci} = \bar{r}_{Bi} + \bar{r}_{CBi}$, where $\bar{r}_{CBi}$ is the relative displacement of point C relative to point B. The introduction of the relative displacement made it possible to determine the angle of rotation α_{2i}, describing the angular vibrations of link 2 relative to point B. The performed analysis of the displacement distribution shows that the first mode of vibration consists in the rotation of the links in the same directions, while the second mode of vibration consists in the rotation of the links in opposite directions.
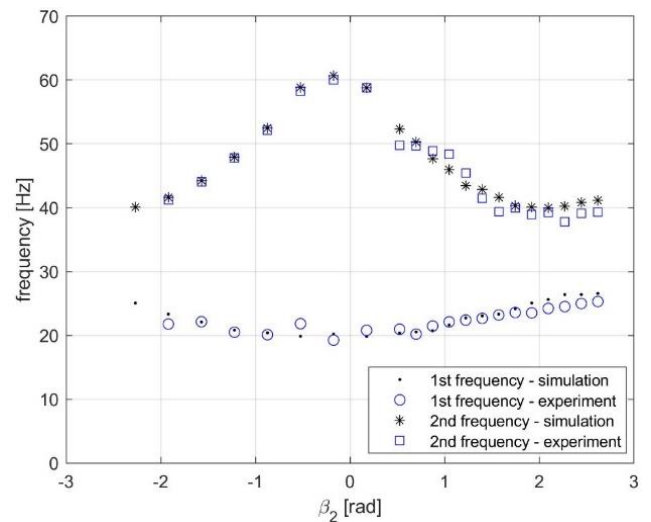

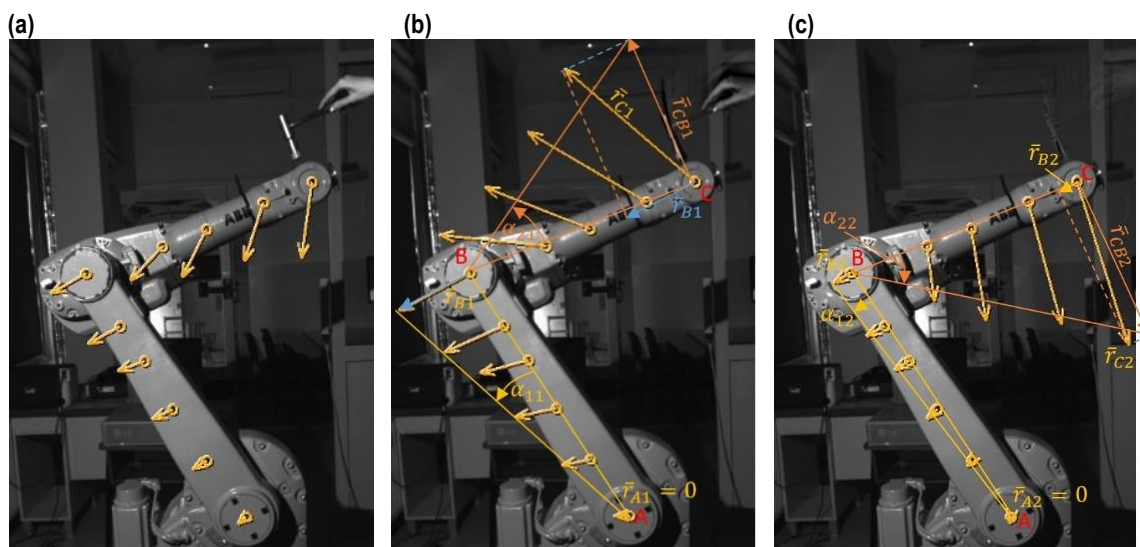Fig. 8. Frequencies of resonant vibration in simulation and experimental studies

Fig. 9. Robot arm vibrations: (a) total vibrations, (b) first vibration mode, (c) second vibration mode

5. CONCLUSIONS

The article presents the results of a study of the dependence of the resonant frequencies of a manipulator on its configuration, understood as the angular position of the links. The dynamic equations of motion were formulated, in which only the motion of the arms related to the flexibility in the joints, that is, the motion of a vibrational nature, was taken into account, and the other effects related to the slow-moving motion of the links were omitted. From the obtained results of simulation studies, it is clear that the mutual positioning of the manipulator's links significantly affects vibration effects, including the values of resonant vibration frequencies. The results of simulation studies based on the mathematical model were confirmed by experimental studies. In addition, it should be noted that the values of resonant frequencies determined in simulation and experimental studies differ by only a few percent, with a maximum of 6.43% for the first frequency of 7.66% for the second frequency and in the configuration $\beta_2 = 2.269$ [rad].

The next stages of the research will be related to the inclusion of the arm's interaction with the environment in the mathematical model, taking into account damping and increasing the number of degrees of freedom of the manipulator model.

The equations obtained in the proposed approach, although simpler than those found in the literature, are characterised by high complexity. Their analytical solution requires the use of simplifications leading to linearisation or the use of an approximation by expanding the non-linearity into series, which will be one of the next stages of the work.

REFERENCES

1. Bauer J, Friedmann M, Hemker T, Pischan M, Reinl C, Abele E, Stryk OV. Analysis of Industrial Robot Structure and Milling Process Interaction for Path Manipulation, in: Denkena, B., Hollmann, F. (Eds.), Process Machine Interactions, Lecture Notes in Production Engineering. Springer Berlin Heidelberg, Berlin, Heidelberg, 2013; 245–263. https://doi.org/10.1007/978-3-642-32448-2_11
2. Ji W, Wang L. Industrial robotic machining: a review. Int. J. Adv. Manuf. Technol. 2019; 103, 1239–1255. https://doi.org/10.1007/s00170-019-03403-z
3. Iglesias I, Sebastián MA, Ares JE. Overview of the State of Robotic Machining: Current Situation and Future Potential. Procedia Engineering. 2015;132, 911–917. https://doi.org/10.1016/j.proeng.2015.12.577
4. Burghardt A, Szybicki D, Kurc K, Muszyńska M. Robotic Grinding Process of Turboprop Engine Compressor Blades with Active Selection of Contact Force. Teh. Vjesn. 2022; 29(1), 15-22. https://doi.org/10.17559/TV-20190710141137
5. Gierlak P. Adaptive Position/Force Control of a Robotic Manipulator in Contact with a Flexible and Uncertain Environment. Robotics. 2021; 10, 32. https://doi.org/10.3390/robotics10010032
6. Bisu C, Cherif M, Gerard A. K'nevez JY. Dynamic Behavior Analysis for a Six Axis Industrial Machining Robot. 2011; AMR 423, 65–76. https://doi.org/10.4028/www.scientific.net/AMR.423.65
7. Huynh HN, Assadi H, Rivière-Lorphèvre E, Verlinden O, Ahmadi K. Modelling the dynamics of industrial robots for milling operations. Robot. Comput-Integr. Manuf. 2020; 61, 101852. https://doi.org/10.1016/j.rcim.2019.101852
8. Nguyen V, Johnson J, Melkote S. Active vibration suppression in robotic milling using optimal control. Int. J. Mach. Tools Manuf. 2020; 152, 103541. https://doi.org/10.1016/j.ijmachtools.2020.103541
9. Busch M, Schnoes F, Elsharkawy A, Zaeh MF. Methodology for model-based uncertainty quantification of the vibrational properties of machining robots. Robot. Comput-Integr. Manuf. 2022; 73, 102243. https://doi.org/10.1016/j.rcim.2021.102243
10. Tunc LT, Gonul B. Effect of quasi-static motion on the dynamics and stability of robotic milling. 2021; CIRP Annals 70, 305–308. https://doi.org/10.1016/j.cirp.2021.04.077
11. İlman MM, Yavuz Ş, Karagülle H, Uysal A. Hybrid vibration control of an industrial CFRP composite robot-manipulator system based on reduced order model. Simulation Modelling Practice and Theory, 2022; 115: 102456. https://doi.org/10.1016/j.simpat.2021.102456
12. İlman MM, Yavuz Ş, Yildirim TP. Generalized input preshaping vibration control approach for multi-link flexible manipulators using machine intelligence. Mechatronics, 2022; 82: 102735. doi.org/10.1016/j.mechatronics.2021.102735
13. Dwivedy SK, Eberhard P. Dynamic analysis of flexible manipulators, a literature review. Mech. Mach. 2006; Theory 41, 749–777. https://doi.org/10.1016/j.mechmachtheory.2006.01.014
14. Siciliano B, Wit CC, Bastin G. Theory of Robot Control. Springer Science & Business Media. 2012.
15. Goldsmith PB, Francis BA, Goldenberg AA. Stability of hybrid position/force control applied to manipulators with flexible joints. Int. J. Robot. Autom. 1999; 14(4), 146-160.
16. Vukobratovic M, Potkonjak V, Matijevic V. Dynamics of Robots with Contact Tasks. Springer Netherlands, Dordrecht. 2003. https://doi.org/10.1007/978-94-017-0397-0
17. Zhu Q, Mao Y, Xiong R, Wu J. Adaptive Torque and Position Control for a Legged Robot Based on a Series Elastic Actuator. Int. J. Adv. Robot. Syst. 2016; 13, 26. https://doi.org/10.5772/62204
18. Do T.-T, Vu V.-H, Liu Z. Linearization of dynamic equations for vibration and modal analysis of flexible joint manipulators. Mech. Mach. 2022; Theory 167, 104516. https://doi.org/10.1016/j.mechmachtheory.2021.104516
19. Endo T, Kawasaki H. Bending moment-based force control of flexible arm under gravity. Mech. Mach. 2014; Theory 79, 217–229. https://doi.org/10.1016/j.mechmachthory.2014.04.013
20. Cheong J, Youm Y. System mode approach for analysis of horizontal vibration of 3-D two-link flexible manipulators. J. Sound Vib. 2003; 268, 49–70. https://doi.org/10.1016/S0022-460X(02)01474-8
21. Thomsen DK, Søe-Knudsen R, Balling O, Zhang X. Vibration control of industrial robot arms by multi-mode time-varying input shaping. Mech. Mach. 2021; Theory 155, 104072. https://doi.org/10.1016/j.mechmachtheory.2020.104072
22. Yavuz Ş, İlman M. M. Modified reduced-order modeling of a flexible robot-manipulator and model-associative vibration control implementation. Extreme Mechanics Letters. 2020; 37, 100723.
23. Khorasani K. Adaptive control of flexible joint robots. Proceedings. 1991 IEEE International Conference on Robotics and Automation, Sacramento, CA, USA, 1991; vol.3, 2127-2134. https://doi: 10.1109/ROBOT.1991.131942
24. Mejri S, Gagnol V, Le TP, Sabourin L, Ray P. Dynamic characterization of machining robot and stability analysis. Int J Adv Manuf Technol 82, 2016; 351–359. https://doi.org/10.1007/s00170-015-7336-3

Paulina Pietruś: https://orcid.org/0000-0002-6428-0959

Piotr Gierlak: https://orcid.org/0000-0003-4545-8253

EFFECT OF LUFFA SPONGE FIBRE MATS
EMBEDDED IN THE PLASTER MATRIX

Khaled KHARRATI*,**, **Madiha SALHI***, **Abdelmoumen HIDOURI*****, **Ridha ABDELJABAR***

*Research Lab TEMI, Faculty of Science, University of Gafsa, cité Sidi Ahmed Zarroug, Gafsa 2112 Tunisia
**National Engineering School of Gabes, University of Gabes, V432+8QR Zrig Eddakhlania 6029, Tunisia
***Institut Superieur of Technological Studies of Gafsa, University of Gafsa, Gafsa 2112, Tunisia

khaledkharrati27@gmail.com, salhimadiha2@gmail.com, abdelmomnhidouri@gmail.com, ridha.abdeljabar@enit.rnu.tn

Abstract: The present experimental research work aims to elaborate a new composite material (CM) composed of plasters reinforced with mats of long unidirectional luffa sponge fibres, treated chemically by 1% NaOH solution during 90 min at a temperature of 50°C, in orderto improve its thermomechanical and physical properties. The influence of fibre mat and fibre napping numbers of luffa sponge on density, porosity, flexural strength, thermal conductivity, thermal diffusivity, thermal effusivity and specific heat capacity properties was investigatedto lower building energy consumption. As far as our case is concerned, we processed a composite using single, double and triple-layer luffa sponge fibre mats. In our study, we are basically confined our experiments to three-layer mats. The experimental results revealed that the networking structure of fibres increases the flexural strength and decreases the thermal conductivity for a two-layer fibre wire mesh imbedded in the plaster matrix as compared with the neat plaster. However, there is a decrease in strength for a triple-layer composite, which referred to poor wetting of the fiber with the matrix material.

Key words: Luffa sponge fibre, reinforced plaster, mechanical characteristics, thermo-physical properties

1. INTRODUCTION

Gypsum materials were used for various applications hundreds of years ago and are still used to date. They are very cheap and suitable for multiple uses. However, nowadays, most of the surfaces inside building are either composed of synthetic or natural fibres or lined with gypsum products selected by architects for their high performance and outstanding qualities [1].

Gypsum (calcium sulphate dehydrate, $CaSO_4$, $2H_2O$) is frequently used as a finishing material in the construction and building industry owing to its feasibility, simplicity of application, fire resistance and environmental friendliness [2]. A gypsum network is formed when these crystals are implicated. Despite its numerous advantages, gypsum as a building material displays several disadvantages as well, including brittleness, weight and low water resistance [3, 4]. A composite material (CM) is a compound that is made up of two or more unique materials with diverse qualities on a macro scale to generate a new material with attributes that are completely different from those of the individual elements. A matrix is the basic phase of a CM with a continuous nature. In other words, the matrix corresponds to a substance that works as a binder, holding the fibres in place and transferring the external load to reinforcement. These matrices are considered as softer and more malleable. Notably, the main weakness of gypsum resides in its brittleness and poor mechanical properties, mainly under tension. Therefore, it is interesting to investigate different additives that can improve the mechanical properties of gypsum, focussing on the use of reinforcing fibres or additives in the gypsum matrix. Additionally, vegetable fibres also exhibit great tensile strength, toughness, extreme lightness and good thermal insulation properties with regard to their composition and structure [5]. These properties seem to favour construction material reinforcement. Most research works undertaken on vegetable fibres have been particularly oriented towards the improvement of mechanical properties of building materials.

Acda [6] performed a study on the mechanical resistance of CMs based on cement and natural additives. The inclusion of vegetable fibres in the concrete matrix can improve its mechanical strength [7]. Synthetic or natural fibres can be used as reinforcements. Several natural fibre-reinforced polymer composites (NFPCs) were introduced into the competitive market to meet the demand for growing environmental security. Basically, NFPCs outperform synthetic fibre-based composites in several ways. Since natural fibre composites have superior characteristics, these have grown in popularity and appeal [8].In 2021, Djoudi et al. [9] examined the physico-mechanical properties of CMs based on date palm tree fibres. Amelioration within the mechanical properties was reported corresponding to the fiber mass proportion up to 10%. In 2014, Djoudi et al. [10] investigated date palm fibers as a reinforcement in plasters. In consistency with the test findings obtained by these researchers, the consolidation of various concentrations of date palm fibres within the plaster increments the modulus of flexibility and water absorption. These outstanding properties indicating the low density of these fibres prompted many researchers to use these fibres for the development of bioderived composites [11–14].

Alcaraz et al. [15] explored the mechanical behaviour of materials composed of plaster and jute fabric, as well as the grip of jute fabric with plasters. The impact of jute fabric on the flexural, compressive and flexibility of the composite wasequally studied. They emphasised that the jute fabric reinforcement improves the

Khaled Kharrati, Madiha Salhi, Abdelmoumen Hidouri, Ridha Abdeljabar
Effect of Luffa Sponge Fibre Mats Embedded in the Plaster Matrix

DOI 10.2478/ama-2023-0061

mechanical properties of the composite. They focussed on the improvement the mechanical properties of gypsum through the use of polymeric or metallic fibres. Eve et al. [16] mixed different concentrations of polyamide fibres with plasters. They asserted that all mechanical characteristics of the composite decrease with increasing fibre concentrations, except for fracture toughness. Gencel et al. [17] created a gypsum composite containing diatomite and polypropylene fibres. It is inferred that the addition of diatomite porosity contributes to reducing thermal conductivity and the addition of polypropylene fibres enhances mechanical properties. Loculano et al. [18] used treated hemp fibres as a reinforcement in gypsum boards. Results revealed increased toughness and reduced damage in low-impact tests. Basaran et al. [19, 20] investigated the behaviour of masonry walls with gypsum fortified in different ratios of polypropylene and steel fibres, which reinforced significantly the rigidity of walls. Khali et al. [21] reported gypsum plaster composites synthesised into plasters with different waste materials such as furnace slag, calcium carbonate and commercial alcohol polymer.The results demonstrated an increase in the compressive strength for lower concentrations of waste. The impact of chicken feather waste on thermal features of mortar composites was investigated by Ouakarrouch et al. [22]. They unveiled that chicken feathers enhance the thermal features of reinforced mortar. Sakthieswaran and Sophia [23] examined the mechanical characteristics of the *P. Juliflora* fibre reinforced gypsum composites and indicated that the flexural strength of the composites increases with the incorporation of 2% weight of *P. Juliflora* fibre, referring to the ability of the fibre to fill voids of the composites. Maaloufa et al. [24] opted forthe best percentage of cork and fibre in a gypsum matrix to optimise thermal insulation and mechanical properties. The thermal conductivity considerably improved. The alpha fibre enhanced the resistance to bending, but the cork makes the composite more vulnerable. Miraoui et al. [25] explored the effect of alpha fibres on the mechanical properties of mortar. They argued that alpha fibres improve the flexural strength of reinforced mortar. In 2019, Salim et al. [26] specified the mechanical characteristics of plaster-based composites with plastic fibres and glass powder. Furthermore, the fibre additions at various rates results in improvement in terms of mechanical properties. The thermal and mechanical performance of a gypsum composite reinforced with rice husk and oil palm trunk fibres was tackled by Selamat et al. [27]. According to the test results, the gypsum composite manufactured with 20% fibre loading has good thermal and mechanical stability. In this respect, Touil et al. [28] assessed the influence of alpha fibres on thermal-mechanical characteristics of the plaster. The results suggested that by increasing the fibre concentration, the thermal features can be significantly enhanced. The mechanical assays, on the other side, indicated that adding fibres to the plaster permits a reduction in its resistance to bending, but an enhancement in the failure mechanismleads to a nonlinear and ductile behaviour.

In this research paper, our central focus is on the physico-thermo-mechanical properties of bio-CMs made up of plasters and luffa sponge fibres. Fibres wire meshes are formed into mats of various layers that are embedded in a matrix of plasters such that they act together to resist forces. The major purpose of reinforcement is to provide additional strength for plasters where it is needed, as well as toexplore the physical and thermal properties of CMs.

2. MATEIALS AND METHODS

2.1. Materials

2.1.1. Plaster

The plaster used for the study was KNAUF maknessy plaster (staff plaster), which is noted for its simplicity of application and exceptional degree of finishing that can be put manually on all supports [En fait, ce matériau est connu par sa facilité d'application et aussi par son degré exceptionnel de finition, s'ap-pliquant ainsi manuellement sur tous les supports]. The plaster is derived from gypsum through the heating process, as described in the following Eq. (1):

$$CaSO_4.2H_2O + Heat \longrightarrow CaSO_4.1/2H_2O \qquad (1)$$
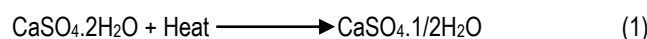
X-ray diffraction allowed us to better investigate the mineralogical composition of plasters. Fig. 1 illustrates the diffractogram that characterises the different mineralogical components of anhydrous plasters. It reveals that the plaster in our study is composed of some elements, which are indicated in Tab.1. The percentages of the elements making up the plaster are provided using TOPAS software, which is based on Rietveld analysis.

Tab. 1. Mineralogical composition of plaster

Mineralspecies	Formula	Content (%)
Bassanite	$CaSO_4.0, 5H_2O$	92.43
Calcium sulphate	$Ca(SO_4)$	4.14
Dolomite	$CaMg(CO_3)_2$	3.43
Crystallinity rate		78.6

2.1.2. Luffa sponge

Luffa is a climbing plant in the Cucurbitaceae family, and its dry fruit (luffa sponge) has a fibrous net-like vascular system (see Fig. 2).

Relying on previous studies [29, 30], the percentages of alkaline solution rates, such as, 0.5%, 1%, 2%, 3% and 5%,were selected to better enhance fibre characteristics. The alkaline treatment targeted the changes in chemical compositions of luffa sponge fibres [41]. The cellulose content in treated luffa sponge fibre increased while hemicellulose and lignin contents decreased as compared with untreated luffa sponge fibres. It corresponds to one of the treatment methods commonly applied to adjust the surfaces of natural fibres in order to enhance the interface compatibility among fibre and plaster matrixes. It induces a better contact and bonding mechanism between fibre and plaster matrixes.

The treatment was carried out through performing a series of chronological steps under laboratory conditions. These steps are described as follows.

First, the dry luffa sponge (see Fig. 2 (a)) was anatomised longitudinallyto transform it into a parallelepiped shape instead of a cylindrical one (see Fig. 2 (b)). Then, it was cut into rectangular webs of predefined dimensions (see Fig. 2 (c)). Subsequently, these luffa sponge webs were chemically treated under different conditions. Then, they were dried. In this way, the luffa sponge fibres could be easily extracted from the web. Finally, these fibres were cut according to the required dimensions (see Fig. 2 (d)).
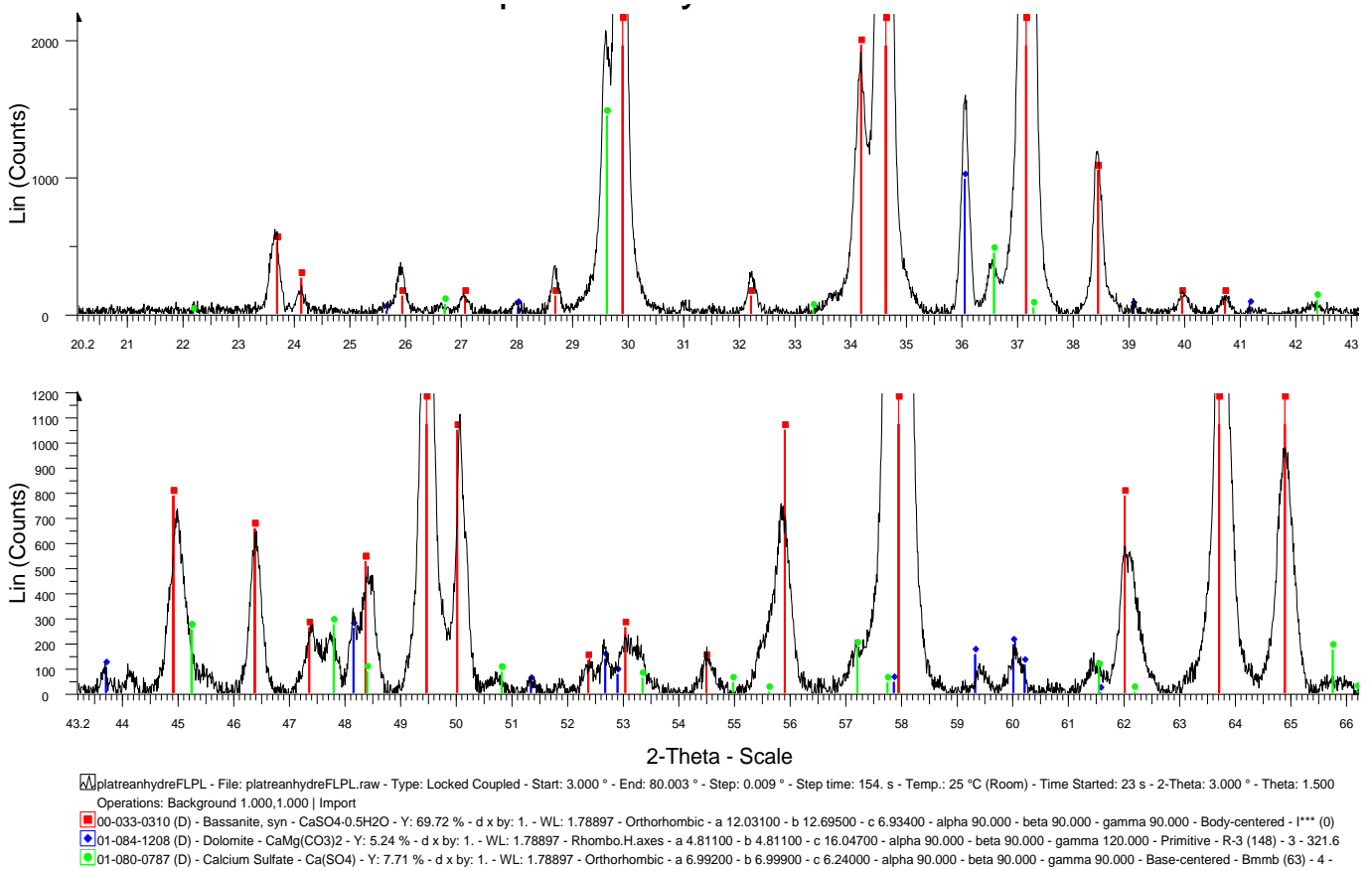
platreanhydreFLPL - File: platreanhydreFLPL.raw - Type: Locked Coupled - Start: 3.000 ° - End: 80.003 ° - Step: 0.009 ° - Step time: 154. s - Temp.: 25 °C (Room) - Time Started: 23 s - 2-Theta: 3.000 ° - Theta: 1.500
Operations: Background 1.000,1.000 | Import
■ 00-033-0310 (D) - Bassanite, syn - CaSO4·0.5H2O - Y: 69.72 % - d x by: 1. - WL: 1.78897 - Orthorhombic - a 12.03100 - b 12.69500 - c 6.93400 - alpha 90.000 - beta 90.000 - gamma 90.000 - Body-centered - I*** (0)
◆ 01-084-1208 (D) - Dolomite - CaMg(CO3)2 - Y: 5.24 % - d x by: 1. - WL: 1.78897 - Rhombo.H.axes - a 4.81100 - b 4.81100 - c 16.04700 - alpha 90.000 - beta 90.000 - gamma 120.000 - Primitive - R-3 (148) - 3 - 321.6
● 01-080-0787 (D) - Calcium Sulfate - Ca(SO4) - Y: 7.71 % - d x by: 1. - WL: 1.78897 - Orthorhombic - a 6.99200 - b 6.99900 - c 6.24000 - alpha 90.000 - beta 90.000 - gamma 90.000 - Base-centered - Bmmb (63) - 4 -

Fig. 1. X-ray diffraction analysis of anhydrous plaster (Meknassy)

Fig. 2. (a) Luffa sponge, (b) The portion of the luffa open as mat, (c) luffa mat and (d) luffa fibres

The fibers must, first of all, be washed with hot distilled water at a temperature T= 40°C so as to remove any natural hazards (dust, dirt, etc.). They were next dried in an electric oven. Subsequently, the specimens were soaked in different concentrations of NaOH solutions: 0.5%, 1%, 2%, 4% and 5%, at different temperatures (25°C, 50°C and 75°C) and different time intervals (1/2 h, 1h, 3/2h, 2h and 3h), as demonstrated in Fig. 3. After finishing the treatment operation with the NaOH solution, some contamina-

tions related to this operation may appear on the luffa sponge fibre surfaces. These contaminations may equally have a negative impact on the quality of these fibres. To shun this risk, we resorted to wash the fibres well several times (3–4 times) using hot distilled water T= 40°C in order to remove all remaining NaOH residues to reach a neutral pH. Afterwards, the fibres were dried at a temperature of 50°C, for 7 h.
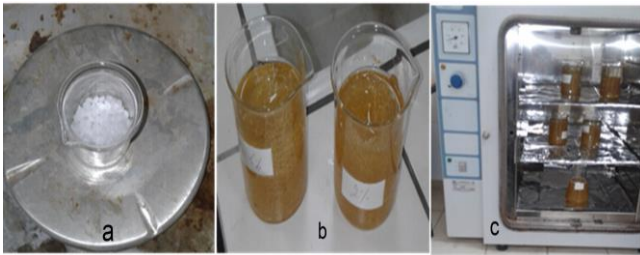
Fig. 3. Step of laboratory treatment: (a) NaOH solid, (b) NaOH solution and (c) fiber soaking in NaOH solution in oven

The tensile strength of treated fibres under various conditions, such as concentration of alkaline solution, time of soaking and temperature, was assessed. It has been found that the fibres drenched in an alkaline solution of 1% NaOH concentration for 90 min at 50°C temperature, which are regarded as an optimum condition, bring about an increase in the rate of tensile strength of around 61% as compared with the untreated fibre. Fig. 4 outlines the obtained results.
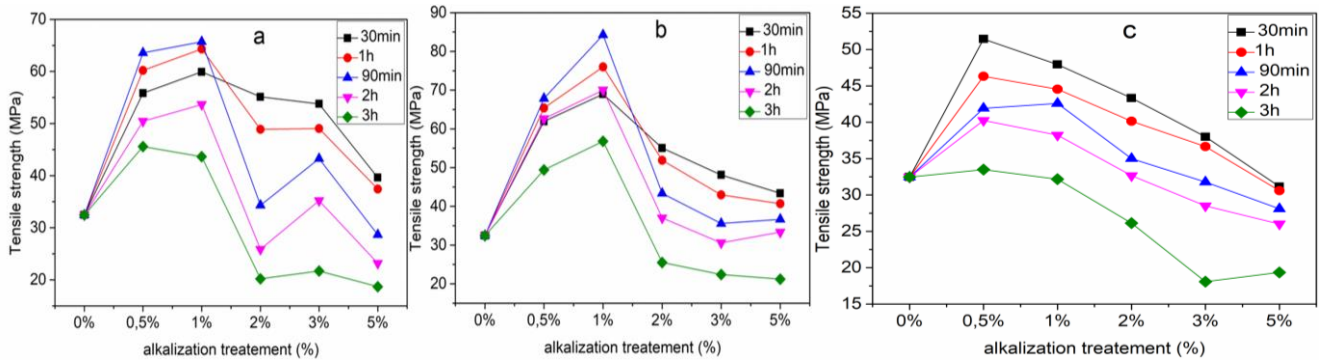
Fig. 4. The effect of NaOH on the tensile strength of luffa sponge's fibers treated with different concentrations and duration (a) for 25°C, (b) for 50°C and (c) for 75°C [31]

2.2. Experimental methods

2.2.1. Fibres preparation

Mathematical formulas should be type written in mathematical style, aligned to left and numbered irrespective of chapter numbering.

After cutting fibres manually from luffa sponge into rectangular mats, they are soaked in an alkaline solution of 1% NaOH concentration for 90 min at 50°C. After being dried, the outer core and a micro channel section of the sponge guard were opened without regard to the end portion so as to maintain the same thickness of the mat, as portrayed in Fig. 5 (a) (luffa sponge fibre mats were invested to manufacture the layered composite; see Fig. 6).
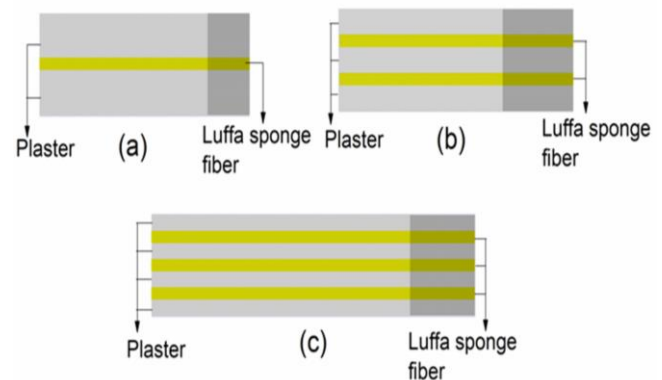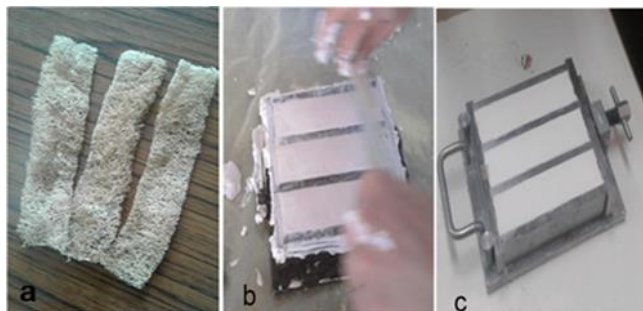

Fig. 5. (a) The luffa part in the form of a rectangular shape with dimensions (150mm- 30mm- 5mm) and mass (1.85g), (b) Hand scraping the surface of the filled mold and (c) three identical specimens preparation

Fig. 6. Graphic views of the composites : (a) Single layer composite (SL), (b) Double layer composite (DL) and (c) Triple layer composite (TL)

2.2.2. Plaster matrix preparation

The preparation of a blend of mortar was carried out through blending plasters with water, utilising a water-to-plaster proportion (w/g) of 0.6 in the blending method. Afterwards, the specimens were put away and dried for 28 days at laboratory ambient temperature.

In our case, we did this through selecting a composite using single-layer (SL), double-layer (DL) and triple-layer (TL) luffa sponge fibre mats, as shown in Fig. 6. We cannot opt for more than three-mat layers, as the thickness does not match the total height of the specimens. Four different specimens for various layers (neat plaster, SL, DL and TL) produced in three examples were tested, as shown in Fig. 5 (c). In total, 12 specimens were tested

2.2.3. Flexural strength

Flexural tests were conducted with a three-point bending device. The specimens were manufactured with a dimension (40 mm $\times$ 40 mm $\times$ 160 mm, see Fig. 7) in accordance with the requirements of NF EN 196-1, which is the standard determined for mechanical tests (three-point bending, Fig. 8). The machine was computer controlled, with a constant speed loading of 2 mm/min until the material broke down.

The flexural strength is denoted by the following Eq. (2):

$$R_f = \frac{3 \times F_f \times L}{2 \times b \times h^2} \tag{2}$$

where: R_f is flexural strength (MPa), F_f is force applied (N), b is the width of specimen (mm), h is the thickness of the specimen (mm) and L is the length of the specimen (mm).

When the specimen gives up bending, this corresponds to a yield point.
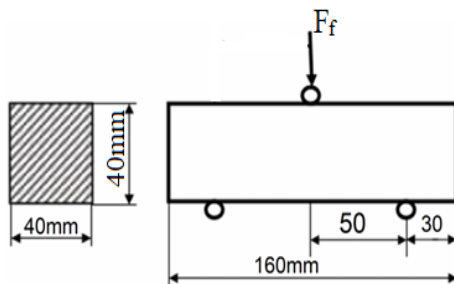

Fig. 7. Three points bending test machine

Fig. 8. Sketch of Device for the three-point bending strength test

2.2.4. Porosity calculation

The experimental method invested in this work to determine the porosity of specimens was identified in the following steps. First, we weighed each specimen in the dry state with an electronic balance. Second, each specimen was dipped in distilled water for 48 h. Third, each specimen was weighed in the wet state; then, the void volume of each specimen was specified by computing the difference between the wet mass and the dry solid mass. Finally, the void volume of each specimen was estimated through computing the difference between the wet mass and the solid mass and then dividing by the density of water. The porosity

was obtained according to the following Eq. (3):

$$P = \frac{void\ volume}{Total\ volume} \times 100 \tag{3}$$

where: P expresses porosity (%).

2.2.5. Density

The density (ρ) of the materials was evaluated after they had dried. It stands for the mass unit volume of the material that makes up the aggregate, considering the voids that may exist within or between the grains. The density (ρ) is computed using the following Eq. (4):

$$\rho = \frac{M}{V} \tag{4}$$

where: M is the total mass of specimen (g) and V is the volume of the specimen (cm^3).

2.2.6. Thermal apparatus

The "blue box" LEI700 measurement cell was used to determine this procedure. The measurement instrument was made up of a well-insulated box called "A" that was kept cool by glycol water flowing from a cryostat. Two identical and independent measurement boxes, namely "B1" and "B2," were insulated with polystyrene inside and invested to measure steady-state thermal conductivity and transient thermal diffusivity, respectively (see Fig. 9).

Fig. 9. Photo of EI700 measuring Apparatus

2.2.6.1. Thermal conductivity

Measuring thermal conductivity using the box method in the steady state rests on creating two atmospheres: hot and cold, on both sides of the material to be tested (a low temperature and highly insulated enclosure), and a box is equipped with a heating film controlled by a rheostat in order to maintain a temperature close to ambient temperature. The surface temperatures of the specimen of lathhot and cold face as well as the ambient temperature were controlled and measured, as displayed in Fig. 10. When the temperatures stabilise with variation of the order of 0.1° in 1 h, we suppose that the steady state is achieved. This lies basically between 4 h and 7 h after mounting the specimen.

The thermal conductivity is provided by the following Eq. (5):

$$\lambda = \frac{e}{S(T_C - T_F)} \left[\frac{U^2}{R} - C(T_B - T_A) \right] \tag{5}$$

where: e is the thickness of the sample (m), S is the area of the sample (m²), A is the value of the heating resistor (Ω), C is the heat loss coefficient (W/K), U is the voltage across the resistor (V), T_C and T_F are the temperatures of the hot side and the cold sides (°C), respectively, and T_B and T_A are temperatures inside the box and ambient temperature (°C), respectively.
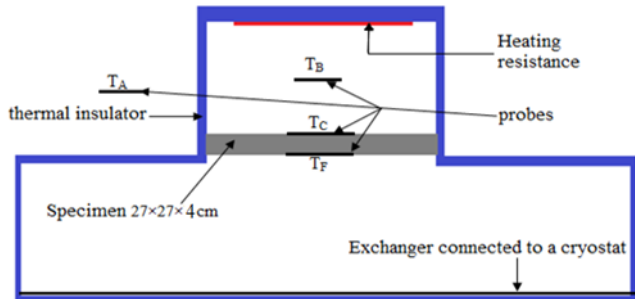

Fig. 10. Descriptive diagram of the device for measuring thermal conductivity

2.2.6.2. Thermal diffusivity

As for the measurement of thermal diffusivity in a transient state, a measurement cell is composed of two identical boxes, perfectly symmetrical (see Fig.11) and strongly insulated from the external environment by polystyrene. To send a heat flux, a constant high-power halogen lamp (1,000 W) was used for a controlled duration on the upper face of the specimen.The thermal diffusivity was deduced departing from the experimental thermogram (Fig. 12), using the DEGIOVANNI model.
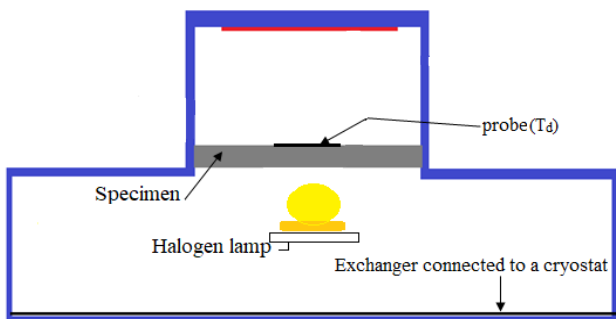

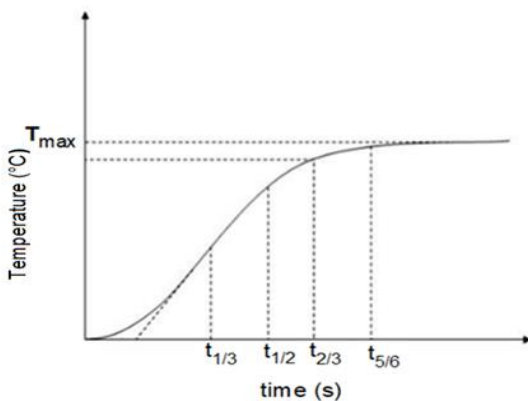**Fig. 11.** Descriptive diagram of the device for Thermal diffusivity measurement

Fig. 12. Typical thermogram for the determination of thermal diffusivity [39]

DEGIOVANNI model

Actually, in order to specify the thermal diffusivity, we applied the DEGIOVANNI model [39]. Eq. (9) makes it possible to estimate the thermal diffusivity by knowing the times for which several pairs of points were considered, at characteristic times: $t_{1/3}$, $t_{1/2}$, $t_{2/3}$ and $t_{5/6}$. In addition, we need to take into account heat losses during diffusivity measurement [32].

$$\alpha_1 = \frac{e^2}{t_{\left(\frac{5}{6}\right)}^2}\left(\left(1{,}15 \times t_{\frac{5}{6}}\right) - \left(1{,}25 \times t_{\frac{2}{3}}\right)\right) \tag{6}$$

$$\alpha_2 = \frac{e^2}{t_{\left(\frac{5}{6}\right)}^2}\left(\left(0{,}761 \times t_{\frac{5}{6}}\right) - \left(0{,}926 \times t_{\frac{1}{2}}\right)\right) \tag{7}$$

$$\alpha_3 = \frac{e^2}{t_{\left(\frac{5}{6}\right)}^2}\left(\left(0{,}761 \times t_{\frac{5}{6}}\right) - \left(0{,}862 \times t_{\frac{1}{3}}\right)\right) \tag{8}$$

$$\alpha = \left(\frac{\alpha_1 + \alpha_2 + \alpha_3}{3}\right) \tag{9}$$

2.2.6.3. Thermal effusivity

One of the prominent ideas regarding how thermal insulation materials operate is thermal effusivity. It corresponds to the material's capacity to both absorb and release heat from its surface. Materials with high thermal effusivity cannot retain heat for very long since they lose it rapidly from their surface when the surrounding temperature decreases.

Thermal effusivity [37] of the CMs was calculated according to the Eq. (10) by determining the experimental values of thermal conductivity and thermal diffusivity.

$$E = \frac{\lambda}{\sqrt{\alpha}} \tag{10}$$

where: E is thermal effusivity ($J \cdot K^{-1} \cdot m^{-2} \cdot s^{-1/2}$), λ is thermal conductivity ($W \cdot m^{-1} \cdot K^{-1}$) and α is thermal diffusivity ($m^2 \cdot s^{-1}$).

2.2.6.4. The specific heat capacity

An intrinsic factor that characterises the thermal inertia of materials is the specific heat capacity. It is obvious to determine the specific heat capacity of CM whenever its density, thermal conductivity and diffusivity are computed. The relationship is provided as follows:

$$C_p = \frac{\lambda}{\rho \cdot \alpha} \tag{11}$$

where: C_p is specific heat capacity ($J \cdot kg^{-1} \cdot K^{-1}$) and ρ is density ($kg \cdot m^{-3}$).

3. RESULTS AND DISCUSSION

The experimental findings for each specimen are outlined in Tab. 2.

Tab. 2. Test results

Specimen	Porosity (%)	Flexural Strength (MPa)	Density (kg · m⁻³)	Thermal diffusivity (m² · s⁻¹)	Thermal Conductivity (W · m⁻¹ · K⁻¹)	Thermal effusivity (J · K⁻¹ · m⁻² · s⁻¹ᐟ²)	Specific heat capacity (J · kg⁻¹ · K⁻¹)
Plaster	38±0.7	1.3±0.02	1168±8	$2.8\pm0.011\ 10^{-7}$	0.27±0.002	510.25±3	825.58±2
Plaster+ SL	43±0.9	1.5±0.03	1103±9	$2.7\pm0.012\ 10^{-7}$	0.252±0.003	484.97±4	846.18±2.7
Plaster+ DL	47±0.8	1.6±0.02	1048±8	$2.61\pm0.01\ 10^{-7}$	0.236±0.002	461.95±3.5	862.8±2.3
Plaster+ TL	54±1	1.4±0.04	983±9	$2.49\pm0.013\ 10^{-7}$	0.215±0.003	430.86±4.3	878.39±2.8

4. MECHANICAL PROPERTIES

4.1. Behaviours of plaster are reinforced with mats of long unidirectional luffa sponge fibres

A load deflection curve for plasters with and without reinforcement is depicted in Fig. 13. The behaviour of reinforced plaster is characterised by DL luffa sponge fibre mats, as shown in Fig. 13 (plaster + DL):

1. The first region presents a non-linear behaviour. It corresponds to the behaviour of a pure plaster (matrix).
2. The second zone is an intermediate zone from which there may be a slight load drop corresponding to the first macroscopic damage to the composite. Then, the load is taken up by luffa fibre mats up to the maximum strength.
3. The third region corresponds to the manifestation of nonlinear behaviour from the maximum force applied to the test sample. One notes a slight reduction in load associated with tearing and damage to the reinforced plaster.
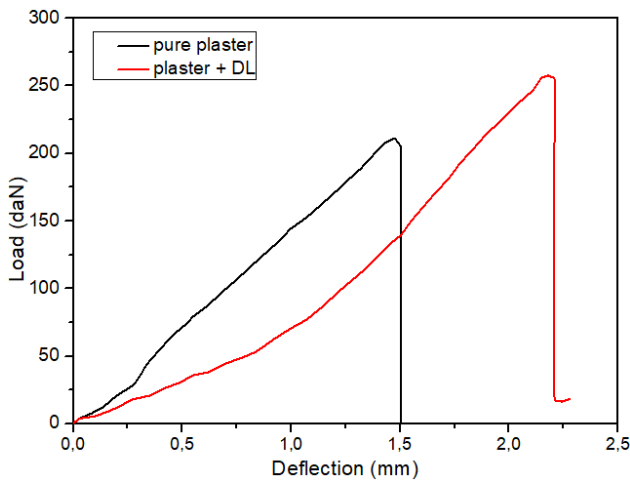

Fig. 13. Load deflection curve: Plaster with reinforced mats of long unidirectional Luffa sponge fibers, pure plaster

The specimen behaviour reinforced with luffa fibre mats displays an improvement in deflection at failure, see Fig. 13 (plaster + DL) and (pure plaster).

Fig. 14 illustrates the failure stages of unidirectional long luffa fibre mat-reinforced plasters after the three-point bending tests. One notices that the reinforced plaster is cracked first; then, the load is carried by the fibres up to F_{max}. Next, failure occurs as the luffa fibres slip, see Fig. 14.

Fig. 14. Failure stages of plaster reinforced with mats of long unidirectional Luffa sponge fibers

4.2. Flexure tests

The specimens were subjected to a three-point flexural test. The flexural tests in Fig.15 revealed that the plaster with fibre mats resisted to flexural strength more than specimens of pure plaster. According to the test results, a change in the flexure behaviour was observed during each test. A maximum resistance was detected for a specimen with DL. The maximum flexural strength and deflection were 1.6 MPa and 2.2 mm, respectively, as shown in Fig.13. It was inferred that with the addition of luffa fibre mats, the mechanical features of CM improved. It was observed that various layers of fibre mat reinforcement had different failure and deflection impacts on the CM. There was no significant change in terms of bending, but stiffness, strength and ductility enhanced with the addition of fibres mats. Similar observations were reported by Babu et al. [33] and Djoudi et al. [34], while they had been working on reinforced fibres.
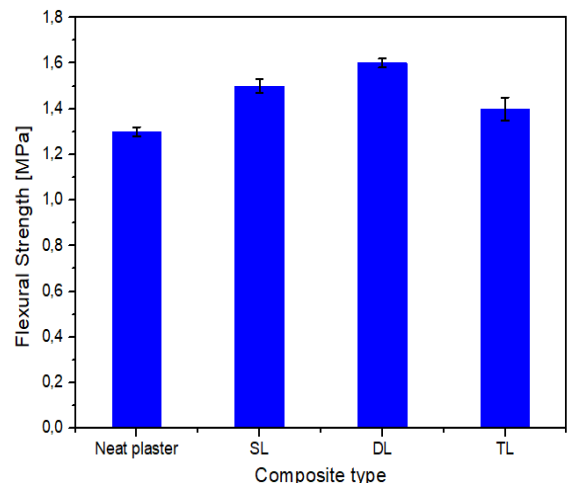

Fig. 15. Flexural strength of luffa fibers plaster composite

Khaled Kharrati, Madiha Salhi, Abdelmoumen Hidouri, Ridha Abdeljabar
Effect of Luffa Sponge Fibre Mats Embedded in the Plaster Matrix

DOI 10.2478/ama-2023-0061

5. PHYSICAL PROPERTIES

5.1. Porosity

Fig. 16 traces the evolution of porosity of a plaster mortar reinforced with sponge luffa fibres. Note that porosity increases as a function of the percentage of spongy fibres.This refers basically to the significant vacuum resulting fromthe addition of fibres as natural layers. Porosity changes from 38% in pure plaster to 54% with a TL composite. Porosity is a very critical property that positively affects the thermal conductivity of CM. Similar observations were reported by Djoudi et al. [34].
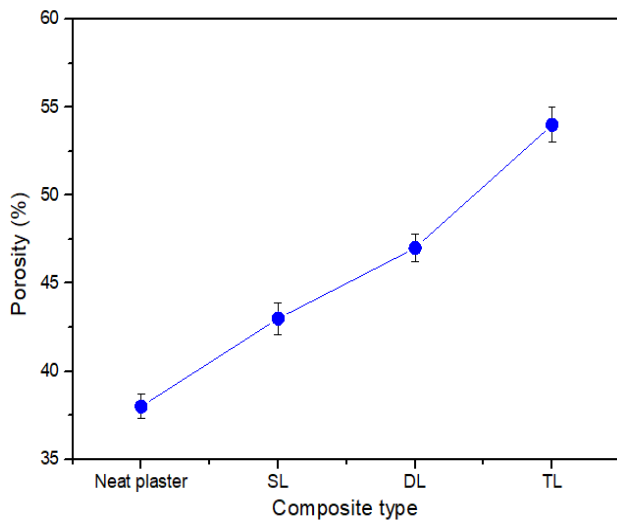

Fig. 16. Reinforcement Layers Effect on Porosity

5.2. Density

Fig.17 clarifies the variation of the density according to the layers of luffa sponge fibres. It can be therefore noted that the density decreases progressively as the layers of fibres increase. The combination density ranged from 1168 kg $\cdot$ m^{-3} for pure plaster to 983 kg $\cdot$ m^{-3} for a TL reinforcing concentration. This result goes in a good agreement with that obtained in the research of Babu et al. [33].
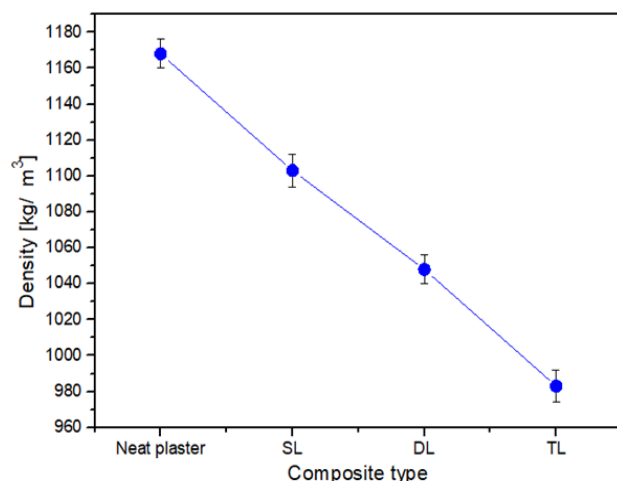

Fig. 17. Effect of reinforcement layers on density

6. THERMAL PROPERTIES

6.1. Thermal conductivity

Thermal conductivities of the various composite specimens with different layers numbers of luffa sponge fibres are displayed in Fig. 18. It is obvious that as the rate of luffa sponge fibres increases, the thermal conductivity decreases since the conductivity of CM decreases, whereas porosity increases. As far as our research is concerned, thermal conductivity of CM varies from 0.27 W $\cdot$ m^{-1} $\cdot$ K^{-1} when the material is fibreless to 0.215 W $\cdot$ m^{-1} $\cdot$ K^{-1} with a TL composite. It's worth noting that with the TL, CM displays the best thermal behaviour and the lowest density. The obtained results go in good consistency with the studies [38, 34], which confirmed that the thermal insulation of CM significantly improved with the increase of natural fibres in the base material. Similarly, Touil et al. [28] investigated the influence of alpha fibres on plaster thermal properties.

The results corroborated that by increasing the fibre concentration in both cases, the thermal properties cansignificantly improve. In terms of thermal performance, the sandwich structure proved to be noticeably more effective since an optimal thermal conductivity of 0.227 W $\cdot$ m^{-1} $\cdot$ K$^-$1 was obtained with 4% of fibres as opposed to 0.25 W $\cdot$ m^{-1} $\cdot$ K^{-1} which was achieved with the second model.
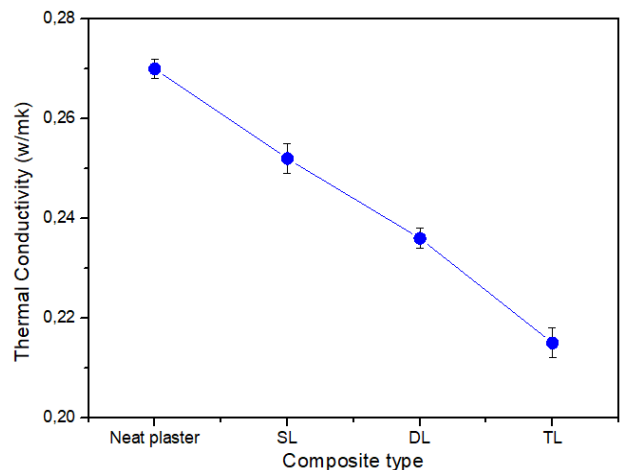

Fig. 18. The effects of luffa fibers layers of thermal conductivity

6.2. Thermal diffusivity

In Fig. 19, we inferred that the addition of fibre mats decreases the thermal diffusivity of the CM. It varies from 2.8. 10^{-7} (m^2 $\cdot$ s^{-1}) for the specimen without fibres to 2.49. 10^{-7} (m^2 $\cdot$ s^{-1}) for the specimen the TL composite. It has been proved that the increment of the fibre layer proportion reduces the thermal diffusivity. In addition, it has the merit of being a natural, safe and less-expensive product. Therefore, the more luffa sponge fibre layers exist in the medium, the less heat transfer there is. According to this significant result, the thermal insulation material not only displays a low thermal conductivity but also delays heat transfer. It is clear that the thermal diffusivity value of the composite depends on the porosity of the matrix. Likewise, Amara et al. [35] confirmed that the thermal diffusivity of date palm fibre reinforced gypsum was reduced as compared with pure gypsum.
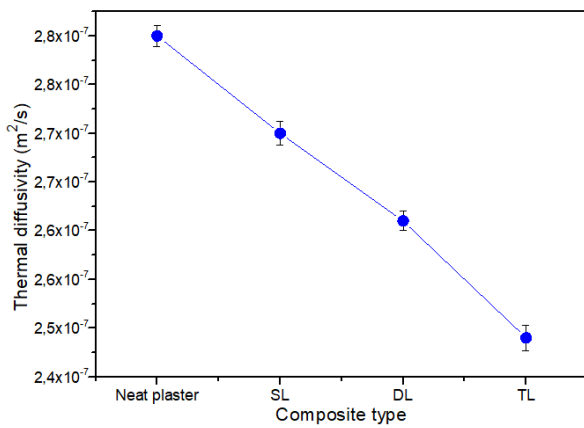
Fig. 19. Variation of the thermal diffusivity of plaster for the number of layers of luffa fibers

6.3. Thermal effusivity

Variation of thermal effusivity is plotted in Fig. 20. It indicates that the thermal effusivity of the CMs goes down accordingly with the rise of the number of luffa fibres mats in the plaster matrix. It can drop to 15.56% when the reinforcement fibres mats are at their maximum with a number of TLs. It is inferred that the plaster reinforced with luffa sponge fibres displays a certain weakness in exchanging heat with its environment as compared with the pure plaster. A similar finding was recorded by Djoudi et al. [36] and Boumhaout et al. [37] who tackled gypsum reinforced with the date palm fibre mesh.
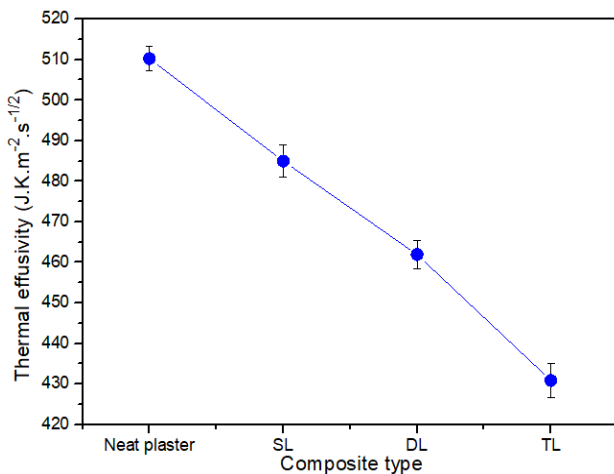

Fig. 20. Effect of reinforcement layers on thermal effusivity

6.4. The specific heat capacity

Fig. 21 traces the evolution of the specific heat capacity of the plaster reinforced with a luffa sponge fibre mats. It is noteworthy that the specific heat capacity rises to 6.4%. This increase refers to the combined effects of thermal conductivity, density and thermal diffusivity. The specific heat capacity rises from 825.58 $(J \cdot kg^{-1} \cdot K^{-1})$ in pure plaster to 878.39 $(J \cdot kg^{-1} \cdot K^{-1})$ with TL reinforcement mats.
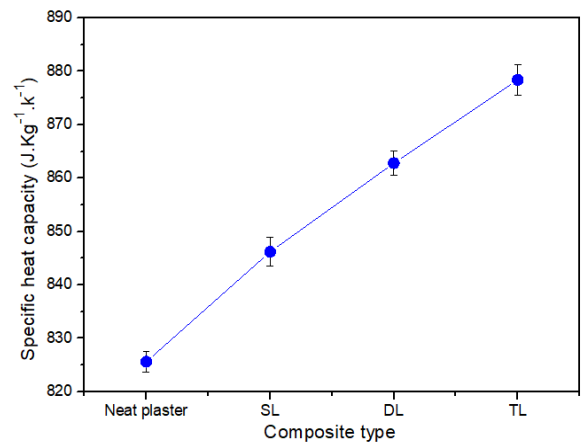

Fig. 21. Reinforcement Layers Effect on thermal capacity

7. CONCLUSION

This work contributes to the public issue of sustainable development, which has triggered significant scientific concern and whetted the widest interest among researchers, as well as industrialists. From this perspective, we attempted to enhance and control the characteristics of CMs. A study was conducted on the influence of fibre layers on the thermomechanical and physical properties of this type of material. A new set of composites was successfully manufactured using luffa sponge fibre reinforced plaster composites.

In terms of mechanical properties, the flexural strength is equal to a maximum value of 1.6 MPa at the DL. The analysis of results revealed that the thermal conductivity decreasedwhen the layer of luffa sponge fibres increased. The most insulating specimen observed far TL luffa sponge fibres to the composite yielded optimal results: with a conductivity equal to 0.215 $(Wm^{-1} \cdot K^{-1})$ and a diffusivity equal to 2.49 $10^{-7} \cdot (m2 \cdot s^{-1})$. At this stage of analysis, we would assert that this CM based on plasters reinforced with luffa sponge fibre layers has significant thermal properties that contribute to lower energy consumption in the building process.

REFERENCES

1. Gartner Ellis M. Cohesion and expansion in polycrystalline solids formed by hydration reactions the case of gypsum plasters. Cem. Concr. 2009; 39 (4): 289-295.
2. Khalil AA, Tawfik A, Hegazy AA. Plaster composites modified morphology with enhanced compressive strength and water resistance characteristics. Constr. Build. Mater. 2018; 167: 55-64.
3. Kondratieva N, Barre M, Goutenoire F, Sanytsky M. Study of modified gypsum binder. Constr. Build. Mater. 2017; 149: 535-542.
4. Shim H, Choi GJ. Study of construction convergence technology for performance improvement in functional building materials. Build. Eng. 2017; 11:108–114.
5. Tesfaye T, Sithole B, Ramjugernath D, Mokhothu T. Valorisation of chicken feathers: Characterisation of thermal, mechanical and electrical properties, Sustain. Chem. Pharm. 2018; 9: 27–34.
6. Acda MN. Waste chicken feather as reinforcement in cement-bonded composites. Philippine J. Sci. 2010; 139 (2): 161-166.
7. Wahab ESA., Osmi SFC. Properties of Concrete Added with Chicken Rachis as Reinforcement, in: Appl. Mech. Mater. Trans. Tech. Publ. 2012; 147: 37–41.
8. Rames M, Palanikumar K, Reddy KH. Mechanical property evaluation of sisal–jute–glass fiber reinforced polyester composites, Compos. B. 2013; 48: 1–9.

Khaled Kharrati, Madiha Salhi, Abdelmoumen Hidouri, Ridha Abdeljabar
Effect of Luffa Sponge Fibre Mats Embedded in the Plaster Matrix

DOI 10.2478/ama-2023-0061

9. Djoudi T, Hecini M., Scida D, Djebloun Y, Djemai HJ. Physico-mechanical characterization of composite materials based on date palm tree fibers, Nat. Fibers. 2021; 18 (6): 789-802.

10. Djoudi A, Khenfer MM, Bali A, Bouziani T. Effect of the addition of date palm fibers on thermal properties of plaster concrete, experimental study and modeling, Adhes. Sci. Technol. 2014; 28 (20): 2100-2111.

11. Saadaoui N, Rouilly A, Fares K, Rigal L. Characterization of date palm lignocellulosic by-products and self-bonded composite materials obtained thereof. Mater. Design. 2013; 50: 302–308.

12. Elbadry E. A. Agro-residues: Surface treatment and characterization of date palm tree fiber as composite reinforcement. Journal of Composites ID. 2014;2014.

13. Djoudi T, Hecini M, Scida D, Djebloun Y, Djemai H. Physico-mechanical characterization of composite materials based on date palm tree fibers. Journal of Natural Fibers, 2021; 18 (6): 789-802.

14. Bezazi A, Amroune S, Scarpa F. Analyse statistique et effet des traitements chimique sur le comportement physico-mécanique des fibres des bras de grappe des palmiers dattier. Synthèse: Revue des Sciences et de la Technologie. 2015; 31: 08–20.

15. Alcaraz JS, Belda IM, Sanchis EJ, Borrell JMG. Mechanical properties of plaster reinforced with yute fabrics. Compos. B. Eng. 2019; 178: 107390.

16. Eve S, Gomina M, Gmouh A, Samdi A, Moussa R, Orange GJ. Microstructural and mechanical behaviour of polyamide fibre-reinforced plaster composites. Eur. Ceram. Soc. 2002; 22 (13): 2269-2275.

17. Gencel O, del Coz Diaz JJ, Sutcu M, Koksal F, Rabanal FPA, Martinez-Barrera G. A novel lightweight gypsum composite with diatomite and polypropylene fibers. Constr. Build. Mater. 2016; 113: 732-740.

18. Iucolano F, Liguori B, Aprea P, Caputo D. Caputo, Evaluation of bio-degummed hemp fibers as reinforcement in gypsum plaster. Composites Part B: Engineering. 2018; 138: 149-156.

19. Basaran H, Demir A, Bagci M. The behavior of masonry walls with reinforced plaster mortar. Advances in Materials Science and Engineering. 2013; 2013.

20. Basaran H. Demir A, Bagci M, Ergun S. Experimental and numerical investigation of walls strengthened with fiber plaster. Structural engineering and mechanics: An international journal. 2015; 56 (2): 189-200.

21. Khalil A.A, Tawfik A, Hegazy AA, El-Shahat MF. Effect of some waste additives on the physical and mechanical properties of gypsum plaster composites. Constr. Build. Mater. 2014; 68: 580-586.

22. Ouakarrouch M, El Azhary K, Laaroussi N. Garoum M, Kifani-Sahban F. Thermal performances and environmental analysis of a new composite building material based on gypsum plaster and chicken feathers waste. Thermal Science and Engineering Progress. 2020; 19:100642.

23. Sakthieswaran N, Sophia M. Prosopis juliflorafibre reinforced green building plaster materials—An eco-friendly weed control technique by effective utilization. Environmental Technology & Innovation. 2020; 20: 101158.

24. Maaloufa Y, Mounir S, Khabbazi A, Kettar J. Thermal And Mechan The Plaster Reinforc Or Granula. International Journal of Civil Engineering. 2017; 8 (7).

25. Miraoui I, Jaballi S, Hassis H. Analysis of the mechanical properties of mortar reinforced with long unidirectional alfa fibers in different curing conditions, Mech. Compos. Mater. 2016; 52 (4): 545–554.

26. Salim K, Houssam A, Belaid A, Brahim H. Reinforcement of building plaster by waste plastic and glass. Procedia Structural Integrity. 2019; 17: 170-176.

27. Selamat ME, Hashim R, Sulaiman O, Kassim MHM, Saharudin NI, Taiwo OFA. Comparative study of oil palm trunk and rice husk as fillers in gypsum composite for building material. Constr. Build. Mater. 2019; 197: 526-532.

28. Touil M, Lachheb A, Saadani R, Kabiri MR, Rahmoune M. A new experimental strategy assessing the optimal thermo-mechanical properties of plaster composites containing Alfa fibers. Energy and Buildings. 2022; 262: 111984.

29. Chen Y, Su N, Zhang K, Zhu S, Zhu Z, Qin W, Yang Y, Shi Y, Fan S, Wang Z, Guo Y. Effect of fiber surface treatment on structure, moisture absorption and mechanical properties of luffa sponge fiber bundles. Industrial Crops and Products. 2018; 123: 341-352.

30. Taimur-Al-Mobaraka, Minaa MF, Gafurb MA, Ahmedb AN, Dhar SA. Im-provement in structural and mechanical properties of spongegourd natural fibers through dif-ferent common chemical treatments. International Conference on Engineering Materials and Metallurgical Engineering. 2016; 22- 24.

31. Kharrati K, Salhi M, Sliman J, Abdeljabar R. An Investigation of Thermomechanical Behavior of Tunisian Luffa Sponges' Fibers. Materials Sciences and Applications. 2022; 13 (12): 519-531.

32. Ayvazyan V. Etude de champs de température séparables avec une double décomposition en valeurs singulières: quelques applications à la caractérisation des propriétés thermophysiques des matérieux et au contrôle non destructif (Doctoral dissertation, Bordeaux. 2012; 1.

33. Babu KS, Ratnam C. Ratnam, Mechanical and thermophysical behavior of hemp fiber reinforced gypsum composites. Materials Today: Proceedings. 2021; 44: 2245-2249.

34. Djoudi A, Khenfer MM, Bali A. Performance of date palm fibres reinforced plaster concrete, International journal of physical sciences. 2012; 7(21): 2845-2853.

35. Amara I, Mazioud A, Boulaoued I, Mhimid A. Experimental study on thermal properties of bio-composite (gypsum plaster reinforced with palm tree fibers) for building insulation. International journal of heat and technology. 2017; 35 (1): 576-584.

36. Djoudi A, Khenfer MM, Bali A, Bouziani T. Effect of the addition of date palm fibers on thermal properties of plaster concrete: experimental study and modeling, J. Adhes. Sci. Technol. 2014; 28 (20): 2100–2111.

37. Boumhaout M, Boukhattem L, Hamdi H, Benhamou B, Nouh FA. Thermomechanical characterization of a bio-composite building material: Mortar reinforced with date palm fibers mesh. Construction and Building Materials. 2017; 135: 241-250.

38. Kharrati K, Salhi M, Sliman J, Abdeljabar R. Thermomechanical and Physical Properties of plaster concrete reinforced with natural fibers. Mechanics Of Advanced Composite Structures. 2023; 10 (2):295-308.

39. El Rhaffari Y, Boukalouch M, Khabbazi A, Samaouali A, Geraud Y. 2010 Conductivité et diffusivité thermiques des matériaux poreux: application aux pierres du monument historique Chellah. In Materiaux. 2010; 18.

40. Chen Y, Su N, Zhang K, Zhu S, Zhu Z, Qin W, Yang Y, Shi S, Fan Z,Wang Z, Guo Y. Effect of fiber surface treatment on structure, moisture absorption and me-chanical properties of luffa sponge fiber bundles. Industrial Crops and Products. 2018; 123: 341-352.

41. Taimur-Al-Mobaraka MF, Minaa MA, Gafurb A.N, Ahmedb, Dhar SA. Improvement in structural and mechanical properties of spongegourd natural fibers through different common chemical treatments. International Conference on Engineering Materials and Metallurgical Engineering, 2016; 22- 24.

Khaled Kharrati : https://orcid.org/0000-0001-9188-892X

Madiha Salhi: https://orcid.org/0000-0001-5263-2171

Abdelmoumen Hidouri: https://orcid.org/0009-0009-2945-6646

Ridha Abdeljabar: https://orcid.org/0009-0008-2601-3869

THE STUDY OF TEMPERATURE-DEPENDENT MAGNETIC PROPERTIES VARIATION
IN CoCr2O4 NANOPARTICLES WITH (y = 0.8) AND WITHOUT
COATING CONCENTRATION OF NON-MAGNETIC (SiO2)y

Ghazanfar MEHBOOB*, Kashif NADEEM**, Amjad IQBAL***
Gohar MEHBOOB****, Shahnawaz HUSSAIN*, Mohamed RAGAB*****
Mazhar IQBAL******, Sohaib AJMAL*******, Adel EL-MARGHANY*******

*State Key Laboratory for Mechanical Behavior of Materials, School of Materials Science and Engineering,
Xi'an Jiaotong University, Xi'an, 710049, China
**Department of Physics, International Islamic University Islamabad, Pakistan
***Faculty of Materials Engineering, Sileisan University of Technology, Gliwice 44-100, poland
****School of Materials Science and Engineering, South China University of Technology, Guangzhou, China
*****Department of Mechanical Engineering (Production and Design), Shoubra Faculty of Engineering, Benha University, Benha 13512, Egypt
******Department of Physics, University Azad Jammu and Kashmir, Muzaffarabad, Pakistan
*******Institute for Advanced Ceramics, School of Materials Science and Engineering, Harbin Institute of Technology, Harbin, 150080 China
********Department of Chemistry, College of Science, King Saud University, P.O. Box 2455, Riyadh 11451, Saudi Arabia

ghazanfar3152@stu.xjtu.edu.cn, kashif.nadeem@iiui.edu.pk, amjad.iqbal@polsl.pl
goharmehboob125@hotmail.com, shahnwazhussain904@hotmail.com, mohamed.emam01@feng.bu.edu.en
mazhariqbal5252@gmail.com, sohaibajmal905@hit.edu.cn, amarghany@ksu.edu.sa

Abstract: The present study investigates the temperature-dependent magnetic (MT) properties of CoCr2O4/(SiO2)y (y = 0 and 0.8) nanoparticles. Nanoparticles were synthesised by using the conventional sol–gel technique. The X-ray diffraction (XRD) method confirmed the normal spinel structure of CoCr2O4 nanoparticles. The main peak analysis of the XRD pattern using Debye–Scherrer's formula probes the mean crystallite sizes for coated and uncoated nanoparticles, and the sizes based on which the probes have been carried out amount to 19 nm and 28 nm, respectively. The transmission electron microscopy (TEM) image showed the non-spherical shape of these nanoparticles. Field-cooled (FC) and zero field-cooled (ZFC) MT plots were taken by using a superconducting quantum interference device (SQUID) magnetometer. Pure CoCr2O4 nanoparticles showed the ferrimagnetic transition at Curie temperature (Tc = 99 K) on an applied field (H) of 50 Oe. Tc decreased up to 95 K with the increase in 80% SiO2 concentration in CoCr2O4 nanoparticles. For pure samples, conical spiral temperature (TS) and lock-in transition temperature (TL) remain unchanged with increasing magnetic field because of strong spin–lattice coupling. However, for 80% SiO2 impurity, the decrease in Tc was attributed to the reduction in surface disorder with a minor decline in TS and TL. The Ms declined with a decrease in temperature because of the existence of stiffed/strong conical spin-spiral and lock-in states in pure CoCr2O4 nanoparticles, while nanoparticles with 80% coating SiO2 concentration showed abnormal behavior. The coercivity increases with a decrease in temperature due to a decrease in thermal fluctuations at low temperatures for both samples. The fitting of coercivity (Hc) versus temperature plot by using Kneller's law has given the values of coercivity constant (α) and coercivity at average blocking temperature (TB) for both samples, which are α = 0.54, TB = 75 K and α = 1.59, TB = 81 K, respectively. Hence, the increase in the concentration of SiO2 decreased nanoparticles size and surface disorder in CoCr2O4 nanoparticles while enhancing Ms below spin-spiral state ordering.

Key words: cobalt chromite, sol-gel synthesis, nanoparticles, corrosion, magnetic properties

1. INTRODUCTION

Ferri/ferromagnetism and ferroelectric coupling in heterostructure material or single material are used in many electronic devices as sensors and data storage devices and are chemically used as ferro-fluids, radar-absorbing paint, drug delivery, power transformer cores, the oxidation of 2-propanol [1] industrial inorganic pigment [2], solar absorber [3], electrode in solid oxide fuel cell (SOFCs) [4,5], catalyst support [6], etc. Most of the research activities have been precipitated due to the scientific engrossment in multiferroicity [7]. Scientists have an attraction towards nanometre range spinel metal oxides because

of their broad range of functions in solid-state sciences [8]. Chromites with the general formula ACr2O4 have a normal spinel structure, where A indicates the divalent metallic ions (Ni2+, Zn2+, Mn2+, Cu2+, Fe2+, Co2+, Mg2+, etc.) at the tetrahedral (T) site and trivalent chromite ion (Cr3+) lies at the octahedral site [9, 10]. A majority of the applications of spinel magnetic nanoparticles as multiferroic material are due to their intrinsic properties such as low dielectric losses, low coercivity (Hc), high resistivity, high chemical stability and high saturation magnetisation (Ms) [11]. Cobalt chromite (CoCr2O4) has greenish-blue pigments, which are crystallised in cubic Fd3m structure having lattice constant a = 8.33 Å with Co2+ ions at the tetrahedral site and Cr3+ ions at the

octahedral site [12]. Bulk CoCr2O4 has paramagnetic (PM) to ferromagnetic (FM) magnetic phase transition temperature (Tc), conical spiral temperature (TS) and lock-in transition temperature (TL) of 94 K, 27 K and 15 K, respectively [13]. According to Menyuk et al. [14], the cobalt chromite magnetic order incorporates a spin-spiral FM state below Tc. The spiral component exhibits short-range order at a temperature of 86 K, which then transmutes into long-range order at a temperature of 31 K, while the FiM component for all temperatures below Tc exhibits long-range order. The spiral long-range order of FiM was estimated by cone angle 'u' [15] as

$$u = 4SBJBB/3SAJAB.$$ (1)

Here, SA and SB are the magnitudes of spin at A site and B site, respectively; similarly, JAB and JBB are the nearest exchange interactional spins between A–B sites and B–B sites, respectively. It was experimentally found that the value of cone angle for FM long-range spiral order is u = 2. In the case of bulk CoCr2O4, JBB interactions are strong between two chromium ions and have a significant role in cone angles of the long-range spiral state (TS) [16]. The cobalt chromite (CoCr2O4) nanomaterial has no magnetic response in the low-temperature range. The magnetic phase transition is gigantic and uncommon in CoCr2O4 with $TL = 8$ K, $TS = 31$ K and $Tc = 100$ K [17]. It was observed that TS remained the same for bulk along with nano CoCr2O4 due to strong interaction between B–B sites. The long-range spiral states stipulate the supremacy of B–B interactions on A–B interactions.

The spins at the surface of the nanoparticles efficiently control magnetic properties for surface action and other applications [18]. CoCr2O4 nanoparticles have a high tendency to agglomerate due to their magnetic nature [19]. Agglomeration can be reduced by coating nanoparticles with non-magnetic material. Usually, Al2O3, SiO2 and TiO2 are used for this purpose [20]. SiO2 is the most efficient and commonly used non-magnetic material for the coating of nanoparticles [21], as it controls the interparticle interactions through its shell thickness, and controls also the surface effects and the size of particles; additionally, it is also characterised by excellent stability [22]. A large number of nucleation sites are formed smaller in size and single phase during the synthesis process when nanoparticles are coated with SiO2 as SiO2 reduces the growth of nanoparticles [23–25]. Consequently, the magnetic properties of multiferroic nanomaterials can be controlled by SiO2 coating, which will also affect the magneto-electric coupling [26].

Therefore, the SiO2 non-magnetic material coating has a great effect on the CoCr2O4 nanoparticle's magnetic properties, which is required to be studied for its useful applications in modern technology. In this study, we have probed the magnetic response on both coated and uncoated CoCr2O4 nanoparticles with SiO2 at different temperature ranges.

2. RESULTS AND DISCUSSION:

Figure 1 displays the X-ray diffraction (XRD) plots for CoCr2O4/(SiO2)y nanoparticles produced by the sol–gel method at y = 0% and 80%. Indexed peaks (111), (220), (311), (400), (422), (511) and (440) of XRD plots revealed the cubic structure of

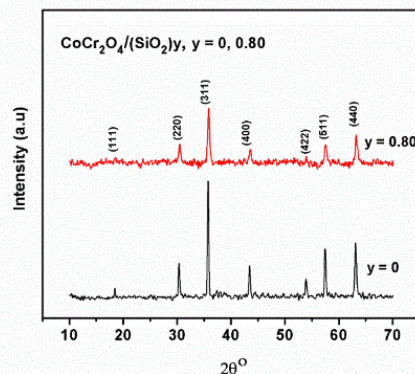both coated and uncoated CoCr2O4 nanoparticles (JCPDS file No.: 780711).

Fig. 1. The XRD patterns of CoCr2O4/(SiO2)y (y = 0% and 80%) nanoparticles. XRD, X-ray diffraction

For both cases, the positions of peaks almost remain the same, which indicated that the coating of SiO2 did not alter the internal structure of CoCr2O4 nanoparticles. The intensities of all the peaks have been reduced for coated nanoparticles. No peaks of silica were found in the XRD scan because its nature is amorphous.

The sizes of nanoparticles (D) were probed by the main peak (311) investigation of XRD patterns by using Debye–Scherrer's equation:

$$D = \frac{0.9\lambda}{\beta cos\theta},$$ (2)

where λ is the wavelength of the X-ray, β is the full width at half maximum (FWHM) of the plane hkl and θ is the Bragg angle.

The mean crystallite sizes of CoCr2O4/(SiO2)y (y = 0 or 0.80) nanoparticles with y = 0 and y = 0.80 are 28 nm and 19 nm, respectively. The mean crystallite size of nanoparticles is decreased with an increase in the concentration of silica because of the increase in the number of nucleation sites in the SiO2 matrix under the process of synthesis, which stops the further growth of nanoparticles [24, 25, 27, 28].

Transmission electron microscopy (TEM) was used to observe the nanoparticles' shape, size and agglomeration. Figure 2 reveals the TEM image, at 100 nm scale, of cobalt chromite (CoCr2O4/(SiO2)y) nanoparticles with y = 0. From Fig. 2, we observe the elongated/irregular shape of nanoparticles. However, a certain degree of agglomeration is also exhibited because of the magnetic interactions among nanoparticles [29, 30].

The superconducting quantum interference device magnetometer (SQUID Quantum Design, MPMS-XL-7) was used to measure the magnetic properties of CoCr2O4/(SiO2)y (y = 0 or 0.80) nanoparticles.

Figures 3(a,b) reveal the T-dependent zero field-cooled (ZFC) and field-cooled (FC) magnetisation curves of CoCr2O4/(SiO2)y (y = 0 or 0.80) nanoparticles at different applied magnetic fields of 50 Oe, 500 Oe and 1,000 Oe. The sample was cooled from 145 K to 4.2 K and then magnetisations were recorded with FC and without ZFC applied magnetic field in increasing temperature from 4.2 K to 145 K. FC measurements were taken for different applied magnetic fields of values 50 Oe, 500 Oe and 1,000 Oe [31]. Negative magnetisation was observed in ZFC curves for both

samples with y = 0 and y = 0.8 in the temperature ranges of 4.2–87 K and 4.2–71 K, respectively, owing to uncompensated spins at the grain boundaries. The negative magnetisation decreases with increasing the external magnetic field in both cases as more and more magnetic moments are aligned along the magnetic field direction concomitant with an increase in the external magnetic field. From graphs of CoCr2O4/(SiO2)y (y = 0 and 0.80) nanoparticles, the obtained results show that the negative magnetisation decreased with the silica coating of CoCr2O4 nanoparticles. It means that SiO2 coating results in a decrease in the orderings of surface spins of nanoparticles [13, 32, 33]. The temperature at which the material changes its state from paramagnetic to ferrimagnetic in both ZFC and FC conditions is called Curie temperature (*TC*), while the dip associated with *Ts* is responsible for the conical spiral state. ZFC/FC plots for a sample with y = 0 taken at 50 Oe, 500 Oe and 1,000 Oe have conical spinal state *TS* = 27 K and *TC* at 99 K, 100 K and 101 K, respectively, which were confirmed by the values already reported by Plocek et al. [34] and Plumier et al. [35]. ZFC/FC plots for the sample with y = 0.80 at 50 Oe, 500 Oe and 1,000 Oe have conical spinal state *TS* at 19 K, 25 K and 25 K, respectively, and similarly *TC* at 95 K, 99 K and 100 K, respectively.
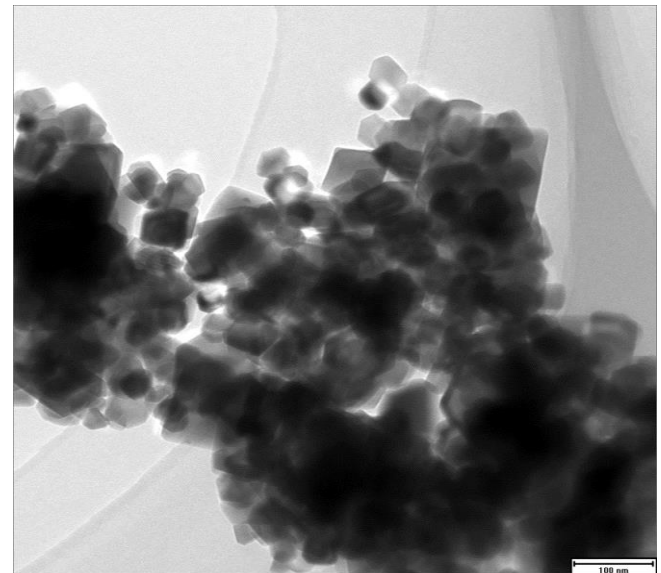

Fig. 2. TEM image of cobalt chromite without silica concentration nanoparticles at 100 nm scale. TEM, transmission electron microscopy
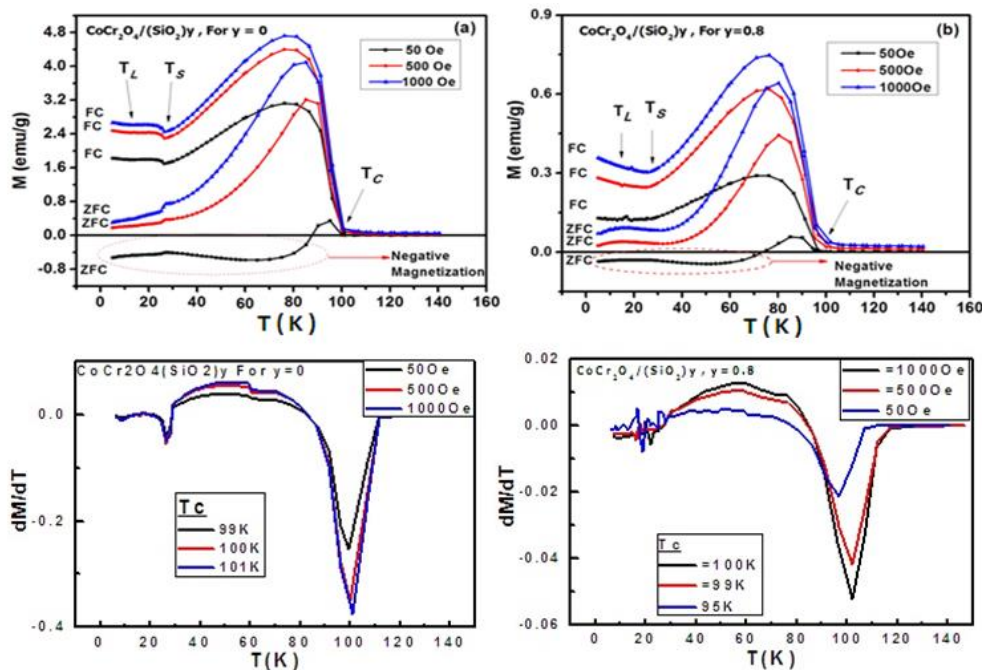

Fig. 3. ZFC/FC curves for cobalt chromite nanoparticles with (a) 0% silica concentration and (b) 80% silica concentration at different applied fields. FC, field cooled; ZFC, zero field cooled

Low-temperature lock-in state (at which spiral spins lock to lattice parameter) occurs at TL = 12 K for the sample with y = 0 and occurs at TL = 11.5 K, TL = 15 K and TL = 17 K under applied fields of 50 Oe, 500 Oe and 1,000 Oe, respectively, for the sample with y = 0.8. TL and TS did not exhibit any dependence on the external field due to strong spin–lattice coupling at low temperatures [36] for the sample with y = 0. TL, TS and TC are decreased for the sample with y = 0.80 due to the decrease in their crystallite size as compared to the sample with y = 0 [37, 38]. The values of TL, TS and TC for CoCr2O4/(SiO2)y (y = 0 and y =

0.80) nanoparticles at the various external fields of 50 Oe, 500 Oe and 1,000 Oe are mentioned in Table 1.

In order to study the coercivity (*HC*) and saturation magnetisation (*MS*) of cobalt chromite nanoparticles owing to surface and magnetic transitional effects, the T-dependent M–H loops have been taken into consideration. Figure 4 depicts M–H loops of cobalt chromite (CoCr2O4) nanoparticles with 0% concentration of silica under ±5 T field at the different constant temperatures of 5 K, 25 K, 50 K and 75 K. The inset of Figure 4 displays the expanded region for *HC*. All loops show a ferrimagnetic trend that contains the ZFC/FC results. The M–H loops of nanoparticles are not fully saturated at field ±5 T because

Ghazanfar Mehboob, Kashif Nadeem, Amjad Iqbal, Gohar Mehboob, Shahnawaz Hussain, Mohamed Ragab,
Mazhar Iqbal, Sohaib Ajmal, Adel El-Marghany
The Study of Temperature Dependent Magnetic Properties Variation in CoCr2O4 Nanoparticles with (y = 0.8) and without Coating Concentration of Non-Magnetic (SiO2)y

DOI 10.2478/ama-2023-0062

of their random surface spins, which necessitated a rather high field for complete saturation.

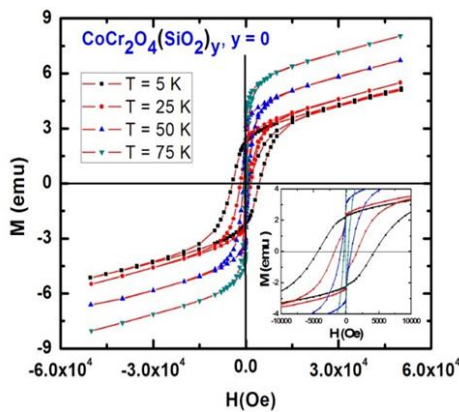| Concentration	Field	T_C	T_S	T_L
0%	50 Oe	99 K	27 K	12 K
	500 Oe	100 K	27 K	12 K
	1,000 Oe	101 K	27 K	12 K
80%	50 Oe	95 K	19 K	11.5 K
	500 Oe	99 K	25 K	15 K
	1,000 Oe	100 K	25 K	17 K

Fig. 4. M–H loops of cobalt chromite nanoparticles with 0% concentration of silica at the different constant temperatures of 5 K, 25 K, 50 K and 75 K

The values of *MS* and *HC* are presented in Figure 4. The value of *MS* is calculated at constant temperature $T = 5$ K, which is 5.1 emu/g. Figure 5(a) shows variation in *Ms* with respect to different temperatures for CoCr2O4 nanoparticles with 0% silica concentration. The *Ms* graph has shown decreasing trend with decreasing temperature, which does not show an accordance with the prediction of Bloch's law for ferro-ferrimagnetic materials. This trend is attributable to the presence of stiffed/strong conical spin-spiral and lock-in states at low temperatures. From M–H loops, we have also found the value of *HC*. Figure 5(b) reveals the value of *HC* at different temperatures. *HC* reveals a decreasing trend with increasing temperature by a decrease in thermal fluctuations [39–41]. At high temperatures, the spin-flip time is less than the measurement time because thermal energy is greater than anisotropic energy; therefore, the particle reveals a lower value of *HC*. By decreasing the temperature, the thermal energy will be decreased, and the thermal energy is less than anisotropic energy at low temperatures and shows a higher *HC* value.

Figure 6 exhibits the M–H loops of cobalt chromite (CoCr2O4) nanoparticles with an 80% concentration of silica at the different temperatures of 5 K, 15 K, 25 K, 50 K and 75 K. The value of *MS* is 2.16 emu/g at a temperature of 5 K. Since the crystallite size of nanoparticles without silica concentration is greater than that of nanoparticles with silica concentration, as far as the nanoparticles with a 0% silica concentration are concerned, their *Ms* value is higher in comparison with nanoparticles with an 80% silica concentration. This means that the *MS* value depends mainly upon the crystal size. The smaller the size of the crystal, the lower

will be the value of *Ms*. The reduction in *MS* value is also owing to the fact of increase in the surface-to-volume ratio [42]. The M–H loops of cobalt chromite (CoCr2O4) nanoparticles with silica concentrations at various temperatures are less saturated even at a high field (5 T) if compared to the nanoparticles without silica concentration due to surface effects.
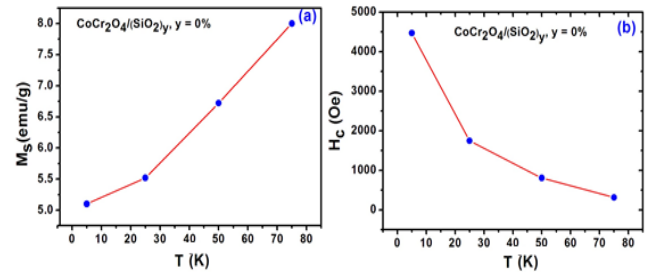

Fig. 5. The variation in (a) saturation magnetisation and (b) coercivity with the temperature of CoCr2O4 nanoparticles with 0% concentration of silica
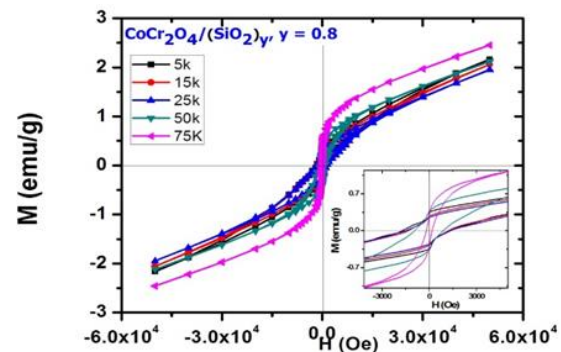

Fig. 6. M–H loops of cobalt chromite nanoparticles with 80% concentration of silica at the different temperatures of 5 K, 15 K, 25 K, 50 K and 75 K
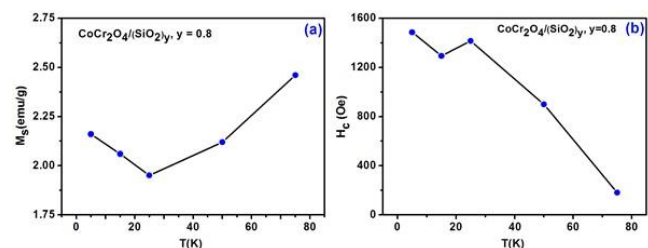

Fig. 7. The variation in (a) saturation magnetisation and (b) coercivity with temperature of CoCr2O4 nanoparticles with 80% concentration of silica (solid lines just show the trend)

Figure 7a shows the trend of the *Ms* value of nanoparticles with silica concentration at different constant temperatures. From M–H loops of CoCr2O4 nanoparticles with silica concentration, the *MS* values reveal abnormal behaviour attendant with changes in temperature due to non-magnetic silica coating. The SiO2 coating can enhance surface disorder by creating a surrounding layer around the nanoparticles [43]. There is an increase in *Ms* value below 25 K, which is attributed to a change in the spin-spiral state due to SiO2 coating. Figure 7b reveals the trend of temperature-dependent *Hc* for CoCr2O4 nanoparticles with an 80% concentration of silica. The value of *Hc* also shows a decreasing trend with increasing temperature. *Hc* of nanoparticles

depends upon many factors such as core anisotropy, coating material, annealing temperature, size of the particle, dipole interaction and surface anisotropy [44].

Figure 8 reveals the combined behaviour of saturation magnetisation and coercivity with the temperature of CoCr2O4 nanoparticles for both 0% and 80% concentrations of silica. The saturation magnetisation behaviour with temperature for nanoparticles with silica concentration is different from nanoparticles without silica concentration, as observed in Figure 8a. The saturation magnetisation for nanoparticles with no silica concentration has decreased with decreasing temperature, while for nanoparticles with silica concentration, its value has increased with decreasing the temperature at a temperature below 25 K. Therefore, this region is called the conical spin-spiral region, in which both magnetic dipoles and electric dipoles are existing at the same phase. The behaviour of coercivity with temperature for CoCr2O4 nanoparticles without silica concentration was changed with the concentration of silica, as shown in Figure 8b. The sharp increment in coercivity in nanoparticles without silica concentration is not observed in nanoparticles with silica concentration, which means that surface anisotropy has reduced in nanoparticles with the concentration of silica.
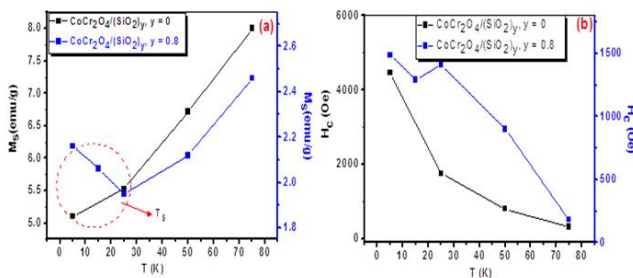

Fig. 8. (a) Saturation magnetisation with temperature and (b) coercivity with temperature of CoCr2O4 nanoparticles with and without silica concentration (solid lines just show the trend)
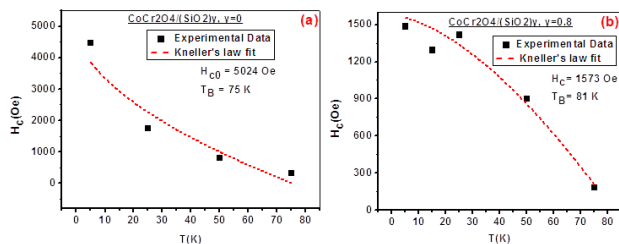

Fig. 9. Kneller's law fit for CoCr2O4 nanoparticles (a) without and (b) with silica concentration

The experimental data of coercivity of CoCr2O4 nanoparticles without and with silica concentration are fitted using Kneller's law. The HC for randomly oriented non-interacting nanoparticles (uniaxial anisotropy and single domain) can be clarified using Kneller's law [45] as follows:

$$Hc = Hc0 \left[1 - (T/TB)\alpha\right], \tag{3}$$

where HC, $HC0$ and TB are the coercivities at any temperature, at a temperature of 0 K and at average blocking temperature, respectively. Figure 9 reveals Kneller's law fitting for CoCr2O4 nanoparticles with and without silica concentration. The best of Kneller's law fit for nanoparticles with no silica concentration reveals fitting parameters as $\alpha = 1.54$ and $TB = 75$ K, and for

nanoparticles with silica concentration as $\alpha = 1.59$ and $TB = 81$ K. Kneller's law diverges at lower temperatures for nanoparticles with no silica concentration due to strong interparticle interactions or/and surface disorder [46].

3. MATERIALS AND METHODS

CoCr2O4/SiO2 nanoparticles were synthesised by a sol–gel technique using cobalt nitrate (Co(NO3)2 6H2O), chromium nitrate (Cr(NO3)3 9H2O), citric acid (C6H8O7 H2O) and ammonia and tetraethyl orthosilicate (TEOS) materials with citric acid as a fuel agent. Sol–gel technique is defined as a low-cost, homogenous formation and non-destructive technique, which results from the uniform distribution of particle size. To obtain solution-1, 30 mL ethanol was used as a medium in which to stoichiometrically mix 99.9% pure (Co(NO3)2 6H2O) and (Cr(NO3)3 9H2O) salts. The distilled water and citric acid are mixed stoichiometrically in the desired ratio (0% and 80%) of TEOS to obtain solution-2. Solution-2 was injected drop-wise with a droplet in solution-1 to obtain solution-3. Some drops of ammonia were also introduced in solution-3 to maintain its pH value at 5. Solution-3 was stirred at 70°C to obtain its gel. The gel was dried in an oven at a temperature of 110°C for 12 h. The dry gel was ground for 2 h to obtain a homogeneous dry solution, and then the dry solution was purred in an alumina boat. The dry solution was annealed at 900°C for 4 h. The annealing results in the desired CoCr2O4/SiO2 nanoparticles. The single-phase crystalline structures of the CoCr2O4/(SiO2)y (y = 0 or 0.80) nanoparticles were confirmed with the use of XRD.
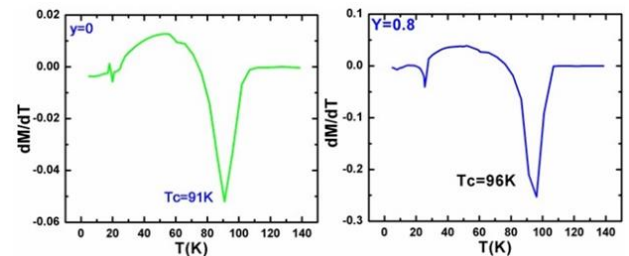

Fig. 10. Temperature dependence of magnetization and graph of dM/dT vs. T under magnetic field

4. CONCLUSIONS

T-dependent magnetic properties of CoCr2O4 nanoparticles without and with silica concentration were studied in detail. XRD patterns show the normal spinel structure of nanoparticles for the cases of both presence and absence of silica concentration. The average size of the crystal has reduced for nanoparticles with silica concentration due to the amorphous nature of silica, which confines the growth of nanoparticles. The ZFC/FC curves of cobalt chromite nanoparticles with and without silica concentration at 50 Oe, 500 Oe and 1,000 Oe have been studied. The values of Tc at 50 Oe, 500 Oe and 1,000 Oe were 99 K, 100 K and 101 K, respectively, for nanoparticles with no silica concentration. For SiO2-coated nanoparticles, Tc values at 50 Oe, 500 Oe and 1,000 Oe were 95 K, 99 K and 100 K, respectively. The values of Ts and TL were 27 K and 12 K, respectively, for nanoparticles with no silica concentration, which are found to be field-independent due

to strong lattice coupling as compared with nanoparticles with silica concentration. For cobalt chromite nanoparticles without silica concentration, the ZFC curve shows negative magnetisation, which perseveres up to 87 K due to the presence of uncompensated spin at grain boundaries, and this negative magnetisation has reduced for nanoparticles with silica concentration. The M_s value is decreased with decreasing temperature for nanoparticles without silica concentration. For nanoparticles with silica concentration, it reveals abnormal behaviour due to the amorphous nature of silica coating. At a temperature below 25 K, the M_s value is decreasing for nanoparticles without silica concentration, while it is increasing for nanoparticles with silica concentration. The H_c value is increased by reducing the temperature for both concentrations due to a reduction in thermal fluctuations at lower temperatures. The experimental data of H_c for both concentrations have been fitted by Kneller's law. The fitting parameters are $\alpha = 0.54$ and $T_B = 75$ K for nanoparticles without silica concentration, and $\alpha = 1.59$ and $T_B = 81$ K for those with silica concentration. In conclusion, SiO2 coating interferes with the disordered spin-spiral state ordering and decreases surface effects in these chromite nanoparticles.

REFERENCES

1. Hosseini SA, Alvarez-Galvan MC, Fierro JLG, Niaei A, Salari D. MCr2O4 (M= Co, Cu, and Zn) nanospinels for 2-propanol combustion: correlation of structural properties with catalytic performance and stability. Ceramics International. 2013;39(8):9253–61.
2. Knyazev AV, Mączka M, Bulanov EN, Ptak M, Belopolskaya SS. High-temperature thermal and X-ray diffraction studies, and room-temperature spectroscopic investigation of some inorganic pigments. Dyes and Pigments. 2011;91(3):286–93.
3. Avila AG, Barrera EC, Huerta LA, Muhl S. Cobalt oxide films for solar selective surfaces, obtained by spray pyrolisis. Solar Energy Materials and Solar Cells. 2004;82(1–2):269–78.
4. BaZr0.2Ce0.8−xYxO3−δ solid oxide fuel cell electrolyte synthesized by sol–gel combined with composition-exchange method - ScienceDirect [Internet]. [cited 2020 Jun 24]. Available from: https://www.sciencedirect.com/science/article/abs/pii/S036031991400384X
5. Effect of stoichiometry on (La0.6Sr0.4)xCo0.2Fe0.8O3 cathode evolution in solid oxide fuel cells - ScienceDirect [Internet]. [cited 2020 Jun 24]. Available from: https://www.sciencedirect.com/science/article/abs/pii/S0378775314008076
6. Fino D. Diesel emission control: Catalytic filters for particulate removal. Science and Technology of Advanced Materials [Internet]. 2007 Jan 1 [cited 2020 Jun 24];8(1–2):93–100. Available from: https://doi.org/10.1016/j.stam.2006.11.012
7. Eerenstein W, Mathur ND, Scott JF. Multiferroic and magnetoelectric materials. Nature [Internet]. 2006 Aug [cited 2020 Jun 24]; 442(7104):759–65. https://www.nature.com/articles/nature05023
8. Mancic L, Marinkovic Z, Vulic P, Moral C, Milosevic O. Morphology, Structure and Nonstoichiometry of ZnCr2O4 Nanophased Powder. Sensors [Internet]. 2003 Oct [cited 2020 Jun 24];3(10):415–23. Available from: https://www.mdpi.com/1424-8220/3/10/415
9. Anthony R. Solid state chemistry and its applications. John Wiley & Sons; 1990.
10. Choudhary P, Varshney D. Structural, vibrational and dielectric behavior of Co1-xMxCr2O4 (M = Zn, Mg, Cu and x = 0.0, 0.5) spinel chromites. Journal of Alloys and Compounds [Internet]. 2017 Nov 25 [cited 2020 Jun 24];725:415–24. Available from: http://www.sciencedirect.com/science/article/pii/S0925838817325380
11. Wang LG, Zhu CM, Chen L, Yuan SL. Exchange bias effect in CoCr2O4/NiO system prepared by two-step method. Solid State Communications [Internet]. 2017 Feb 1 [cited 2020 Jun 24];251: 39–42. Available from: http://www.sciencedirect.com/science/article/pii/S0038109816303490
12. Gingasu D, Mindru I, Culita DC, Patron L, Calderon-Moreno JM, Osiceanu P, et al. Structural, magnetic and catalytic properties of cobalt chromite obtained through precursor method. Materials Research Bulletin [Internet]. 2015 Feb 1 [cited 2020 Jun 25];62:52–64. Available from: http://www.sciencedirect.com/science/article/pii/S0025540814006904
13. Lawes G, Melot B, Page K, Ederer C, Hayward MA, Proffen Th, et al. Dielectric anomalies and spiral magnetic order in ${\mathrm{CoCr}}_{2}{\mathrm{O}}_{4}$. Phys Rev B [Internet]. 2006 Jul 17 [cited 2020 Jun 24];74(2):024413. Available from:https://link.aps.org/doi/10.1103/PhysRevB.74.024413
14. Menyuk N, Dwight K, Wold A. Ferrimagnetic spiral configurations in cobalt chromite. J Phys France [Internet]. 1964 May 1 [cited 2020 Jun 24];25(5):528–36. Available from: http://dx.doi.org/10.1051/jphys:01964002505052801
15. Manikandan A, Sridhar R, Arul Antony S, Ramakrishna S. A simple aloe vera plant-extracted microwave and conventional combustion synthesis: Morphological, optical, magnetic and catalytic properties of CoFe2O4 nanostructures. Journal of Molecular Structure [Internet]. 2014 Nov 5 [cited 2020 Jun];1076:188–200.http://www.sciencedirect.com/science/article/pii/S002228601400790X
16. Rath C, Mohanty P. Magnetic Phase Transitions in Cobalt Chromite Nanoparticles. J Supercond Nov Magn [Internet]. 2011 Jan 1 [cited 2020 Jun 24];24(1):629–33. Available from: https://doi.org/10.1007/s10948-010-0958-7
17. Galivarapu JK, Kumar D, Banerjee A, Sathe V, Aquilanti G, Rath C. Effect of size reduction on cation distribution and magnetic transitions in CoCr2O4 multiferroic: EXAFS, magnetic and diffused neutron scattering measurements. RSC Adv [Internet]. 2016 Jul 1 [cited 2020 Jun 24];6(68):63809–19. Available from : https://pubs.rsc.org/en/content/articlelanding/2016/ra/c6ra10189e
18. Huang DJ, Okamoto J, Huang SW, Mou CY. Magnetic Transitions of Multiferroic Frustrated Magnets Revealed by Resonant Soft X-ray Magnetic Scattering. J Phys Soc Jpn [Internet]. 2010 Jan 12 [cited 2020 Jun 24];79(1):011009. Available from: https://journals.jps.jp/doi/abs/10.1143/JPSJ.79.011009
19. Chen CC, Herhold AB, Johnson CS, Alivisatos AP. Size Dependence of Structural Metastability in Semiconductor Nanocrystals. Science [Internet]. 1997 Apr 18 [cited 2020 Jun 24];276(5311):398–401. Available from: https://science.sciencemag.org/content/276/5311/398
20. Tsoukatos A, Wan H, Hadjipanayis GC, Papaefthymiou V, Kostikas A, Simopoulos A. Origin of coercivity in (Fe,Co)-based granular films. Journal of Applied Physics [Internet]. 1993 May 15 [cited 2020 Jun 24];73(10):6967–9. Available from:https://aip.scitation.org/doi/abs/10.1063/1.352399
21. Hee Kim E, Sook Lee H, Kook Kwak B, Kim BK. Synthesis of ferrofluid with magnetic nanoparticles by sonochemical method for MRI contrast agent. Journal of Magnetism and Magnetic Materials [Internet]. 2005 Mar 1 [cited 2020 Jun 24];289:328–30. Available from: http://www.sciencedirect.com/science/article/pii/S0304885304013186
22. Nadeem K, Ali L, Gul I, Rizwan S, Mumtaz M. Effect of silica coating on the structural, dielectric, and magnetic properties of maghemite nanoparticles. Journal of Non-Crystalline Solids [Internet]. 2014 Nov 15 [cited 2020 Jun 24];404:72–7. Available from: http://www.sciencedirect.com/science/article/pii/S0022309314003494
23. Abarra EN, Gill P, Min Zheng, Zhou JN, Acharya BR, Choe G. Preconditioning, write width, and recording properties of Co-Cr-Pt-O perpendicular media with various underlayer designs. IEEE Transactions on Magnetics. 2005 Feb;41(2):581–6.
24. Wu KH, Chang YC, Wang GP. Preparation of NiZn ferrite/SiO2 nanocomposite powders by sol–gel auto-combustion method. Journal of Magnetism and Magnetic Materials [Internet]. 2004 Feb 1 [cited 2020 Jun 24];269(2):150–5. Available from:http://www.sciencedirect.com/science/article/pii/S0304885303005857

25. Chaudhuri A, Mandal M, Mandal K. Preparation and study of NiFe2O4/SiO2 core–shell nanocomposites. Journal of Alloys and Compounds [Internet]. 2009 Nov 13 [cited 2020 Jun 24];487(1):698–702. Available from: http://www.sciencedirect.com/science/article/pii/S0925838809016089

26. Zhang S, Dong D, Sui Y, Liu Z, Wang H, Qian Z, et al. Preparation of core shell particles consisting of cobalt ferrite and silica by sol–gel process. Journal of Alloys and Compounds [Internet]. 2006 May 18 [cited 2020 Jun 24];415(1):257–60. Available from: http://www.sciencedirect.com/science/article/pii/S0925838805012661

27. Kamran M, Ullah A, Mehmood Y, Nadeem K, Krenn H. Role of SiO2 coating in multiferroic CoCr2O4 nanoparticles. AIP Advances [Internet]. 2017 Feb 1 [cited 2020 Jun 24];7(2):025011. Available from: https://aip.scitation.org/doi/full/10.1063/1.4973732

28. Nadeem K, Krenn H, Shahid M, Letofsky-Papst I. Influence of SiO2 matrix and annealing time on properties of Ni-ferrite nanoparticles. Solid State Sciences [Internet]. 2013 May 1 [cited 2020 Jun 24];19:27–31. Available from: http://www.sciencedirect.com/science/article/pii/S129325581300068X

29. Zi Z, Sun Y, Zhu X, Yang Z, Dai J, Song W. Synthesis and magnetic properties of CoFe2O4 ferrite nanoparticles. Journal of Magnetism and Magnetic Materials [Internet]. 2009 May 1 [cited 2020 Jun 24];321(9):1251–5. Available from: http://www.sciencedirect.com/science/article/pii/S0304885308011578

30. Gopalan EV, Joy PA, Al-Omari IA, Kumar DS, Yoshida Y, Anantharaman MR. On the structural, magnetic and electrical properties of sol–gel derived nanosized cobalt ferrite. Journal of Alloys and Compounds [Internet]. 2009 Oct 19 [cited 2020 Jun 24];485(1):711–7. Available from: http://www.sciencedirect.com/science/article/pii/S0925838809012092

31. Krenke T, Acet M, Wassermann EF, Moya X, Mañosa L, Planes A. Ferromagnetism in the austenitic and martensitic states of $\mathrm{Ni}\text{\ensuremath{-}}\mathrm{Mn}\text{\ensuremath{-}}\mathrm{In}$ alloys. Phys Rev B [Internet]. 2006 May 15 [cited 2020 Jun 24];73(17):174413. Available from: https://link.aps.org/doi/10.1103/PhysRevB.73.174413

32. Kahn O. The magnetic turnabout. Nature [Internet]. 1999 May [cited 2020 Jun 24];399(6731):21–2. Available from: https://www.nature.com/articles/19862

33. Ohkoshi S ichi, Yorozu S, Sato O, Iyoda T, Fujishima A, Hashimoto K. Photoinduced magnetic pole inversion in a ferro–ferrimagnet: (Fe0.40IIMn0.60II)1.5CrIII(CN)6. Appl Phys Lett [Internet]. 1997 Feb 24 [cited 2020 Jun 24];70(8):1040–2. Available from: https://aip.scitation.org/doi/abs/10.1063/1.118475

34. Plocek J, Holec P, Kubickova S, Pacakova B, Matulkova I, Mantlikova A, et al. Stabilization of Transition Metal Chromite Nanoparticles in Silica Matrix. International Journal of Chemical and Molecular Engineering [Internet]. 2014 Oct 5 [cited 2020 Jun 24];8(11):1219–28. Available from: http://publications.waset.org/9999702/stabilization-of-transition-metal-chromite-nanoparticles-in-silica-matrix

35. Plumier R. Reinvestigation of Magnetic Structures of CoCr2O4 and MnCr2O4 Obtained by Neutron Diffraction. Journal of Applied Physics [Internet]. 1968 Feb 1 [cited 2020 Jun 24];39(2):635–6. Available from: https://aip.scitation.org/doi/abs/10.1063/1.2163559

36. Mufti N, Nugroho AA, Blake GR, Palstra TTM. Magnetodielectric coupling in frustrated spin systems: the spinels MCr2O4(M = Mn, Co and Ni). J Phys: Condens Matter [Internet]. 2010 Feb [cited 2020 Jun 24];22(7):075902. Available from: https://doi.org/10.1088%2F0953-8984%2F22%2F7%2F075902

37. Tang ZX, Chen JP, Sorensen CM, Klabunde KJ, Hadjipanayis GC. Tang et al. reply. Phys Rev Lett [Internet]. 1992 May 18 [cited 2020 Jun 24];68(20):3114–3114. Available from: https://link.aps.org/doi/10.1103/PhysRevLett.68.3114

38. Binder K. Statistical mechanics of finite three-dimensional Ising models. Physica [Internet]. 1972 Dec 15 [cited 2020 Jun 24]; 62(4):508–26. Available from: http://www.sciencedirect.com/science/article/pii/0031891472902376

39. Tartaj P, González-Carreño T, Serna CJ. Magnetic Behavior of γ-Fe2O3 Nanocrystals Dispersed in Colloidal Silica Particles. J Phys Chem B [Internet]. 2003 Jan 1 [cited 2020 Jun 24];107(1):20–4. Available from: https://doi.org/10.1021/jp0260898

40. Grinbom G, Duveau D, Gershinsky G, Monconduit L, Zitoun D. Silicon/Hollow γ-Fe2O3 Nanoparticles as Efficient Anodes for Li-Ion Batteries. Chem Mater [Internet]. 2015 Apr 14 [cited 2020 Jun 24];27(7):2703–10. Available from: https://doi.org/10.1021/acs.chemmater.5b00730

41. Zeb F, Nadeem K, Shah SKA, Kamran M, Gul IH, Ali L. Surface spins disorder in uncoated and SiO2 coated maghemite nanoparticles. Journal of Magnetism and Magnetic Materials [Internet]. 2017 May 1 [cited 2020 Jun 24];429:270–5. Available from: http://www.sciencedirect.com/science/article/pii/S03048853316313762

42. Caizer C, Stefanescu M. Magnetic characterization of nanocrystalline Ni Zn ferrite powder prepared by the glyoxylate precursor method. J Phys D: Appl Phys [Internet]. 2002 Nov [cited 2020 Jun 24];35(23):3035–40. Available from: https://doi.org/10.1088%2F0022-3727%2F35%2F23%2F301

43. Aslibeiki B, Kameli P. Magnetic properties of MnFe2O4 nano-aggregates dispersed in paraffin wax. Journal of Magnetism and Magnetic Materials [Internet]. 2015 Jul 1 [cited 2020 Jun 25];385:308–12. Available from: http://www.sciencedirect.com/science/article/pii/S0304885315002449

44. Xu ST, Ma YQ, Zheng GH, Dai ZX. Simultaneous effects of surface spins: rarely large coercivity, high remanence magnetization and jumps in the hysteresis loops observed in CoFe2O4 nanoparticles. Nanoscale [Internet]. 2015 Apr 2 [cited 2020 Jun 25];7(15):6520–6. Available from: https://pubs.rsc.org/en/content/articlelanding/2015/nr/c5nr00582e

45. Obaidat IM, Issa B, Albiss BA, Haik Y. Temperature Dependence of Saturation Magnetization and Coercivity in Mn0.5Zn0.5Gd0.02 Fe1.98O4Ferrite Nanoparticles. IOP Conf Ser: Mater Sci Eng [Internet]. 2015 Oct [cited 2020 Jun 25];92:012012. Available from: https://doi.org/10.1088%2F1757-899x%2F92%2F1%2F012012

46. Kneller EF, Luborsky FE. Particle Size Dependence of Coercivity and Remanence of Single-Domain Particles. Journal of Applied Physics [Internet]. 1963 Mar 1 [cited 2020 Jun 25];34(3):656–8. Available from: https://aip.scitation.org/doi/abs/10.1063/1.1729324

Ghazanfar Mehboob: https://orcid.org/0009-0009-3912-1743

Amjad Iqbal: https://orcid.org/0000-0001-7405-0324

Mohamed Ragab: https://orcid.org/0000-0001-8878-760X

Sohaib Ajmal: https://orcid.org/0000-0002-3234-943X

Adel El-Marghany: https://orcid.org/0009-0002-6464-7113

ENERGY CONVERSION IN SYSTEMS-CONTAINED LASER-IRRADIATED METALLIC NANOPARTICLES – COMPARISON OF RESULTS FROM ANALYTICAL SOLUTIONS AND NUMERICAL METHODS

Piotr RADOMSKI*, **Paweł ZIÓŁKOWSKI***, **Dariusz MIKIELEWICZ***

* Faculty of Mechanical Engineering and Ship Technology, Institute of Energy,
Gdańsk University of Technology, Gabriela Narutowicza 11/12, 80-233 Gdańsk, Poland

piotr.radomski@pg.edu.pl, pawel.ziolkowski1@pg.edu.pl, dariusz.mikielewicz@pg.edu.pl

Abstract: This work introduces the theoretical method of metallic nanoparticles' (NPs') heat and mass transfer where the particles are coated on a surface (base), together with considering the case wherein nanoparticles move freely in a pipe. In order to simulate the heat transfer, energy and radiative transfer equations are adjusted to the considered issue. NPs' properties are determined following the nanofluidic theories, whereas absorption and scattering coefficients are described using either Mie-Lorenz theory or Rayleigh-Drude approximation. Thermal boundary conditions are implemented based on the microscale heat transfer and Smoluchowski theory. Results are compared with the classical Fourier transport differential solutions that have been adjusted to laser irradiation.

Key words: energy conversion, heat transfer, metallic nanoparticles, Smoluchowski theory

1. INTRODUCTION

Gold nanoparticles (NPs) commonly appeared inside the red-stained glasses in gothic cathedrals during the medieval ages. At that time, however, no one was aware of the dormant potential or the physical reason why these structures possessed a red color instead of a yellowish one. The reason for this phenomenon was discovered by Gustav Mie and Ludvig Lorenz, who proposed around the same time a theoretical explanation for the red-shifted gold properties, stating their theories on the Maxwell equations. Although those works appeared to be perfect for every spherical NP size, there was a problem to describe the interaction for other shapes, e.g. rods, cubes and triangles. However, it has been ascertained that for most shapes, an explicit formulation cannot be determined, and numerical methods should be considered [1–7].

On the other hand, the Rayleigh–Drude approximation is being commonly proposed for calculations of small NPs and gasses, regardless of working environment. As long as this theory is only approximation of the Mie–Lorenz one, and fails under condition $d \ll \lambda$, where d is the nanoparticle diameter, and λ represents the incident wavelength, there are virtually no restrictions on the NP shape, regardless of its complicity.

Both approaches, however, indicate that there exists at least one spectra peak wherein the absorption cross section is maximized. The maximum is searched at the local surface plasmon resonance phenomenon (LSPR) which treats each NP as a set of vibrations – plasmons. If the vibrations' frequency is near the incident wavelength, NPs produce a collective single vibration that, in the absence of electrical or magnetic outlet, is capable only converting of the whole absorbed energy into heat. This potential was generally discerned generally a dozen years ago in

inactivation bioprocesses, e.g. hyperthermia tumors, where temperature increases locally, which minimizes the process invasiveness.

Nevertheless, there is still a lack of theoretical models that may be utilized for such nanomaterials' irradiation. Some of them require complex models that are usually based on DPM models, as has been discussed in [8–11]. This paper considers NPs as a heat source of converted energy. In the literature, such a case was proposed for thin films in the study of Bohren et al. [2,6,12], and now the model has been being developed scrupulously by authors in [13–15] for particles irradiation. The present research also highlights that the irradiation process may be automated in specific cases. Fig. 1. outlines the heat generation processes, which are responsible for the temperature increase, and which may be divided into two general parts – electromagnetic energy conversion into heat and heat transport into the material from NPs' location. Therefore, the control input parameter here is the laser power that establishes principally the heat generation rate and provides the temperature increase. Subsequently, the temperature increase due to the heat transfer model in a material can be stated as the output.

Moreover, it has been emphasized that laser ablation in simple cases may be described and analyzed via classical Fourier heat transfer and its adequate differential solutions. Likewise, the considered model enables the determination of heat transfer between solids. Therefore, the main work's purpose is to propose the heat flux model as a response for the applied laser power as a result of electromagnetic energy conversion into heat. Furthermore, the response is compared with the adapted-to-system temperature relationships that describe the unsteady heat transfer between a solid and metallic NPs or thin films.
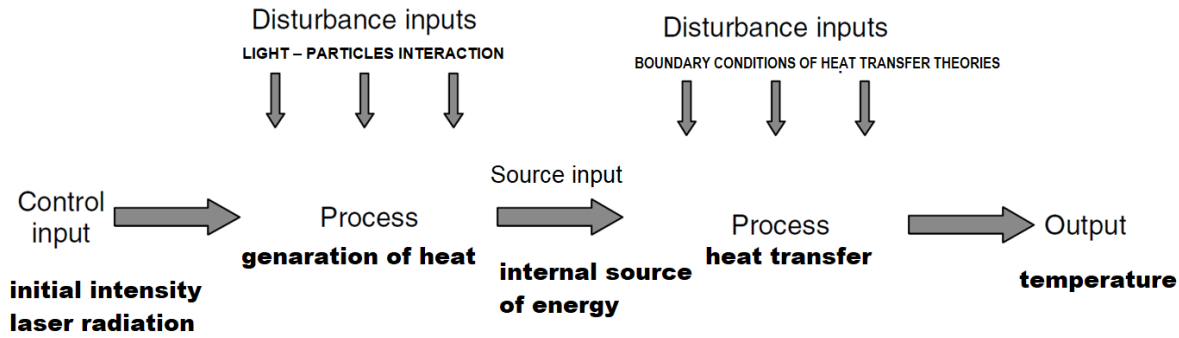
Fig. 1. Process of heat transfer modelling for metallic NPs and thin metallic films

2. LIGHT – PARTICLES INTERACTION

2.1. Heat transfer equations

Light-matter interaction that includes all classical phenomena is generally described following Eqs. (1) – (4) using the radiative heat transfer approach [12,14,16]:

$$\frac{1}{c}\frac{\partial I_o(r,\Omega,t)}{\partial t} + \text{div}\left(I_o(r,\Omega,t)\cdot\vec{S}(\Omega)\right) +$$
$$+ \left(\sigma_{abs_h} + \sigma_{sca_p} + \sigma_{abs_p}\right)\cdot I_o(r,\Omega,t) =$$
$$= \sigma_{abs_h}\cdot m_h^2\cdot\frac{\sigma_{SB}\cdot T^4}{4\pi} + E_p +$$
$$+ \frac{\sigma_{sca_p}}{4\pi}\int_0^{4\pi}\left(I_o(r,\Omega,t)\cdot\Phi\left(\vec{S}(\Omega)\right)\right)d\Omega$$

(1)

$$\sigma_{abs_p} = \xi\cdot\sum_i^N\left(C_{ext_i} - C_{sca_i}\right)$$

(2)

$$\sigma_{sca_p} = \xi\cdot\sum_i^N\left(C_{sca_i}\right)$$

(3)

$$E_p = \xi\cdot\sum_i^N \epsilon_i\cdot A_i\cdot\frac{\sigma_{SB}\cdot T^4}{4\pi}$$

(4)

where: c – speed of light in vacuum ($m\cdot s^{-1}$), $I_o(r,\Omega,t)$ – spatial profile of light incident intensity ($W\cdot m^{-2}$), t – time (s), $\vec{S}(\Omega)$ – oriented surface (m^2), Ω – angle of orientation (rad), σ_{abs_h} – absorption coefficient of the surrounding medium (m^{-1}), σ_{sca_p} – scattering coefficient of particles (m^{-1}), σ_{abs_p} – absorption coefficient of particles (m^{-1}), m_h – refractive index of the surrounding medium (-) , σ_{SB} – Stefan-Boltzmann constant ($W\cdot m^{-2}\cdot K^{-4}$), T – temperature (K), E_p – emissivity coefficient of particles due to black-body radiation ($W\cdot m^{-3}$), C_{ext_i} – extinction cross section of the i-particle (m^2), C_{sca_i} – scattered cross section of the i-particle (m^2), ξ – nanoparticles concentration (m^{-3}), ϵ_i – emissivity of the i-particle (-), A_i – projected area of the i-particle (m^2), $\sum_i^N$ — sum of particle from i = 1 to i = N.

In case of temperature changes, the energy balance equation would be applied, treating particles as inclusions in fluid or at a solid boundary, basing on the literature, described by Eqs. (5) – (7) [12,14,15,17–19]:

$$\frac{\partial}{\partial t}\left((\alpha_p\cdot\rho\cdot e)\right) + \text{div}\left(\alpha_p\cdot\rho\cdot e\vec{v} + \alpha_p\cdot p\vec{v}\right) =$$
$$= div\left(k_{eff}\cdot grad(T) + \left(\left(grad\left(\overrightarrow{X^\dagger}\right) - \mu I_{\vec{d}}\overleftrightarrow{I} + 2\mu\vec{d}\right)\cdot\vec{v}\right)\right)$$
$$- g_{e-ph}\cdot\left(T - T_{ph}\right) + S^f + S_i^p$$
$$+ \sum_i \Theta_i^{p-f} + \sum_i \Theta_i^{p-p} + Q_{in}$$

(5)

$$S_i^p = \sum_i^N \sigma_{abs_p}\cdot I_{abs_i} = \xi\cdot\left(1 - exp(-\sigma_{abs_h}\cdot l_f)\right)\cdot$$
$$\cdot\left(1 - \left(\frac{(m_p - m_h)^2 + (\widetilde{m_p} - \widetilde{m_h})^2}{(m_p + m_h)^2 + (\widetilde{m_p} + \widetilde{m_h})^2}\right)\right)\cdot$$
$$\cdot\sum_i^N\left(C_{ext_i} - C_{sca_i}\right)\cdot I_o(r,\Omega,t)\cdot$$
$$\cdot\left(1 - \left(\frac{(m_h - m_a)^2 + \widetilde{m_h}^2}{(m_h + m_a)^2 + \widetilde{m_h}^2}\right)\right)\cdot$$
$$\cdot\left(1 - exp(-\xi\cdot\left(C_{ext_i} - C_{sca_i}\right)\cdot l_i)\right)$$

(6)

$$S^f = \sigma_{abs_h}\cdot I_{abs_h} = \sigma_{abs_h}\cdot I_o(r,t)\cdot$$
$$\cdot\left(1 - \left(\frac{(m_h - m_a)^2 + \widetilde{m_h}^2}{(m_h + m_a)^2 + \widetilde{m_h}^2}\right)\right)$$
$$\cdot\left(1 - \exp(-\sigma_{abs_h}\cdot l_f)\right)$$

(7)

where: α_p – volume of particles' occupation in fluid (-), ρ – density of a material ($kg\cdot m^{-3}$), e – specific energy ($J\cdot kg^{-1}$), $\vec{v}$ – velocity of the fluid ($m\cdot s^{-1}$), p – pressure (Pa), k_{eff} – effective thermal conductivity coefficient ($W\cdot m^{-1}\cdot K^{-1}$), $\overrightarrow{X^\dagger}$ – diffusive momentum flux ($kg\cdot m\cdot s^{-2}$), μ – molecular viscosity ($kg\cdot m^{-1}\cdot s^{-1}$), $I_{\vec{d}}$ – first invariant of the strain rate (s^{-1}), $\overleftrightarrow{I}$ – unit tensor (-), $\vec{d}$ – symmetric rate of deformation (s^{-1}), g_{e-ph} – electron-phonon coupling for nanoparticles ($W\cdot m^{-3}\cdot K^{-1}$), T_{ph} – temperature of crystal lattice (phonon heat) (K), S^f – source of energy for fluids ($W\cdot m^{-3}$), S_i^p – source of energy for the i-particle ($W\cdot m^{-3}$), Θ_i^{p-f} – heat exchange between the i-particle and fluid ($W\cdot m^{-3}$), Θ_i^{p-p} – heat exchange between particles ($W\cdot m^{-3}$), Q_{in} – internal source of energy, e.g. as a result of the magnetic field presence ($W\cdot m^{-3}$), I_{abs_i} – absorbed part of the i-particle ($W\cdot m^{-2}$), l_f – path's length that light passes through fluid (m), m_p – real part of the refractive index of particle's material (-), $\widetilde{m_p}$ – imaginary part of the refractive index of particle's material (-), $\widetilde{m_h}$ – imaginary part of the refractive index of the surrounding medium (-), m_a – refractive index of air (-), l_i – path's length that light passes through the i-particle (m), I_{abs_h} – absorbed part of the surrounding medium ($W\cdot m^{-2}$).

Eqs. (6) and (7) were previously examined for metallic thin films [15,17]. In the present study they are adapted to the considered system containing particles. For metallic thin films, specific heat capacity and thermal conductivity are ruled by the heat exchange between electron and crystal lattice interaction regardless of the incident intensity [12,17]. In case of particles as well, this coupling, i.e. g_{e-ph}, exists as well, however, is much stronger, which reduces the temperature increase [20,21].

Piotr Radomski, Paweł Ziółkowski, Dariusz Mikielewicz

Energy Conversion in Systems-Contained Laser-Irradiated Metallic Nanoparticles – Comparison of Results From Analytical Solutions and Numerical Methods

DOI 10.2478/ama-2023-0063

Nonetheless, many other problems, pertaining to the NPs' orientation and strain deformation, appear, which cannot be solved accurately. The first one refers to the thermal conductivity that may be treated following many approaches. The most crucial issue here, however, is to include a size and a shape dependence that diminish the thermal conductivity value significantly. For the NP that is of a noble metal, the proceeding may follow Eq. (8) [22–25]:

$$k_{\mathrm{eff}_{\mathrm{p},i}} = \frac{\rho_{\mathrm{p},i} \cdot c_{\mathrm{p,p},i} \cdot \vec{v}_{\mathrm{F}} \cdot \Lambda_{\mathrm{o}}}{3} \cdot \frac{\Lambda_{\mathrm{p},i}}{\Lambda_{\mathrm{o}}} = k_{\mathrm{o}} \cdot \frac{1}{1+\mathrm{Kn}} \tag{8}$$

where: $k_{\mathrm{eff}_{\mathrm{p},i}}$ – thermal conductivity coefficient of the i-particle ($\mathrm{W} \cdot \mathrm{m}^{-1} \cdot \mathrm{K}^{-1}$), $\rho_{\mathrm{p},i}$ – density of the i-particle ($\mathrm{kg} \cdot \mathrm{m}^{-3}$), $c_{\mathrm{p,p},i}$ – specific heat capacity of the i-particle ($\mathrm{J} \cdot \mathrm{kg}^{-1} \cdot \mathrm{K}^{-1}$), $\vec{v}_{\mathrm{F}}$ – Fermi velocity ($\mathrm{m} \cdot \mathrm{s}^{-1}$), Λ_{o} – mean free path of an electron for a bulk metal (m), $\Lambda_{\mathrm{p},i}$ – mean free path (particle size) of an electron for the i-particle (m), k_{o} – thermal conductivity coefficient of a pure metal ($\mathrm{W} \cdot \mathrm{m}^{-1} \cdot \mathrm{K}^{-1}$), Kn – Knudsen number (-).

Other issues, which are related to the fluid flow, are discussed in the forthcoming subsections.

2.2. Cross sections

The most paramount parameters, which are worth a deeper investigation, are NPs' concentration, ξ, and cross sections. Nanoparticles concentration, ξ, which is defined as the number of NPs in a selected volume, is not a separated parameter, and indicates the interaction rate between single NPs. Its relationship with cross sections is dependent on the applied theory. This topic was discussed in Gouesbet's study [4,26]. The issue stays the number of nanoparticles concentration at which the interaction starts to be significant, and so far there has been no precise value.

Scattering and extinction cross-section, however, are well-known and may be calculated differently depending on the considered theory. The Mie–Lorenz one presents them as for spheres [2,5,6,12] following Eqs. (9) and (10):

$$C_{\mathrm{ext}_i} = \sum_{i}^{N} \frac{\lambda^2}{2\pi} \sum_{j=1}^{\infty} (2j+1) \cdot \mathbb{re}(\mathrm{a}_{j,i} + \mathrm{b}_{j,i}) \tag{9}$$

$$C_{\mathrm{sca}_i} = \sum_{i}^{N} \frac{\lambda^2}{2\pi} \sum_{j=1}^{\infty} (2j+1) \cdot \left(\left| \mathrm{a}_{j,i} \right|^2 + \left| \mathrm{b}_{j,i} \right|^2 \right) \tag{10}$$

where: λ – Incident wavelength (m), j – selected rank of Mie coefficients' accuracy, $\mathrm{a}_{j,i}$ – first Mie coefficient (-), $\mathrm{b}_{j,i}$ – second Mie coefficient (-), N – number of nanoparticles.

Meanwhile, the Rayleigh–Drude approximation yields Eqs. (11) – (13) [1,6]:

$$C_{\mathrm{ext}_i} = 4\pi \cdot \left(\frac{2\pi}{\lambda} \right) \cdot \mathbb{im}(\alpha_i) \tag{11}$$

$$C_{\mathrm{sca}_i} = \frac{8\pi}{3} \cdot \left(\frac{2\pi}{\lambda} \right)^4 \cdot |\alpha_i|^2 \tag{12}$$

$$\alpha_i = \frac{3V_i}{4\pi} \cdot \frac{(\varepsilon_{\mathrm{p}} + \mathbb{I} \cdot \widetilde{\varepsilon_{\mathrm{p}}}) - (\varepsilon_h + \mathbb{I} \cdot \widetilde{\varepsilon_{\mathrm{h}}})}{(\varepsilon_{\mathrm{p}} + \mathbb{I} \cdot \widetilde{\varepsilon_{\mathrm{p}}}) + 2 \cdot (\varepsilon_h + \mathbb{I} \cdot \widetilde{\varepsilon_{\mathrm{h}}})} \tag{13}$$

where: α_i – polarizability of the i-particle (m^3), V_i – volume of the i-particle (m^3), ε_{p} – real part of the permittivity of the considered metal (-), $\widetilde{\varepsilon_{\mathrm{p}}}$ – imaginary part of the permittivity of the considered metal (-), ε_h – real part of the permittivity of the host medium (-), $\widetilde{\varepsilon_{\mathrm{h}}}$ – Imaginary part of the permittivity of the host medium (-).

It is generally alleged that, for several reasons, the second approach is more amicable compared to the Mie-Lorenz theory. Firstly, the Rayleigh-Drude approximation introduces simple and distinguishable formulas depending on the mean distance between NPs. It has been presented in particular in Bohren and Huffman [6], van de Hulst [2], Siegel and Howell [12] and Voltz [26]. On the other hand, both the Mie-Lorenz and the Rayleigh-Drude approaches may be introduced via the particle's polarizability whose methodology involve to calculate one formula for each shape.

The relationship, however, is usually very tangled for non-spherical particles. Nonetheless, the simplest shapes, spherical and ellipsoidal ones, are well-known for both approaches, and they enable the number of shapes to be expanded with needle (stretched to infinity) and disk (flattened-to-zero thickness) structures at the mathematical limits of a depolarization factor, $\varLambda_i$. Then, for the particle oriented along the $\hat{i}$-axis [2,6,12,13], polarizability is presented by Eq. (14):

$$\alpha_{i,\hat{i}} = \frac{V_i}{4\pi} \cdot \left(\varLambda_i + \left(\frac{(\varepsilon_{\mathrm{p}} + \mathbb{I} \cdot \widetilde{\varepsilon_{\mathrm{p}}})}{(\varepsilon_{\mathrm{h}} + \mathbb{I} \cdot \widetilde{\varepsilon_{\mathrm{h}}})} - 1 \right)^{-1} \right)^{-1} \tag{14}$$

For prolate (stretched) structures, Eqs. (15) and (16) are governed:

$$\varLambda_{i,\hat{i}}{}^{\mathrm{str}} = \frac{1-\phi_{i,\mathrm{s}}{}^2}{\phi_{i,\mathrm{s}}{}^2} \cdot$$
$$\left(\frac{1}{2 \cdot \phi_{i,\mathrm{str}}} \cdot \ln\left(\frac{1+\phi_{i,\mathrm{str}}}{1-\phi_{i,\mathrm{str}}} \right) - 1 \right) \tag{15}$$

$$\phi_{i,\mathrm{str}} = \sqrt{1 - \left(\frac{d_{s_i}}{d_{l_i}} \right)^2} \tag{16}$$

whereas for oblate (flattened) ones, Eqs. (17) and (18) yields:

$$\varLambda_{i,\hat{i}}{}^{\mathrm{fl}} = \frac{1+\phi_{i,\mathrm{fl}}{}^2}{\phi_{i,\mathrm{fl}}{}^2} \cdot \left(1 - \frac{1}{\phi_{i,\mathrm{fl}}} \cdot \tan^{-1} \phi_{i,\mathrm{fl}} \right) \tag{17}$$

$$\phi_{i,\mathrm{fl}} = \sqrt{\left(\frac{d_{l_i}}{d_{s_i}} \right)^2 - 1} \tag{18}$$

where: d_{l_i} – longer diameter of the i-nanoparticle (m), d_{s_i} – shorter diameter of the i-nanoparticle (m).

Some other shapes have been explored using numerical methods, yielding near-accurate results. A 5% approximation was proposed by Kang et al. [27], where it is possible to implement any arbitrary shape, albeit it requires the use of complex hypergeometric mathematical functions. The majority of presented structures are also capable of the "coating" process, which presents an opportunity to investigate another group of hybrid materials or surfactants that are unreacted or attached to a NP's surface compounds. The topic has been detailed in many studies in the literature [2,6,13,28].

3. NANOPARTICLES COATED ON A SURFACE

Deposited NPs that are present freely on a surface, or those embedded ones inside a material, seem to be relatively simple, and all nanoparticles may be assumed as stable and non-moving granules at a wall. It should be taken into account, however, that there exist a few issues worth investigating. Firstly, when the prolate or oblate structures are considered, the biggest part of

NPs are oriented in one direction owing to gravity and electrostatic forces. Therefore, the particle's polarizability would be discussed for the one oriented axis.

Another relevant problem is that the LSPR phenomenon implies changing of the light-particle-base interaction. For smooth, polished non-charged materials, such as glasses, it is commonly assumed that the change exists only at the refractive index of the host medium that is defined as (Eq. (19)):

$$m_{h_{sur}} = \frac{m_h + m_{base}}{2} \tag{19}$$

where: m_{base} – refractive index of the base material on which particles are coated.

If the wall is a charged surface, interaction may be calculated treating NPs and surface as a crib structure at which legs are the NPs and the manger is a base material. Noticeably, the crib becomes a thin film if its thickness is very high and NPs' presence are negligible. Nonetheless, this topic requires sophisticated mathematics and is beyond the considered subject in this work. Some more sophisticated elements have been introduced by Royer et al.[29,30], where the interaction is developed with the NPs' distance.

Furthermore, it has been discovered in the course of research that the heat interaction between particles and fluid, Θ_i^{p-f}, cannot be treated separately. Among models that perceive the interaction as nanofluids or are based on property's slips, the Smoluchowski model [15,31,32] defines the temperature jump at the body boundaries as a result of conductivity discontinuity. In the case of a fluid containing metallic nanoparticles, this model is extremely major owing to the ranges (for noble metals $k \sim 400 \text{ W} \cdot \text{m}^{-1} \cdot \text{K}^{-1}$, for fluids $k \sim 0.4 \text{ W} \cdot \text{m}^{-1} \cdot \text{K}^{-1}$). For particles, the Smoluchowski model follows the energy equation, described by Eq. (20):

$$\frac{\partial}{\partial t}\left(\rho_{p,i} \cdot \left(c_{p,p,i} \cdot T_p + \frac{\vec{v}_{p,i}^2}{2}\right)\right) +$$
$$+ \text{div}\left(\rho_{p,i} \cdot \left(c_{p,p,i} \cdot T_p + \frac{\vec{v}_{p,i}^2}{2}\right) \cdot \overleftrightarrow{I}_p \cdot \vec{v}_{p,i}\right) +$$
$$+ \text{div}\left(k_{\text{eff}_{p,i}} \cdot \text{grad}(T_p)\right) +$$
$$+ l_T^f \cdot (T_S^f - T_S) - l_T^p \cdot (T_S^p - T_S) + \tag{20}$$
$$+ \alpha_d^f \cdot (T^f - T_S^f) - \alpha_{d,i}^p \cdot (T^p_i - T_S^p) +$$
$$+ (\vec{q}^f - \vec{q}^p) \cdot \vec{n} + (\vec{F}_m^f \times \vec{v}_{\text{slip}}^f - \vec{F}_m^p \times \vec{v}_{\text{slip}}^p) \cdot \vec{n}$$
$$= S^f + S_i^p + Q_{\text{in}} - g_{e^- - ph} \cdot (T - T_{ph})$$

in which: T_p – temperature of particles (K), $\vec{v}_{p,i}$ – velocity of the i-particle $(\text{m} \cdot \text{s}^{-1})$, $\overleftrightarrow{I}_p$ – idemfactor in reference to particles (-), l_T^f – discontinuity at the boundary from fluid side, T_S^f – temperature at the boundary from fluid side (K), T_S – Smoluchowski temperature jump (K), α_d^f – thermal diffusivity of the considered fluid $(\text{m}^2 \cdot \text{s}^{-1})$, T^f – temperature of fluid (K), $\alpha_{d,i}^p$ – thermal diffusivity of the i-particle $(\text{m}^2 \cdot \text{s}^{-1})$, T^p_i – temperature of particles (K), T_S^p – temperature at the boundary from particle side (K), $\vec{q}^f$ – Fourier heat flux of fluid $(\text{W} \cdot \text{m}^{-2})$, $\vec{q}^p$ – Fourier heat flux of the particles $(\text{W} \cdot \text{m}^{-2})$, $\vec{n}$ – normal vector of the boundary layer (-), $\vec{F}_m^f$ – mechanical forces of the fluid $(\text{kg} \cdot \text{m} \cdot \text{s}^{-2})$, $\vec{v}_{\text{slip}}^f$ – velocity slip at fluid boundary $(\text{m} \cdot \text{s}^{-1})$, $\vec{F}_m^p$ – mechanical forces of the particles $(\text{kg} \cdot \text{m} \cdot \text{s}^{-2})$, $\vec{v}_{\text{slip}}^p$ – velocity slip at particle boundary $(\text{m} \cdot \text{s}^{-1})$.

The similar approach can be adopted in case of fluids. On the other hand, the Smoluchowski approach seems to be an applicable model in case particles melt locally. The problem, however, occurs at the light–particle interaction. Due to the fact the size and shape decreases, the absorption cross section becomes a function of time, which is not a trivial problem in reference to determination of its form. Moreover, virtually all material properties undergo changes, and the electron-phonon coupling undergoes severe changes.

4. NUMERICAL RESULTS AND HEAT TRANSFER THEORIES

Solving heat differential solutions is not a trivial issue and often requires utilizing numerical methods. Such a situation appears to be applicable to the Smoluchowski theory owing to its complicity. Nevertheless, if only solids are studied, the problem is shortened to the classical Fourier flux systems that have been well-known in the [15,33–35].

The approach is general and offers the solutions for various boundary conditions, and may be adjusted for the irradiated NPs simply. The semi-infinite solid system assumes that the metallic NPs are kept under adiabatic condition ($\dot{q} = 0$), and Eqs. (21) and (22) [34–36] offer:

$$T(x,t) = \sum_i^N I_{\text{abs}_i} \cdot \frac{\sqrt{4 \cdot t \cdot \alpha_d}}{\lambda} \cdot \text{ierfc}\left(\frac{x}{\sqrt{4 \cdot t \cdot \alpha_d}}\right) \tag{21}$$

$$\text{ierfc}(\Psi) = \frac{1}{\sqrt{\pi}} \cdot \exp(-\Psi^2) -$$
$$- \Psi \cdot \frac{2}{\pi} \cdot \int_0^\Psi \exp(-\psi^2) d\psi \tag{22}$$

where: x – the dimension inside the material (m), α_d – thermal diffusivity, Ψ – parameter describing heat flow rate (-), ψ – selected mathematical variable (-).

Eq. (21), however, should be adjusted for a finite thickness of a material (or distance from a wall), δ, in accordance with the specification in Eq. (23):

$$T(x,t) = T_o + \sum_i^N I_{\text{abs}_i} \cdot \frac{\sqrt{4 \cdot t \cdot \alpha_d}}{\lambda} \cdot$$
$$\left(\sum_{\Bbbk=0}^{\Bbbk_\infty} \left(\text{ierfc}\left(\frac{(2\Bbbk+1) \cdot \delta - x}{\sqrt{4 \cdot t \cdot \alpha_d}}\right)\right) + \tag{23}\right.$$
$$\left. \sum_{\Bbbk=0}^{\Bbbk_\infty} \left(\text{ierfc}\left(\frac{(2\Bbbk+1) \cdot \delta + x}{\sqrt{4 \cdot t \cdot \alpha_d}}\right)\right)\right)$$

where: δ – thickness of the considered material (m), $\Bbbk$ – selected rank of the heat transfer accuracy, $\Bbbk_\infty$ – rank of the heat transfer, here: 500 (-).

For the perfect case where only one wall is under a heat flux, the formula would be easily simplified to [33,34] Eq. (24):

$$T(x,t) \sim \exp(-\psi \cdot t) \tag{24}$$

For Dirichlet boundary conditions ($T_w = const$), however, temperature increase changes the relationship, yielding Eq. (25):

$$T(x,t) = T_o + \sum_i^N I_{\text{abs}_i} \cdot \frac{\sqrt{4 \cdot t \cdot \alpha_d}}{\lambda} \cdot$$
$$\cdot \left(\sum_{\Bbbk=0}^{\Bbbk_\infty} (-1)^\Bbbk \cdot \left(\text{ierfc}\left(\frac{(2\Bbbk+1) \cdot \delta - x}{\sqrt{4 \cdot t \cdot \alpha_d}}\right) - \tag{25}\right.\right.$$
$$\left.\left. \text{ierfc}\left(\frac{(2\Bbbk+1) \cdot \delta + x}{\sqrt{4 \cdot t \cdot \alpha_d}}\right)\right)\right)$$

where, if every wall is kept under the same outer T_w, the relationship might be reduced to Eq. (26) [34,36]:

$$T(x,t) \sim \ln(\psi \cdot t) \tag{26}$$

The abovementioned formulas may easily be extended into pulse lasers where heat flux becomes a specified function of time. For metallic NPs, this value refers to the absorbed part of irradiation as long as the NPs do not vary their orientation and are not melted locally [17,34,37]. Although the approach offers a simple relationship and allows estimation of temperature after infinite time, it is dedicated for short-pulse lasers – on the contrary for the continuous ones that do not reach this maximum temperature. It should be emphasized, however, that the comparison appears to correspond to the majority of simple experimental systems.
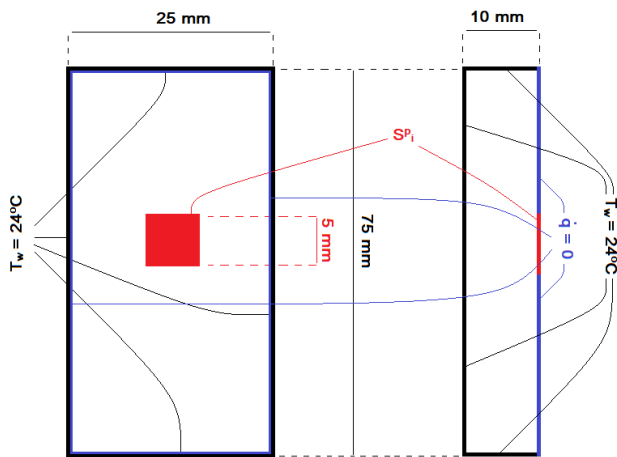
Fig. 2. Scheme of the considered system and applied boundary conditions from [15]

Hence, the temporal results are adopted from the authors' article [15], and demonstrated with the abovementioned temperature relationship due to the fact that the Smoluchowski equation, Eq. (20), is reduced then to the standard energy equation. Fig. 2 repeats the geometry that was utilized in the Radomski et al. [15], whereas Fig. 3 presents the calculated heat generation value (source input). Likewise, Tab. 1, outlines the applied material properties from [15]. Particles, whose diameter is assumed to be 15 nm, are irradiated by a 532-nm laser with the output power 0.8 W. The heat generation rate is calculated analytically using

Mie–Lorentz theory. Boundary conditions are supported with the Dirichlet ($T_w = const$) and Neumann approaches using a second-order upwind scheme and the timestep equaled 2 ms. Process of heating was repeated from Fig. 1. Obtained isotherms are highlighted in Figs. 4 whereas output results (points) and the abovementioned relationships (straight curves) are provided in Figs. 5.

The obtained results suggest that the approach corresponds satisfactorily with numerical results. The mismatch might be explained by the complexity of the second approach in the formula and the numerical methods' error.
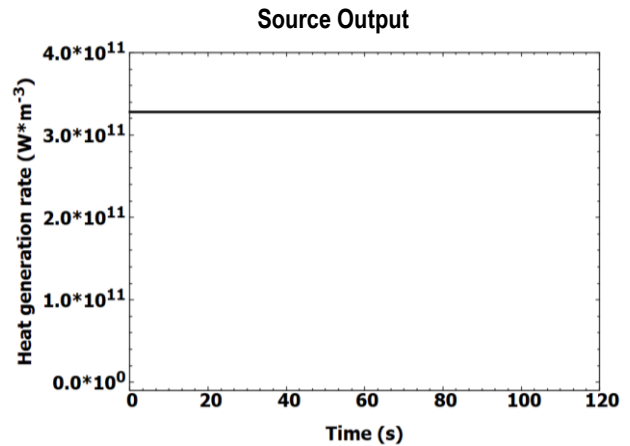

Fig. 3. Time course of the calculated heat generation rate

Considering isotherms, it may be noticed in relation to spherical temperature distributions where x tends to infinity, which is typical in classical heat transfer solutions, whereas squared shapes appear as a result of heat transfer of gold plate into the isotropic solid. Temperature values depends strongly on thermal diffusivity and heat transfer between gold NPs and the considered base, which indicates that the base's thermal properties should possess lower thermal conductivity in order to maximize temperature, although heat transfer would be more sluggish.

In fluids, however, convection starts to do the lion's share and strongly affects temperature increase. At that situation, temperature relationships become much more tangled to derive and generally numerical methods are indicated to be applied.

Tab. 1. Rewritten material parameters from [15] for the theoretical confrontation

Parameter	PDMS	PC	PMMA	Silica glass	Soda-lime glass	Borosilicate glass
Density, ρ	965.0	1,198.0	1,184.9	2,200.0	2,464.9	2,124.9
Specific heat capacity, c_p	1,460.0	1,199.0	1,456.4	840.0	898.6	779.7
Thermal conductivity, k	0.1500	0.2051	0.1912	0.2800	0.1007	1.1489

5. NANOPARTICLES IN A PIPE

Free moving NPs incorporated in a fluidic pipe can be treated as a typical phase, e.g. with a mixture or DDPM model regardless of whether the fluid is a gas or liquid. Heat generation may then be ruled based on the Eqs. (6), (7), (9), (20) and (21), and refractive index from Eq. (19) which is governed only near pipe walls

and in most cases might be omitted. Likewise, appropriate boundary conditions in reference to microchannels and heat transfer coefficients should be considered. Nevertheless, effective thermal conductivity coefficient, k_{eff}, should be modeled based on nanofluids for heterogeneous materials. The topic has been considered in the literature that pertains to selected materials [8,12,38–42]. Since particles are not arranged, k_{eff} follows Eq. (27) [22]:

$$k_{\text{eff}} = k_{\text{f}} \cdot \left(\frac{k_{\text{eff}_{\text{p},i}}}{k_{\text{f}}} \right)^{\varphi} \tag{27}$$

in which: k_{f} – thermal conductivity coefficient of fluid ($\text{W} \cdot \text{m}^{-1} \cdot \text{K}^{-1}$), φ – fraction of occupied particles in fluid (-).

Effective thermal conductivity is realized to be strongly dependent on the occupation fraction of NPs, such as in the Kumar's et al. studies [8,11], and, considering single-phase approach, it may reach even $10 \, \text{W} \cdot \text{m}^{-1} \cdot \text{K}^{-1}$ for $\varphi = 0.4$.

In case of forced convection, however, $\vec{F}_m^{\text{f}}$ and $\vec{F}_m^{\text{p}}$ are governed by drag forces and they are responsible for particles' rotation. For spherical NPs, the drag coefficient was described by Dennis et al. [43], and Morsi et al. [44], and is governed by Stokes–Cunningham drag law, whereas for non-spherical struc-

tures the topic was discussed in particular by Haider and Levenspiel [45].

However, heat generation becomes much more difficult to estimate for non-spherical particles that are characterized by the full symmetry. For prolate/oblate structures as long as particles are attached to the ground, Eq. (15) or (17) is preserved. At the critical point when particles start to be swept away from the base material, the particles' polarizability ceases to be oriented, changing light–particle interaction into the randomly distributed particles, governed by Eq. (28):

$$\alpha_i = \frac{\alpha_{i,\hat{\imath}} + \alpha_{i,\hat{\jmath}} + \alpha_{i,\hat{k}}}{3} \tag{28}$$

where: $\hat{\imath}, \hat{\jmath}, \hat{k}$ – rectangular coordinates' axes, and $\hat{\imath}$ is the oriented one.
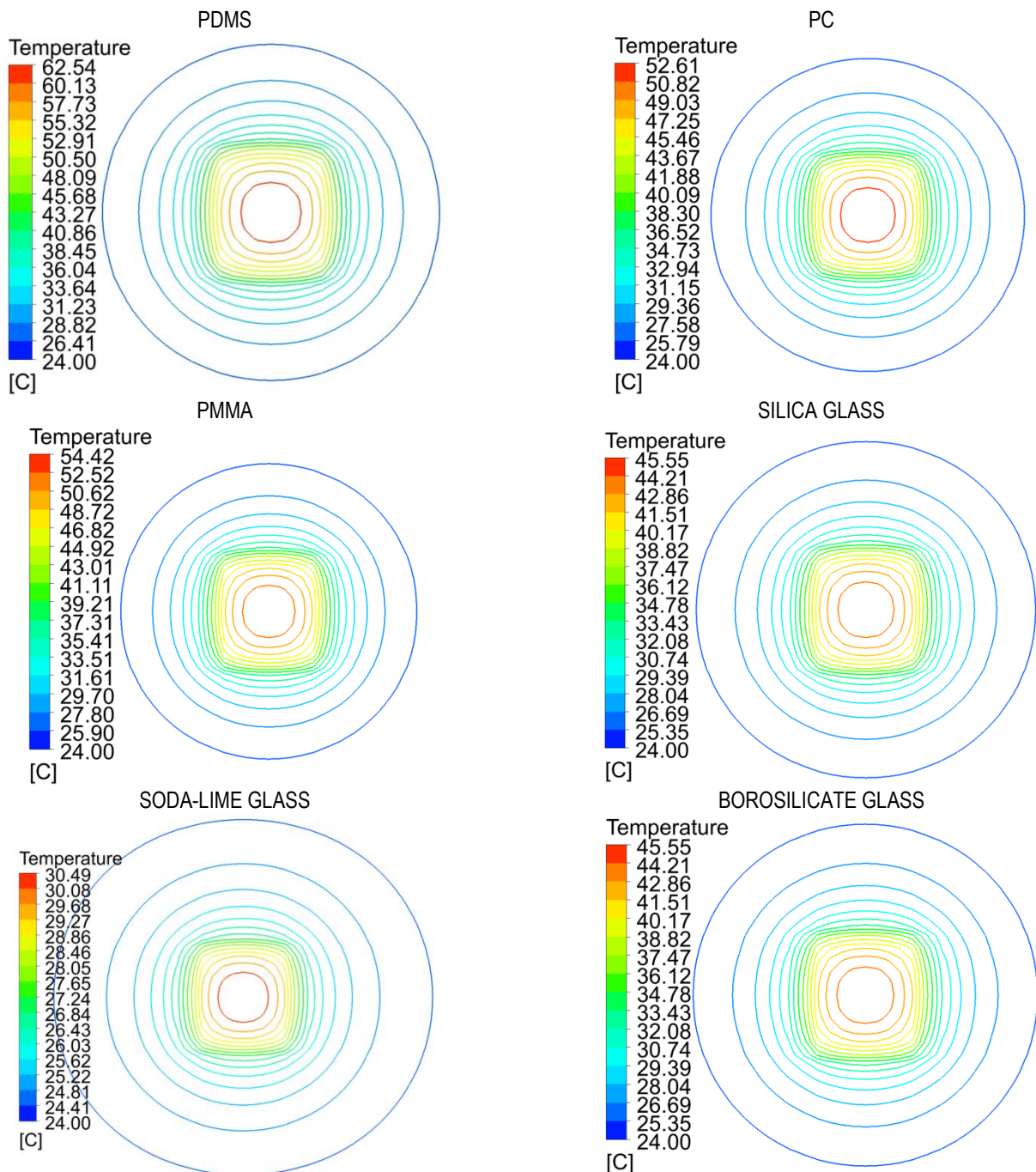

Fig. 4. Isotherms of laser-irradiated materials after 120 seconds using numerical results from [15]
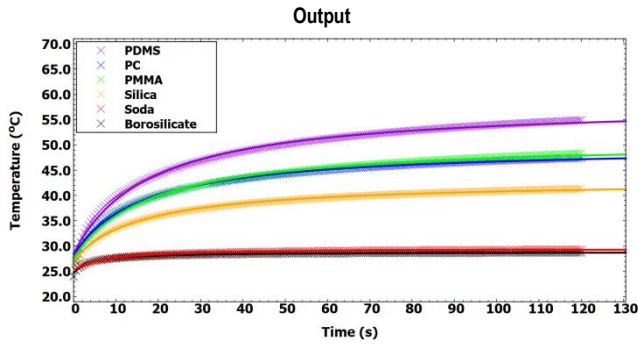
Fig. 5. Temperature time response for the utilized heat generation rate using numerical results (color points) from [15] and the (23)-and-(25)-based relationship (straight curves)

Eq. (15) or (17) is continued if particles stop rotating and every streamline is parallel along the great diameter, which occurs at high speed flows and at a high Reynolds number, however, shear stresses do the lion's share and it should be assumed that they do not affect the particle's shape during its movement.

The problem disappears while the NPs are substituted with a continuous thin film. Although its discretization requires to omit many multiscale issues, treating the material as a slab this problem can be reduced, and only appropriately determination of the heat transfer coefficient and the heat flux rate is needed.

Moreover, for high speed flows, particles are exposed to high shear stresses. This situation is much further complicated if a pipe is highly curved. In that case, NPs' heat generation rate should be governed by the full Mie theory including particle orientation [6,46]. Shear stresses may be modeled based on condensation phenomena between liquid and solid or liquid and gas [47,48]. Nevertheless, a Smoluchowski temperature jump might still be applied, investigating microscale heat transfer between fluid and particles.

6. SUMMARY

The present research involves conducting an investigation of ascertaining which parameters are crucial to the simulation of heat transfer of the radiated particles, and discovering that it is a complex issue. On the one hand, both interactions between particles and fluid and particles themselves should be considered, which is also not trivial. For instance, heat generation rate is dependent on many different factors that become highly tangled. Nevertheless, the Rayleigh-Drude approximation provides concisely the particles-particles interaction that may be modeled and implemented easily. However, there is a conflict with regard to the NP's size between the Mie–Lorenz theory, which is only relatively simple for spheres, and the Rayleigh–Drude approximation, which enables modeling any NP's shapes, although it fails when NP's diameter is similar to the incident wavelength. Mie theory is suggested to support the spherical and coated spheres, whereas for more complicated shapes the Rayleigh-Drude approximation can be preferred.

Moreover, fluid-particles interaction is still being studied at present and there is no one, general theory that may be performed to describe heat transport due to different material phenomena. Nonetheless, Smoluchowski theory is highly recommended for any particles-contained system due to its versatile legitimacy, starting from a high difference of thermal conductivity

between particles and fluids and extending up to fluid–particles interaction, which includes boundary phenomena, velocity slips and materials melting. This theory is subjected to the considered system, providing the results' accuracy and a scientific framework under which both the theory and the model would be studied.

NOMENCLATURE

Roman letters:

A_i	–	Projected area of the i-particle (m^2)
$a_{j,i}$	–	First Mie coefficient (-)
$b_{j,i}$	–	Second Mie coefficient (-)
C_{ext_i}	–	Extinction cross section of the i-particle (m^2)
$C_{p,p,i}$	–	Heat capacity of the i-particle ($\text{J} \cdot \text{K}^{-1}$)
C_{sca_i}	–	Scattered cross section of the i-particle (m^2)
c	–	Speed of light in vacuum ($\text{m} \cdot \text{s}^{-1}$)
c_p	–	Specific heat capacity of a material ($\text{J} \cdot \text{kg}^{-1} \cdot \text{K}^{-1}$)
$c_{p,p,i}$	–	Specific heat capacity of the i-particle ($\text{J} \cdot \text{kg}^{-1} \cdot \text{K}^{-1}$)
$\vec{d}$	–	Symmetric rate of deformation (s^{-1})
d_{l_i}	–	Longer diameter of the i-nanoparticle (m)
d_{s_i}	–	Shorter diameter of the i-nanoparticle (m)
E_p	–	Emissivity coefficient of the i-particle due to black-body radiation ($\text{W} \cdot \text{m}^{-3}$)
e	–	Specific energy ($\text{J} \cdot \text{kg}^{-1}$)
$\vec{F}_m^f$	–	Mechanical forces of the fluid ($\text{kg} \cdot \text{m} \cdot \text{s}^{-2}$)
$\vec{F}_m^p$	–	Mechanical forces of the particles ($\text{kg} \cdot \text{m} \cdot \text{s}^{-2}$)
$g_{e^- - ph}$	–	Electron-phonon coupling for nanoparticles ($\text{W} \cdot \text{m}^{-3} \cdot \text{K}^{-1}$)
$I_o(r, \Omega, t)$	–	Spatial profile of light incident intensity ($\text{W} \cdot \text{m}^{-2}$)
I_{abs_h}	–	Absorbed part of the surrounding medium ($\text{W} \cdot \text{m}^{-2}$)
I_{abs_i}	–	Absorbed part of the i-particle ($\text{W} \cdot \text{m}^{-2}$)
$I_{\vec{d}}$	–	First invariant of the strain rate (s^{-1})
$\overleftrightarrow{I}$	–	Unit tensor (-)
$\overleftrightarrow{I}_p$	–	Idemfactor in reference to particles (-)
$\hat{\imath}, \hat{\jmath}, \hat{k}$	–	rectangular coordinates' axes
j	–	Selected rank of Mie coefficients' accuracy
Kn	–	Knudsen number (-)
$\Bbbk$	–	Selected rank of the heat transfer accuracy
k	–	Thermal conductivity coefficient ($\text{W} \cdot \text{m}^{-1} \cdot \text{K}^{-1}$)
$\Bbbk_\infty$	–	Rank of the heat transfer, here: 500 (-)
k_o	–	Thermal conductivity coefficient of a pure metal ($\text{W} \cdot \text{m}^{-1} \cdot \text{K}^{-1}$)
k_{eff}	–	Effective thermal conductivity coefficient ($\text{W} \cdot \text{m}^{-1} \cdot \text{K}^{-1}$)
k_f	–	Thermal conductivity coefficient of fluid ($\text{W} \cdot \text{m}^{-1} \cdot \text{K}^{-1}$)
$k_{eff_{p,i}}$	–	Thermal conductivity coefficient of the i-particle ($\text{W} \cdot \text{m}^{-1} \cdot \text{K}^{-1}$)
l_f	–	Path's length that light passes through fluid (m)
l_i	–	Path's length that light passes through the i-particle (m)
l_T^f	–	Discontinuity at the boundary from fluid side (m)
l_T^p	–	Discontinuity at the boundary from particle side (m)
m_a	–	Refractive index of air (-)
m_h	–	Real part of refractive index of the surrounding medium (-)
m_p	–	Real part of the refractive index of particle's material (-)
$\widetilde{m}_h$	–	Imaginary part of the refractive index of the surrounding medium (-)

$\widetilde{m_p}$	–	Imaginary part of the refractive index of particle's material (-)
$\vec{n}$	–	Normal vector of the boundary layer (-)
p	–	Pressure (Pa)
Q_{in}	–	Internal source of energy, e.g. as a result of the magnetic field presence $(\mathrm{W} \cdot \mathrm{m}^{-3})$
$\vec{q}^f$	–	Fourier heat flux of fluid $(\mathrm{W} \cdot \mathrm{m}^{-2})$
$\vec{q}^p$	–	Fourier heat flux of particles $(\mathrm{W} \cdot \mathrm{m}^{-2})$
r	–	Radius – spherical coordinate (m)
S^f	–	Source of energy for fluids $(\mathrm{W} \cdot \mathrm{m}^{-3})$
S_i^p	–	Source of energy for the i-particle $(\mathrm{W} \cdot \mathrm{m}^{-3})$
$\vec{S}$	–	Oriented surface (m^2)
T	–	Temperature (K)
T^f	–	Temperature of fluid (K)
T^p_i	–	Temperature of particles (K)
T_o	–	Initial temperature at the $t = 0$ s (K)
T_{ph}	–	Temperature of crystal lattice (phonon heat) (K)
T_S	–	Smoluchowski temperature jump (K)
T_S^f	–	Temperature at the boundary from fluid side (K)
T_S^p	–	Temperature at the boundary from particle side (K)
T_w	–	Wall temperature (K)
t	–	Time (s)
V_i	–	Volume of the i-particle (m^3)
$\vec{v}_F$	–	Fermi velocity $(\mathrm{m} \cdot \mathrm{s}^{-1})$
$\vec{v}$	–	Velocity of the fluid $(\mathrm{m} \cdot \mathrm{s}^{-1})$
$\vec{v}_{p,i}$	–	Velocity of the i-particle $(\mathrm{m} \cdot \mathrm{s}^{-1})$
$\vec{v}_{slip}^f$	–	Velocity slip at fluid boundary $(\mathrm{m} \cdot \mathrm{s}^{-1})$
$\vec{v}_{slip}^p$	–	Velocity slip at particle boundary $(\mathrm{m} \cdot \mathrm{s}^{-1})$
$\overrightarrow{X^\dagger}$	–	Diffusive momentum flux $(\mathrm{kg} \cdot \mathrm{m} \cdot \mathrm{s}^{-2})$
x	–	Selected dimension (m)

Greek letters:

α_i	–	Polarizability of the i-particle (m^3)
α_p	–	Volume of particles' occupation in fluid (-)
α_d	–	Thermal diffusivity $(\mathrm{m}^2 \cdot \mathrm{s}^{-1})$
α_d^f	–	Thermal diffusivity of the considered fluid $(\mathrm{m}^2 \cdot \mathrm{s}^{-1})$
$\alpha_{d,i}^p$	–	Thermal diffusivity of the i-particle $(\mathrm{m}^2 \cdot \mathrm{s}^{-1})$
δ	–	Thickness of the considered material (m)
ε_h	–	Real part of the permittivity of the host medium (-)
ε_p	–	Real part of the permittivity of the considered metal (-)
$\widetilde{\varepsilon_h}$	–	Imaginary part of the permittivity of the host medium (-)
$\widetilde{\varepsilon_p}$	–	Imaginary part of the permittivity of the considered metal (-)
ϵ_i	–	Emissivity of the i-particle (-)
Θ_i^{p-f}	–	Heat exchange between the i-particle and fluid $(\mathrm{W} \cdot \mathrm{m}^{-3})$
Θ_i^{p-p}	–	Heat exchange between particles $(\mathrm{W} \cdot \mathrm{m}^{-3})$
Λ_o	–	Mean free path of an electron for a bulk metal (m)
$\Lambda_{p,i}$	–	Mean free path (particle size) of an electron for the i-particle (m)
λ	–	Incident wavelength (m)
μ	–	Molecular viscosity $(\mathrm{kg} \cdot \mathrm{m}^{-1} \cdot \mathrm{s}^{-1})$
ξ	–	Nanoparticles concentration (m^{-3})
ρ	–	Density of a material $(\mathrm{kg} \cdot \mathrm{m}^{-3})$
$\rho_{p,i}$	–	Density of the i-particle $(\mathrm{kg} \cdot \mathrm{m}^{-3})$
σ_{SB}	–	Stefan-Boltzmann constant $(\mathrm{W} \cdot \mathrm{m}^{-2} \cdot \mathrm{K}^{-4})$
σ_{abs_h}	–	Absorption coefficient of the surrounding medium (m^{-1})
σ_{abs_p}	–	Absorption coefficient of particles (m^{-1})
σ_{sca_p}	–	Scattering coefficient of particles (m^{-1})
φ	–	Fraction of occupied particles in fluid (-)

Φ	–	Oriented surface
$\phi_{i,fl}$	–	Parameter describing aspect ratio of the flattened i-particle (-)
$\phi_{i,str}$	–	Parameter describing aspect ratio of the stretched i-particle (-)
Ψ	–	Parameter describing heat flow rate (-)
ψ	–	Selected mathematical variable (-)
Ω	–	Angle of orientation (rad)

Others:

∂	–	Symbol of partial derivative
Λ_i	–	Depolarization factor of the i-nanoparticle (-)
Λ_i^{fl}	–	Depolarization factor of the flattened i-nanostructure (-)
Λ_i^{str}	–	Depolarization factor of the stretched i-nanostructure (-)
$\mathbb{I}$	–	Symbol of imaginary unit
$\mathbb{im}$	–	Imaginary part of a complex expression
$\mathbb{re}$	–	Real part of a complex expression

Subscripts and superscripts:

$'$	–	Symbol of derivative
$\cdot$	–	Symbol of scalar product
$\times$	–	Symbol of vector product
a	–	Air
d	–	Diffusivity
e^-	–	Electron
F	–	In reference to Fermi (crystallography)
f	–	Fluid
i	–	Selected number
m	–	Mechanical
N	–	Number of nanoparticles
o	–	In reference to initial conditions
p	–	Particle
$\dagger$	–	Transposition

Abbreviations:

abs	–	Absorption
$base$	–	Base – a material on which nanoparticles are coated
div	–	Divergence
eff	–	Effective
exp	–	Exponent
ext	–	Extinction
fl	–	Flattened
$grad$	–	Gradient
$ierfc$	–	Short form for error-based functions
in	–	Internal
ln	–	Symbol of natural logarithm
NPs	–	Nanoparticles
ph	–	Phonon
SB	–	Stefan-Boltzmann
sca	–	Scattering
$slip$	–	Slip at the boundary
str	–	Stretched
sur	–	Surface

REFERENCES

1. Strutt JW. On the scattering of light by small particles. London, Edinburgh, Dublin Philos Mag J Sci. 1871;41(275):447–54.
2. van de Hulst HC. Light scattering by small particles. Dover Publications, Inc. New York: John Wiley & Sons; 1957.
3. Lorenz L. Light propagation in and outside a sphere illuminated by plane waves of light. Eur Phys J H. 2019;44(2):77–135.

4. Gouesbet G. Generalized Lorenz-Mie theories and mechanical effects of laser light, on the occasion of Arthur Ashkin's receipt of the 2018 Nobel prize in physics for his pioneering work in optical levitation and manipulation: A review. J Quant Spectrosc Radiat Transf. 2019;225:258–77.

5. Mie G. Beiträge zur Optik trüber Medien, speziell kolloidaler Metallösungen. Ann Phys. 1908;25(3):377–445.

6. Bohren CF. Absorption and scattering of light by small particles. Absorption and scattering of light by small particles. 1983.

7. Martin RJ. Mie scattering formulae for non-spherical particles. J Mod Opt. 1993;40(12):2467–94.

8. Kumar S, Prasad SK, Banerjee J. Analysis of flow and thermal field in nanofluid using a single phase thermal dispersion model. Appl Math Model [Internet]. 2010;34(3):573–92. Available from: http://dx.doi.org/10.1016/j.apm.2009.06.026

9. Hussain SM, Goud BS, Madheshwaran P, Jamshed W, Pasha AA, Safdar R, et al. Effectiveness of Nonuniform Heat Generation (Sink) and Thermal Characterization of a Carreau Fluid Flowing across a Nonlinear Elongating Cylinder: A Numerical Study. ACS Omega. 2022;7(29):25309–20.

10. Hussain SM, Jamshed W, Pasha AA, Adil M, Akram M. Galerkin finite element solution for electromagnetic radiative impact on viscid Williamson two-phase nanofluid flow via extendable surface. Int Commun Heat Mass Transf [Internet]. 2022;137:106243. Available from: https://doi.org/10.1016/j.icheatmasstransfer.2022.106243

11. Shamshuddin MD, Abderrahmane A, Koulali A, Eid MR, Shahzad F, Jamshed W. Thermal and solutal performance of Cu/CuO nanoparticles on a non-linear radially stretching surface with heat source/sink and varying chemical reaction effects. Int Commun Heat Mass Transf [Internet]. 2021;129:105710. Available from: https://doi.org/10.1016/j.icheatmasstransfer.2021.105710

12. Siegel R, Howell JR. Thermal radiation heat transfer - Third Edition. Hemisphere Publishing Corporation. 1992.

13. Zaccagnini F, Radomski P, Sforza ML, Ziółkowski P, Lim S-I, Jeong K-U, et al. White light thermoplasmonic activated gold nanorod arrays enable the photo-thermal disinfection of medical tools from bacterial contamination. J Mater Chem B. 2023;

14. Radomski P, Ziółkowski P, De Sio L, Mikielewicz D. Importance and form of source element in the energy equation in reference to the photothermoablation of thin films and nanoparticles. In: 9th Wdzydzeanum Workshop on Fluid-Solid Interaction. 2021. p. 24.

15. Radomski P, De Sio L, Mikielewicz D. Computational fluid dynamics simulation of heat transfer from densely packed gold nanoparticles to isotropic media. Arch Thermodyn. 2021;42(3):87–113.

16. Michaelides EE. Transport properties of nanofluids. A critical review. Vol. 38, Journal of Non-Equilibrium Thermodynamics. 2013. 1–79 p.

17. E.Black S. Laser Ablation: Effects and Applications. New York; 2011. 99–226 p.

18. Ziółkowski P, Szewczuk-Krypa N, Butterweck A, Stajnke M, Głuch S, Drosińska-Komor M, et al. Comprehensive thermodynamic analysis of steam storage in a steam cycle in a different regime of work: A zero-dimensional and three-dimensional approach. J Energy Resour Technol. 1899;143(5):050905.

19. Mochnacki B, Paruch M. Cattaneo-Vernotte bio-heat transfer equation. Identification of external heat flux and relaxation time in domain of heated skin tissue. Comput Assist Methods Eng Sci. 2018;25(2–3):71–80.

20. Zheng Q, Shen X, Sokolowski-Tinten K, Li RK, Chen Z, Mo MZ, et al. Dynamics of Electron-Phonon Coupling in Bicontinuous Nanoporous Gold. J Phys Chem C. 2018;122(28):16368–73.

21. Medvedev N, Milov I. Electron–Phonon Coupling and Nonthermal Effects in Gold Nano-Objects at High Electronic Temperatures. Materials (Basel). 2022;15(14):1–11.

22. Warrier P, Teja A. Effect of particle size on the thermal conductivity of nanofluids containing metallic nanoparticles. Nanoscale Res Lett. 2011;6(1):247.

23. Feng B, Li Z, Zhang X. Prediction of size effect on thermal conductivity of nanoscale metallic films. Thin Solid Films. 2009;517(8):2803–7.

24. Wang BX, Zhou LP, Peng XF. Surface and size effects on the specific heat capacity of nanoparticles. Int J Thermophys. 2006;27(1):139–51.

25. Smoluchowski M. O przewodnictwie cieplnem gazów według dotychczasowych teoryj i doświadczeń. Pr Mat. 1898;10(12):33–64.

26. Sebastian V, Carminat R, Chantrenne P, Dilhaire S. Microscale and Nanoscale Heat Transfer. Vol. 9, Optics & Laser Technology. Berlin; 2007.

27. Kang Y, Zhao Z, Li B. A method for calculating average electric polarizability density of arbitrary small aperture. J Phys Conf Ser. 2018;1074(1).

28. Sihvola A, Lindell I V. Polarizability and effective permittivity of layered and continuously inhomogeneous dielectric ellipsoids. J Electromagn Waves Appl. 1990;4(1):1–26.

29. Royer P, Bijeon JL, Goudonnet JP, Inagaki T, Arakawa ET. Optical absorbance of silver oblate particles. Substrate and shape effects. Surf Sci. 1989;217(1–2):384–402.

30. Royer P, Goudonnet JP, Warmack RJ, Ferrell TL. Substrate effects on surface-plasmon spectra in metal-island films. Phys Rev B. 1987;35(8):3753–9.

31. Smoluchowski M. On conduction of heat by rarefied gases. Vol. 46, The London, Edinburgh, and Dublin Philosophical Magazine and Journal of Science. 1898. p. 192–206.

32. Smoluchowski M V. Über den Temperatursprung bei Wärmeleitung in Gasen. Vol. 108, Akademie der Wissenschaften, Wien. 1898. p. 304--329.

33. Adamowicz A. Determination of Thermal Diffusivity Values Based on the Inverse Problem of Heat Conduction - Numerical Analysis. Acta Mech Autom. 2022;16(4):399–407.

34. Carslaw HS, Jaeger JC. Conduction of Heat in Solids. Oxford University Press. London; 1959.

35. Domański R. Promieniowanie laserowe - oddziaływania na ciała stałe. Wydawnictwa Naukowo-Techniczne. Warszawa; 1990. 85–220 p.

36. Ready JF. Mechanism of electron emission produced by a giant-pulse laser. Phys Rev. 1965;137(2A):A620–3.

37. Bhandari A. Mathematical Modelling of Water-Based Fe3O4Nanofluid Due to Rotating Disc and Comparison with Similarity Solution. Acta Mech Autom. 2021;15(3):113–21.

38. Kumar R, Singh G, Mikielewicz D. A New Approach for the Mitigating of Flow Maldistribution in Parallel Microchannel Heat Sink. J Heat Transfer. 2018;140(7).

39. Szymanski P, Mikielewicz D. Additive Manufacturing as a Solution to Challenges Associated with Heat Pipe Production. Materials (Basel). 2022;15(4).

40. Blauciak K, Szymanski P, Mikielewicz D. The influence of loop heat pipe evaporator porous structure parameters and charge on its effectiveness for ethanol and water as working fluids. Materials (Basel). 2021;14(22).

41. Miri R, Abbassi MA, Ferhi M, Djebali R. Second Law Analysis of MHD Forced Convective Nanoliquid Flow Through a Two-Dimensional Channel. Acta Mech Autom. 2022;16(4):417–31.

42. Hafeez MB, Krawczuk M, Shahzad H. An Overview of Heat Transfer Enhancement Based Upon Nanoparticles Influenced By Induced Magnetic Field with Slip Condition Via Finite Element Strategy. Acta Mech Autom. 2022;16(3):200–6.

43. Dennis SCR, Singh SN, Ingham DB. The steady flow due to a rotating sphere at low and moderate Reynolds numbers. J Fluid Mech. 1980;101(2):257–79.

44. Morsi SA, Alexander AJ. An investigation of particle trajectories in two-phase flow systems. J Fluid Mech. 1972;55(2):193–208.

45. Levenspiel O., Haider A. Drag Coefficient and Terminal Velocity of Spherical and Nonspherical Particles. Powder Technol. 1989;58:63–70.

46. Yang P, Wendisch M, Bi L, Kattawar G, Mishchenko M, Hu Y. Dependence of extinction cross-section on incident polarization state and particle orientation. J Quant Spectrosc Radiat Transf. 2011;112(12):2035–9.

47. Mikielewicz D. Hydrodynamics and heat transfer in bubbly flow in the turbulent boundary layer. Int J Heat Mass Transf. 2003;46(2):207–20.

48. Mikielewicz D, Wajs J, Andrzejczyk R, Klugmann M. Pressure drop of HFE7000 and HFE7100 during flow condensation in minichannels. Int J Refrig [Internet]. 2016;68:226–41. Available from: http://dx.doi.org/10.1016/j.ijrefrig.2016.03.005

Piotr Radomski: https://orcid.org/0000-0002-4778-8670

Paweł Ziółkowski: https://orcid.org/0000-0001-7480-0420

Dariusz Mikielewicz: https://orcid.org/0000-0001-8267-7194

LINEAR ANALYSIS OF THIN-WALLED COMPOSITE PROFILES WEAKENED BY HOLES

Katarzyna FALKOWICZ*

*Faculty of Mechanical Engineering, Department of Machine Design and Mechatronics,
Lublin University of Technology, Nadbystrzycka 36, 20-618 Lublin, Poland

k.falkowicz@pollub.pl

Abstract: The paper presents the results of the numerical analysis of the stability of C-section profiles together with the determination of the influence of the geometrical parameters of the holes and their arrangement on the strength properties of the profile, made of multilayer composite materials in a symmetrical arrangement of layers, which is deformed under the influence of the compressive force. Numerical calculations were carried out in the linear range (solution of the eigenvalue problem - critical state) using the finite element method (FEM) using the ABAQUS calculation package. Based on the obtained results, it was possible to determine the influence of the type and number of holes, their arrangement and geometric dimensions on the values of critical loads as well as the buckling modes of the profiles.

Key words: stability, composites, FEM, thin-walled structures, linear analysis

1. INTRODUCTION

Intensive industrial development requires from constructors used modern materials with more favorable operational properties. In addition, there is a constant effort to reduce the weight of elements while maintaining or increasing their strength and stiffness properties. The main way to ensure the minimum weight of the structure is making various types of holes in the structures. However, by weakened the structure, it is necessary to take into account the critical load where the structure may lose its stability and be destroyed. In this case, the most optimal solution should be selected. It is worth mentioning here, that Author in previous tests analysed the stability of thin-walled composite plate elements weakened by cut-outs and subjected to axial compression [1–6]. The obtained results showed that we can influence on buckling and postbuckling behaviour of plate elements by changing the shape and geometric parameters of cut-out. This paper analyzes the commonly used C-section profiles, which are used, among others, in aviation, in construction industry, in drywall constructions or in the creation of frames. Profiles of this type are mainly made of steel or aluminium , as well as composite. However, in the case of composite, they are mainly made as profiles without holes. The analysis of the stability issue of thin-walled structures under operational conditions of static loads was dealt with, among others, in the works [7–12].

In this work, composite columns with a common C-shaped cross-section, weakened by holes, were investigated. The influence of the holes geometric dimensions and their arrangement on the value of the critical load, as well as on the forms of loss of stability, in order to obtain the highest value of the critical force by minimizing the mass of the structure, was analysed. Analysed profiles were subjected to an axial compressive load. The tests included the critical state in order to determine the values of forces for which the structure loses its stability. There are many publications devoted to the study of the critical state of thin-walled composite structures in the aspect of structural stability [13–16].

The key aspect of analysis was to determine the value of the critical forces, where the linear eigenvalue problem with the criterion of the minimum potential energy was used. The scope of research include issue of linear stability of composite profiles subjected to axial compression. Numerical calculations were performed with commercial ABAQUS program used the FEM (Finite Element Method), which has currently a very wide applications [17–23].

This work is continuation of Author research, which part of them was published in [24–27]. The obtained results showed that we can influence on buckling and postbuckling behaviour of thin-walled columns by changing the shape and cut-out geometric parameters. In literature, it can be found number of already conducted analysis of the stability of composite plate elements weakened by holes. However, the buckling area with composite perforated columns has not yet been thoroughly analyzed. Moreover, there is no specific standards for the perforation of composite profiles.

2. CHAPTER TITLE SUBJECT AND RESEARCH METHODOLOGY

The subject of the research were thin-walled composite profiles with a C-cross-section with various hole configurations. The overall dimensions of the tested column were chosen according to the previous analysis [28, 29].

The scheme of geometric parameters of the tested channel section profiles has shown in Figure 1.

The tested columns had circular and bean-shape holes. Figure 2 shows selected variants of the arrangement of holes. The

holes were arranged symmetrically and evenly in relation to each wall of the column. Figure 3 shows a set of columns corresponding to the same cases, but without holes on the side walls (dimensions on the middle walls are the same). In total, 32 cases of different profile configurations were analysed.
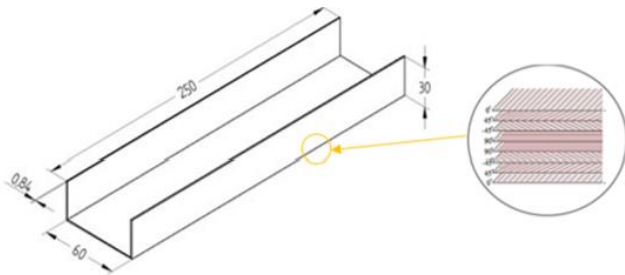

Fig. 1. Geometric parameters of the channel section profile: column length l = 250 mm, wall width h = 60 mm, wall height = 30 mm, wall thickness g = 0,84 mm
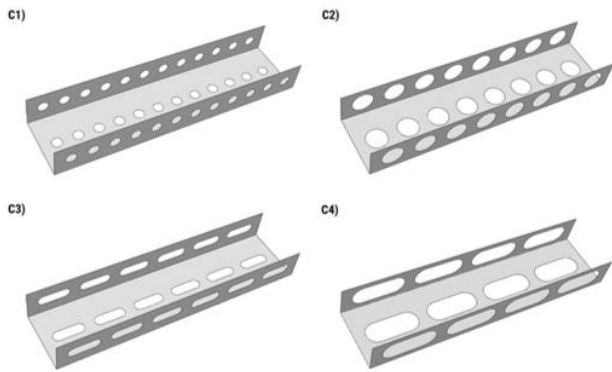

Fig. 2. Models of C-section profiles in a variant of arrange-ment of holes on the web and walls: (C1) circular holes with a diameter of 10 mm, (C2) circular holes with a di-ameter of 20 mm, (C3) bean-shaped holes with a di-mension of 30 mm × 10 mm (R = 5 mm), (C4) bean-shaped holes with a dimension of 50 mm × 20 mm (R = 10 mm)
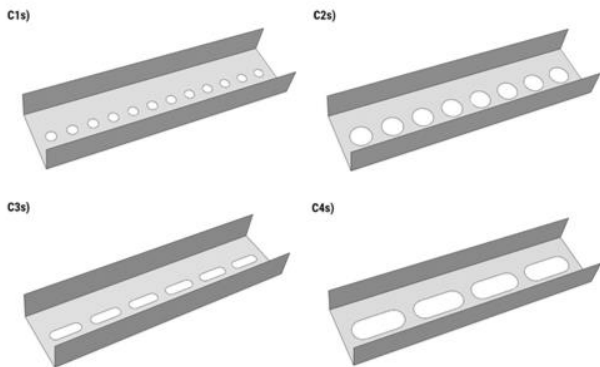
Fig. 3. Models of C-section profiles in a variant of arrangement of holes on the web: (C1s) circular holes with a diameter of 10 mm, (C2s) circular holes with a diameter of 20 mm, (C3s) bean-shaped holes with a dimension of 30 mm ×10 mm (R = 5 mm), (C4s) bean-shaped holes with a dimension of 50 mm × 20 mm (R = 10 mm)

In the case of C1 (Figure 4), the tested column has 12 circular holes with a diameter of 10 mm on each wall. The distance between the centers of the holes is 20mm. The distance from the

side edge to the center of the first hole is 15mm, both at the beginning and at the end of the column. The distance from the center of the side wall hole to the middle wall is 15mm and the distance from the center of the middle wall hole to the side wall is 30mm (these distances are the same for all tested cases with the holes arranged in one row along the entire wall). Case C2 (Figure 5) has 8 circular holes on each face with a diameter of 20mm. The distance between the centers of the holes is 30mm. The distance from the side edge to the center of the first hole is 20mm both at the beginning and at the end of the column walls.

In the case of C3 (Figure 6), the profile has 6 bean holes on all walls. Each with the following dimensions: length = 30mm, width = 10mm, rounding radius R = 5mm. The distance between the edges of the holes is 10mm. The distance from the side edge to the edge of the first hole is also 10mm at both the start and end of the column walls.

In the case of C4 (Figure 7), the profile has 4 bean holes on all walls, each with the following dimensions: length = 50mm, width = 20mm, rounding radius R = 10mm. The distance between the edges of the holes is 10mm. The distance from the side edge to the edge of the first hole is also 10mm at both the start and end of the column walls.
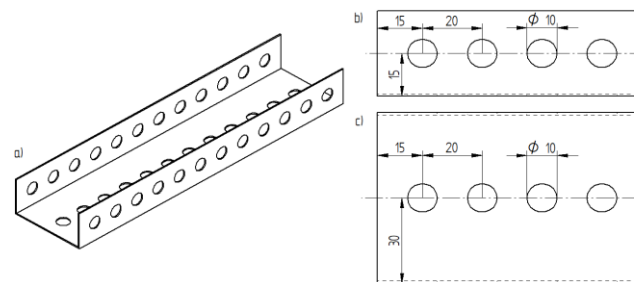
Fig. 4. (a) Model C1 with circular holes with a diameter of 10 mm, (b) geometric dimensions on the side wall part, (c) geometric dimensions on the web part
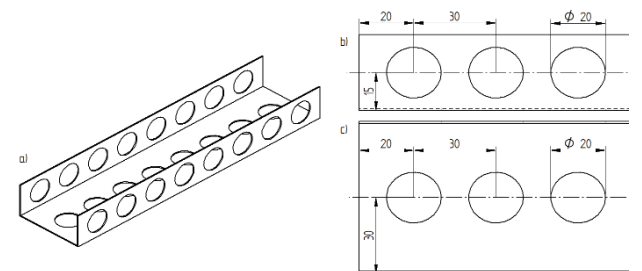

Fig. 5. (a) Model C2 with circular holes with a diameter of 20 mm, (b) geometric dimensions on the side wall part, (c) geometric dimensions on the web part
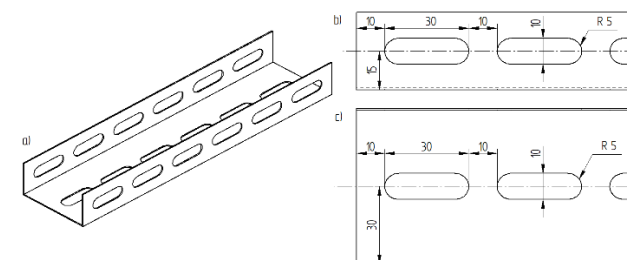

Fig. 6. (a) Model C3 with bean-shaped holes with dimensions 30 mm × 10 mm (R = 5 mm), (b) geometric dimensions on the side wall part, (c) geometric dimensions on the web part

Figure 8 shows variants of the arrangement of holes in a chess sequence. The spacing of the holes on the web was set so that each hole center was exactly midway between two holes on the sidewall. Figure 9, on the other hand, shows a set of columns corresponding to the same cases, but without openings on the side walls (dimensions on the middle walls are the same).
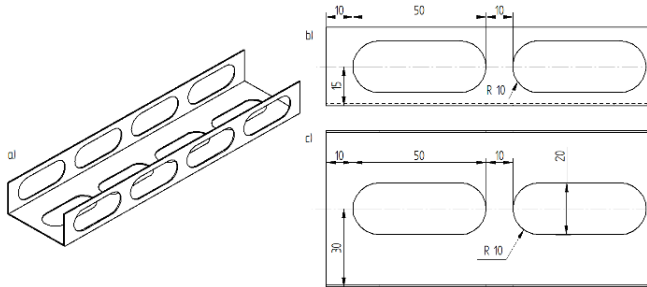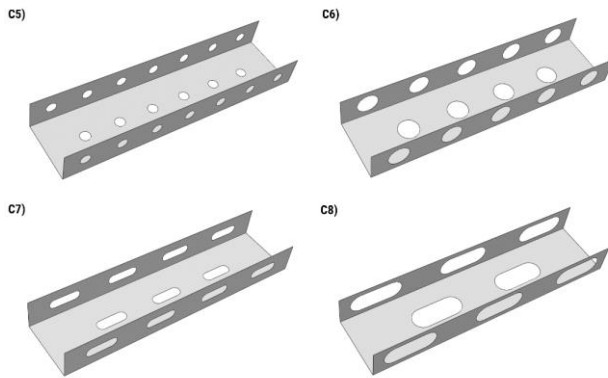

Fig. 7. (a) Model C4 with bean-shaped holes with dimensions 50 mm × 20 mm (R = 10 mm) (b) geometric dimen-sions on the side wall part, (c) geometric dimensions on the web part

Fig. 8. Models of C-section profiles with a variant of arrange-ment of holes in a chess sequence: (C5) circular holes with a diameter of 10 mm, (C6) circular holes with a di-ameter of 20 mm, (C7) bean-shaped holes with a di-mension of 30 mm × 10 mm (R = 5 mm), (C8) bean-shaped holes with a dimension of 50 mm × 20 mm (R = 10 mm)
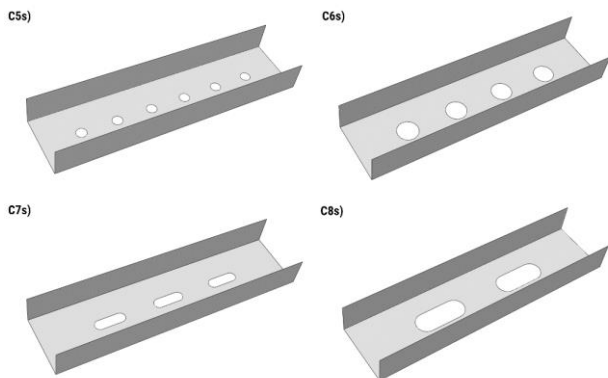
Fig. 9. Models of C-section profiles with a variant of arrange-ment of holes in a chess sequence (without holes on side walls): (C5s) circular holes with a diameter of 10 mm, (C6s) circular holes with a diameter of 20 mm, (C7s) bean-shaped holes with a dimension of 30 mm × 10 mm (R = 5 mm), (C8s) bean-shaped holes with a dimension of 50 mm × 20 mm (R = 10 mm)

Figure 10 shows variants of symmetrical arrangement of circu-lar holes with diameters of 10mm and bean holes with dimensions of 30mm × 10mm (R = 5mm). The central walls of the profiles have holes arranged in two rows. Cases C9 and C11 present symmetrical configurations of hole placement, while cases C10 and C12 present chess configurations. Figure 11 shows a set of columns corresponding to the same cases, but without holes on the side walls (dimensions on the middle walls are the same).
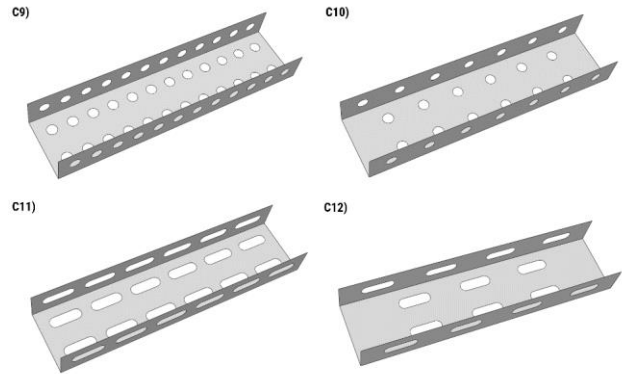
Fig. 10. Models of C-section profiles with a variant of arrange-ment of holes in two rows – 1st way: (C9) circular holes with a diame-ter of 10 mm, (C10) circular holes with a diameter of 10 mm in a chess sequence, (C11) bean-shaped holes with a dimension of 30 mm × 10 mm (R = 5 mm), (C12) bean-shaped holes with a di-mension of 30 mm × 10 mm (R = 5 mm) in a chess se-quence
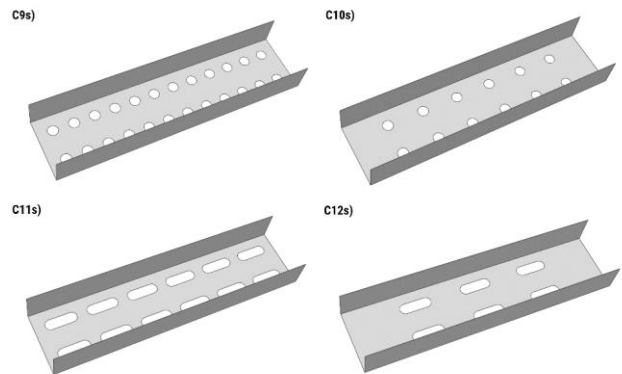

Fig. 11. Models of C-section profiles with a variant of arrange-ment of holes in two rows – 1st way (without holes on side walls): (C9s) circular holes with a diameter of 10 mm, (C10s) circular holes with a diameter of 10 mm in a chess sequence, (C11s) bean-shaped holes with a dimension of 30 mm × 10 mm (R = 5 mm), (C12s) bean-shaped holes with a dimension of 30 mm × 10 mm (R = 5 mm) in a chess sequence

Figure 12 shows the last variants of arrangement of circular holes with diameters of 10mm and bean-shape holes with dimen-sions of 30mm × 10mm (R = 5mm). The central walls of the pro-files have holes arranged in two rows. The geometric dimensions correspond to the above variants with the arrangement of holes in two rows on the central wall, only with the distance between the centers of the openings arranged along the width of the column equal to 20mm. Cases C13 and C15 refer to the symmetrical configuration of the arrangement of holes, while cases C14 and

C16 refer to the chess configuration. Figure 13, on the other hand, shows a set of columns corresponding to the same cases, but without holes on the side walls (dimensions on the middle walls are the same).
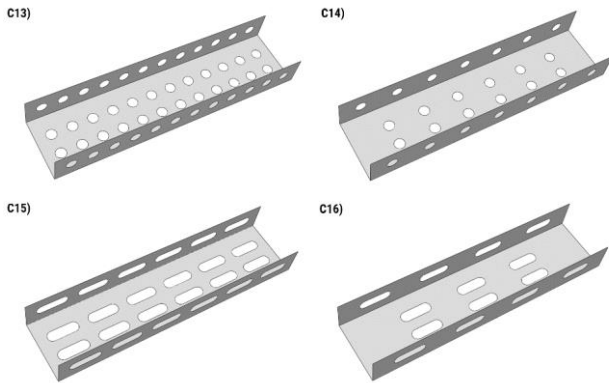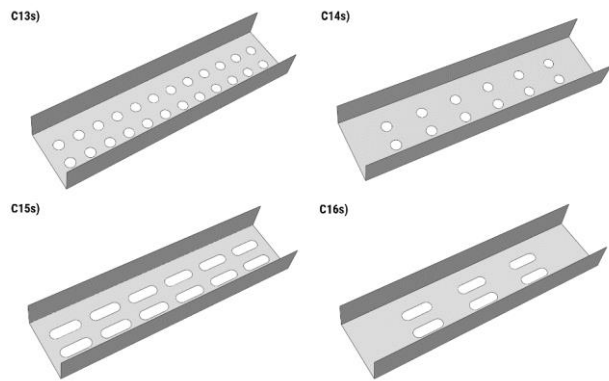

Fig. 12. Models of C-section profiles with a variant of arrange-ment of holes in two rows – 2nd way: (C13) circular holes with a diameter of 10 mm, (C14) circular holes with a diameter of 10 mm in chess sequence, (C15) bean-shaped holes with a dimension of 30 mm × 10 mm (R = 5 mm), (C16) bean-shaped holes with a di-mension of 30 mm ×10 mm (R = 5 mm) in a chess se-quence

Fig. 13. Models of C-section profiles with a variant of arrange-ment of holes in two rows – 2nd way (without holes on side walls): (C13s) round holes with a diameter of 10 mm, (C14s) circular holes with a diameter of 10 mm in a chess sequence, (C15s) bean-shaped holes with a dimension of 30 mm × 10 mm (R = 5 mm), (C16s) bean-shaped holes with a dimension of 30 mm × 10 mm (R = 5 mm) in a chess sequence

Tab. 1. Mechanical and strength properties of the tested com-posite material

Mechanical properties	
Young's modulus E_1 [MPa]	14,3528.5
Young's modulus E_2 [MPa]	5,826.3
Poisson's ratio [-]	0.36
Kirchhoff modulus G_{12} [MPa]	3,845.5
Strength properties	
Tensile strength (0°) F_{T1} [MPa]	2,220.7
Compressive strength (0°) F_{C1} [MPa]	641
Tensile strength (90°) F_{T2} [MPa]	49
Compressive strength (90°) F_{C2} [MPa]	114
Shear strength F_{12} [MPa]	83.5

The tested profiles consist of eight layers of laminate with the same thickness equal 0.105 mm (summary 0.84 mm). The layers are arranged symmetrically to the middle plane of the laminate in the following configuration: [0/45/-45/90]S. The composite configu-ration was assumed based on previous analyses [30]. In this paper, one layer layout was considered because the focus was on the arrangement and geometrical parameters of the holes. The material used to the analysis was a carbon-epoxy composite with the designation of EP137-CR527/100–35. The mechanical proper-ties of the material presented in Table 1.

The scope of the conducted research included the analysis of the critical state using the finite element method. The tests con-sisted of solving the eigenvalue problem, which allowed to deter-mine the critical load for each analyzed model and to determine the corresponding form of the loss of stability. The eigenproblem was solved using the maximum potential energy principle – the equilibrium state of the system was equal to the minimum poten-tial energy. That meant that for stable systems the second varia-tion of potential energy has to be positive. Stability problems of such systems are solved with the following equation [31]:

$$([K] + \lambda i[H])\{\psi\}i = 0 \qquad (1)$$

where [K] is the structural stiffness matrix, [H] is the stress stiff-ness matrix, and λi is the i-th eigenvalue and ψ is the i-th eigen-vector of displacement. Equality (1) is satisfied if the eigenvector of displacement is equal to zero or if the determinant of the term in brackets is equal to zero. When the {ψ}i = 0 it is a trivial solution and it is out of interest. It means that the structure remains in the initial state of equilibrium. The term in brackets in (1) gives the following solution:

$$|[K] + \lambda i[H]|= 0 \qquad (2)$$

Equation (2) represents the eigenvalue problem which allows for finding n values of the buckling load multiplier λ and the corre-sponding buckling mode shape.

Numerical analysis was performed in the ABAQUS program. The profile model was loaded by applying a uniform compressive force to all upper edges of the column. Boundary conditions for profile together with the discrete model are shown in Figure 14.
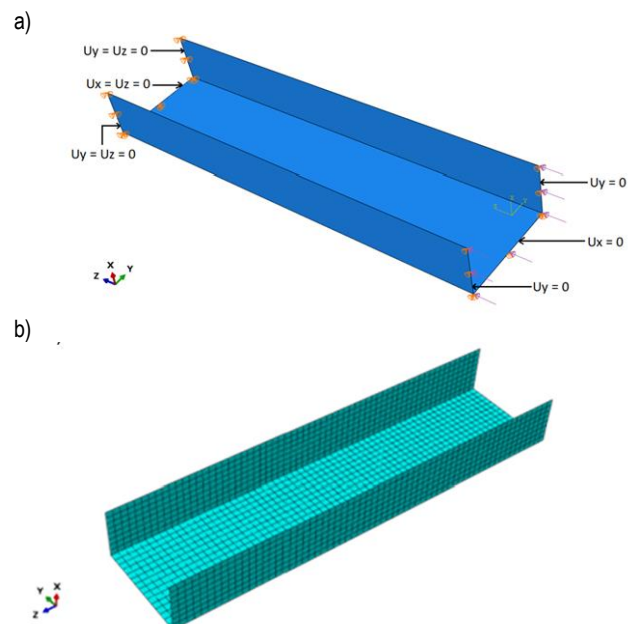

Fig. 14. (a) Boundary conditions, (b) discrete model

The tested profiles were discretized with 8-node shell elements (S8R) with six degrees of freedom at each node, with quadratic shape function and reduced integration. The Composite Lay-up technique was used to define thickness an material properties of each layer separately. Mesh density which was used for analysis equal 4 mm and it was based on the previous analysis of Author and others, where the mesh convergence test was performed [26, 32].

The boundary conditions were defined by locking some degrees of freedom of the bottom and top nodes of the column. For the upper middle edge, the translational degree of freedom Ux = 0 was blocked, and for the two upper side edges, the translational degree of freedom was blocked Uy = 0. For the lower middle edge, the displacement along the x and z axes was blocked, i.e. Ux = Uz = 0. For the two lower side edges the displacement along the y and z axes was blocked, i.e. Uy = Uz = 0. The possibility of rotation relative to the column axis was also blocked (URz=0). The profile model was loaded by applying a uniform compressive force to all upper edges of the column.

3. RESULTS

As a result of the numerical analysis, the values of critical loads were obtained for all tested C-section columns with the same geometrical dimensions and different types of holes. In addition, the form of loss of stability corresponding to the previously obtained load values were determined. Examples of obtained modes are shown in Fig. 15-17. Critical load values for all considered cases have been collected and presented in the form of graphs (Fig. 17).

On the basis of the obtained results, it was possible to determine the influence of the type and number of holes, their arrangement and geometric dimensions on the values of critical loads as well as the buckling modes of the profiles. Buckling form for the analysed C-section profiles is characterized by the formation of two half-waves on the web and side walls of the columns, symmetrically distributed in relation to the channel's symmetry plane. In almost all cases, the first half-wave (from the side where the compressive force is applied) bends inwards of the profile, while the second half-wave bends the other way around – outwards.
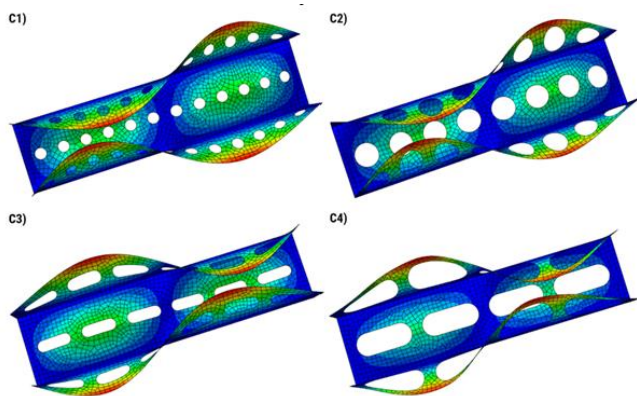

Fig. 15. Results of numerical analysis – models of C-section profiles with a variant of arrangement of holes on the web and walls: (C1) circular holes with a diameter of 10 mm, (C2) circular holes with a diameter of 20 mm, (C3) bean-shaped holes with a dimension of 30 mm × 10 mm (R = 5 mm), (C4) bean-shaped holes with a di-mension of 50 mm × 20 mm (R = 10 mm)
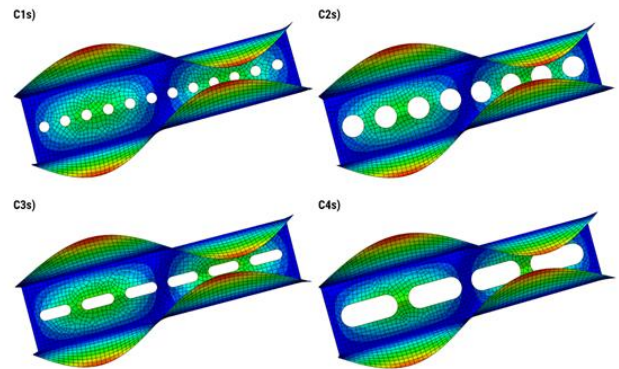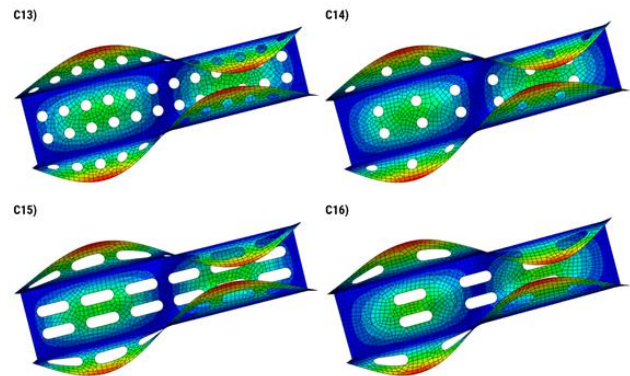

Fig. 16. Results of numerical analysis – models of C-section profiles with a variant of arrangement of holes on the web: (C1s) circular holes with a diameter of 10 mm, (C2s) circular holes with a diameter of 20 mm, (C3s) bean-shaped holes with a dimension of 30 mm × 10 mm (R = 5 mm), (C4s) bean-shaped holes with a di-mension of 50 mm × 20 mm (R = 10 mm)

Fig. 17. Results of numerical analysis – models of C-section profiles with a variant of arrangement of holes in two rows – 2nd way: (C13) circular holes with a diameter of 10 mm, (C14) circular holes with a diameter of 10 mm in a chess sequence, (C15) bean-shaped holes with a dimension of 30 mm × 10 mm (R = 5 mm), (C16) bean-shaped holes with a dimension of 30 mm × 10 mm (R = 5 mm) in a chess sequence
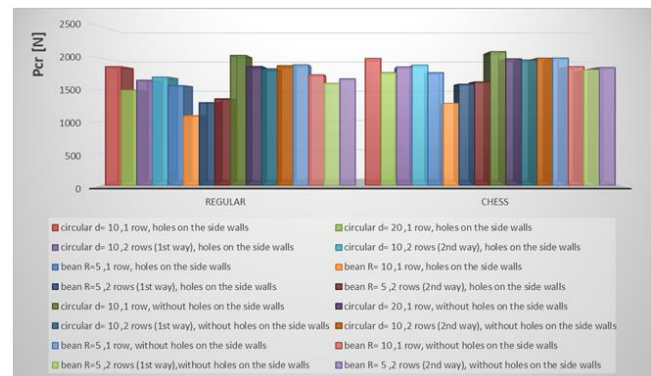

Fig. 18. Diagram of dependence of the critical load values on the arrangement of holes for all tested profiles

The obtained results showed a significant influence of the geometrical parameters of the holes and their arrangement on the value of the critical load. In all analysed configurations, the critical force decreased with the increase of the number of holes and their size.

In addition, in order to simplify the analysis of the above dependence graph, a comparison between the models with the usual arrangement of holes and the arrangement of holes in the chess configuration was made - separately for all profiles with circular holes (Fig. 18) and for all profiles with bean-shape holes (Fig. 19).

The largest decrease in the critical force by 19.8% was observed when the configuration of the column with circular holes with a diameter of 10mm was change to the configuration with circular holes with a diameter of 20mm, while the increase of bean-shape holes, dimensions 30mm × 10mm (R = 5mm) to bean-shape holes with dimensions 50mm × 20mm (R = 10mm) caused the critical force drop by 30.52%, and this applies to the standard arrangement of holes. Changing the profile configuration from smaller holes to larger holes, arranged in a chess sequence, is also characterized by a decrease of the critical loads value: for circular holes by 11.16%, and for bean-shape holes by 27.22%. Columns without side wall holes have much higher values of critical forces. There is a 9.44% drop in force with changing the profile configuration with smaller circular holes to a configuration with larger holes and by 20.9% for bean-shape hole configurations with regular spacing.
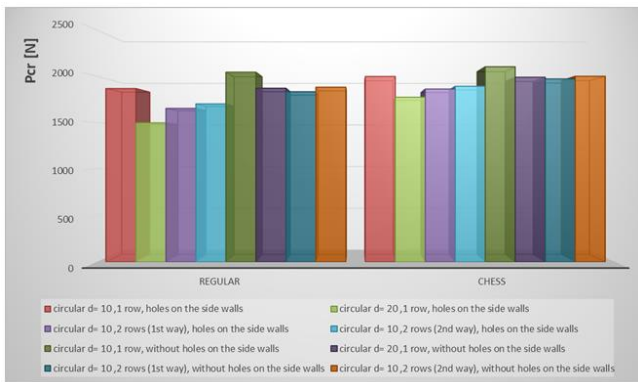

Fig. 19. Diagram of dependence of the critical load values on the arrangement of holes for all tested profiles with cir-cular holes
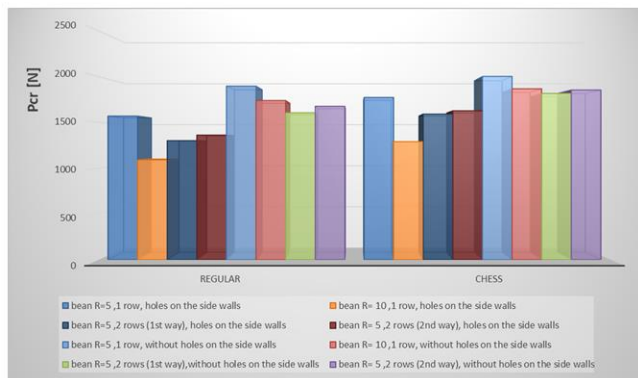

Fig. 20. Diagram of dependence of the critical load values on the arrangement of holes for all tested profiles with bean-shaped holes

Figures 20 and 21 show a comparison between models with normal hole pattern and chess pattern, only for profiles with circular holes - arranged in two rows on the middle walls, and separately for profiles with bean-shape holes - arranged in two rows on the middle walls.
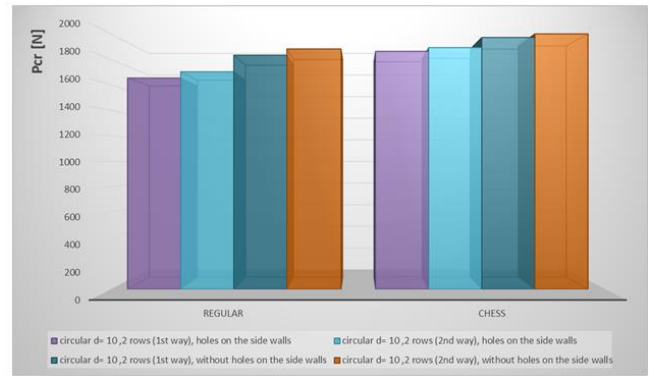

Fig. 21. Diagram of the dependence of the critical load values on the arrangement of holes for the tested profiles with round holes arranged in two rows on the central wall
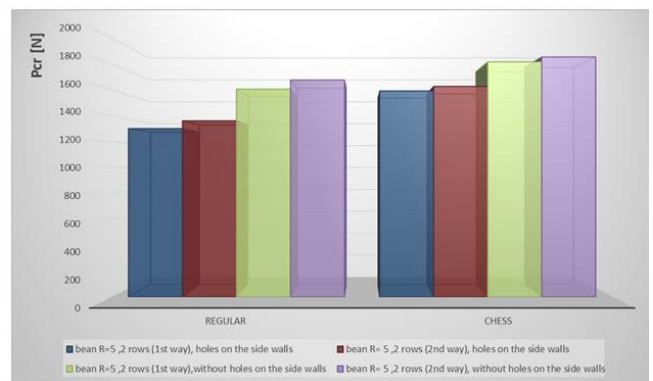

Fig. 22. Diagram of the dependence of the critical load values on the arrangement of holes for the tested profiles with bean-shaped holes arranged in two rows on the central wall

Analyzing the first and second way of arrangement of holes in two rows on the central wall of the profile, it was observed that when the distance between the centers of holes located along the width of the column is reduced, the value of the critical force increases. Thus, the value of the force is greater at a distance between the centers of the holes equal 20mm (2nd way) and lower at a distance of 30mm (1st way). In addition, the force value is by 2.88% greater for the distance between the centers of circular holes and by 4.44% greater for bean-shape holes, with the regular arrangement. Comparing the greater force value of the column with holes in two rows and the force value with holes in one row with the usual arrangement, it was determined that the force value decreases by 8.82% when adding a second row of circular holes and by 13.22% when adding a second row of bean-shape holes. With the arrangement of the holes in two rows on the central wall, however, in the chess configuration, the value of the force is greater by 1.56% at the distance between the centers of the circular holes of 20mm (2 way) and greater by 2.17% at the distance between the centers of the bean-shape holes, also of 20mm. Comparing the greater value of the critical force of the column with holes in two rows and the value of the critical force with holes in one row, with the arrangement of holes in a chess configuration, it was noticed that the value of the force decreases by 5.24% when adding a second row of round holes and by 8.2 % when adding a second row of bean holes. In the case of profiles with a variant of arrangement of holes in two rows, without holes on the side walls, similar changes in percentage values were

observed for configurations of holes in two rows, with holes on the side walls.

Summing up all the analyzed hole configurations, the greatest attention should be paid to profiles with a variant of arrangement of holes in two rows, in a chess configuration. This configuration gives a high critical load value and is superior to a profile configuration with normal hole spacing, provided that the distance between the centers of the holes spaced along the width of the column is relatively small.

4. SUMMARY

Based on the performed analysis and the obtained results, it was possible to determine the influence of the type and number of holes, their arrangement and geometric dimensions on the values of critical loads and buckling modes of C-section profiles. The obtained results showed a significant influence of the geometrical parameters of the holes and their arrangement on the value of the critical load. The greatest attention should be paid to profiles with a variant of arrangement of holes in two rows, in a chess configuration (Fig. 22). The given profile configuration gives a high critical load value and is higher than the profile configuration with normal hole spacing, provided that the distance between the centers of the holes along the width of the column is relatively small.
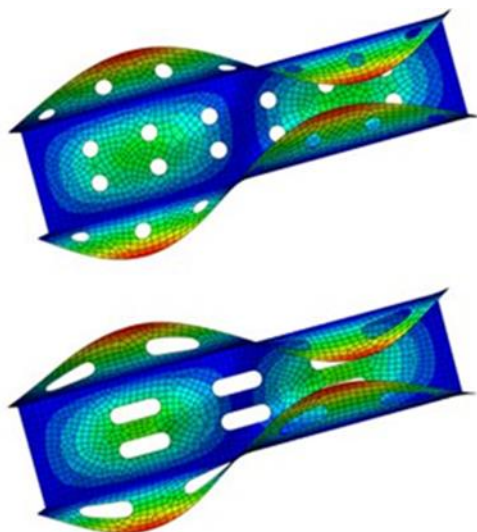

Fig. 23. Results of numerical analysis – models of C-section profiles with a variant of arrangement of holes in a chess sequence, in two rows – 2nd way

The obtained results may have a practical importance in terms of the use of this type of profiles as load-bearing elements, in which it is necessary to make holes, even for assembly purposes.

What is more, thanks to numerical analysis, which is a powerful tool for examining the state of load-bearing capacity in thin-walled structures, we are able to quickly find the optimal solution and determine which one is the most advantageous.

REFERENCES

1. Falkowicz K, Debski H. The work of a compressed, composite plate in asymmetrical arrangement of layers. W Depok, Indonesia; 2019. 020005. http://aip.scitation.org/doi/abs/10.1063/1.5092008

2. Falkowicz K, Ferdynus M, Rozylo P. Experimental and numerical analysis of stability and failure of compressed composite plates. Composite Structures. 2021;263:113657.

3. Falkowicz K, Debski H, Teter A. Design solutions for improving the lowest buckling loads of a thin laminate plate with notch. W Lublin, Poland; 2018. s. 080004. http://aip.scitation.org/doi/abs/10.1063/1.5019075

4. Falkowicz K, Szklarek K. Analytical method for projecting the buckling form of composite palates with a cut-out. IOP Conf Ser: Mater Sci Eng. 2019;710(1):012021.

5. Falkowicz K. Experimental and numerical failure analysis of thin-walled composite plates using pro-gressive failure analysis. Composite Structures. 2023;305:116474.

6. Falkowicz K, Samborski S, Valvo PS. Effects of Elastic Couplings in a Compressed Plate Element with Cut-Out. Materials. 2022; 15(21):7752.

7. Kopecki T, Mazurek P, Lis T. Experimental and Numerical Analysis of a Composite Thin-Walled Cylindrical Structures with Different Variants of Stiffeners, Subjected to Torsion. Materials. 2019; 12(19):3230.

8. Singer J, Arbocz J, Weller T. Buckling experiments: experimental methods in buckling of thin-walled structures. Chichester; New York: Wiley; 1998.

9. Banat D, Mania RJ. Progressive failure analysis of thin-walled Fibre Metal Laminate columns subject-ed to axial compression. Thin-Walled Structures. 2018;122:52–63.

10. Banat D, Mania RJ. Failure assessment of thin-walled FML profiles during buckling and post-buckling response. Composites Part B: Engineering. 2017;112:278–89.

11. Debski H, Rozylo P, Gliszczynski A, Kubiak T. Numerical models for buckling, postbuckling and failure analysis of pre-damaged thin-walled compo-site struts subjected to uniform compression. Thin-Walled Structures. 2019;139:53–65.

12. Rozylo P, Falkowicz K, Wysmulski P, Debski H, Pasnik J, Kral J. Experimental-Numerical Failure Analysis of Thin-Walled Composite Columns Using Advanced Damage Models. Materials. 2021; 14(6):1506.

13. Debski H, Teter A, Kubiak T. Numerical and experimental studies of compressed composite columns with complex open cross-sections. Compo-site Structures. 2014;118:28–36.

14. Rozylo P, Debski H, Wysmulski P, Falkowicz K. Numerical and experimental failure analysis of thin-walled composite columns with a top-hat cross section under axial compression. Composite Structures. 2018;204:207–16.

15. Vannucci P. Anisotropic Elasticity [Internet]. Sin-gapore: Springer Singapore; 2018. (Lecture Notes in Applied and Computational Mechanics; t. 85). http://link.springer.com/10.1007/978-981-10-5439-6

16. Ribeiro ML, Vandepitte D, Tita V. Damage Model and Progressive Failure Analyses for Filament Wound Composite Laminates. Appl Compos Ma-ter. 2013;20(5):975–92.

17. Jonak J, Karpiński R, Wójcik A, Siegmund M. The Influence of the Physical-Mechanical Parameters of Rock on the Extent of the Initial Failure Zone un-der the Action of an Undercut Anchor. Materials. 2021;14(8):1841.

18. Jonak J, Karpiński R, Siegmund M, Wójcik A, Jonak K. Analysis of the Rock Failure Cone Size Relative to the Group Effect from a Triangular Anchorage System. Materials. 2020;13(20):4657.

19. Kowal M, Rozylo P. Effect of bond end shape on CFRP/steel joint strength. Composite Structures. 2022;284:115186.

20. Bulzak T, Winiarski G, Wójcik Ł, Szala M. Application of Numerical Simulation and Physical Mod-eling for Verifying a Cold Forging Process for Rotary Sleeves. J of Materi Eng and Perform. 2022; 31(3):2267–80.

21. Rogala M, Ferdynus M, Gawdzińska K, Kochmański P. The Influence of Different Length Aluminum Foam Filling on Mechanical Behavior of a Square Thin-Walled Column. Materials. 2021;14(13):3630.

22. Ferdynus M, Szklarek K, Kotełko M. Crashworthiness performance of thin-walled hollow and foam-filled prismatic frusta, Part 2: Experimental study. Thin-Walled Structures. 2022;181:110070.

23. Paśnik J, Samborski S, Rzeczkowski J. Application of the CZM Technique to Delamination Analysis of Coupled Laminate Beams. IOP Conf Ser: Mater Sci Eng. 26 października 2018;416:012075.

24. Falkowicz K. Numerical Investigations of Perforated CFRP Z-Cross-Section Profiles, under Axial Compression. Materials. 2022;15(19): 6874.

25. Falkowicz K. Numerical analysis of behaviour of compressed thin-walled Z-profiles weakened by holes. Kulisz M, Szala M, Badurowicz M, Cel W, Chmielewska M, Czyż Z, i in., redaktorzy. MATEC Web Conf. 2019;252:07010.

26. Falkowicz K. Stability Analysis of Thin-Walled Perforated Composite Columns Using Finite Element Method. Materials. 2022;15(24):8919.

27. Falkowicz K. Numerical Buckling Analysis of Thin-Walled Channel-Section Composite Profiles Weakened by Cut-Outs. Adv Sci Technol Res J. 2022;16(6):88–96.

28. Debski H, Rozylo P, Wysmulski P, Falkowicz K, Ferdynus M. Experimental study on the effect of eccentric compressive load on the stability and load-carrying capacity of thin-walled composite profiles. Composites Part B: Engineering. 2021;226:109346.

29. Wysmulski P, Debski H, Falkowicz K. Sensitivity of Compressed Composite Channel Columns to Eccentric Loading. Materials. 2022;15(19):6938.

30. Falkowicz K, Valvo P. Influence of Composite Lay-Up on the Stability of Channel-Section Pro-files Weakened by Cut-Outs – A Numerical Investigation. Adv Sci Technol Res J. 2023;17(1):108–15.

31. Kubiak T. Static and Dynamic Buckling of Thin-Walled Plate Structures [Internet]. Heidelberg: Springer International Publishing; 2013. http://link.springer.com/10.1007/978-3-319-00654-3

32. Wysmulski P. Non-linear analysis of the postbuckling behaviour of eccentrically compressed compo-site channel-section columns. Composite Structures. 2023;305:116446.

Katarzyna Falkowicz: https://orcid.org/0000-0002-3007-1462

USING COMPUTER TECHNIQUE FOR DEVELOPING METHOD
FOR VIBRATION DAMAGE ESTIMATION
UNDER COMBINED RANDOM AND DETERMINISTIC LOADING

Michał PTAK*, Jerzy CZMOCHOWSKI*

*Department of Machine Design and Research, Wroclaw University of Technology and Science,
ul. Ignacego Łukasiewicza 7/9, 50-371 Wrocław, Poland

michal.ptak@pwr.edu.pl, jerzy.czmochowski@pwr.edu.pl

Abstract: This paper is focusses on developing a novel method for vibration damage estimation for military helicopters, fighter aircrafts and any other aircraft exposed to combined stochastic and deterministic loading. The first stage of the research focused on frequency domain damage prediction, which is the legacy method proposed by Bishop and developed by Sweitzer, Schlesinger, Woodward, Kerr, Murthy, Datta and, Atkins. The mentioned frequency domain-based method is used in commercial software, e.g., MSC CAE Fatigue. Frequency domain damage prediction is based on superposition of spectral moments and Dirlik method of Rainflow Cycle Counting algorithm in frequency domain. The first phase of the research showed the legacy algorithm based on transfer function developed using FEM (Finite Element Method) method in Abaqus environment and is very conservative. The second stage of the research aims to develop a novel method which allowing for more robust and accurate damage estimation. For this purpose, the Monte Carlo method for retrieving random signal in the time domain from signal in frequency domain was used. To obtain the system transfer function, – the 1 g load harmonic system response was obtained using FEM analysis. It was subsequently scaled linearly by the PSD input curve for random loading and sine wave, or sine sweep function for deterministic loading to calculate the cumulative system response of the linear system. The research allows the development of a novel method to precisely estimate vibration damage using combined time and frequency domains approach, based on effective frequency domain FEM   analysis of the linear system. The new proposed method can be also used for precise replication of test conditions via considering signal clipping and frequency resolution used for real testing.

Key words: vibration damage, random vibration, FEM, Monte Carlo method, frequency, time domain Rainflow Cycle Counting algorithms

1. INTRODUCTION

Rainflow Cycle Counting algorithm in frequency domain is commonly used for vibration damage estimation under stochastic loading of linear systems in synergy with FEM analysis. A precursor of Rainflow Cycle Counting algorithm in frequency domain was the study of Bendat and Rice [1–4], whose authors provided a method for use in narrow band signals. The next milestone was the development of the Rainflow Cycle Counting algorithm in the frequency domain made by Dirlik, using Monte Carlo method 5. This approach is now considered one of the most accurate techniques used in commercial software applications [6, 7] for assessment of damage under random loading. Other researchers were Lalanne [8–10] and Steinberg 11, who provided their methods for Rainflow Cycle Counting in the frequency domain. All aforementioned methods have been tested by Halfpenny [12–14], albeit only for evaluation of damage under pure stochastic loading.

The aforementioned methods have been developed for vibration damage estimation for purely stochastic loading. However, these methods have been adopted for more general usage i.e. damage estimation under combined stochastic and deterministic loading in the studies of Bishop, Sweitzer, Schlesinger, Woodward, Kerr, Murthy, Datta and Atkins in their publications [15–24]; and the loading scenario for using this method is e.g. simultane-ous deterministic sine sweep and random load – as can be seen in Fig. 1. This combination is required by the US Department of Defence Test Method Standard 27 or other specific requirement specified by military aircraft manufacturers.

The first stage of research introduced in this paper shows that using the abovementioned methods has resulted in highly conservative damage results.

The second stage of research was the development of a novel method for precise damage estimation under combined loads, and this method introduces combined frequency and time domain calculation instead of using only frequency domain for vibration damage estimation in the legacy method. Superposition of the stochastic and deterministic loading approaches has been introduced by NASA 28. The novel method presented in this paper assumes an extension of this approach for analysis of the PSD Response of the system, realising the stochastic and deterministic signals' superposition and damage analysis by use of the Monte Carlo method. The novel method introduced in this paper is much more accurate, as well as offers an opportunity to replicate test parameters e.g., clipping the stochastic signal at a considered sigma level. Additionally, this method allows consideration of the large population of time series to assess the damage distribution for a considered PSD input curve.

In this paper, for combined loads, a simultaneous deterministic linear sine sweep was used (which represents, e.g. shooting with the variable firing gun installed on an aircraft or helicopter),

and stochastic loads were defined with the use of a PSD input curve (Fig. 1), which represents normal operating dynamic loading, e.g. turbulences.

The novel technique introduced in this paper expands research carried out by Dirlik in consideration of frequency resolution, populational studies [27, 28], combination stochastic and deterministic loading, and additionally uses FEM for transfer function estimation.
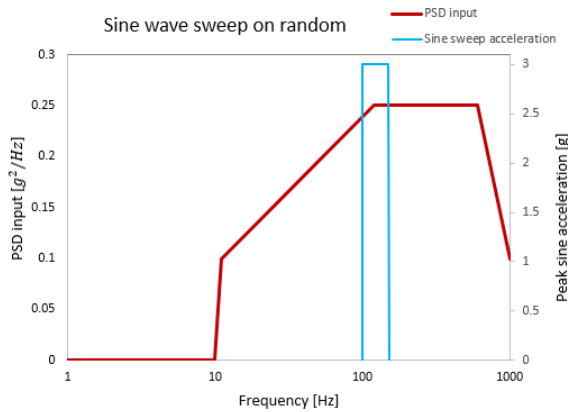

Fig. 1. Sine waves sweep simultaneous with random background

2. FREQUENCY DOMAIN VIBRATION DAMAGE ESTIMATION

Vibration damage assessment, based on transfer function of system, was derived using the mode superposition method in Abaqus environment. The PSD Response functions were founded based on a complex stress tensor (that assumed real and imaginary values), and are used for the evaluation of Huber–Mises–Hencky (σHMH) stress based on Eq. 1:

$$\sigma_{HMH} = \frac{1}{2}[(\sigma_{11} - \sigma_{22})^2 + (\sigma_{22} - \sigma_{33})^2 + (\sigma_{11} - \sigma_{33})^2 + 6(\sigma_{23}^2 + \sigma_{31}^2 + \sigma_{12}^2)] \quad (1)$$

where each stress tensor component is evaluated as shown in Eq. 2:

$$\sigma_{ij} = Re(\sigma_{ij}) + Im(\sigma_{ij}) \quad (2)$$

where $Re(\sigma_{ij})$ is the real part of stress tensors, and $Im(\sigma_{ij})$ the imaginary part.

The equivalent stress has been used for demonstration of the algorithm; additionally, this approach is widely used in related publications [12–14, 30, 31], and commercial software applications such as nCode 7 and MSC CAE Fatigue 6, for isotropic material. Future research will focus also on developing algorithms by means of using the Critical Plane approach, which is treated as a more robust approach [6, 7, 30. 31]; however, such an approach would be much more computationally expensive.

It needs to be noted that the original development of this method in the present study is intended for application concerning isotropic, metallic material; any other consideration with reference to usage of this method for orthotropic material will be a subject of future research.

Additionally, the aforementioned further research will focus also on the possibility for using the proposed method in such a way that synergy with the energetic fracture mechanics model is achieved, as can be observed in relevant studies comprised in the literature [32–34], where the Cohesive Zone Model has been used

for assessing damage and life prediction.

The derived transfer function H(f) was then multiplied by the PSD input G(f) defined for the considered test duty, and resultantly the PSD Response function in frequency (see Fig. 2) domain was obtained, as indicated in Eq.   (3).
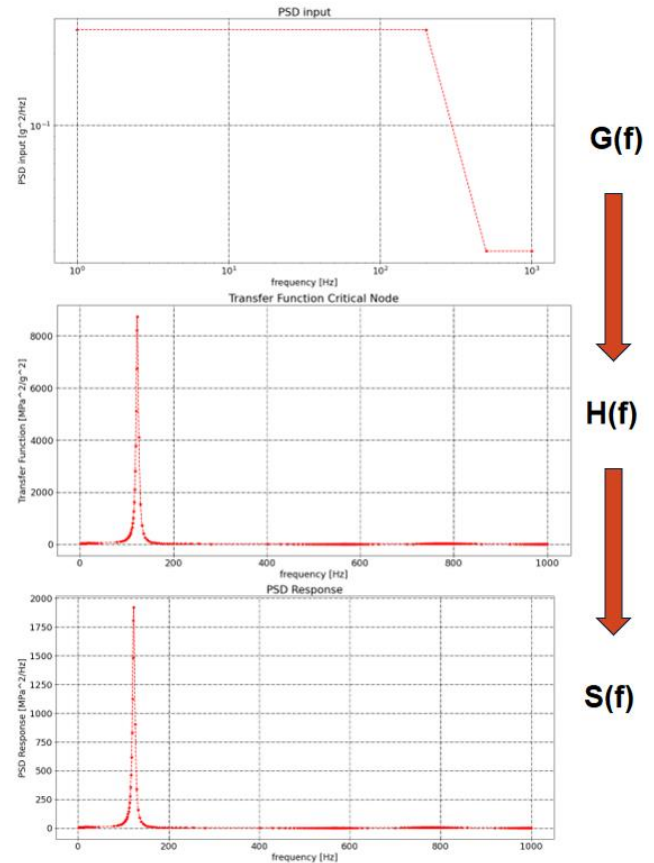
$$S(f) = H(f) \cdot G(f) \quad (3)$$

Fig. 2. Evaluation of the PSD Response workflow based on PSD input load and Transfer Function of the considered unit

The PSD Response function has been derived for each integration point of the discrete model. Spectral analysis was the next step to be based on the PSD Response of the considered unit, and it involved numerical integration of the 0th, 1st, 2nd and 4th spectral moments (m_n) in the frequency domain, based on Eq.   (4):

$$m_n = \int_0^\infty f^n \cdot S(f) df \quad (4)$$

where m_n represents the n spectral moment, f the considered frequency and $S(f)$ the PSD Response function.

Spectral moments are used for derivation of signal statistic parameters in frequency domain:

Upward zero crossing ($E[0]$) – Eq.   (5):

$$E[0] = \sqrt{\frac{m_2}{m_0}} \quad (5)$$

where m_2 stands for the second spectral moment and m_0 the zero spectral moment.

Number of peaks ($E[P]$) (local maximum of signal function) – Eq. (6):

Michał Ptak, Jerzy Czmochowski
Using Computer Technique for Developing Method for Vibration Damage Estimation under Combined Random and Deterministic Loading

DOI 10.2478/ama-2023-0065

$$E[P] = \sqrt{\frac{m_4}{m_2}} \tag{6}$$

where m_4 stands for the fourth spectral moment.

Irregular factor (γ) – Eq. (7):

$$\gamma = \frac{m_2}{\sqrt{m_0 \cdot m_4}} \tag{7}$$

Signal statistic parameters in frequency domain constitute the basis for the Dirlik method of executing the Rainflow Cycle Counting algorithm in frequency domain, as can be ascertained from the studies of Dirlik 5 and Bishop et al. 19.

The Probability Density Function (PDF) of Dirlik method (PDFD) can be written in the form indicated by Eq. (8):

$$PDFD = \left(\frac{D_1}{Q} e^{\frac{Z}{Q}} + \frac{D_2 Z}{R^2} e^{\frac{-Z^2}{2R^2}} + D_3 Z e^{\frac{-Z^2}{2}} \right) \cdot \frac{dS}{2RMS} \tag{8}$$

where the normalised Dirlik stress variable is represented by Z (Note: The value of the Dirlik normalised stress variable is twice that of the Bendat normalised stress variable.); as indicated in Eq. (9),

$$Z = \frac{S}{2\sqrt{m_0}} \tag{9}$$

where S is the stress at the considered histogram bin.

The "mean frequency" (X_m) would be as presented in Eq. (10):

$$X_m = \frac{m_1}{m_0} \cdot \sqrt{\frac{m_2}{m_4}} \tag{10}$$

Expressions of the remaining Dirlik empirical variables (D_1, D_2, D_3, Q and R) are presented in Equations (11)–(15):

$$D_1 = \frac{2(X_m - \gamma^2)}{1 + \gamma^2} \tag{11}$$

$$D_2 = \frac{1 - \gamma - D_1 + D_1^2}{1 + \gamma^2} \tag{12}$$

$$D_3 = 1 - D_1 - D_2 \tag{13}$$

$$Q = \frac{1.25 \cdot (\gamma - D_2 \cdot R - D_3)}{D_1} \tag{14}$$

$$R = \frac{\gamma - X_m - D_1^2}{1 - \gamma - D_1 + D_1^2} \tag{15}$$

The final equation for estimation of the actual number of cycles with the use of the Dirlik method (n_{Dirlik}) can be presented as indicated in Eq. (16):

$$n_{Dirlik} = PDFD(S) \cdot T \cdot E[P] \tag{16}$$

where T is the time of exposure on random loading.

Total damage was evaluated using the Palmgren-Miner rule 37 and the failure criterion equivalent to damage value exceeds 1, as indicated in Eq. (17):

$$\text{Total Damage} = \sum_{0}^{\infty} \frac{n_{i\_Dirlik}}{N(S_i)} \tag{17}$$

where n_{i_Dirlik} is the actual number of cycles for the considered stress at bins, and $N(S_i)$ the allowable number of cycles for the considered stress at bins, based on S-N curve (fatigue curve – stress versus available cycles).

As part of the present research, the authors created a tool for damage estimation using an exemplary unit for benchmarking against commercial software. Fatigue damage estimation is based on FEM analysis 39 unit loading with the use of a linear dynamic method in an Abaqus software application 40. This research used the example of a cantilever beam with a cut U notch. The geometry, discrete model and graphical support representation are presented in Fig. 3. The harmonic load input is a unit load (1 g) acceleration applied to the base (supported region).
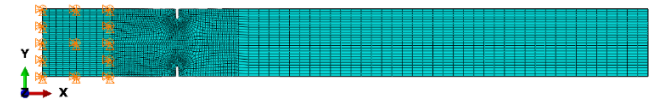

Fig. 3. Geometry, discrete model and graphical support representation of a sample taken for the research results' visualisation

For this paper, it is assumed that the sample is made of steel 17-4PH (H1025), and accordingly, fatigue material properties from MMPDS-15 31 were used; thus, for the considered steel sample, a value of Kt = 3 was used as the reference.

Tab. 1. Steel 17-4PH (H1025) material properties used for demonstrational analysis

Steel 17-4PH (H1025)		
Young modulus E [MPa]	Poisson ratio v [–]	Density ρ [t/mm³]
195,000	0.27	7.89E–09

To enable an effective consideration of the aforementioned factors, the authors of the present study assumed a constant critical damping ratio for the entirety of the frequency bandwidth (0–1,000 Hz) and equal to 2.5%. (Note that the created method and software need input, which would need to consist of a model correlated against test results; however, for benchmarking, we assumed artificial parameters of damping.)
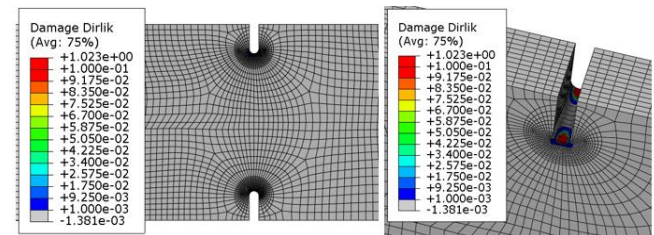

Fig. 4. Frequency domain vibration damage estimation using Dirlik method
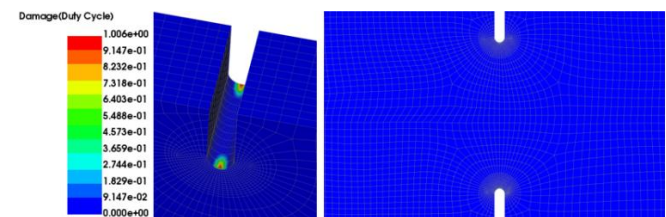

Fig. 5. Visualisation of Dirlik Damage obtained in MSC CAE Fatigue commercial software environment

Damage results can then be presented on a discrete model using Abaqus 40 visualisation module and the authors' scripts, as demonstrated in Fig. 4.

For the considered method, benchmarking has been made against the MSC CAE Fatigue software. An exemplary result for duty matched to the above example is presented in Fig. 5.

The obtained damage values have been benchmarked against commercial software and the differences in results do not exceed 1%. This result is the basis for the first stage of the research – damage estimation for combined stochastic and deterministic loading in frequency domain.

3. FREQUENCY DOMAIN VIBRATION FATIGUE ESTIMATION UNDER COMBINED STOCHASTIC AND DETERMINISTIC LOADING – THE LEGACY METHOD

The methodology introduced in Section 2 of this paper is the basis for damage estimation under only stochastic loading. Research carried out by Bishop, Sweitzer, Schlesinger, Woodward, Kerr, Murthy, Datta and Atkins in their publications [15–24] describe the idea for damage estimation based on superimposition of spectral moments generated by random and deterministic loads. The abovementioned approach was used in these studies.

The transfer function $(Hi(f))$, which consists of e.g. Huber–Mises–Hencky complex stress or critical plane stress, needs to be evaluated for finite i numbers of frequency sub-ranges, e.g. for a sweep between 100 Hz and 150 Hz, there is a need for the evaluation to be conducted in consideration of a sub-ranges' size of e.g. 0.1 Hz. For each sub-range, a single sine wave is considered, and signal statistic needs to be introduced.

The response function $S(f)$ is then evaluated based on the transfer function H(f), and the sine sweep amplitude (G(f)), as indicated in Eq. (18).

$$S_i(f_i) = \sqrt{H_i(f_i)} \cdot G_i(f_i) \tag{18}$$

The root mean square (RMS) of a single sine wave can then be evaluated, as indicated in Eq. (19).

$$RMS = \frac{\sqrt{2}}{2} \cdot S_i(f_i) \tag{19}$$

The next step is evaluation of spectral moments for every considered single sine wave function using the following equations for the 0th, 1st, 2nd and 4th spectral moments [Equations (20)–(23)]:

$$m_{0\_sine\_wave}(f_i) = RMS^2 \tag{20}$$

$$m_{1\_sine\_wave}(f_i) = m_0(f_i) \cdot f_i \tag{21}$$

$$m_{2\_sine\_wave}(f_i) = m_0(f_i) \cdot f_i^2 \tag{22}$$

$$m_{4\_sine\_wave}(f_i) = m_0(f_i) \cdot f_i^4 \tag{23}$$

where f_i represents the considered frequency.

Signal statistic in frequency domain was based on spectral analysis made iteratively for the considered frequency sub-ranges e.g., 0.1 Hz sub-ranges' width. Spectral moments from deterministic loading $(m_{0\_sine\_wave}, m_{1\_sine\_wave}, m_{2\_sine\_wave}, m_{4\_sine\_wave})$ need to be summed with spectral moments from stochastic background (m_0, m_1, m_2, m_4) as introduced in Equa-

tions (24)–(27).

$$m_{0\_mixed\_mode}(f_i) = m_0 + m_{0\_sine\_wave}(f_i) \tag{24}$$

$$m_{1\_mixed\_mode}(f_i) = m_1 + m_{1\_sine\_wave}(f_i) \tag{25}$$

$$m_{2\_mixed\_mode}(f_i) = m_2 + m_{2\_sine\_wave}(f_i) \tag{26}$$

$$m_{4\_mixed\_mode}(f_i) = m_4 + m_{4\_sine\_wave}(f_i) \tag{27}$$

where $m_{0\_mixed\_mode}(f_i)$, $m_{1\_mixed\_mode}(f_i)$, $m_{2\_mixed\_mode}(f_i)$ and $m_{4\_mixed\_mode}(f_i)$ are, respectively, the spectral 0th, 1st, 2nd and 4th moments for superimposed signal at the considered frequency.

It is also required to be noted that during superposition, the spectral moment sum used the full moment from the stochastic part of duty (m_0, m_1, m_2, m_4), as the allowable number of cycles is also calculated iteratively for the considered T_i, which is equal to total time (T_{Total}) divided by the number of sub-ranges; as indicated in Eq. (28),

$$T_i = \frac{T_{Total}}{n} \tag{28}$$

where n is the number of sub-ranges.

So far as Rainflow Cycle Counting in frequency domain was concerned, the same was evaluated with the use of Dirlik or Narrow Band method, or alternatively damage evaluation was provided for each of the sub-ranges in the same way as introduced in Section 2 of this paper, that is to say by expressing the number of actual cycles according to the Dirlik Rainflow Cycle Counting in frequency domain (n_i); as indicated in Eq. (29),

$$n_i = PDF_i(S) \cdot T_i \cdot E_i[P] \tag{29}$$

where $PDF_i(S)$ is the PDF at the considered stress bin, and $E_i[P]$ the number of peaks at the considered stress bin.

The damage value for the considered sub-range (D_i) is as expressed in Eq. (30):

$$D_i = \frac{n_i}{N(S)_i} \tag{30}$$

where $N(S)_i$ is the allowable number of cycles at the considered stress bin based on the considered S-N curve.

The total damage (D_{Total}) under combined stochastic and deterministic loading is the sum of damage from each of the sub-ranges, as indicated in Eq. (31):

$$D_{Total} = \sum_{i=1}^{n} D_i \tag{31}$$

The damage value obtained by the created algorithm has been benchmarked against the damage value obtained using commercial software, and resultant to this benchmarking, a great correlation was obtained (exemplary results have been introduced in Section 5 of this paper).

4. COMBINED FREQUENCY AND TIME DOMAINS VIBRATION DAMAGE ESTIMATION UNDER COMBINED STOCHASTIC AND DETERMINISTIC LOADING – THE NOVEL METHOD

The new original method developed in the present study assumes the need for processing of the combined frequency and time domain consideration for superimposing the stochastic and

sciendo

Michał Ptak, Jerzy Czmochowski
Using Computer Technique for Developing Method for Vibration Damage Estimation under Combined Random and Deterministic Loading

DOI 10.2478/ama-2023-0065

deterministic responses of the considered system. The second stage of the study focussed on developing a novel method for precise vibration damage estimation under combined loading. The idea is based on retrieving time series signal from the frequency domain PSD Response as proposed by Dirlik 5 – with the use of the Monte Carlo method, which is discussed in an extended form in the study of Ptak and Czmochowski 29. The PSD Response function and its corresponding frequency constitute elements of the vector used in retrieval of the time domain signal by employing the inverse discrete Fourier transformation. The equation for time series signal ($S(k\Delta t)$) can be written as follows [Eq. (32)], 5:

$$S(k\Delta t) = \sum_{n=\frac{-N}{2}}^{\frac{N}{2}-1} \theta(j \cdot n2\pi f) \cdot e^{j \cdot 2\pi k_n/N} \qquad (32)$$

where f is the considered frequency and N the natural number.
k can be written in the form of the following Eq. (33):

$$k = 0,1,2,3,\dots,N-1 \qquad (33)$$

The θ function can be written in the form of the following Eq. (34), 42:

$$\theta(j \cdot n2\pi f) = \sqrt{S(n \cdot 2\pi\Delta f)}e^{j\Phi_n} \qquad (34)$$

for n defined as in Eq. (35).

$$n = 0,1,2,3,\dots,N/2-1 \qquad (35)$$

The Φ_n represents a random phase angle, defined as to be uniformly distributed in the bandwidth <–π; π>. To summarise, the time series is obtained using the Monte Carlo approach and inverse discrete Fourier transformation.

The time series signal can be defined by the function $S(k\Delta t)$ and needs to be a real function of time. This is so as for the introduction of information about stress sign for Rainflow Cycle Counting algorithm, which will be omitted if the complex value of this function is not equal to zero. It implies that the spectrum defined by the function θ in Eq. (34) has to exhibit a complex conjugate symmetry as per the following Eq. (36), 42:

$$\theta(j \cdot n2\pi f) = \theta(-j \cdot n2\pi f) \qquad (36)$$

for n defined as in Eq. (35).

A graphical representation of the conjugate symmetry can be found in the figure below (Fig. 6):
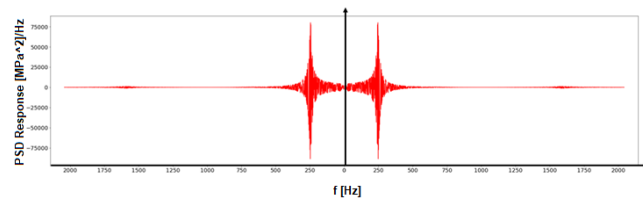

Fig. 6. The complex conjugate symmetry of the PSD Response function

An additional restriction for the θ function is that this function needs to cross zero (37):

$$\theta(0) = 0 \qquad (37)$$

Meeting this condition implies that the signal in the time domain $S(k\Delta t)$ has a mean value equal to zero.

An additional implication is that the imaginary portion of the signal will be equal to zero, and therefore the magnitude of the signal will be equal to the real portion of this signal; and this would

moreover imply that the sign can be saved for further fatigue consideration.

For verification of the obtained signal, we evaluated the RMS of the time series signal S(kΔt) using the standard deviation equation, which can be written as shown below in Eq. (38):

$$\text{RMS}_{\text{time series}} = \sqrt{\frac{1}{N}\sum_{k=0}^{N-1} S(k\Delta t)^2} \qquad (38)$$

The time signal has a zero-mean value, and the standard deviation equal to RMS was estimated for a signal in the frequency domain. Therefore, retrieval of a signal defined in the frequency domain to one in the time domain has been carried out successfully, and this methodology will be used for retrieving the fatigue information by employing time series Rainflow Cycle Counting algorithm, which is implemented in the Python language (as documented 44).

For evaluating the damage in the time domain, the authors of the Rainflow Cycle Counting algorithm have used a Python language program 46, which allows the fatigue cycles to be counted and appropriate range values for time series signal (peak and trough extraction from time series signals) to be ascertained.

Time series signals retrieved from the PSD Response signal with the use of the developed Python algorithms are indicated in Fig. 7 (frequency resolution based on N = 216). Additionally, the Rainflow Cycle Counting histogram for this signal has been introduced in Fig. 8.

Note: In the present research, the stress life method has been introduced as an example. Further research will focus on using the strain life method, and would involve the use of e.g. Morrow or Smith–Watson–Topper mean stress correction and Neuber correction [48–50].
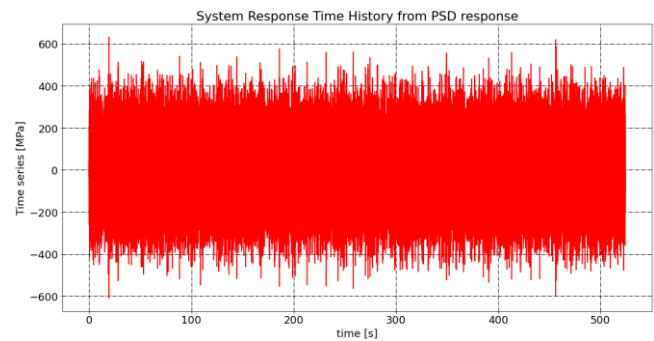

Fig. 7. Initial time series processing extracting peak and trough for Rainflow Counting algorithm, white noise signal, irregular factor 0.3, block size N = 2^16
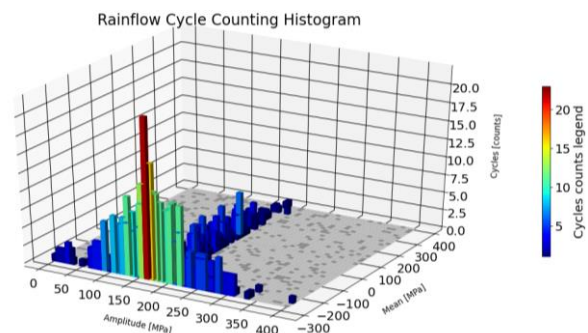

Fig. 8. Rainflow Cycle Counting algorithm histogram, white noise signal, irregular factor 0.3, block size N = 2^16

The specified linear sine sweep frequency ($f_{spec}(t)$) dependence from time can be written as a function of time and frequency, as indicated in Eq. (39):

$$f_{spec}(t) = f_1 + K \cdot T \tag{39}$$

where T is the total sweep time, K the sweep rate and f_1 the initial sweep frequency.

Specified frequency ($f_{spec}(t)$) can be written in an alternative form, as indicated in Eq. (40):

$$f_{spec}(t) = f_1 + (f_2 - f_1)\frac{t}{T} \tag{40}$$

where f_2 is the end sweep frequency and t the time variable.

Sine sweep frequency ($f(t)$) is the integral of specified frequency and can be written as indicated in Eq. (41):

$$f(t) = \int f_{spec}(t)dt = f_1 \cdot t + \frac{f_2 - f_1}{T} \cdot \frac{t^2}{2} \tag{41}$$

Input sine sweep ($G(t)$) with constant acceleration amplitude can be written as indicated in Eq. (42):

$$G(t) = u(t) \cdot \sin(\omega t) = u(t) \cdot \sin(2\pi f(t) \cdot t) \tag{42}$$

where $u(t)$ is the displacement in time and ω the circular frequency.

Additionally, the equivalent version for implementation in the Python programming language 44 can be written as indicated in Eq. (43):

$$G(t) = u(t) \cdot \sin\left(2\pi \cdot t \cdot \left(f_1 + \frac{f_2 - f_1}{T} \cdot \frac{t}{2}\right)\right) \tag{43}$$

As the sine sweep frequency is deterministic, that is to say since it depends on time, the same can thus be scaled by the transfer function H(f) to obtain a time series sweep including the system response, as indicated in Fig. 9.
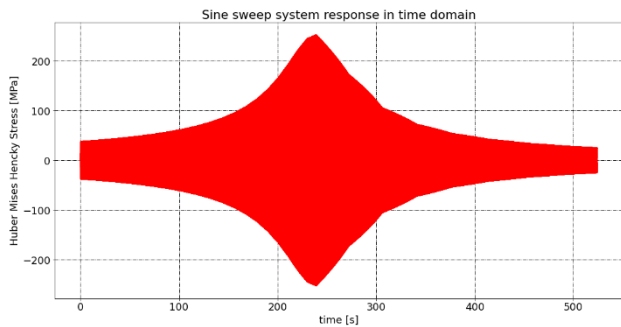

Fig. 9. Sine sweep system response in the time domain,
sweep rate K = 0.095367 Hz/s

Sine sweep response ($S(t)$) can be written as indicated in Eq. (41):

$$S(t) = \sqrt{H(t)} \cdot G(t) \tag{44}$$

where H(f) is the transfer function and G(t) the input sine sweep acceleration.

This signal, which consists of the PSD Response stress values, can now be superimposed to the random time series PSD Response retrieved using the Monte Carlo method (assuming system linearity, with a restriction pertaining to the time sequence of the retrieved random signal needing to match with the time sequence of the sine sweep) – as can be seen from Fig. 10.

For the superimposed signal corresponding to the Rainflow Cycle Counting algorithm in the time domain to be capable of being used, the S–N curve for the stress life method needs to be introduced, and it is only then that the damage for the combined stochastic–deterministic input can be evaluated.

It also needs to be noticed that sweep rate can be fitted to background random loading to obtain one sweep during acting random loading if there is no specific requirement specified by the aircraft manufacturer.
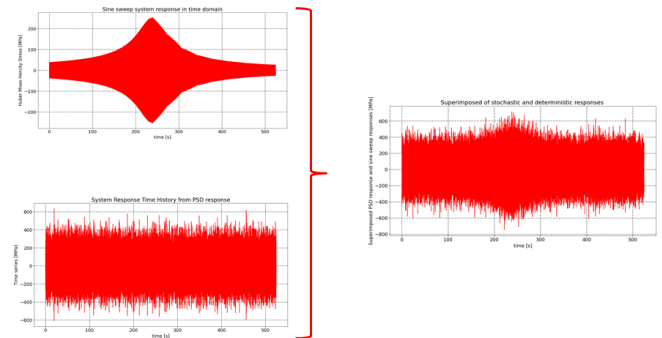

Fig. 10. Superimposition of stochastic and deterministic responses
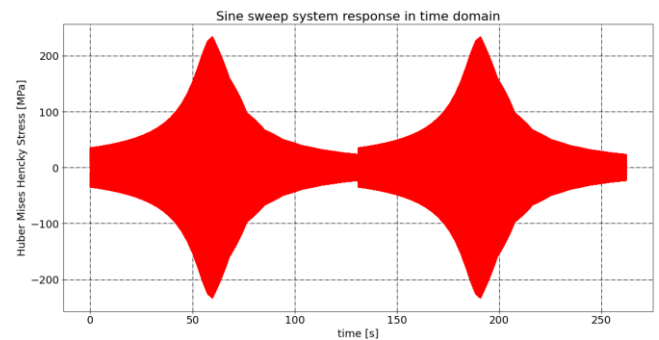in the time domain

Fig. 11. Sine sweep system response in the time domain,
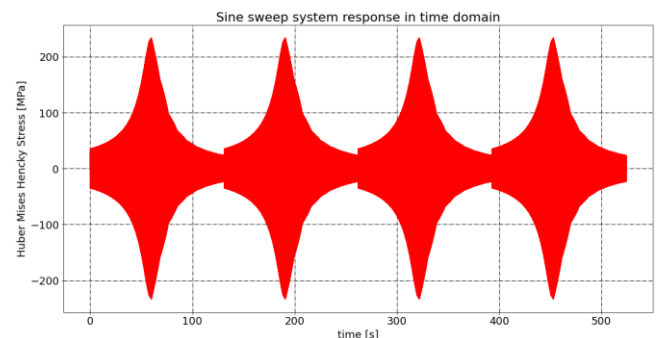sweep rate K·2 = 0.190735 Hz/s

Fig. 12. Sine sweep system response in the time domain,
sweep rate K·4 = 0.38147 Hz/s

It has been ascertained that n number of sine sweeps with n times higher than the reference sweep rate (Fig. 11 for n = 2 and Fig. 12 for n = 4) cause the same theoretical damage as one sweep with the reference sweep rate. For benchmark signals have been merged in a theoretical way, there is no continuous link between sweeps; however, the impact on the quoted damage is negligible as the maximum stress cycles for the considered sam-

sciendo

Michał Ptak, Jerzy Czmochowski   DOI 10.2478/ama-2023-0065
Using Computer Technique for Developing Method for Vibration Damage Estimation under Combined Random and Deterministic Loading

ples are much higher than those in the link region. It needs to be noticed that only one sweep acting during random loading duration should give the highest damage as increasing the sweep rate can cause a situation wherein the system will not respond with full amplitude during the resonance and the maximum resonance amplitude will decrease.

A proposed algorithm flow chart for damage estimation under combined stochastic and deterministic loading in the time domain is presented in Fig. 13.
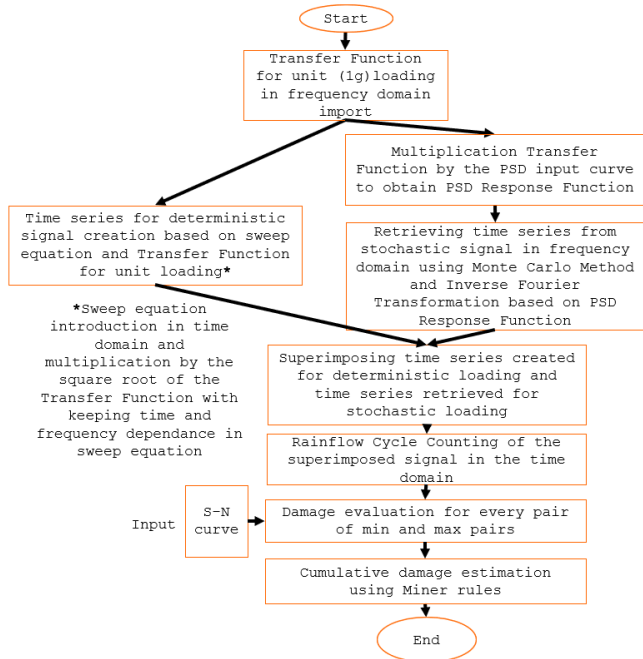

Fig. 13. Algorithm flow chart for damage estimation under combined stochastic and deterministic loading in the time domain

5. COMPARISON RESULTS OBTAINED FOR LEGACY METHOD AND PROPOSED METHOD

The abovementioned legacy method for combined stochastic–deterministic loading proved to be highly conservative. Two loops of analysis under vibration loading were calculated. The 1st loop, based on algorithms for vibration damage estimation under deterministic loading (pure sine sweep), obtained a damage value of 0.009 for the critical integration point. The 2nd loop was based on algorithms for combined stochastic–deterministic loading and a low-level non-damaging random load (giving rise to a damage of 0 after evaluation using the algorithm for pure random loading and peaking at 9 MPa in the case of a stress of 5 σ). For the combined load scenario, a damage of 0.58 was calculated for the same sine sweep as in the 1st loop (resulting in a damage of 0.009). The results above have shown that the legacy approach is characterised by a high conservatism and have initialised the subsequent phase of our research. A summary of the obtained result is provided in Tab. 2.

Note: Even when assuming that maximum stress from resonance for sine sweep (258 MPa) occurs for every cycle in sweep (conservatively assuming that the maximum peak in a resonance occurs through 50 Hz) and superimposing a 5 σ stress amplitude equal to 9 MPa, the damage obtained is equal to 0.21.

The research results show that the legacy method is highly conservative, and therefore the need arises for developing a new method for this loading scenario, to remove the conservativism during damage estimation. This is important from the point of view of requirements associated with aerospace, especially for military application, where e.g., the mass of the components can be reduced.

Tab. 2. Comparison damage evaluated with spectral method in the frequency domain (legacy method) and new proposed method (damage evaluated in the time domain)

Test No.	1	2
Damage proposed method	0.00875	0.06718
Damage legacy method authors algorithm for combined loading	0.58110	1.00792
Damage legacy method MSC CAE Fatigue algorithm for combined loading	0.60804	1.07479
Damage for sine sweep only using authors algorithm for deterministic harmonic loading	0.00875	0.00875
Damage for sine sweep only using authors algorithm for deterministic harmonic loading	0.00944	0.00944

6. ADDITIONAL RESULTS DERIVED FROM RESEARCH ON PROPOSED METHOD

Results derived from research on the pure stochastic loading scenario show that damage varies, and the variation depends on the block size (N) used in the inverse Fourier transformation. Since there was a need for obtaining information about the statistic of the damage as well as for deriving the damage distribution, the research has been extended to a large search population consisting of 5,000 samples.

The research was performed for white noise signal. Wide and narrow band signals will be introduced in further research. Additionally introduced were three different block sizes: 212, 214 and 216. For fitting distribution, we used the Kolmogorov–Smirnov criterion, which assesses the probability of distribution. For testing, we used the different distribution types available in the Python library 44. The best-fitted distributions have been narrowed down to three with the highest probability of fitting: Gaussian, Exponentiated Weibull and Generalized Extreme Value distributions.

Note that variation of damage for the considered distribution is low as per Tabs. 3–8.

In Fig. 14, Fig. 16 and Fig. 18, corresponding damage values were presented for the searched population for white noise signal for three mentioned block sizes for signal clipped at 3 standard deviation. Proceeding based on analogy, the same results for signal clipped at 5 standard deviation have been presented in Fig. 20, Fig. 22 and Fig. 24.

The best-fitted distributions' visualisations for signal clipped at 3 standard deviation for three block sizes have been presented in Fig. 15, Fig. 17 and Fig. 19. Proceeding based on analogy, the results for signal clipped at 5 standard deviation have been presented in Fig. 21, Fig. 23 and Fig. 25.

In Tab. 3–Tab. 5, we introduced a populational research results' summary made for white noise signal clipped at 3 standard deviation and in Tab. 6–Tab. 8 a summary of results for signal clipped at 5 standard deviation.
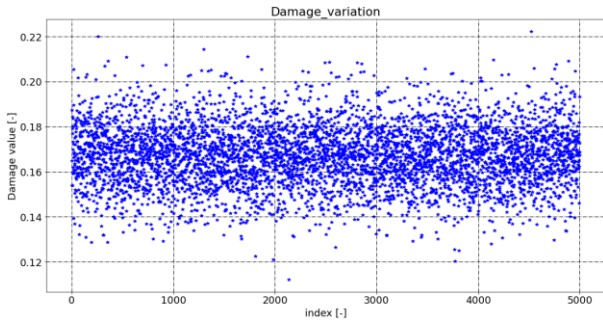
Fig. 14. Damage values for searched population for white noise signal, signal clipped at 3 standard deviations, block size $N = 2^{12}$
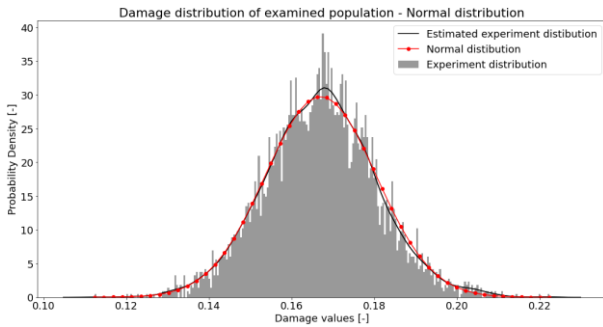

Fig. 15. Best-fitted distribution for damage values for searched population for white noise signal, signal clipped at 3 standard deviations, block size $N = 2^{12}$ – Normal distribution

Tab. 3. Statistical parameters for white noise signal clipped at 3 standard deviations, block size $N = 2^{12}$

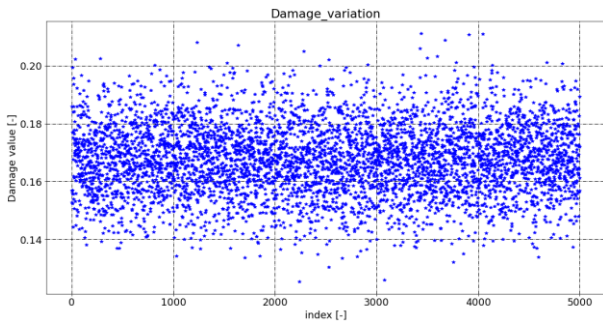| Distribution type	Normal	Exponentiated Weibull	Generalized Extreme Value
Probability of fitted distribution [-]	0.27452	0.00000	0.00091
Mean damage [-]	0.16697	0.15973	0.16708
Standard deviation of damage [-]	0.01341	0.04217	0.01380
0.13% not lower than quoted value of damage [-]	0.12660	0.11231	0.13093
99.73% not exceed quoted value of damage [-]	0.20427	0.33518	0.20641

Fig. 16. Damage values for searched population for white noise signal, signal clipped at 3 standard deviations, block size $N = 2^{14}$

Fig. 17. Best-fitted distribution for damage values for searched population for white noise signal, signal clipped at 3 standard deviations, block size $N = 2^{14}$ – Exponentiated Weibull distribution

Tab 4. Statistical parameters for white noise signal clipped at 3 standard deviations $N = 2^{14}$

Distribution type	Normal	Exponentiated Weibull	Generalized Extreme Value
Probability of fitted distribution [-]	0.80900	0.90471	0.05506
Mean damage [-]	0.16763	0.16763	0.16768
Standard deviation of damage [-]	0.01217	0.01217	0.01235
0.13% not lower than quoted value of damage [-]	0.13098	0.13269	0.13450
99.73% not exceed quoted value of damage [-]	0.20149	0.20201	0.20164

Fig. 18. Damage values for searched population for white noise signal, signal clipped at 3 standard deviations, block size $N = 2^{16}$
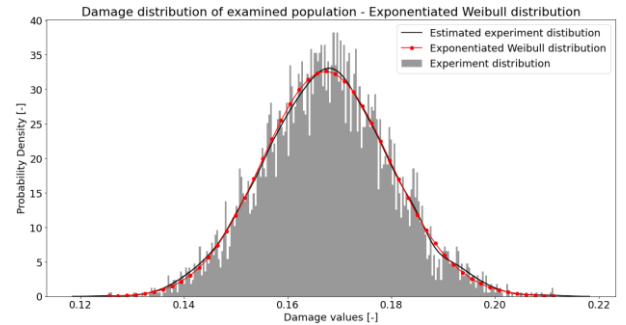

Fig. 19. Best-fitted distribution for damage values for searched population for white noise signal, signal clipped at 3 standard deviations, block size $N = 2^{16}$ – Exponentiated Weibull distribution

Michał Ptak, Jerzy Czmochowski

Using Computer Technique for Developing Method for Vibration Damage Estimation under Combined Random and Deterministic Loading

DOI 10.2478/ama-2023-0065

Tab. 5. Statistical parameters for white noise signal clipped at 3 standard deviations N $= 2^{16}$

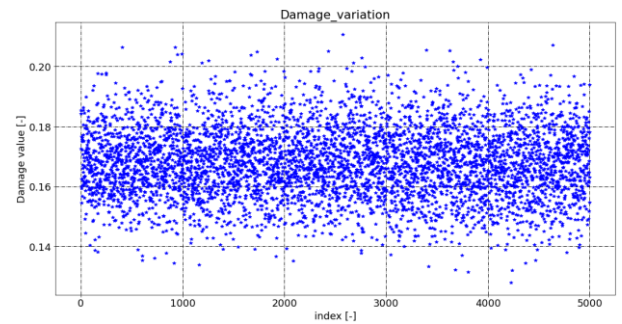| Distribution type	Normal	Exponentiated Weibull	Generalized Extreme Value
Probability of fitted distribution [-]	0.49042	0.99708	0.26514
Mean damage [-]	0.16785	0.16783	0.16789
Standard deviation of damage [-]	0.01161	0.01162	0.01175
0.13% not lower than quoted value of damage [-]	0.13287	0.13473	0.13660
99.73% not exceed quoted value of damage [-]	0.20016	0.20152	0.20064

Fig. 20. Damage values for searched population for white noise signal, signal clipped at 5 standard deviations, block size N $= 2^{12}$
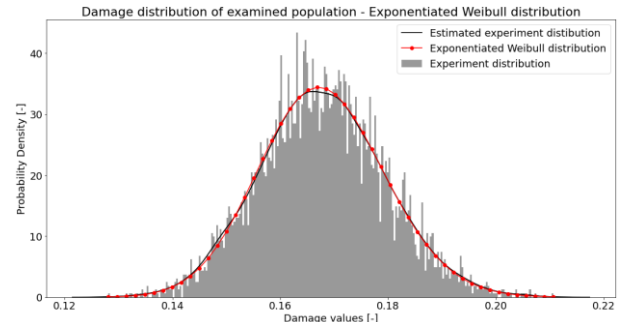

Fig. 21. Best-fitted distribution for damage values for searched population for white noise signal, signal clipped at 5 standards deviations, block size N $= 2^{12}$ – Generalized Extreme Value distribution

Tab. 6. Statistical parameters for white noise signal clipped at 5 standard deviations, block size N $= 2^{12}$

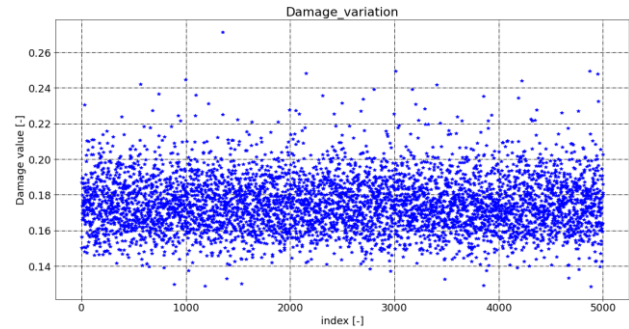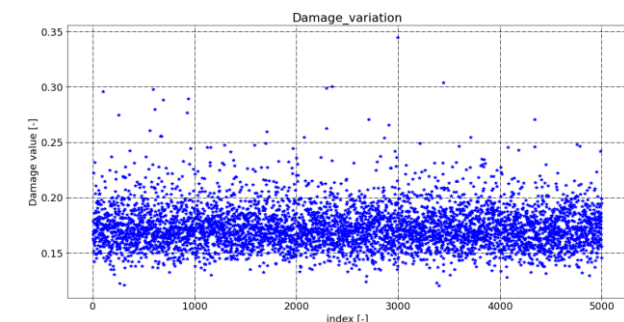| Distribution type	Normal	Exponentiated Weibull	Generalized Extreme Value
Probability of fitted distribution [-]	0.00000	0.00001	0.00049
Mean damage [-]	0.17292	0.17277	0.17313
Standard deviation of damage [-]	0.01933	0.01827	0.01932
0.13% not lower than quoted value of damage [-]	0.11472	0.12702	0.13327
99.73% not exceed quoted value of damage [-]	0.22669	0.23245	0.24754

Fig. 22. Damage values for searched population for white noise signal, signal clipped at 5 standard deviations, block size N $= 2^{14}$
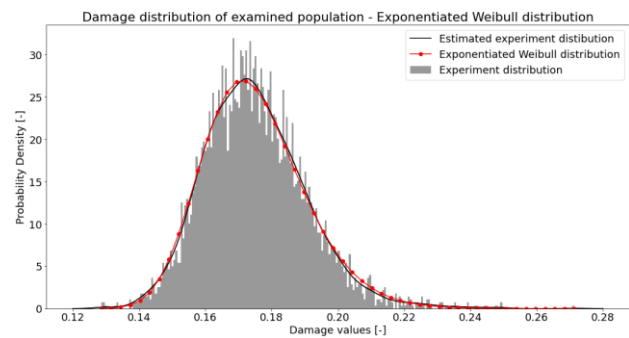

Fig. 23. Best-fitted distribution for damage values for searched population for white noise signal, signal clipped at 5 standard deviations, block size N $= 2^{14}$ – Exponentiated Weibull distribution

Tab. 7. Statistical parameters for white noise signal clipped at 5 standard deviations, block size N $= 2^{14}$

Distribution type	Normal	Exponentiated Weibull	Generalized Extreme Value
Probability of fitted distribution [-]	0.00000	0.68282	0.07246
Mean damage [-]	0.17498	0.17495	0.17512
Standard deviation of damage [-]	0.01547	0.01541	0.01576
0.13% not lower than quoted value of damage [-]	0.12840	0.13748	0.13901
99.73% not exceed quoted value of damage [-]	0.21801	0.22694	0.22855

Fig. 24. Damage values for searched population for white noise signal, signal clipped at 5 standard deviations, block size N $= 2^{16}$

Fig. 25. Best-fitted distribution for damage values for searched population for white noise signal, signal clipped at 3 standard deviations, block size $N = 2^{16}$ – Exponentiated Weibull distribution
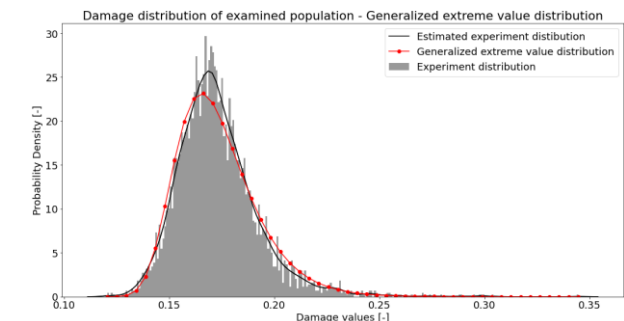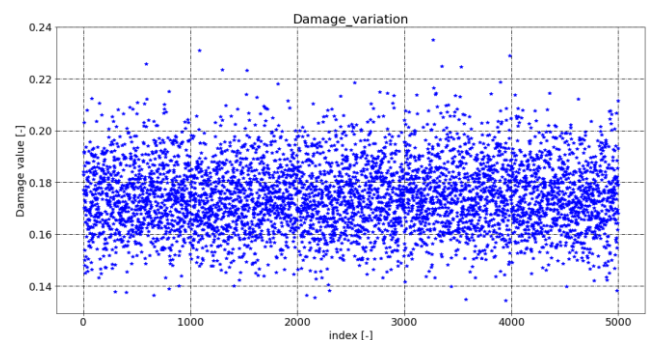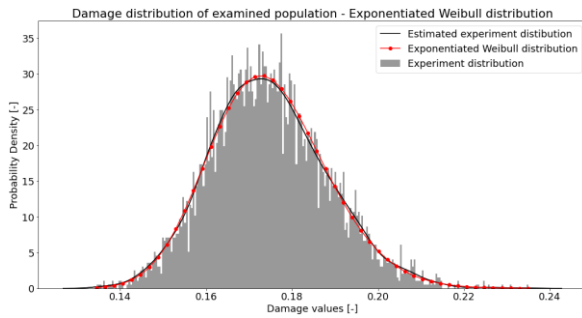
Tab. 8. Statistical parameters for white noise signal clipped at 5 standard deviations, block size $N = 2^{16}$

Distribution type	Normal	Exponentiated Weibull	Generalized Extreme Value
Probability of fitted distribution [-]	0.00193	0.83692	0.52516
Mean Damage [-]	0.17462	0.17463	0.17467
Standard Deviation of Damage [-]	0.01354	0.01354	0.01370
0.13% not lower than quoted value [-]	0.13384	0.13902	0.14047
99.73% not exceed quoted value [-]	0.21230	0.21650	0.21627

The conclusion, based on the aforementioned research results, is that every three distributions selected as final give similar mean value and standard deviation for the considered signal, which match to the experimental mean value and standard deviation. Additionally quoted is the value of damage involved in assessing the damage variation. For this purpose, the quoted value of damage for which 99.73% of the population have a lower value of damage is: mean, +3 standard deviation in normal distribution; and the damage value for which 0.13% of the population have a lower value of damage is: mean, –3 standard deviation. The first damage value quoted will be needed for sizing units for the considered load scenario. The second damage quoted can be used to avoid undertesting during real testing. For example, for damage quoted in Tab. 8, testing should be carried out for the increased duty to obtain a mean –3 standard deviation that is higher than or equal to the +3 standard deviation obtained for the original duty (mean –3 standard deviation damage needs to be increased from 0.13902 for original duty to a minimum of 0.21650 for increased duty) – this approach would ensure that unit will not be undertested during real testing.

Research results show that the Exponentiated Weibull distribution is the best fitted, when the block size is adequately large – i.e., $N_x \geq N = 214$. (Some anomalies were observed in Weibull distribution for smaller values, as shown in Tab. 3, and additionally damage variation is higher than for larger block size.) Therefore, for the final choice, we may decide to use the Exponentiated Weibull distribution to arrive at a statistical description of damage values for the considered population.

Additionally, research results show that for stochastic and deterministic combination loading scenario, the variability of damage is closed for different block sizes used, in opposition to the situa-

tion prevailing concerning the only random load scenario (3 standard variation is around +/–20% for N = 212, N = 214 and N = 216, as shown in Tab. 3–Tab. 5 andTab. 6–Tab. 8). For the only random loading scenario, damage variability for block size N = 212 can be around +/−60%; however, for block size N = 216, the same can be around 13% and for block size N = 220 it can be around 2%. Therefore, for combined stochastic and deterministic loading, N = 214 is recommended, as for this block size we observed stabilisation of damage variation and obtained a calculation accuracy close to those associated with higher block sizes. This value of block size implies the best relational performance with regard to accuracy.

7. SUMMARY AND CONCLUSION

A summary of the computer experiments conducted with the use of the two combined methods is provided in this section. FEM, Monte Carlo method and Python programming allow identification of the high conservativism of the legacy frequency domain-based method. The research results presented in this paper show that the legacy method used by commercial software for combined stochastic–deterministic loading scenarios gives highly conservative damage results, which might result in oversizing military aircraft or helicopters units.

The introduction of a novel method of calculation (based on combined frequency and time approach) of damage under the mentioned loading scenario allows us to precisely perform damage estimation in the time domain together with maintaining the efficiency benefit related to frequency domain calculation. Using the novel method introduced in this paper allows us to obtain a higher accuracy of the results than the legacy method, as well as an efficiency of computation that, in comparison with the legacy method, is at least comparable if not higher.

The research result reveals that damage variation is constant (characterised by a small variability depending on the block size used in the inverse Fourier transformation, in opposition to the only random loading scenario as quoted in related research 29). Therefore, the conclusion of the presented research is that for high amplitude sweep having a simultaneous random nature, it is recommended to use N = 214 as the block size.

This novel method allows also for analysis of time series population to assess the damage variation, which is impossible with use of the legacy method. An additional conclusion is that for populational analysis, it is recommended to use Exponentiated Weibull distribution for statistical consideration.

An additional benefit related to using the proposed method is that the signal can be clipped with a requested standard deviation level e.g., in aerospace industry, it is common to clip the input to 3 standard deviations. Therefore, this method can replicate real test conditions, which is not possible with the use of the spectral method.

Another aspect is that an algorithm can be also fitted to align with frequency resolution (block size) during conduction of real tests to assess what the variability of damage will be for test rig equipment. As for block sizes smaller than N = 214, the variability might increase, which can imply undertesting.

Further research results will focus on research on wide band and narrow band signals. Additional aspects are an implementation strain life method for highly loaded parts and the development of software for aerospace application with the use of the research

results presented in this paper.

Additionally, the Critical Plane approach will be introduced for defining PSD Response function. Future research will also be expanded to ascertain whether it is possible to synergistically use energy fracture mechanics methods, e.g., Cohesive Zone Model method, for damage estimation and life prediction.

REFERENCES

1. Bendat J. Probability functions for random responses. NASA report contract NAS-5-4590, 1964. Available from: https://ntrs.nasa.gov/citations/19640008076
2. Bendat J. Random data: Analysis and measurement procedures. John Wiley & Sons Inc., New York United States 2010
3. Bendat J. Principles and Applications of Random Noise Theory. John Wiley, New York,1958
4. Rice S. Mathematical analysis of random noise. Selected papers on noise and stochastic processes, Dover, New York, 1954
5. Dirlik T. Application of computers to fatigue analysis, PhD Thesis, Warwick University, 1985. Available from: http://wrap.warwick.ac.uk/2949/
6. CAEfatigue VIBRATION (CFV) User Guide & Verification Manual (Release 2020). CAEfatigue Limited, UK, Nov 2020.
7. nCode 2022.0 documentation, HBK 2022.
8. Lalanne C. Mechanical vibration and shock, Vol. 4, Hermes Penton Science, London, 2009
9. Lalanne C. Mechanical vibration and shock analysis: Specification Development, 3rd edition, Vol. 5, Wiley, London, 2014
10. Lalanne C. Mechanical vibration and shock analysis: Fatigue Damage, 3rd edition, Vol. 4, Wiley, London, 2014
11. Steinberg D. Vibration analysis for electronic equipment (2nd edition). Jon Wiley & Sons, New York, 1988
12. Halfpenny A, Kichim F. Rainflow cycle counting and acoustic fatigue analysis technique for random loading. 10th International Conference RASD, Southampton UK, 2010. Available from:
13. http://www.vibrationdata.com/tutorials2/Paper_RASD2010_005_Halfpenny_Kihm.pdf
14. Halfpenny A. Rainflow Cycle Counting and Fatigue Analysis from PSD, Proceedings of the ASTELAB conference, France, 2007. Available from: https://core.ac.uk/download/pdf/42735102.pdf
15. Halfpenny A, Bishop N. Vibration Fatigue, HBM-nCode, UK, 1997
16. Sweitzer K., Bishop N, Genberg V. Efficient computation of spectral moments for determination of random response statistics. International Conference on Noise and Vibration Engineering - ISMA, Leuven, BE, 2004. Available from:https://citeseerx.ist.psu.edu/docment?repid=rep1&type=pdf&doi=dd17f690eeac37cf88649cdf823507ca0ffd1f1c
17. Bishop N, Sherratt F. Finite Element Based Fatigue Calculation. NAFEMS Ltd., 2000, https://doi.org/10.59972/ta5h05jd
18. Bishop N. Methods for the rapid evaluation of fatigue damage on the Howden HWP330 wind turbine. Proceedings of 13th British Wind Energy Conference, Swansea, UK, p. 317-321, 1991
19. Bishop N, Sweitzer K, Schlesinger D, Woodward A. Fatigue calculation for multi input random and deterministic loads in the frequency domain. UK NAFEMS Conference, Oxford IK, Accelerating the Future of CAE, 10-11 June 2014.
20. Bishop N, Kerr S, Murthy P, Sweitzer K. Advances Relating to Fatigue Calculations for Combined Random and Deterministic Loads. SAE Technical Paper 2014-01-0725, 2014 https://doi.org/10.4271/2014-01-0725
21. Bishop N, Murthy P, Sweitzer K. Advances Relating to Fatigue Calculation for Combined Random and Deterministic Loads. 13th International ASTM/ESIS Symposium on Fatigue and Fracture Mechanics (39th National Symposium on Fatigue and Fracture Mechanics), November 13-15, 2013, Jacksonville, FL https://doi.org/10.4271/2014-01-0725
22. Bishop N, Murthy P, Sweitzer K., Kerr S. Time vs frequency domain analysis for large automotive systems. SAE Technical Paper 2015-01-0535, 2015. https://doi.org/10.4271/2015-01-0535
23. Bishop N, Murthy P, Sweitzer K., Kerr S. Time vs frequency domain analysis for large automotive systems. SAE Technical Paper 2015-01-0535, 2015, doi: https://doi.org/10.4271/2015-01-0535
24. Ferreira W, Meehan T, Cardoso V, Bishop N. A comparative study of automotive system fatigue models processed in the time and frequency domain. SAE Technical Paper 2016-01-0377, 2016, https://doi.org/10.4271/2016-01-0377
25. Datta S, Bishop N, Sweitzer K, Atkins A. Simultaneous durability assessment and relative random analysis under base shake loading conditions. SAE Technical Paper 2017-01-0339, 2017
26. https://doi.org/10.4271/2017-01-0339
27. MIL-STD-810H, Department of Defence Test Method Standard: Environmental Engineering Consideration and Laboratory Test, USA, 2019.
28. Brown AM, McGhee DS. Statistical Evaluation and Improvement of Method for Combining Random and Harmonic Loads. Marshall Space Flight Centre, Alabama 35812, 2003. Available from: https://ntrs.nasa.gov/citations/20030017832
29. Ptak M, Czmochowski J. Using computer techniques for vibration damage estimation under stochastic loading using the Monte Carlo Method for aerospace applications. Probabilistic Engineering Mechanics. 2023, vol. 72, p. 1-13. https://doi.org/10.1016/j.probengmech.2023.103452
30. Ptak M, Czmochowski J. Using computer techniques for vibration damage estimation of aircraft structures under stochastic loading. W: Computer Aided Engineering. Nauka i przemysł / red. Tadeusz Smolnicki. Wrocław : Oficyna Wydawnicza Politechniki Wrocławskiej, 2022. p. 169-179. ISBN: 978-83-7493-223-3
31. Metallic Materials Properties Development and Standardization (MMPDS-15), Battelle Memorial Institute, July 2020.
32. Delprete C, Sesana R, Vercelli A. Multiaxial damage assessment and life estimation: application to an automotive exhaust manifold. Procedia Engineering Vol. 2, April 2010, p. 725-734. Available from: doi: 10.1016/j.proeng.2010.03.078
33. Engin Z., Coker D. Comparison of Equivalent Stress Method with Critical Plane Approaches for Multiaxial High Cycle Fatigue Assessment. 2nd International Conference on Structural Integrity, ICSI 2017, 4-7 September 2017, Funchal, Madeira, Portugal. Procedia Structural Integrity Vol. 5 2017, p. 1229-1236. Available from: doi: 10.1016/j.prostr.2017.07.049
34. Smolnicki M, Ptak M, Lesiuk G. Static failure load predictions in notched steel components using a combined experimental-numerical approach. International Journal of Structural Integrity. 2017, vol. 8, no. 6, p. 683-693.https://doi.org/10.1108/IJSI-05-2017-0032
35. Wang JT. Relating Cohesive Zone Models to Linear Elastic Fracture Mechanics. NASA/TM-2010-216692, May 2010. Available from: https://ntrs.nasa.gov/api/citations/20100021117/downloads/20100021117.pdf
36. Kucharski P, Lesiuk G, Czapliński T, Fratczak R, Maciejewski Ł. Numerical Estimation of Stress Intensity Factors and Crack Propagation in Lug Connector with Existing Flaw. AIP Conference Proceedings. Fatigue Failure and Fracture Mechanics XXVI: Proceedings of the XXVI Polish National Conference on Fatigue Failure and Fracture Mechanics 17-20 May 2016 Fojutowo, Poland. https://doi.org/10.1063/1.4965949
37. Miner A. Cumulative damage in fatigue. J Applied Mechanics, Vol. 67, 1945, pp A159-A164, 1945.
38. Palmgren A. Die lebensdauer von kugellagern, zeitschrift des vereinesdeutscher ingenierure, Vol. 68, No. 14, 1924, pp. 339-341, 1924
39. Zienkiewicz O.C. Finite Element Method. McGraw-Hill, Dallas (1977)
40. ABAQUS User Manual V2018. Dassault Systems (2017)
41. Ptak M, Czmochowski J. Analysis of the impact of dynamic loads on transmission shafts of a civil aircraft. Modelling in engineering 2020: applied mechanics, Springer 2021. p. 245-257. Available from: doi: 10.1007/978-3-030-68455-6_22

42. Newland D. An introduction to random vibrations, spectral & wavelet analysis. Longman Inc., England 1995

43. Langtangen H. Python Scripting for Computational Science, Third Edition, Simula Research Laboratory. Springer, Berlin, Heidelberg, 2009

44. Python 3.8.12 Documentation (https://docs.python.org/3.8/)

45. Python 2.7.3 Documentation (https://docs.python.org/release/2.7.3/)

46. ESDU 06010 Cycle counting methods for the estimation on fatigue life

47. Matsuishi M, Endo T. Fatigue of metals subject to varying stress. Japan Society of Mechanical Engineers, Fukuoka, March 1968

48. Downing S, Socie D. Simple Rainflow counting algorithms. International Journal of Fatigue, January 1982

49. Watson P, Dabell B. Cycle counting and fatigue damage. Society of Environmental Engineers, September 1976

50. Dowling NE.. Local Strain Approach to Fatigue. Comprehensive Structural Integrity, Vol 4, 2003 p. 77-94. Available from: https://www.researchgate.net/publication/309717379_Comprehensive_Structural_Integrity

51. Meggiolaro MA, Castro JTP. Statistical evaluation of strain-life fatigue crack initiation predictions. International Journal of Fatigue, Vol 26, Issue 5, May 2004, p. 463-476. Available from: doi:10.1016/j.ijfatigue.2003.10.003

52. Lee YL, Hathaway R, Barkey M. Fatigue Testing and Analysis. Theory and Practice. Elsevier Butterworth Heinemann, 1st Edition July 29, 2004.

Michal Ptak: https://orcid.org/0000-0001-7308-8881

Jerzy Czmochowski: https://orcid.org/0000-0001-9547-7802

AVOIDENCE STRATEGIES FOR FRACTIONAL ORDER SYSTEMS WITH CAPUTO DERIVATIVE

Ewa PAWŁUSZEWICZ*

*Faculty of Mechanical Engineering, Department of Mechatronics Systems and Robotics,
Bialystok University of Technology, ul. Wiejska 45c, 15-351 Białystok, Poland

e.pawluszewicz@pb.edu.pl

Abstract: A control strategy is derived for fractional-order dynamic systems with Caputo derivative to guarantee collision-free trajectories for two agents. To guarantee that one agent keeps the state of the system out of a given set regardless of the other agent's actions a Lyapunov-based approach is adopted. As a special case showing that the given approach to choosing proposed strategy is constructive for a fractional-order system with the Caputo derivative, a linear system as an example is discussed. Obtained results extend to the fractional order case the avoidance problem Leitman's and Skowronski's approach.

Key words: Avoidance; fractional order systems, Caputo derivative, Lyapunov stability

1. INTRODUCTION

Avoidance system, in a colloquial sense means "a safety system designed to warn, alert, or assist drivers to avoid imminent collisions and reduce the risk of incidents". In fact the subject of collision avoidance is much broader than just pre-crash systems. One only has to look at the game as a conflict situation in which the parties to the conflict choose the strategy suits them, see for example [16]. So, this problem can be met not only in problems of traffic and transport [19,24], navigation [15] but also in communication networks, economic, control [18,25,28], social sciences [6], and others. Generally the problem for the case of two agents is the following: There are two agents. How to determine the strategy of one of them in such way that for given initial state no solution of one system intersects the avoidance zone no matter what a strategy of the second is?

Several approaches to avoidance control have been considered. The Lyapunov based approach as the first was proposed in [14] and next generalized to the system with an arbitrary time domain [22]. Based on [14] conditions for collision avoidance between two agents were given in a non-cooperative case in [8]. The cooperative control law using the concept of Lyapunov function for multi-agent system were designed in [27] and next extended to multi-agent system with bounded input disturbances in [27,29].

Taking into account accelerating development of both fractional differential equations and their applications, the other extension of approach to collision avoidance is important. This derives from the fact that fractional-order equations are more adequate for modeling physical processes than differential equations with an integer order and provides} some explanation of discontinuity and singularity formations in nature, see [9,11]. One can find many applications of fractional calculus and control in viscoelasticity, electrochemistry, electromagnetism, ecnophysics, and others, see for example [1,12,13,23,26]. It cannot be ignore that many modeled systems contain non-local dynamics, which can be better

described using integro-differential operators with a fractional order, [9,10,20,21]. Attention should be also paid on the fact when a real phenomenon is mathematically modelled, not all variables are precisely known. This implies that to aim of studding ordinary differential equations with uncertain determined dynamics it is natural to use differential inclusions as the generalization and a good tool for analyses of properties and behaviours' of systems described by ODE.

The goal of this study is to extend to the fractional order case the Lyapunov based approach to collision avoidance. Since we consider the system starting from given initial state and the kind of history of the system is not consider, the Caputo fractional order derivative is taken into account, [3,4,11].

The paper is organized as follows. In Section 2 the needed notation and facts are presented. Fractional order nonlinear control systems with Caputo differential and its relation with fractional order differential inclusion are introduced. It is shown then the set of trajectories of fractional order continuous-time inclusion associated with the given system is closed. In Section 3 there is considering the avoidance problem. Basing on [14] and [22] conditions for giving the constructive strategy allowing keeping one agent in the avoidance zone no matter what the admissible action of the other agent are given. To this aim the Lyapunov approach is used. As an example of determination the proposed avoidance strategies linear fractional order systems are consider in Section 4.

2. FRACTIONAL CONTROL SYSTEMS AND INCLUSIONS

Let $x \colon [a, b] \to \mathbb{R}$ be an absolutely continuous real valued function. The Caputo fractional derivative of order α, $0 < \alpha \leq 1$, of a function x is defined by, [11]:

$$\,_a^C D^\alpha x(t) = \frac{1}{\Gamma(1-\alpha)} \int_a^t \frac{x\prime(\tau)}{(t-\tau)^\alpha} d\tau,$$

where Γ denotes the gamma function.

Consider the fractional order differential control system

$$(\; {}_{a}^{C}D^{\alpha}x(t))(t) = f(t,x(t),u(t)), \;\; x(0) = x_0 \tag{1}$$

where $t \in \mathbb{R}_+$, $x(t) = \big(x_1(t) \dots x_n(t)\big)^T \in \mathbb{R}^n$ is a state vector with bounded entries, $u(\cdot) \in \mathcal{U} \subseteq \mathbb{R}^m$ is a control function defined on the set of admissible controls

$$\mathcal{U} = \{u(\cdot) \text{ mesurable}, u(t) \in U \text{ for all } t \in \mathbb{R}_+\}$$

such that $U \subset \mathbb{R}^m$ is a compact set of control values, $f : \Omega \supseteq \mathbb{R} \times \mathbb{R}^n \to \mathbb{R}^n$. We assume that Ω is an open subset of $\mathbb{R} \times \mathbb{R}^n$, the dynamics of system (1), i.e. function $f : \Omega \times U \to \mathbb{R}^n$, of $C^1 -$ class with the respect to x and continuous with respect to each other variable.

An absolutely continuous function $x(\cdot) : [t_0, t_1] \to \mathbb{R}^n$ is a solution of (1) if its graph $\{(t, x(t)) : t \in [t_0, t_1]\}$ is entirely contained in Ω and there exists a measurable u with values inside U, so that $\big(\; {}_{t_0}^{C}D^{\alpha}x(t)\big)(t) = f\big(t, x(t), u(t)\big)$ for almost every $t \in [t_0, t_1]$. This solution forms the trajectory of system (1). The motion of this system can be described by the multifunction

$$F(x) = \{f\big(t, x(t), u(t)\big) : u(\cdot) \in U\}.$$

Consider the fractional order differential inclusion

$$(\; {}_{0}^{C}D^{\alpha}x)(t) \in F(t,x) \tag{2}$$

Theorem 1: A function $x : [t_0, t_1] \to \mathbb{R}^n$ is a trajectory of (1) if and only if it satisfies (2) almost everywhere.
Proof: In fact the reasoning is similar to the classical continuous-time case, see [5], so we only sketch the proof. The fact that a solution of (1) is the solution of (2) is immediate. Suppose that $x(\cdot)$ is a solution to (2). For the fixed arbitrary element $\overline{\omega} \in U$ let us define the multifunction

$$W(t) = \begin{cases} \{\omega \in U : f(t, x(t), \omega) = (\; {}_{0}^{C}D^{\alpha}x)(t)\} \text{ if} \\ \qquad (\; {}_{0}^{C}D^{\alpha}x)(t)\,(t) \in F(t,x); \\ \{\overline{\omega}\} \qquad\qquad\qquad\quad \text{otherwise.} \end{cases}$$

The equality $W(t) = \{\overline{\omega}\}$ holds only on a set of the measure zero, so $(\; {}_{0}^{C}D^{\alpha}x(t))(t) = f(t, x(t), \omega)$ is fulfilled for almost every $t \in [t_0, t_1]$. Define a control u in such way that $u(t)$ is the first element of this set with respect to the lexicographical order. Using the same arguments as in [5,22] one can conclude that function $u(\cdot)$ is measurable. $\square$
Example: Consider the system

$$(\; {}_{0}^{C}D^{\alpha}x)(t) = u(t), \;\; x(0) = 0 \tag{3}$$

with $u(t) \in U = \{-1; 1\}$. Then $x(t) = \frac{1}{\Gamma(\alpha)} \int_0^t \frac{u}{(t-\tau)^{1-\alpha}} d\tau = \frac{t^{\alpha}u}{\Gamma(1+\alpha)}$. Let $u_n = 1$ if $sin(nt) \geq 0$ and $u_n = -1$ if $sin(nt) < 0$. Then the sequence of trajectories $\{x_{u_n}(t)\}$ converges uniformly to zero for any t. On the other hand, it is easy to check $x(t) \equiv 0$ is not a solution of (3).

Below we answer on the question when the limit of system's trajectories coincides with the set of its solutions.

2.1 Closure of the Set of Trajectories

Let $A \subset \mathbb{R}^n$ be a nonempty set. Recall that a distance of point $x \in \mathbb{R}^n$ from set A, denoted by $d(x, A)$, is defined as $d(x, A) := \inf_{a \in A} d(x, a)$. Recall also that a multifunction F

with compact values is Hausdorff continuous if $lim_{x_2 \to x_1} d\_H(F(x_2), F(x_1)) = 0$, for every $x_1 \in \mathbb{R}^n$, where d_H is the Hausdorff distance between two nonempty compact sets $F(x_2)$ and $F(x_1)$ from $\mathbb{R}^n$ defined as

$$d_H\big(F(x_2), F(x_1)\big) := max\{d(x, F(x_1), d\big(x', F(x_2)\big) : x \\ \in F(x_1), x' \in F(x_2)$$

Theorem 2: Assume that $(t, x) \mapsto F(t, x)$ is Hausdorff continuous map on $\mathbb{R} \times \mathbb{R}^n$ with compact convex values. Then the set of trajectories of inclusion (2) is closed in $C^0([0,T], \mathbb{R})$.
Proof: Although the basic idea of proof itself comes from [5] there will be needed some facts on approximation of solution to continuous-time fractional order dynamic system by the solution to discrete fractional order dynamic systems, that can be found in the Appendix.

Suppose that $x_n(\cdot)$, $n \in \mathbb{N}$, is a sequence of trajectories of (2) converges uniformly to $x(\cdot)$ on $[0,T]$. Note also that the sets $F(t, x_n)$ are uniformly bounded. This implies that $x_n(\cdot)$ are uniformly Lipschitz continuous. It follows that also function $x(\cdot)$ is uniformly Lipschitz continuous and therefore, absolutely continuous on $[0,T]$. Thus, $x(\cdot)$ is differentiable a.e. on $[0,T]$ in the Caputo sense, see [11].

Suppose that $(\; {}_{0}^{C}D^{\alpha}x)(t)$ exists, but it does not fulfil inclusion $(\; {}_{0}^{C}D^{\alpha}x)(t) \in F(t, x)$. By Separation Theorem there exist $\varepsilon > 0$ and a vector $p \in \mathbb{R}$ such that

$$p(\; {}_{0}^{C}D^{\alpha}x)(t) \geq max_{y \in F(t,x(t))}(py) + \varepsilon \geq py + \varepsilon$$

for all $y \in F\big(t, x(t)\big)$. Let $h > 0$. By continuity there exists $\delta > 0$ such that for $|t - t_h| \leq \delta$ and $|x(t) - x(t_h)| \leq \varepsilon$, one has

$$py \leq p (\; {}_{0}^{C}D^{\alpha}x)(t) - \varepsilon \tag{4}$$

for all $y \in F(t, x(t))$. By Proposition 6 in Appendix there exists ϵ, for example $\epsilon = \varepsilon$, such that

$$|(\; {}_{0}^{C}D^{\alpha}x)(t) - (\; {}_{a}^{C}\Delta_h^{\alpha}x)(t_h)| < \varepsilon \tag{5}$$

for h small enough, where ${}_{a}^{C}\Delta_h^{\alpha}x$ denotes the Caputo-type difference operator (see Appendix). Then, by the uniform convergence and (5) one gets

$$\lim_{\nu \to \infty} p(\; {}_{a}^{C}\Delta_h^{\alpha}x)(t_h) = p(\; {}_{a}^{C}\Delta_h^{\alpha}x)(t_h) >$$

$$p (\; {}_{0}^{C}D^{\alpha}x)(t) - \varepsilon.$$

Putting $y = (\; {}_{a}^{C}\Delta_h^{\alpha}x)(t_h)$ from (4) one gets

$$p(\; {}_{a}^{C}\Delta_h^{\alpha}x)(t_h) \leq (\; {}_{0}^{C}D^{\alpha}x)(t) - \varepsilon$$

what leads to the contradiction. $\square$
Corollary 3: Assume that $(t, x) \mapsto F(t, x)$ is Hausdorff continuous map on $\mathbb{R} \times \mathbb{R}^n$ with compact convex values. Let $x_n(\cdot)$ be a sequence of trajectories of (2) converges uniformly to $x(\cdot)$ on $[0, T]$.
 i. If the graph $\{(t, x(t)) : t \in [0, T]\}$ is entirely contained in Ω and all sets $F(t, x) = \{f(t, x, u) : u \in U\}$ are convex, then $x(\cdot)$ is also a trajectory of the system

$$(\; {}_{0}^{C}D^{\alpha}x)(t) = f\big(x(t), u(t)\big), \;\; u \in U\}. \tag{6}$$

 ii. The set of trajectories of inclusion (6) is closed in $C^0([0, T], \mathbb{R})$.

Proof: Item $i.$) is driven directly from Theorem 2. Item $ii.$) is the consequence of the item $i.$) and Theorem 1. □

3. AVOIDANCE STRATEGY

Let $p_i: \mathbb{R}_+ \cup \{0\} \times \mathbb{R}^n \to U_i \subseteq \mathbb{R}^{d_i}$ $i = 1,2$ be strategies from the given class of set valued functions $\mathcal{U}_i$ with control values u_i ranging in given sets U_i. These strategies could arise from the application of a proper feedback low to the system (1). This implies that $U_i = U_i(t, x(t))$. should be admissible for the given system. So, strategies $p_i, i = 1,2$, have to be such that for given $(t, x(t))$ it holds that $u_i \in p_i(t, x(t)) \subseteq U_i \subseteq \mathbb{R}^{d_i}$ for $i = 1,2$.

Consider a multivalued function

$$F(t,x) := \{\bar{x} \in \mathbb{R}^n : \bar{x} = f(t,x,u_1,u_2), u_i \in p_i(t,x(t)), \quad i = 1,2\}$$

where $f: \mathbb{R}_+ \cup \{0\} \times \mathbb{R}^n \times \mathbb{R}^{d_1} \times \mathbb{R}^{d_2} \to \mathbb{R}^n$ is the dynamic of the system (1). This means that

$$({}^{C}_{0}D^{\alpha}x)(t) \in F(t, x(t), p_1(t, x(t)), p_2(t, x(t))) \qquad (7)$$

From Theorem 1 it follows that the trajectory of the system (7) is absolute continuous function $x: [t_0, t_1] \to \mathbb{R}^n$ satisfying fractional order inclusion

$$({}^{C}_{0}D^{\alpha}x)(t) \in F(t, x(t), p_1(t, x(t)), p_2(t, x(t)))$$

almost everywhere for $t \in [t_0, t_1]$.

Let Λ be an open or the closure of an open set in $\mathbb{R}^n$. Then for the system (7):

1. a set $\mathcal{T}$ such that $\mathcal{T} \subseteq \Lambda$ and into $\mathcal{T}$ there is no solutions of system (7 that must enter for some $p_1(t, x(t)) \in \mathcal{U}$ no matter what $p_2(\cdot, x(\cdot)) \in \mathcal{U}$ is called the *antitarget set*,
2. a closed set $\mathcal{A} \subseteq \Lambda$ such that $\mathcal{T} \subset \mathcal{A}$ is called the *avoidance set*,
3. a set $\Upsilon_{\mathcal{A}} := \Lambda_\varepsilon \setminus \mathcal{A}$, where Λ_ε is a closure of the open set Λ, such that $\mathcal{A} \subset \Lambda_\varepsilon$ is called the *safety zone*.

Note that $\mathcal{T} \subset \mathcal{A} \subset \Lambda_\varepsilon$ and all these sets are subsets of trajectories set of the considered system. Moreover, the avoidance set can be any set that contains the antitarget set $\mathcal{T}$.

Following [14], let us introduce the following notation. Let $\Phi_{\mathcal{A}} := \mathbb{R}_+ \times \Upsilon_{\mathcal{A}}$. By an *attainable set of trajectories* $\gamma(t, x_0)$ at time $t \geq 0$ we will mean the set

$$\gamma(t, x_0) := \{x(t): \text{given } p_1(\cdot, x(\cdot)) \in \mathcal{U}_1 \text{for all}$$

$$p_2(\cdot, x(\cdot)) \in \mathcal{U}_2 \text{ and given } x_0 \in \Phi_{\mathcal{A}}\}.$$

The set $\gamma(t, x_0)$ is the set of all motions of the system (7) from the initial state $x_0 = x(0) \in \Phi_{\mathcal{A}}$ at time t, i.e. it is the set of all motions of the system (7) from x_0 laying in the safety zone $\Phi_{\mathcal{A}}$. The *fuel motion* $\Gamma(t, x_0)$ from $x_0 \in \Phi_{\mathcal{A}}$ is the set

$$\Gamma(t, x_0) := \bigcup_{t \in \mathbb{R}_+} \gamma(t, x_0)$$

and $\Gamma(\Phi_{\mathcal{A}}) := \bigcup_{x_0 \in \Phi_{\mathcal{A}}} \gamma(\mathbb{R}_+, x_0)$.

Theorem 4: A set $\mathcal{A}$ is the avoidance set for the nonlinear fractional order system (7) if there exist:

1. a set $\Phi_{\mathcal{A}}$,
2. strategy $p_1(\cdot, x(\cdot)) \in \mathcal{U}_1$,
3. continuous real function V defined on an open subset of $\overline{\Phi_{\mathcal{A}}}$ such that for all $(t, x(t)) \in \Phi_{\mathcal{A}}$ it holds:

i. $V(t, x(t)) > (t, x(t))V(t_1, x(t_1))$ for $x_1 \in \partial \mathcal{A}$ and $t_1 \geq t$;

ii. $({}^{C}_{0}D^{\alpha}V)(t, x(t)) \geq 0$ for $u_2(t) \in \mathcal{U}_2$ and $\tilde{p}_1((\cdot), x(\cdot)) = p_1(\cdot, x(\cdot))|_{\Phi_{\mathcal{A}}}$.

Proof: Suppose that for some $x_0 = x(0) \in \Phi_{\mathcal{A}}$ there exists $t_2 > 0$ such that $\Gamma(t, x_0) \cap \mathcal{A} \neq \emptyset$ for $t \in [0; t_2]$. By item $i.$) there exist a $t_1 \in (0; t_2]$ and $x_1 = x(t_1) \in \Gamma(t, x_0) \cap \partial \mathcal{A}$ being the end point of the trajectory that lies on the boundary $\partial \mathcal{A}$ such that $V(0, x_0) > V(t_1, x_1)$. Suppose that $u = (u_1, u_2)$ is an admissible control for the system

$$({}^{C}_{0}D^{\alpha}x)(t) \in F(t, x) = \{\bar{x} \in \mathbb{R}^n : \bar{x} = f(t, x, u_1, u_2)\}, \quad x(0) = x_0. \qquad (8)$$

Then $\gamma(t, x_0, u)$ is the solution of (8) describing the trajectory of this system. Consider the maximal solution of

$$({}^{C}_{0}D^{\alpha}x)(t) = f_u(t, x(t)), \quad x(0) = x_0. \qquad (9)$$

and suppose that there is a time interval such that (9) has exactly one maximal solution. From the item $i.$) it follows that $V(t, \gamma(t, x_0, u))$ is nondecreasing continuous function as long as $\gamma(t, x_0, u)$ stays in $\Phi_{\mathcal{A}}$. For this it is sufficient that for some ε it remains in the set $\Psi := \{(t, x): V(t, x) \geq \varepsilon\}$.

Suppose that there is some $s > 0$ such that $V(s, \gamma(s, x_0, u)) \leq \varepsilon$. From continuity of V it follows there is a first such s. So, one can suppose that $V(t, x(t)) > \varepsilon$ for all $t \in [0; s)$. Then $t \mapsto V(t, x(t))$ is nondecreasing map on $[0; s]$ and hence $V(s, \gamma(\iota x_0, u)) \geq V(t, x(t)) > \varepsilon$, so contradiction. This means that γ stays in the compact set Ψ for all $t > 0$. So, the trajectory is defined for all $t > 0$ and V is nondecreasing. □

4. A LINEAR FRACTIONAL ORDER SYSTEM

As an example let consider a linear continuous-time fractional system with order $0 < \alpha < 1$ and with the Caputo derivative

$$({}^{C}_{0}D^{\alpha}x)(t) = Ax(t) + B_1 u_1(t) + B_2 u_2(t) \qquad (10)$$

where state $x(t)$ belongs to some set $\Lambda \subseteq \mathbb{R}^n$, $u_i(t) \in \mathcal{U}_i \subseteq \mathbb{R}^{d_i}$, $i = 1, 2$, $t \in [t_0 = 0, t_1]$ and A, B_1, B_2 are stationary matrices of appropriated dimensions.

Recall that system $({}^{C}_{0}D^{\alpha}x)(t) = Ax(t)$ is [7]

1. *asymptotically stable* iff $|arg(specA)| > \frac{\pi}{2}\alpha$,
2. *stable* iff either it is asymptotically stable or those critical eigenvalues which satisfy $|arg(specA)| = \frac{\pi}{2}\alpha$ have geometric multiplicity one.

In [2] it was shown that linear system
$({}^{C}_{0}D^{\alpha}x)(t) = Ax(t) + Bu(t)$
is controllable on $t \in [0, t_1]$ iff adjoint linear system
$({}^{C}_{t_1}D^{\alpha}x)(t) = A^T x(t),$
$\qquad y(t) = B^T x(t)$
is observable on this interval. Then the matrix (observability gramian)

$$W(t) = \int_0^t E_\alpha(A(t_1 - \tau)^\alpha)BB^T E_\alpha(A^T(t_1 - \tau)^\alpha)d\tau \qquad (11)$$

where $E_\alpha(A\tau^\alpha) = \sum_{k=0}^{\infty} \frac{(A\tau^\alpha)^k}{\Gamma(k\alpha+1)}$ denotes the Mittag-Leffler matrix function, is symmetric positive define and there exists the

positive define symmetric matrix such that $AW + WA^T \geq -Q$.

One can choose the matrix function $V(t) = x^T(t)Px(t)$ with $P = W$. Taking the avoidance set $\mathcal{A} = \{x \in \mathbb{R}^n: x^TPx \leq \text{const}\}$ the condition $ii.$) of Theorem 4 is fulfilled. For such avoidance set, the antitarget set $\mathcal{T}$ should belong to a ball containing the set $\{0\}$. Moreover, taking a stationary matrix D such that $B_2 = B_1D$, and defining set $U_i, i = 1, 2$, as

$$U_i := \{u_i: ||u_i|| \leq \xi_i, \xi_i > 0\}$$

with $\xi_1 \geq \xi_2||D||$, where $||\cdot||$ denotes the Euclidian norm, one meets the condition $ii.$) of Theorem 4. Then, the avoidance strategy can be designed as

$$p_1(t,x) = \frac{B_1^TPx}{||B_1^TPx||}\xi_1$$

for all $(t,x) \notin \Sigma = \mathbb{R}_+ \times \{x \in \mathbb{R}^n: DE_\alpha(A\tau^\alpha) = 0 \text{ for all } t\}$. If $(t,x) \in \Sigma$, then u_1 can be admissible control, so $p_1(t,x) = U_1$.

Example: Let us consider the following system

$$(\ _0^CD^{0,5}x) = \begin{bmatrix} 0 & 1 \\ 1 & 0 \end{bmatrix}x(t) + \begin{bmatrix} 0 \\ 1 \end{bmatrix}u_1(t) + \begin{bmatrix} 0 \\ 1 \end{bmatrix}u_2(t) \quad (13)$$

with $U_2 = \{u_2: |u_2| \leq 1\}$ and $t \in [0; 1]$. Following [2] it can be calculated that at $t = 0$ the Mittag-Lefflet function is as follows

$$E_{0,5}(At^{0,5}) = \begin{bmatrix} \frac{E_{0,5}(t^{0,5})+E_{0,75}(-t^{0,5})}{2} & \frac{E_{0,5}(t^{0,5})+E_{0,5}(t^{0,5})}{2} \\ \frac{E_{0,5}(t^{0,5})+E_{0,5}(t^{0,5})}{2} & \frac{E_{0,5}(t^{0,5})+E_{0,5}(t^{0,5})}{2} \end{bmatrix}$$

and the system

$$(\ _0^CD^{0,5}x) = \begin{bmatrix} 0 & 1 \\ 1 & 0 \end{bmatrix}x(t)$$

is not stable, but system (13) is controllable, so the respective adjoint linear system is observable. The

$$W = \int_0^t E_{0,5}(A(1-\tau)^{0,5})BB^T E_{0,5}(A(1-\tau)^{0,5}) \quad d\tau = \begin{bmatrix} 1,7036 & 2,2882 \\ 2,2882 & 3,1945 \end{bmatrix}$$

The stabilizing feedback matrix gain is, see [2]

$$K = B^TW^{-1}E_{0,5}(A^Tt_1^{0,5}) = [-11,2277 \quad -2,9587]$$

Provided the avoidance set $\mathcal{A} = \{x \in \mathbb{R}^2: x^TPx \leq a, a \in \mathbb{R}_+\}$ the avoidance strategy is $p_1(t,x) = Kx(t) + \frac{B_1^TWx}{||B_1^TWx||}||D||\xi_1$, where D is such that $B_2 = B_1D$. Taking D as identity matrix, we obtain

$$p_1(t,x) = -10,6694x_1 - 2,1793x_2.$$

5. CONCLUSIONS

In the paper collision avoidance control strategy for fractional-order dynamic systems with Caputo derivative is developed. Based on Lyapunov stability method the constructive avoidance conditions of determining strategy $p_1(\cdot, x(\cdot)) \in \mathcal{U}_1$ of one agent from the given initial state $x_0 = x(0)$ such that its collision-free trajectories intersects the avoidance set no matter what strategy of the second agent's is, are given. As example how the obtained avoidance strategies can be easily used it is explained on the linear fractional order system. As an intermediate step it is shown that the set of trajectories of given system are closed in the set of continuous functions on finite time interval. Our future research directions include extending these results to non-cooperative multi-agents fractional case and next for fractional-order dynamic systems with Riemann-Liouville and Grünwald--Letnikov fractional-order operators.

REFERENCES

1. Ambroziak L, Lewon D, Pawluszewicz E. The use of fractional order operators in modeling of RC-electrical systems. Control & Cybernetics 2016; 45(3):275—288.
2. Balachandran K, Govindaraj K, Rodriguez-Germa M, Trujillo JJ. Stabilizability of fractional dynamical system, Fractional & Applied Analisis. 2014; 17(2):511-521.
3. Bandyopadhyay B, Kamal S. Stabilization and control of fractional order systems: a sliding mode approach, Lecture Notes in Electrical Engineering 317, Springer International Publishing, 2015:55-90.
4. Bingi K, Prusty BR, Singh AP. A Review on Fractional-Order Modelling and Control of Robotic Manipulators, Fractal Fract. 2023; 7(1):77. Available from: https://doi.org/10.3390/fractalfract7010077.
5. Bressan A, Piccoli B. Introduction to the Mathematical Theory of Control, AIMS Series on Applied Mathematics 2007.
6. Burns TR, Roszkowska E, Corte U, Machado Des Johansson N. Linking Group Theory to Social Science Game Theory: Interaction Grammars, Group Subcultures and Games for Comparative Analysis, Social Sciences. 2017; 6(3):1-36. Available from: https://doi.org/10.3390/socsci6030107.
7. Chen D, Zhang R, Liu X, Ma X. Fractional order Lyapunov stability theorem and its applications in synchronization of complex dynamical networks, Commun. Nonlinear Sci. Numer. Simulat. 2014; 19(2014):4105-4121.
8. Corless L, Leitmann G. Controller design for uncertain systems via Lyapunov functions. IEEE Proc. of 1988 American Control Conference 1988:2019–2025.
9. Das S. Functonal Fractional Calculus for System Identyfication and Controls, Springer 2008.
10. Djennoune S, Bettayeb M, Al-Saggaf UM. Synchronization of fractional-order discrete-time chaotic systems by exact state reconstructor: application to secure communication, Int. J. App. Math. Comput. Sci. 2018;29(1):179-194.
11. Kilbas AA, Srivastava HM, Trujillo JJ. Theory and applications of fractional differential equations, Elsevier Science B. V. 2006.
12. Koszewnik A, Pawluszewicz E, Ostaszewski M. Experimaental studies of the fractional PID and TID controllers for industrial process, International Journal of Control, Automation and Systems 2021; 19(5): 1847-1862.
13. Kozlowska M, Kutner R. Dynamics of the Warsaw Stock Exchange index as analysed by the nonhomogeneous fractional relaxation equation, Acta Physica Polonica, Series B 2006; 37(11): 3027-3028.
14. Leitmann G, Skowronski J. Avoidance Control, Journal of Optimization Theory and Applications 1977; 23(4): 581–591.
15. Liu Y., Chen H., Zou Q., Du X., Wang Y., Yu J. Automatic Navigation of Microswarms for Dynamic Obstacle Avoidance, IEEE Transaction on Robotics 2023. DOI: 10.1109/TRO.2023.3263773.
16. Marden JR, Shamma JS. Game Theory and Distributed Control, in: Handbook of Game Theory with Economic Applications 2015; 4:861-899.
17. Mozyrska D, Girejko E, Wyrwas M. Fractional nonlinear systems with sequential operators, Cent. Eur. J. Phys. 2013: 11(10):1295-1303.
18. Némcová J, Petreczky M, van Schuppen JH. Towards a system theory of rational systems. in: Bart, H., Horst, S., Ran, A., Woerdeman, H. (eds) Operator Theory, Analysis and the State Space Approach. Operator Theory: Advances and Applications 271. Birkhäuser, Cham 2018:327–359

19. Nguyen HD, Kim D, Son YS, Han K. Linear Time-Varying MPC-based Autonomous Emergency Steering Control for Collision Avoidance, IEEE Transaction on Vehicular Technology 2023; 1109/TVT.2023.3269787

20. Oprzędkiewicz K, Mitkowski W, Rosół M. Fractional order, state space model of the temperature field in the PCB plate, Acta Mechanica et Automatica 2023;17(2):180—187.

21. Pawłuszewicz E, Koszewnik A, Burzynski P. On Grünwald-Letnikov fractional order operator with measureble order on continuous-discrete time scale, Acta Mechanica et Automatica 2020;14(3): 161-165.

22. Pawłuszewicz E, Torres DMF. Avoidance Control on Time Scales, Journal of Optimization Theory and Applications 2010; 145(3): 527 – 542.

23. Rana KPS, Kumar V, Mittra N, Pramanik N. Implementation of fractional order integrator/differentiator on field programmable gate array, Alexandria Engineering Journal 2016; 55:1765—1773.

24. Rodríguez-Seda EJ, Stipanovič DM. Cooperative Avoidance Control With Velocity-Based Detection Regions, IEEE Control Systems Letters 2020: 4(2):432 – 437.

25. Samuelson L. Game Theory in Economics and Beyond, Journal of Economic Perspectives 2016; 30(4):107—130.

26. Sierociuk D, Dzieliński A, Sarwas G, Petras I, Podlubny I., Skovranek T. Modelling heat transfer in heterogenous media using fractional calculus, Phylosophical Transaction of the Royal Society 2013;371(1990).

27. Stipanovič DM, Hokayem P, Spong M, Šiljak, D. Cooperative avoidance control for multiagent systems, J. Dyn. Syst. Measur. Control 2007; 129(5): 699—707.

28. Ungureanu V. Pareto-Nash-Stackelberg Game and Control Theory, Springer 2018.

29. Zhang W, Rodŕiguez-Seda EJ, Deka SA, Amrouche M, Zhou D, Stipanovič DM., Leitmann G. Avoidance Control with Relative Velocity Information for Lagrangian Dynamics, Journal of Intelligent & Robotic Systems 2020; 99:229–244. Available from: https://doi.org/10.1007/s10846-019-01122-x

Ewa Pawłuszewicz: https://orcid.org/0000-0002-3297-7970

APPENDIX 1

Fractional order discrete-time systems

It is known that if $x: h\mathbb{Z} \to \mathbb{R}$ then forward $h-$difference operator is defined as $(\Delta_h x)(kh) = \frac{x(k+h)-x(k)}{h}$. If $q \in \mathbb{N}_0 := \{0,1,2,\dots\}$, then $\Delta_h^q := \Delta_h \circ \cdots \circ \Delta_h$ denotes the $q-$fold application of the operator Δ_h, i.e. $(\Delta_h^q x)(kh) =$
$= \sum_{i=0}^{q} (-1)^{q-1} \binom{q}{k} x(kh + ih) h^q$. The extension of q-fold application of operator Δ_h leads to the fractional h-sum:

$$(\Delta^{-\alpha_h} x)(kh) := \sum_{i=0}^{k} h^\alpha a^{(\alpha)}(i) x(kh - ih) \qquad (1)$$

where $k \in \mathbb{N}_0$ and $a^{(\alpha)}(i) = (-1)^i \frac{\alpha(\alpha-1)\cdots(\alpha-i+1)}{i!}$.

Definition 1: Let $\alpha \in (q-1, q]$, $q \in \mathbb{N}$. Then, the *Caputo - type fractional $h-$difference* of order α for a function $x: h\mathbb{Z} \to \mathbb{R}$ is defined as

$$(\Delta^{\alpha_h} x)(kh) = \left(\Delta_h^{-q-\alpha} \left(\Delta_h^q x \right) \right)(kh) \qquad (2)$$

From Definition 5 it follows that

1. if $q = 1$ then $(\Delta^{\alpha_h} x)(kh) = (\Delta^{-(1-\alpha)_h}(\Delta_h x))(kh)$,
2. if $\alpha = q \in \mathbb{N}$, then $(\Delta^{\alpha_h} x)(k) = \left(\Delta_h^q x \right)(k) = h^q \sum_{i=0}^{q} \binom{q}{k} x(k + i)$.

Consider the discrete fractional system of the form

$$(\Delta_h^\alpha y)(kh) = f\big(kh, y(kh), u(kh)\big), \; y(0) = y_0 \qquad (3)$$

where $y(\cdot) \in \mathbb{R}^n$, $k = \lfloor \frac{t}{h} \rfloor + 1$ with the sign $\lfloor \cdot \rfloor$ being the floor function and $u(\cdot)$ - a control vector function defined on the set $\mathcal{V} = \{u(\cdot) \text{ measurable}, u(kh) \in V \text{ for all } k \in \mathbb{N}\} \subseteq \mathbb{R}^m$ with the set of control values $V \subset \mathbb{R}^m$ being compact. We say that a function $y(\cdot)$ defined on a set $\{\kappa h, (\kappa + 1)h, \dots, kh\}$, $\kappa < k$, $\kappa \in \mathbb{N}$, is a solution of (16) if its graph $\{(nh, y(nh)): \kappa h \le nh \le kh\}$ is entirely contained in $\Omega_h \subseteq (h\mathbb{N})_a \times \mathbb{R}^n$, and there exists a measurable control function $u(\cdot)$ with values inside V, so that $(_a\Delta^{\alpha_h} y)(kh) = f(kh, y(kh), u(kh))$ for almost every $t \in \{\kappa h, (\kappa + 1)h, \dots, kh\}$. This solution forms the $k-$steps trajectory of system (16).

Proposition 1: Suppose that state function $x: \mathbb{R} \to \mathbb{R}^n$ is absolutely continuous. Then the solution x to system

$$(_0^C D^\alpha x)(t) = f\big(t, x(t)\big), \; x(0) = x_0, t \in (0, T]$$

can be approximated by the solution of system:

$$(\Delta_h^\alpha y)(kh) = f(kh, y(kh)), y(0) = y_0, t \in (0, T]_{(h\mathbb{N})_a}$$

where $k = \left\lfloor \frac{t}{h} \right\rfloor + 1$ with in values via the limit $\lim_{h \to 0} y(kh) = x(t)$.

THE EFFECT OF "B" TARGET VOLTAGE
ON WEAR PROPERTIES OF TiCrNb-hBN COATINGS

Yaşar SERT*⊙, Tevfik KÜÇÜKÖMEROĞLU*⊙, Hojjat GHAHRAMANZADEH ASL*⊙, Levent KARA**⊙

*Engineering Faculty, Mechanical Engineering Department, Karadeniz Technical University, 61080, Trabzon, Turkey
**Engineering Faculty, Mechanical Engineering Department, Erzincan Binali Yıldırım University, 24002 Erzincan,Turkey

yasarsert@ktu.edu.tr, tkomer@ktu.edu.tr, h.kahramanzade@ktu.edu.tr, lkara@erzincan.edu.tr

Abstract: The present study aims to determine the effect of target voltage of boron on elevated temperature wear behaviour of newly designed (Ti, Cr, Nb)-hBN PVD coatings. For this purpose, this layer is grown on the AISI L6 (55NiCrMoV7) at various target voltages (600 V, 700 V) using a high-power impulse magnetron sputtering setup. The coating layer has a graded design and has been coated on the substrate surface in adherence with the following order: Cr – CrN – TiCrN – TiCrNbN and finally TiCrNb-hBN (constituting the working layer). The surface properties of the layer were determined using SEM and an optical profilometer. It is seen that the coatings were deposited on the surface in a granular structure pattern away from the deposition defect (such as a droplet or hole), and the roughness values increase as the target voltage increases. Phase analysis is determined using XRD, and average grain size calculations are performed using the XRD data. The coating layer has grown on the surface at TiN (112), CrN (311), NbN (111) and h-BN (001) orientations. Then, mechanical tests including microhardness and scratch tests were conducted on the specimens. Although the layer that is produced with both different parameters improves the hardness of the substrate (4.7 GPa), the hardness of the coating layer at the voltage of 700 V (24.67 GPa) is higher than that of others. Based on scratch tests, scratch crack propagation resistance (CPR) values were determined as 40 N2 and 1,650 N2 for coatings produced at 600 V and 700 V, respectively. The wear behaviours of specimens are specified using a ball-on-disc type tribometer at 450°C. It is seen that the coating with high hardness and scratch resistance offers unique contributions to the wear performance of the substrate. The optimum value of the target voltage to be used in the production of this innovative coating has been introduced into the literature.

Key words: TiCrNb-hBN, target voltage, elevated temperature, scratch, wear

1. INTRODUCTION

The surfaces of the mechanical parts used in industrial applications are damaged owing to friction and wear, and as a result of relative contact, these eventually undergo enough wear so as to require being put out of use [1]. Wear in unsatisfactory service times increases the costs of manufacturing. For industrial companies, it has become an important need to improve the wear performance of the mechanical parts. From past to present, various researches have been carried out to meet this requirement [2]. It has been determined that the service life of the material can be increased by improving the wear performance attributable to some surface treatment methods [3]. Boronising, carburising, nitriding and especially films produced from thin hard coating with vacuum technology are some of the most widely used surface treatments [4, 5]. Among them, PVD coatings stand out with their effective use and successful results [6]. The binary, ternary and quaternary layers in the composite structure are produced from transition metals (Ti, Cr, Zr, Al, Nb, V, Y etc.), and these nitrides are widely used [7–9]. TiN is the first coating produced to improve the hardness, friction and wear properties of components [10]. Afterwards, with the addition of other transition metals to the TiN structure, ternary and quaternary coatings were produced, thus improving the performance of the TiN layer under harsh working conditions [11]. TiCrNb-hBN coating layer, which constitutes the novelty of

this study, was produced to further the usage performance of TiN coatings for the above-mentioned purpose. Various techniques are employed in the production of PVD coatings [12, 13]. Among these techniques, the magnetron sputtering method is effectively used in the production of dense coatings that are free from deposit defects. In the magnetron sputtering method, the coating production parameters are one of the most important factors that control the coating properties. Therefore, the performance of the deposited layer depends on the correct selection of the coating parameters, including deposition parameters such as working pressure, bias voltage, target material voltage, duty time and frequency. Bhaduri et al. [14] deposited TiN coatings on the M2 steel surface using different bias voltage and target frequency values. When the effects of the variable parameters were examined, it was determined that the microhardness value improved steadily with increasing the target frequency from 50 kHz to 300 kHz [14]. Also, the critical load increased up to the bias voltage of −70 V and then decreased with the further increase of the bias voltage. The reason attributed for this is that the coating becomes densely layered, and the grain size decreases with the increase of the bias voltage [14]. In another study, the effect of Mo target current on CrMoSiCN coatings was determined. By increasing the current value from 0.5 A to 2 A, the columnar structure in the coating layer became denser and blurred. The coatings produced with 2 A exhibited the superior hardness and wear performance [15].

Yaşar Sert, Tevfik Küçükömeroğlu, Hojjat Ghahramanzadeh Asl, Levent Kara
The Effect of "B" Target Voltage on Wear Properties of TiCrNb-hBN Coatings

DOI 10.2478/ama-2023-0067

2. MATERIAL AND METHODS

In this study, 1.2714 (55NiCrMoV7) hot work tool steels were prepared based on in-demand dimensions for the coating process and laboratory tests with the use of machining. Before the deposition processes, the substrates were ground via 400, 800, 1,200 and 2,000 mesh SiC papers and then polished with a 1-µm Al_2O_3 solution until surface roughness reached the value of Ra $\cong$ 50 nm. The polished substrates were cleaned with ethanol for the deposition process. Then, steel samples were coated with the TiCrNb-hBN layer using the high-power impulse closed field unbalanced magnetron sputtering method. Ti, Cr, Nb and LaB_6 targets were used to create the desired structure on the substrate surface. In the coating process, Ti current of 6 A, Cr current of 2 A and Nb voltage of 500 V were applied at constant values. In addition, the coating deposition time was 90 min. The coating assembly and the placement of the target materials in the system are shown in Fig. 1. The parameters used in the coating processes are given in Tab. 1.

Tab. 1. Deposition parameters

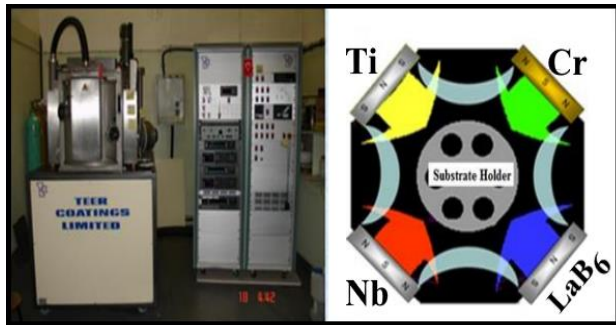| Coating No.	Bias voltage (V)	Working pressure (Torr)	"B" target voltage (V)
B1	100	2.5×10^{-3}	600
B2	100	2.5×10^{-3}	700

Fig. 1. Coating unit and placement of targets in the system

The microstructure and coatings' thickness were examined using a scanning electron microscope (Zeiss EVO LS10, Germany). The average surface roughness of samples was determined using an optical profilometer (Nanofocus, Germany). The phase analyses of coatings were carried out using Bragg-Brentano mode XRD (Panalytical X'Pert3, UK). The hardness and adhesion strength of the coatings were determined using nanohardness (Hysitron Ti 950, USA) and scratch tests (CSM Revetest RST, USA). The wear behaviours of the samples were investigated using a ball-on-disc type tribometer (UTS, Turkey) at 450°C, as shown in Fig. 2. The wear tests were carried out using the parameters of a constant load of 2 N, wear track diameter of 10 mm, cycles of 2,000 and velocity of 60 mm/s. An Al_2O_3 ball with a diameter of 6 mm was used for the counter body. Al_2O_3 counter bodies were preferred owing to their high hardness and toughness. In this way, it is possible to determine the wear resistance of the produced coatings under more difficult challenges. The wear rates of the coatings were determined using the Archard equation: W = V/(P*d), where W is the wear rate (mm^3/Nm), V is the wear volume (mm^3), P is applied load (N) and d is the distance of slid-

ing (m). The wear mechanism was characterised as being a result of SEM investigations of the wear tracks.
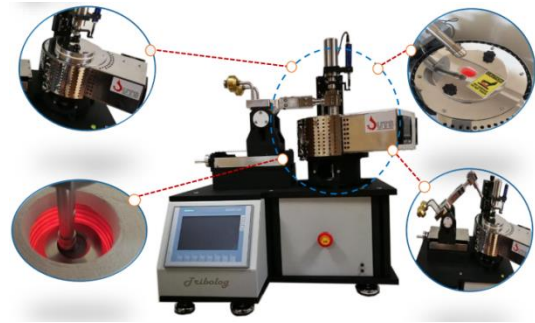

Fig. 2. The ball-on-disc type tribometer (UTS, Turkey)

3. RESULTS AND DISCUSSION

The surface and cross-sectional SEM images of the produced coating layers are shown in Figs 3 and 4. As seen in the figures, the coating layer became denser and fine-grained with increasing "B" target material voltage (600–700 V). It was determined that by increasing the target material voltage, the mobility of the ions sputtered from the target material increased and better absorbed to the substrate surface. On the other hand, the coating thickness values decreased with the increase of the voltage value. While a coating thickness of 1.33 µm is obtained in the B1 coating produced at 600 V, this value decreased to 967 nm at 700 V. Tab. 2 confirms that the obtained elemental proportions of the coatings are consistent with the coating structures.
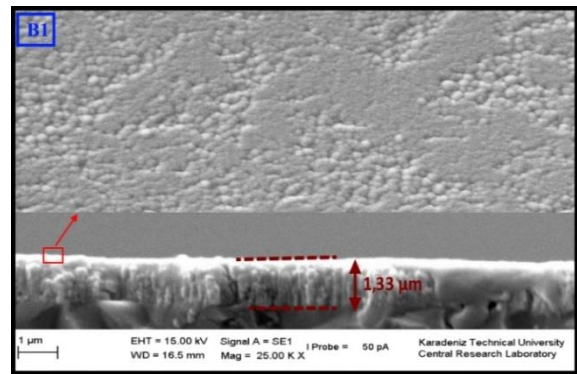

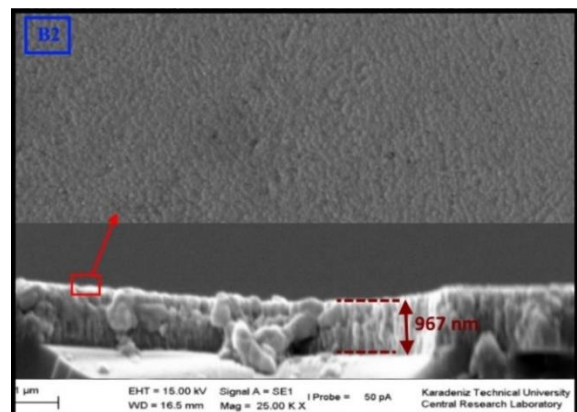**Fig. 3.** The surface and cross-sectional SEM image of B1 coatings

Fig. 4. The surface and cross-sectional SEM image of B2 coatings

Tab. 2. Chemical composition of coatings (wt.%)

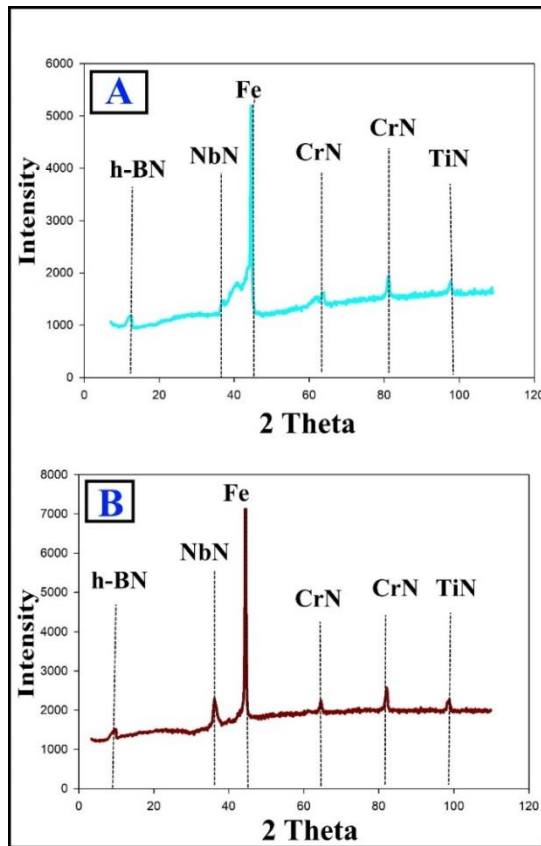| Coating No.	Ti	Cr	Nb	B	N
B1	28.88	21.77	1.9	12.78	29.11
B2	18.25	18.22	0.9	15.9	49.54

Fig. 5. XRD graph of coatings (A) TiCrNb-hBN (600 V)
and (B) TiCrNbN-hBN (700 V)

Tab. 3. The mechanical and tribological properties of samples

Samples	Grain size (µm)	Surface roughness (nm)	Nano-hardness (GPa)	Adhesion strength (N)	CPRs (N²)	CoF (µ)
Substrate	-	50	4.7	-	-	0.67
B1	37.8	55	12.87	13	40	0.62
B2	19.8	72	24.67	85	1,650	0.26

The XRD graphs of coatings are given in Fig. 5. According to this figure, h-BN, NbN, Fe, TiN and CrN phases are formed in these coatings. The lowest intensity of Fe peaks is determined in the B1 (TiCrNb-hBN/600 V) coating layer. It is perceptible on analysis that this finding demonstrates a good consistency with the changes occurring in coating thickness values, i.e. a higher intensity Fe peak, together with the substrate material effect, is observed to characterise coatings that have a lower thickness value. Among the phases forming the coating, CrN and NbN are dominant structures especially in the B2 coating. It is emphasised that the peak widths increase with the increase in the "B" target voltage value in the coatings, which is a sign of a decrease in

grain size. In calculations carried out with the Scherrer approach using XRD data, grain size values are determined as 37.8 nm and 19.8 nm in the B1 and B2 coatings, respectively, as seen in Table 2. The calculated grain size values are also compatible with the surface SEM images given in Fig. 2. In addition, the surface roughness values (Ra) of the coatings are given in Table 3. It is observed that the surface roughness of the coatings is higher than that of the substrate. However, as the B voltage value increased, the surface roughness value also increased.

The hardness, adhesion strength, friction coefficient (COF) and wear rate values of the coatings obtained as a result of mechanical and tribological tests are shown in Table 3. As can be seen from this table, the nanohardness values of the coatings produced under both conditions (600 V and 700 V) are superior in comparison with those of the 1.2714 steel substrate. While the hardness of the substrate is determined as 4.7 GPa, the hardness of the coatings is obtained as 12.87 GPa and 24.67 GPa for the B1 and B2 samples, respectively. It should not be overlooked that the hardness value of the coating increases by approximately 100% with the increase of the target material voltage. It is observed that the hardness value of the B2 coating is superior in comparison with that of the other samples owing to its low grain and dense structure. It is striking that the TiCrNb-hBN coating deposited at a target voltage of 700 V has excellent resistance to plastic deformation. Considering the adhesion strength values of the coatings, a high Lc_2 value of 85 N is obtained in the B2 coating with high nanohardness. On the other hand, a relatively low adhesion strength value of 13 N is obtained in the layer produced at the 600 V voltage. Therefore, the high adhesion strength of the B2 coatings may also be associated with high hardness. Besides, it was obvious that the coating layers were exposed to plastic deformation in the scratch test. The higher hardness also provides higher resistance to plastic deformation. Previous studies pointed out that the adhesion strength values were improved linearly with increasing the hardness, as in agreement with the findings in the present study [16]. The scratch crack propagation (CPR) is a qualitative indicator of coating toughness, which can be formulated as CPRs: $Lc_1 * (Lc_2 – Lc_1)$. It is determined that the strength of fracture toughness increased as the target voltage of boron in the coatings increased.
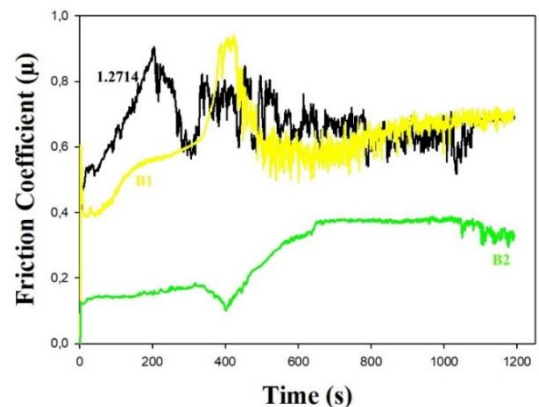

Fig. 6. The COF graph of samples. COF, coefficient of friction

The COF graphs obtained as a result of the wear tests of the samples are given in Fig. 6. In the first stages of the wear tests, the COF values suddenly increased. In the literature, this stage is referred to as the running-in, i.e. the acclimation of the friction caused by the roughness of the surfaces to each other. As the

Yaşar Sert, Tevfik Küçükömeroğlu, Hojjat Ghahramanzadeh Asl, Levent Kara
The Effect of "B" Target Voltage on Wear Properties of TiCrNb-hBN Coatings

DOI 10.2478/ama-2023-0067

surface roughness of the samples is crushed, the graph becomes more stable. In the base material where COF waves are shown in black, the surface roughness that was crushed after the running-in phase was broken by the progress of the cycle and caused wear.
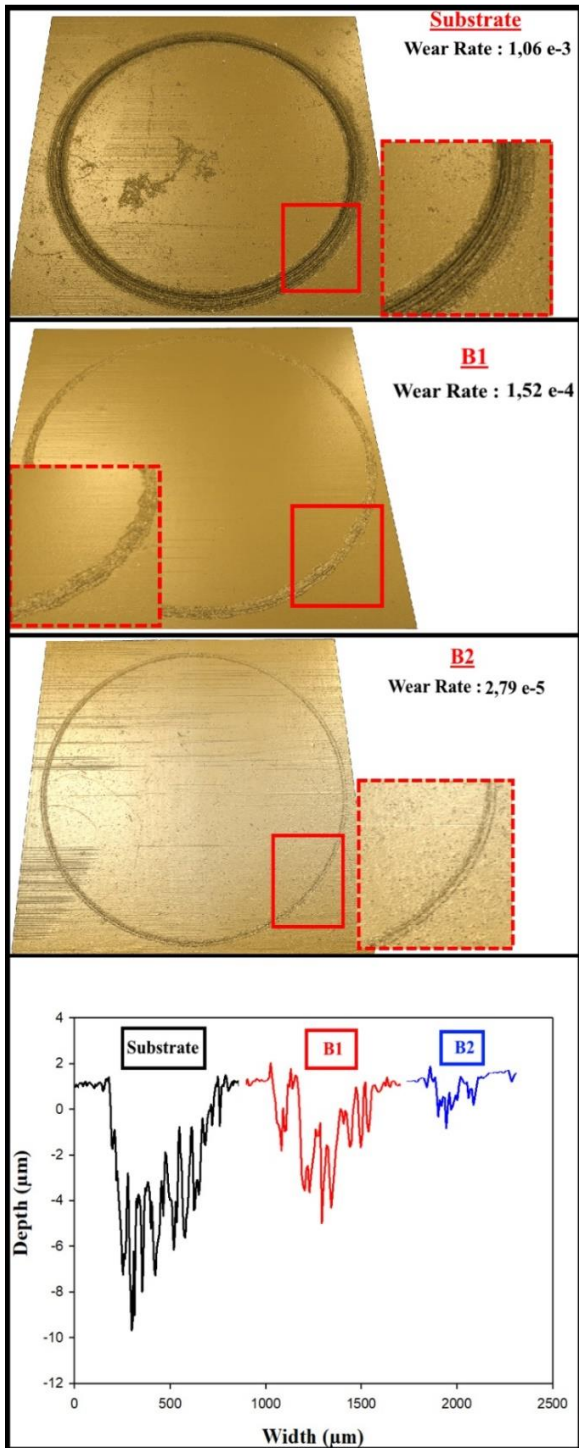

Fig. 7. Optical profilometer image of wear paths of samples

As can be seen from the graph, this wear occurred in the form of third body wear when the particles that were trapped between the mating surfaces underwent detachment from the surface. The wear process undergone by the B1 coating is highly similar to that by the substrate, as demonstrated clearly by the fluctuations apparent in Fig. 6. After the running-in phase, the coating particles
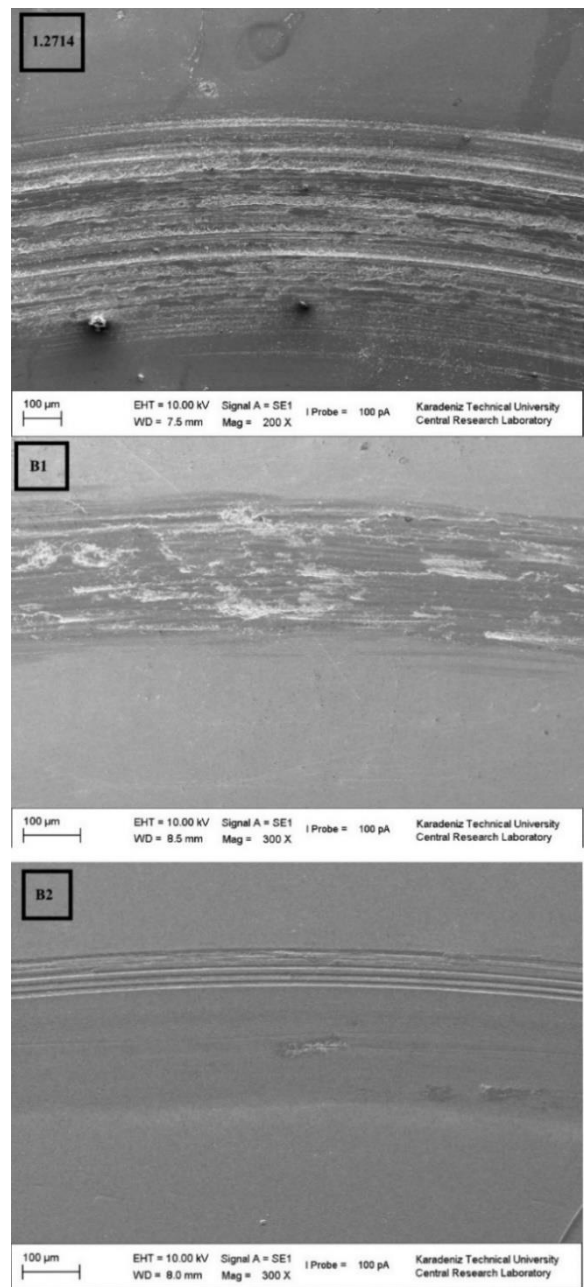
that were broken off in the continuation of the cycle caused abrasive wear here as well. Therefore, the coating layer lost its protection, and the wear continued on the 1.2714 steel. The situation is completely different in the B2 coating. After the sudden increase in the COF value, the graph progressed in a steady state up to 400 s. Subsequently, as manifest in the fluctuations visible in Fig. 6's graph, the partially ruptured par-ticles caused an increase in the COF, and this is attributed to the high hardness of the B2 coating layer. However, the wear seen after the 400th second did not separate the coating layer from the surface until the end of the cycle, thus ensuring that the COF was lower than that of the other samples. The optical profilometer images of the wear paths and the depth profile are shown in Fig. 7. The wear rate values of the coatings are also in a consistent correlation with the COF graph and values. The B2 coating significantly increased the wear performance of the steel (1.065e–3 mm3/Nm), with a wear rate of 2.79e–5 mm3/Nm.

Fig. 8. The SEM image of wear tracks

The SEM images of the wear tracks of samples are given in Fig. 8. As can be seen from this figure, the particles broken off owing to oxidation in the substrate have caused deep grooves and abrasive scratches in 1.2714 steel. It is clearly visible of the wear debris settled in the wear track. This appearance in the wear track of the substrate confirms the statements made in accordance with the COF graph in Fig. 4. On the B1 coating, it was determined that the wear track was similar to that of the substrate. Here, too, the ruptured wear particles entered between the friction surfaces and caused abrasive scratches. Besides, the irregularities in the coating layer are evident. As stated above, local abrasive scratches occurred in the edge of the wear track on the B2 coating. Except for the upper corner of the wear track, no significant damage has occurred. By maintaining its protective coating layer, it has made unique contributions to the wear performance of the substrate.

Tab. 4. Chemical composition of wear paths of coatings under high temperature conditions

Coating No.	O	Fe	Ti	Cr	Nb	B	N
B1	31.3	35.3	16.4	12.4	0.9	0.8	2.9
B2	20.7	10.1	15.6	17.3	0.9	7.3	20.7

Table 4 shows the result of the Energy-dispersive spectroscopy (EDS) analysis of the wear tracks of the coatings. As can be seen from the table, it is evident from the "Fe" value that the layer is separated from the surface in the B1 coating layer. It is also obvious that the "O" value in this coating layer is higher than that in the B2 coating. However, when the coating composition values given in Table 2 are compared with the values taken from the wear path, it can be observed that the element content in the coating layer within the wear path has decreased, and that, as a result of friction heat and relative contact as well as owing to oxidation, O_2 formation has taken place in the structure. The decrease in composition values is less in the B2 coating. This indicates that the protection of the coating layer is superior.

4. CONCLUSIONS

TiCrNb-hBN coatings with various target voltages of boron have been successfully implemented using the closed field unbalanced magnetron sputtering method. The influence of target voltage on microstructure and mechanical and tribological properties of TiCrNb-hBN coatings has been investigated. The results are summarised as follows:

– The TiCrNb-hBN coating layer was deposited on the 1.2714 steel samples in a columnar structure.
– With the increase in the target voltage (600 V to 700 V), the coating structure became more compact and fine-grained. A coating thickness of 1,329 μm was obtained in the B1 coating produced at 600 V. When the voltage value was increased to 700 V, the thickness value decreased to 967 nm.
– In the grain size values obtained from the XRD data, this value is 37.8 nm for the B1 coating and 19.8 nm for the B2 coating.
– While both coating conditions significantly increased the hardness of the substrate, an ultra-hardness value of 24.67 GPa was obtained in the B2 coating layer.
– The adhesion strength values (Lc2) of the B1 and B2 coatings

were determined as 13 N and 85 N, respectively.
– The crack propagation strengths of the B1 and B2 coatings were calculated as 40 N2 and 1650 N2, respectively.
– While the COF value in the B1 coating was similar to that of the substrate, a low COF value of 0.26 was obtained in the B2 coating.
– The friction feature of the steel at high temperature has been improved owing to the h-BN structure in the coatings produced at the voltage of 700 V. The wear performance of the B2 coating is also striking, as is the COF.

REFERENCES

1. Liao L, Gao R, Yang H, Wu S T, Wan Q. A study on the wear and corrosion resistance of high-entropy alloy treated with laser shock peening and PVD coating. Surface and Coatings Technology. 2022; 437: 128281. https://doi.org/10.1016/j.surfcoat.2022.128281
2. Yumusak G, Leyland A, Matthews A. A microabrasion wear study of nitrided α-Ti and β-TiNb PVD metallic thin films, pre-deposited onto titanium alloy substrates. Surface and Coatings Technology.2022;442:128423. https://doi.org/10.1016/j.surfcoat.2022.128423
3. Sert Y, Ghahramazadeh Asl H, Küçükömeroğlu T. Tribological properties of in-situ PVD TiAlN, TiSiN, and TiAlN/TiSiN coatings under ambient air and vacuum environment. Proceedings of the Institution of Mechanical Engineers, Part L: Journal of Materials: Design and Applications.2022;236:1777–1792. https://doi.org/10.1177/14644207221083237
4. Türkmen, İ, Kanbur K, Sargin F. Characteristics of boronized Ti6Al4V alloy using boric acid based boronizing mixture. Materials Characterization.2022;192:112180. https://doi.org/10.1016/j.matchar.2022.112180
5. Prasad Arun M, Dharmalingam G, Salunkhe S. Microstructural evaluation of gas nitrided AISI 316 LN austenitic stainless steel. Materials Today:Proceedings.2022;68:1887–1890. https://doi.org/10.1016/j.matpr.2022.08.060
6. Lee J-K, Yang G-S. Preparation of TiAlN/ZrN and TiCrN/ZrN multilayers by RF magnetron sputtering. Transactions of Nonferrous Metals Society of China. 2009;19:795–799. https://doi.org/10.1016/S1003-6326(08)60352-0.
7. Shukla V N, Saini H, Kumar D, Gupta G. Corrosion Studies of Nanostructured AlN Coating Deposited on 23/8N Nitronic Steel by PVD Method. Materials Today: Proceedings. 2017;4:10216–10220. https://doi.org/10.1016/j.matpr.2017.06.351
8. Yi, J, Mao, Q, Liang W, Ding Z, Qi Y, Liu Y, Zhao H, Yin M, A novel Nb pre-diffusion method for fabricating wear-resistant NbN ceramic gradient coating. Vacuum. 2021;185:109993. https://doi.org/10.1016/j.vacuum.2020.109993
9. Hosokawa A, Saito R, Ueda T, Milling characteristics of VN/AlCrN-multilayer PVD coated tools with lubricity and heat resistance. CIRP Annals. 2020;69:49–52. https://doi.org/10.1016/j.cirp.2020.04.026
10. Hodroj A, Pierson J F. Development of novel titanium nitride-based decorative coatings by calcium addition. Applied Surface Science. 2011;257:8525–8528. https://doi.org/10.1016/j.apsusc.2011.04.144
11. Liang J, Gao H, Xiang S, Chen L, You Z, Lei Y. Research on tool wear morphology and mechanism during turning nickel-based alloy GH4169 with PVD-TiAlN coated carbide tool. Wear. 2022;508–509:204468. https://doi.org/10.1016/j.wear.2022.204468.
12. Tillmann W, Kokalj D, Stangier D, Fu Q, Kruis F E. Influence of the PVD process conditions on the incorporation of TiN nanoparticles into magnetron sputtered CrN thin films. Surface and Coatings Technology.2021;409:126935. https://doi.org/10.1016/j.surfcoat.2021.126935
13. Ravi N, Markandeya R, Joshi S V. Effect of nitrogen pressure on mechanical properties of nc-TiAlN/a-Si3N4 nanocomposite coatings deposited by cathodic arc PVD process. Materials Today: Proceedings. 2016;3:3002–3011. https://doi.org/10.1016/j.matpr.2016.09.014.

14. Bhaduri D, Ghosh A, Gangopadhyay S, Paul S, Effect of target frequency, bias voltage and bias frequency on microstructure and mechanical properties of pulsed DC CFUBM sputtered TiN coating. Surface and Coatings Technology. 2010;204:3684–3697. https://doi.org/10.1016/j.surfcoat.2010.04.047
15. Fu Y, Zhou F, Wang Q, Zhang M, Zhou Z, Yan Li L K. The influence of Mo target current on the microstructure, mechanical and tribological properties of CrMoSiCN coatings in artificial seawater. Journal of Alloys and Compounds. 2019;791:800–13. https://doi.org/10.1016/j.jallcom.2019.03.351
16. Bidev, F, Baran Ö, Arslan E, Totik Y, Efeoğlu İ. Adhesion and fatigue properties of Ti/TiB2/MoS2 graded-composite coatings deposited by closed-field unbalanced magnetron sputtering. Surface and Coatings Technology. 2013; 215: 266–2714. https://doi.org/10.1016/j.surfcoat.2012.08.091

Yaşar Sert: https://orcid.org/0000-0001-7742-0335

Tevfik Küçükömeroğlu: https://orcid.org/0000-0002-4392-9966

Hojjat Ghahramazadeh Asl: https://orcid.org/0000-0002-9078-1933

Levent Kara: https://orcid.org/0000-0002-6982-859X

EXACT ANALYSIS OF FRACTIONALISED JEFFREY FLUID IN A CHANNEL
WITH CAPUTO AND CAPUTO FABRIZIO TIME DERIVATIVE: A COMPARATIVE STUDY

Maryam ASGIR*[ORCID], Muhammad Bilal RIAZ**,***[ORCID], Ayesha ISLAM***[ORCID]

*Department of Mathematics, Riphah International University, Lahore, 54000, Pakistan
**Faculty of Applied Physics and Mathematics, Gdansk University of Technology, 80-233 Gdansk, Poland
**Department of Computer Science and Mathematics, Lebanese American University, Byblos, Lebanon
***Department of Mathematics, University of Management and Technology, 54770 Lahore, Pakistan
**Department of Physics, University of Management and Technology, Lahore, 54770, Pakistan

maryam.asghar90@gmail.com, muhammad.riaz@pg.edu.pl, ayesha.islam@umt.edu.pk

Abstract: The non-integer order derivatives, Caputo (C) and Caputo Fabrizio (CF), were employed to analyse the natural convective flow of magnetohydrodynamic (MHD) Jeffrey fluid. The aim is to generalise the idea of Jeffrey's fluid flow. The fluid flow is elaborated between two vertical parallel plates. One plate is kept fixed while the other is moving with the velocity $U_0 f(t)$, which induces the motion in the fluid. The fluid flow problem is modelled in terms of the partial differential equation along with generalised physical conditions. The appropriate parameters are introduced to the dimensionless system of equations. To obtain the solutions, the Laplace transform (LT) is operated on the fractional system of equations, and the results are presented in series form. The pertinent parameter's influence on the fluid flow is brought under consideration to reveal interesting results. In comparison, we noticed that the C approach shows better results than CF, and graphs are drawn to show the results. The results for ordinary Jeffrey fluid, second-grade and viscous fluid are obtained in a limiting sense.

Keywords: Jeffrey fluid, porous medium, natural convection, magnetohydrodynamic, Laplace transform, Caputo derivative,
Caputo Fabrizio derivative

1. INTRODUCTION

The Navier–Stokes equation cannot characterise the mechanical features of non-Newtonian fluids owing to their complex nature. So, the rheological behaviour of non-Newtonian fluids cannot be described enough with a single constitutive equation. Non-Newtonian fluids with their rheological behaviour makes them valuable for many industrial and technological applications, for instance, in the petroleum, biological, plastic manufacturing, chemical, textile and cosmetic industries. There are several models accorded to describe the resourceful nature of non-Newtonian fluids [1,2]. In addition, Jeffrey fluid is obtained to be the simplest generalisation of the Newtonian fluid. This fluid model is apt for narrating the characteristics of relaxation and retardation times. From the model of Jeffrey fluid, the second-grade and viscous fluid models can be deduced by disregarding the impacts of their generalised parameters. Being mindful of its properties and abilities, the wide application of Jeffrey fluid is noticed in biological science such as in plasma, handling of biological fluid and blood, and in mechanics. Hayat et al. [3] highlighted the chain solution of the magnetohydrodynamic (MHD) Jeffrey fluid in a channel. MHD analysis along with the slip condition on Jeffrey fluid was reported by Das et al. [4]. Imtiaz et al. [5] initiated the study of MHD Jeffrey fluid and highlighted the effects of heterogeneous and homogeneous reactions on the fluid flow. The effects of heat generation on MHD Jeffrey fluid in a porous medium were studied by Jena et al. [6].

Similar studies on MHD Jeffrey fluid are recorded in literature [7–14] and the references therein. The versatile and valuable impacts of fractional calculus in the field of electrical engineering, electrochemistry, control theory, electromagnetism, mechanics, image processing, bioengineering, physics, finance, fluid dynamics and many others make it a valuable tool for study. For systems that have long-term memory, fractional derivatives are very important and suitable because they record not only the present but also the past. It has numerous applications in physical science, such as chemistry, ecology, geology and biology. The mechanism of non-Newtonian models has been elaborated successfully with fractional calculus in the past decades due to its simple and elegant description of the complexity of its behaviour. One of the important non-Newtonian fluids is viscoelastic fluids which exhibit the behaviour of elasticity and viscosity. These fluids have broad implications and importance in several areas of engineering, such as industrial engineering, polymerisation, mechanical engineering and the automobile industry. Fractional calculus is very helpful in interpreting the viscoelastic nature of the materials. Taking into account the enormous properties mentioned, many researchers have paid attention to studying it directly or indirectly in the fractional order derivative field. Bagley and Torvik [15] noted the fractional calculus application on the viscoelastic fluids. Jamil and Khan [16] explored the impacts of slip conditions on the fractional Maxwell fluid and explored the closed solution of shear stress and velocity. Kot and Elmaboud [17] conducted an analysis of heat transfer of the flow of pulsatile time-dependent Maxwell fluid by a vertical stenosed artery with body acceleration. They employed the Cattaneo fractional model to modify the energy equation. Riaz et al. [18] analysed the impacts of heat transfer on MHD fractionalised Oldroyd-B fluid. Semi-analytic and numerical solutions are attained for the

Maryam Asgir, Muhammad Bilal Riaz, Ayesha Islam
Exact Analysis of Fractionalised Jeffrey Fluid in a Channel with Caputo and Caputo Fabrizio Time Derivative: A Comparative Study

DOI 10.2478/ama-2023-0068

electroosmotic flow of the fractionalised Oldroyd-B fluid by Alsharif et al. [19]. The flow takes place in a vertical microchannel that is filled with a porous medium. Khan et al. [20] investigate the Casson fluid with the Caputo (C) time derivative. The C and Caputo Fabrizio (CF) comparative analysis of second-grade fluid with Newtonian heating was investigated by Imran et al. [21]. To reveal the interesting facts on the electroosmotic flow of second-grade fluid, an intriguing study was done by Abdellateef et al. [22]. The flow happens through the vertical microchannel. They considered the heat equation and modified it with the Cattaneo heat flux model and revealed interesting results. Alsharif and Elmaboud [23] considered the above-said problem in the vertical annulus. They solved the problem with the finite Hankel transform and Laplace transform. The results show that as the volume concentration rise, the hybrid nanofluid becomes more viscous, and electroosmotic flow is accelerated by free convection force. Saqib et al. [24] studied the natural convective flow of generalised Jeffrey fluid with the CF approach. Shehzad et al. [25] demonstrate the problem of 3D MHD flow of the Jeffrey fluid along with Newtonian heating. Hayat et al. [26] examined the MHD flow of the Jeffrey fluid through a channel and discovered the series solutions. Farman et al. [27] conducted research to investigate the complex action of the COVID-19 Omicron variant with the CF derivative. A numerical scheme is employed for the computational and simulation of the COVID-19 model. Some of the contributions of the fractional calculus on the viscoelastic fluids are highlighted in literature [28–38].

Inspired by the above literature, this article is devoted to studying the heat and mass transfer analysis of the MHD fractional Jeffrey fluid through a channel along with generalised boundary conditions. In the paper layout, Section 2 describes the governing equation with the geometry of the problem. Preliminaries are stated in Section 3. In Section 4, we have converted the integer-order derivative Jeffrey fluid model with the fractional order derivative C and CF model. The Laplace transform (LT) has been employed to attain the analytical solutions. The analytical expression for velocity, temperature, and concentration are evaluated in a series form. Such exact solutions have never been noted in the literature before. Hence this article makes valuable contributions to the existing literature in view of the pancity of exact solutions of Jeffrey fluid with generalised boundary conditions. In Section 5, limiting cases are discussed. The impacts of parameters on the fluid flow, heat and mass distributions, are captured with the assistance of graphs stated in Section 6. The final conclusions are stated in Section 7.

Tab. 1. Nomenclature

Symbol	Quantity
w	Velocity
B_0	Magnetic force
q	LT Parameter
ϑ	Temperature
k	Heat Conduction
ρ	Density
λ	Relaxation time
σ	Electric Conductivity
μ	Viscosity (Dynamic)
υ	Viscosity (Kinematic)

cp	Specific heat
g	Gravitational force
H_a^2	Hartman number
P_r	Prandtl number
G_r	Grashof number(thermal)
K	Porosity
λ_1	Jeffrey fluid parameter
D	Mass diffusivity
G_c	Grashof number(mass)
S_c	Schmidt number

2. MODEL GOVERNING EQUATIONS

The phenomenon of heat and mass transfer of the convective MHD Jeffrey fluid flow is examined. The fluid is submerged in a permeable medium between two upright plates at $\xi^* = 0$ and $\xi^* = d$. At $t^* = 0$, plates and fluid are both static with the ambient temperature ϑ_∞ and concentration ϕ_∞. As $t^* > 0$, the plate at the $\xi^* = 0$ starts to move with velocity $U_0 f(t^*)$, while the other plate is kept fixed. The temperature of the plate descends or ascends to $\vartheta_d + (\vartheta_w - \vartheta_d)g(t^*)$, and concentration $\phi_d + (\phi_w - \phi_d)h(t^*)$, where $f(t^*), g(t^*)$ and $h(t^*)$ are continuous functions and have zero value at $t^* = 0$. Furthermore, a transverse magnetic force is introduced vertically to the fluid flow. By neglecting the impacts of an induced magnetic field, Joule heating, viscous dissipation and assuming that the velocity is a function of ξ^* and t^* only, the governing equation for the fluid flow description using Boussinesq approximation [39, 40] along with concentration equation will take the form

$$\frac{\partial \omega(\zeta^*, t^*)}{\partial t^*} =$$
$$\frac{\upsilon}{1 + \lambda_1}\left(1 + \lambda_r \frac{\partial}{\partial t^*}\right)\frac{\partial^2 \omega(\zeta^*, t^*)}{\partial \zeta^{*2}} - \left(\frac{\upsilon \phi}{k_1} + \frac{\sigma B_0^2}{\rho}\right)\omega(\zeta^*, t^*) + g\beta_\vartheta(\vartheta_w - \vartheta_d) + g\beta_\phi(\phi - \phi_d), \tag{1}$$

$$\rho C_p \frac{\partial \vartheta(\zeta^*, t^*)}{\partial t^*} = k \frac{\partial^2 \vartheta(\zeta^*, t^*)}{\partial \zeta^{*2}}, \tag{2}$$

$$\frac{\partial \phi(\zeta^*, t^*)}{\partial t^*} = D \frac{\partial^2 \phi(\zeta^*, t^*)}{\partial \zeta^{*2}}. \tag{3}$$

The system imposed conditions related to the present problem are

$$\omega(\zeta^*, 0) = 0, \frac{\partial \omega(\zeta^*, t^*)}{\partial t^*} = 0, \omega(\zeta^*, 0) = 0, \phi(\zeta^*, 0) = 0, \tag{4}$$

$$\omega(0, t^*) = U_0 f(t^*), \ \omega(d, t^*) = 0, \tag{5}$$

$$\vartheta(0, t^*) = \vartheta_d + g(t^*)(\vartheta_w - \vartheta_d), \ \vartheta(d, t^*) = \vartheta_w, \tag{6}$$

$$\phi(0, t^*) = \phi_d + h(t^*)(\phi_w - \phi_d), \ \phi(d, t^*) = \phi_w. \tag{7}$$

For the process of dimensionalisation, the following constants and parameters are introduced as

$$\omega' = \frac{\omega}{U_0}, \zeta' = \frac{\zeta^*}{d}, \vartheta' = \frac{\vartheta - \vartheta_d}{\vartheta_w - \vartheta_d}, t' = \frac{\upsilon t^*}{d^2}, P_r = \frac{\mu c_p}{k}, S_c = \frac{\upsilon}{D}, K = \frac{k_1}{\phi d^2}, \lambda = \frac{\lambda_r \upsilon}{d^2},$$

$$H_a^2 = \sqrt{\frac{\sigma}{\mu}} B_0 d, G_r = \frac{g\beta_\vartheta \upsilon(\vartheta_w - \vartheta_d)}{U_0^3}, G_c = \frac{g\beta_\phi \upsilon(\phi_w - \phi_d)}{U_0^3}. \tag{8}$$

After implementing Eq. (8) into Eqs (1)–(7), the governing equations are expressed after dropping the "/"

$$\frac{\partial \omega(\zeta,t)}{\partial x} = \frac{1}{1+\lambda_1}\left(1 + \lambda\frac{\partial}{\partial t}\right)\frac{\partial^2 \omega(\zeta,t)}{\partial \xi^2} - \left(\frac{1}{K} + H_a^2\right)\omega(\zeta,t) + G_r\vartheta(\zeta,t) + G_c\phi(\zeta,t), \quad (9)$$

$$P_r\frac{\partial \vartheta(\zeta,t)}{\partial t} = \frac{\partial^2 \vartheta(\zeta,t)}{\partial \xi^2}, \quad (10)$$

$$S_c\frac{\partial \phi(\zeta,t)}{\partial t} = \frac{\partial^2 \phi(\zeta,t)}{\partial \xi^2}, \quad (11)$$

The imposed conditions in Eqs (4)–(7) for the velocity, temperature and concentration profiles become

$$\omega(\zeta,0) = 0, \frac{\partial \omega(\zeta,0)}{\partial t} = 0, \; \vartheta(\zeta,0) = 0, \phi(\zeta,0) = 0, \quad (12)$$

$$\omega(0,t) = f(t), \omega(1,t) = 0, \vartheta(0,t) = g(t), \vartheta(1,t) = 1, \phi(0,t) = h(t), \phi(1,t), \quad (13)$$

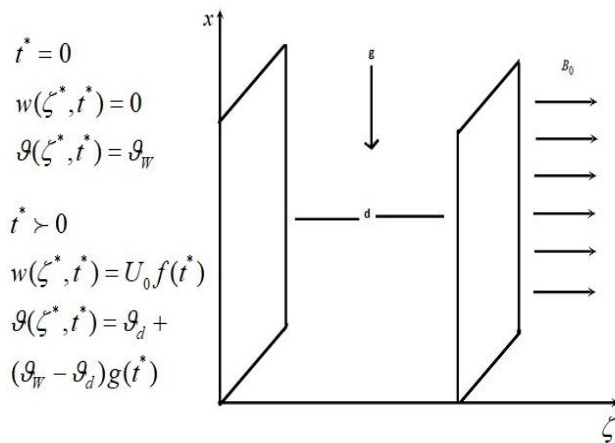where all the quantities and parameters are stated in the nomenclature section.

Fig. 1. Geometrical description of the fluid flow phenomenon

3. PRELIMINARIES

The function/non-integer C time derivative is stated as

$$^{C}D_t^{\eta}h(\sigma,t) = \frac{1}{\Gamma(1-\eta)}\int_0^t (t-\varrho)^{-\eta}R'(\sigma,\varrho)d\varrho, \quad (14)$$

$\eta \in (0,1)$.

Implement the LT on the C time derivative

$$L\left(^{C}D_t^{\eta}R(\sigma,t)\right) = s^n L(R(\sigma,t) - s^{n-1}R(\sigma,0)). \quad (15)$$

The non-integer CF time derivative is defined as

$$^{CF}D_t^{\eta}R(\sigma,t) = \frac{1}{(1-\eta)}\int_0^t e^{\left(\frac{-\eta(t-\varrho)}{1-\eta}\right)}R'(\sigma,\varrho)d\varrho, \quad (16)$$

$\eta \in (0,1)$

Applying the LT on the time fractional CF derivative changes to

$$L\left(^{CF}D_t^{\eta}R(\sigma,t)\right) = \frac{sL(R(\sigma,t)) - R(\sigma,0)}{s(1-\eta)+\eta}. \quad (17)$$

4. FRACTIONAL FORMULATIONS OF GOVERNING EQUATIONS AND SOLUTIONS

4.1. Caputo formulation and solutions

Replace the time derivative with the C fractional derivative into Eqs (9)–(11) as,

$$^{C}D_t^{\eta}\omega(\zeta,t) = \frac{1}{1+\lambda_1}\left(1 + \lambda\,^{C}D_t^{\eta}\right)\frac{\partial^2 \omega(\zeta,t)}{\partial \xi^2} - \left(\frac{1}{K} + H_a^2\right)\omega(\zeta,t) + G_r\vartheta(\zeta,t) + G_c\phi(\zeta,t), \quad (18)$$

$$P_r\,^{C}D_t^{\eta}\vartheta(\zeta,t) = \frac{\partial^2 \vartheta(\zeta,t)}{\partial \xi^2}, \quad (19)$$

$$S_c\,^{C}D_t^{\eta}\phi(\zeta,t) = \frac{\partial^2 \phi(\zeta,t)}{\partial \xi^2}, \quad (20)$$

4.1.1 Investigation of exact solution for temperature profile

Implementing LT on Eq. (19), we will obtain with transform boundary conditions

$$\frac{\partial^2 \bar{\vartheta}(\zeta,q)}{\partial \xi^2} - P_r q^n \bar{\vartheta}(\zeta,q) = 0, \quad (21)$$

$$\bar{v}(0,q) = G(q), \; \bar{v}(1,q) = \frac{1}{q}. \quad (22)$$

Employing the Laplace transformed boundary conditions stated in Eq. (22), the solution for Eq. (21) will be as obtained in literature [40]

$$\bar{v}(\zeta,q) = qG(q)\left(\frac{sinh((1-\zeta))}{qsinh(\sqrt{P_r q^n})}\right) + \left(\frac{sinh(\zeta\sqrt{P_r q^n})}{qsinh(\sqrt{P_r q^n})}\right) = qG(q)\vartheta_1(\zeta,q) + \vartheta_2(\zeta,q). \quad (23)$$

Here,

$$\vartheta_1(\zeta,q) = \frac{e^{(1-\zeta)\sqrt{Prq^n}} - e^{-(1-\zeta)\sqrt{Prq^n}}}{q\left(e^{\sqrt{Prq^n}} - e^{-\sqrt{Prq^n}}\right)} = \sum_{n=0}^{\infty}\left(\frac{e^{-(2n-\zeta)\sqrt{Prq^n}}}{q} - \frac{e^{-(2n+2-\zeta)\sqrt{Prq^n}}}{q}\right). \quad (24)$$

$$\vartheta_1(\zeta,q) = \sum_{n=0}^{\infty}\left(\sum_{k=0}^{\infty}\frac{(-1)^k(2n+\zeta)^k(P_r)^{k/2}}{k!\Gamma\left(1-\frac{k\eta}{2}\right)}t^{-\frac{k\eta}{2}} - \sum_{k=0}^{\infty}\frac{(-1)^k(2n+2-\zeta)^k(P_r)^{k/2}}{k!\Gamma\left(1-\frac{k\eta}{2}\right)}t^{-\frac{k\eta}{2}}\right). \quad (25)$$

The expression of $\vartheta_2(\zeta,q)$ is in an expanded from defined as below

$$\vartheta_2(\zeta,q) = \frac{e^{\zeta\sqrt{Prq^n}} - e^{-\zeta\sqrt{Prq^n}}}{q\left(e^{\sqrt{Prq^n}} - e^{-\sqrt{Prq^n}}\right)} = \sum_{n=0}^{\infty}\left(\frac{e^{-(2n+1-\zeta)\sqrt{Prq^n}}}{q} - \frac{e^{-(2n+1-\zeta)\sqrt{Prq^n}}}{q}\right). \quad (26)$$

Implement the inverse LT in Eq. (26) as

$$\vartheta_2(\zeta,t) = \sum_{n=0}^{\infty}\left(\sum_{k=0}^{\infty}\frac{(-1)^k(2n+1-\zeta)^k(P_r)^{k/2}}{k!\Gamma\left(1-\frac{k\eta}{2}\right)}t^{-\frac{k\eta}{2}} - \sum_{k=0}^{\infty}\frac{(-1)^k(2n+1+\zeta)^k(P_r)^{k/2}}{k!\Gamma\left(1-\frac{k\eta}{2}\right)}t^{-\frac{k\eta}{2}}\right). \quad (27)$$

Maryam Asgir, Muhammad Bilal Riaz, Ayesha Islam
Exact Analysis of Fractionalised Jeffrey Fluid in a Channel with Caputo and Caputo Fabrizio Time Derivative: A Comparative Study

DOI 10.2478/ama-2023-0068

Now apply the inverse LT in Eq. (23) as

$$\vartheta(\zeta,t) = \int_0^t g'(t-\tau)\vartheta_1(\zeta,\tau)d\tau + \vartheta_2(\zeta,t), \qquad (28)$$

where $\vartheta_1(\zeta,t)$ and $\vartheta_2(\zeta,t)$ are presented in Eqs (25) and (27) respectively.

4.1.2 Investigation of exact solution for concentration profile

Implementing LT on Eq. (20), and bearing the definition of LT of C derivative, we get

$$\frac{\partial^2 \phi(\zeta,t)}{\partial \xi^2} = S_c\, q^n \bar{\phi}(\zeta,q) = 0, \qquad (29)$$

Along with the transformed boundary conditions

$$\bar{\phi}(0,q) = H(q), \quad \bar{\phi}(1,q) = \frac{1}{q}. \qquad (30)$$

Inserting the prescribed boundary conditions of Eq. (30) while solving Eq. (29), the solution obtained will be

$$\bar{\phi}(\zeta,q) = qH(q)\left(\frac{sinh\left((1-\zeta)\sqrt{S_c q^n}\right)}{q\,sinh(\sqrt{S_c q^n})}\right) + \left(\frac{sinh(\zeta\sqrt{S_c q^n})}{q\,sinh(\sqrt{S_c q^n})}\right), \quad (31)$$

To find the solution $\phi_1(\zeta,q)$, we write it in a simplified form as below

$$\phi_1(\zeta,q) = \frac{e^{(1-\zeta)\sqrt{S_c q^n}} - e^{-(1-\zeta)\sqrt{S_c q^n}}}{q\left(e^{\sqrt{S_c q^n}} - e^{-\sqrt{S_c q^n}}\right)} =$$
$$\sum_{n=0}^{\infty}\left(\frac{e^{-(2n-\zeta)\sqrt{S_c q^n}}}{q} - \frac{e^{-(2n+2-\zeta)\sqrt{S_c q^n}}}{q}\right). \qquad (32)$$

Implement the inverse LT in Eq. (32) as

$$\phi_1(\zeta,q) = \sum_{n=0}^{\infty}\left(\sum_{k=0}^{\infty}\frac{(-1)^k(2n+\zeta)^k(S_c)^{k/2}}{k!\Gamma\left(1-\frac{k\eta}{2}\right)}t^{-\frac{k\eta}{2}} - \right.$$
$$\left. \sum_{k=0}^{\infty}\frac{(-1)^k(2n+2-\zeta)^k(S_c)^{k/2}}{k!\Gamma\left(1-\frac{k\eta}{2}\right)}t^{-\frac{k\eta}{2}}\right). \qquad (33)$$

The expression of $\phi_2(\zeta,q)$ in the simplest form is

$$\phi_1(\zeta,q) = \frac{e^{\sqrt{S_c q^n}} - e^{-\zeta\sqrt{S_c q^n}}}{q\left(e^{\sqrt{S_c q^n}} - e^{-\sqrt{S_c q^n}}\right)} =$$
$$\sum_{n=0}^{\infty}\left(\frac{e^{-(2n+1-\zeta)\sqrt{S_c q^n}}}{q} - \frac{e^{-(2n+1+\zeta)\sqrt{S_c q^n}}}{q}\right). \qquad (34)$$

And employing the inverse LT on Eq. (34), the solution will be

$$\phi_2(\zeta,t) = \sum_{n=0}^{\infty}\left(\sum_{k=0}^{\infty}\frac{(-1)^k(2n+1-\zeta)^k(S_c)^{k/2}}{k!\Gamma\left(1-\frac{k\eta}{2}\right)}t^{-\frac{k\eta}{2}} - \right.$$
$$\left.\sum_{k=0}^{\infty}\frac{(-1)^k(2n+1+\zeta)^k(S_c)^{k/2}}{k!\Gamma\left(1-\frac{k\eta}{2}\right)}t^{-\frac{k\eta}{2}}\right). \qquad (35)$$

Now apply the inverse LT on Eq. (31) as

$$\phi(\zeta,t) = \int_0^t h'(t-\tau)\phi_1(\zeta,\tau)d\tau + \phi_2(\zeta,t), \qquad (36)$$

where $\phi_1(\zeta,t)$ and $\phi_2(\zeta,t)$ are presented in Eqs (33) and (35), respectively.

4.1.3 Investigation of exact solution for velocity profile

Applying the LT into Eq. (18), we get

$$\left(\frac{1+\lambda q^n}{1+\lambda_1}\right)\frac{\partial^2 \bar{\omega}(\zeta,q)}{\partial \xi^2} - \left(q^n + \frac{1}{k} + H_\alpha^2\right)\bar{\omega}(\zeta,q) = $$
$$-G_r \bar{\vartheta}(\zeta,t) - G_c\bar{\phi}(\zeta,t). \qquad (37)$$

After rearranging the above equation, we attain

$$\frac{\partial^2 \bar{\omega}(\zeta,q)}{\partial \xi^2} - Y_1\bar{\omega}(\zeta,q) = \frac{-G_r}{Y_0}\bar{\vartheta}(\zeta,t) - \frac{-G_c}{Y_0}\bar{\phi}(\zeta,t), \qquad (38)$$

where $Y_0 = \frac{1+\lambda q^n}{1+\lambda_1}$, $Y_1 = q^n + \frac{1}{k} + H_\alpha^2$, $Y_2 = \frac{Y_1}{Y_0}$.

The Laplace boundary conditions are

$$\bar{\omega}(0,q) = F(q), \bar{\omega}(1,q) = \qquad (39)$$

Introducing Eqs (23) and (31) into Eq. (38), the velocity solution in abridged form is

$$\bar{\omega}(\zeta,q) = \frac{F(q)}{sinh\sqrt{Y_2}}sinh\left((1-\zeta)\sqrt{Y_2}\right) +$$
$$\frac{G_r}{qY_0(P_r q^n - Y_2)sinh\sqrt{Y_2}}\left(qG(q)sinh(1-\zeta)\sqrt{Y_2} - \right.$$
$$\left. sinh(\zeta\sqrt{Y_2})\right) -$$
$$\frac{G_r}{qY_0(P_r q^n - Y_2)sinh\sqrt{P_r q^n}}\left(qG(q)sinh(1-\zeta)\sqrt{P_r q^n} - \right.$$
$$\left. sinh(\zeta\sqrt{P_r q^n})\right) +$$
$$\frac{G_c}{qY_0(S_c q^n - Y_2)sinh\sqrt{Y_2}}\left(qH(q)sinh(1-\zeta)\sqrt{Y_2} - \right.$$
$$\left. sinh(\zeta\sqrt{Y_2})\right) -$$
$$\frac{G_c}{qY_0(S_c q^n - Y_2)sinh\sqrt{S_c q^n}}\left(qH(q)\,sinh(1-\zeta)\sqrt{S_c q^n} - \right.$$
$$\left. sinh(\zeta\sqrt{S_c q^n})\right). \qquad (40)$$

In order to find its inverse Laplace, we write the velocity expression in a suitable form

$$\bar{\omega}(\zeta,q) = \omega_1(\zeta,q) + \omega_2(\zeta,q) - \omega_3(\zeta,q) + \omega_4(\zeta,q) - \omega_5(\zeta,q) \qquad (41)$$

where

$$\omega_1(\zeta,q) = \frac{F(q)}{sinh\sqrt{Y_2}}sinh\left((1-\zeta)\sqrt{Y_2}\right),$$
$$= F(q)\frac{e^{(1-\zeta)\sqrt{Y_2}} - e^{-(1-\zeta)\sqrt{Y_2}}}{e^{\sqrt{Y_2}} - e^{-\sqrt{Y_2}}},$$
$$= F(q)\sum_{n=0}^{\infty}\left(e^{-(2n+\zeta)\sqrt{Y_2}} - e^{-(2n+2+\zeta)\sqrt{Y_2}}\right). \qquad (42)$$

Eq. (42) in the simplest form as

$$\omega_1(\zeta,q) = F(q)((P(\zeta,q) - Q(\zeta,q)), \qquad (43)$$

where

$$P(\zeta,q) = e^{-(2n+\zeta)\sqrt{Y_2}} =$$
$$\sum_{n=0}^{\infty}\sum_{k=0}^{\infty}\frac{(-Y_3)^k}{k!}\sum_{l=0}^{\infty}\frac{\Gamma\left(\frac{k}{2}+1\right)}{\left(\frac{k}{2}-l+1\right)}\left(\frac{1}{\lambda}\right)^{\frac{k}{2}-l}\left(b - \right.$$
$$\left.\frac{1}{\lambda}\right)^l\sum_{p=0}^{\infty}(-1)^p\frac{\Gamma(l+p)}{p!\Gamma l}\lambda^p q^{\eta p}, \qquad (44)$$

where $Y_3 = (2n+\zeta)\sqrt{1+\lambda_1}$ and $b = \frac{1}{k} + H_\alpha^2$.

P(ζ,t) can be obtained by applying the inverse LT on the above equation

$$P(\zeta,t) = e^{-(2n-\zeta)\sqrt{Y_2}}$$
$$= \sum_{n=0}^{\infty}\sum_{k=0}^{\infty}\frac{(-Y_3)^k}{k!}\sum_{l=0}^{\infty}\frac{\Gamma\left(\frac{k}{2}+1\right)}{\left(\frac{k}{2}-l+1\right)}\left(\frac{1}{\lambda}\right)^{\frac{k}{2}-m}\left(b - \right.$$
$$\left.\frac{1}{\lambda}\right)^l\sum_{p=0}^{\infty}(-1)^p\frac{\Gamma(l+p)}{p!\Gamma l}\lambda^p\frac{t^{-\eta p+1}}{\Gamma(-\eta p)}. \qquad (45)$$

Here,

$$Q(\zeta, q) = e^{-(2n+\zeta)\sqrt{Y_2}} =$$

$$\sum_{n=0}^{\infty} \sum_{k=0}^{\infty} \frac{(-Y_4)^k}{k!} \sum_{l=0}^{\infty} \frac{\Gamma(\frac{k}{2}+1)}{(\frac{k}{2}-l+1)} \left(\frac{1}{\lambda}\right)^{\frac{k}{2}-l} \left(b - \right.$$

$$\left.\frac{1}{\lambda}\right)^l \sum_{p=0}^{\infty} (-1)^p \frac{\Gamma(l+p)}{p!\Gamma l} \lambda^p q^{\eta p}, \tag{46}$$

where $Y_3 = (2n + 2 - \zeta)\sqrt{1 + \lambda_1}$ and $b = \frac{1}{k} + H_\alpha^2$.

Applying the inverse LT on the above equation

$$Q(\zeta, t) = e^{-(2n-\zeta)\sqrt{Y_2}} =$$

$$\sum_{n=0}^{\infty} \sum_{k=0}^{\infty} \frac{(-Y_4)^k}{k!} \sum_{l=0}^{\infty} \frac{\Gamma(\frac{k}{2}+1)}{(\frac{k}{2}-l+1)} \left(\frac{1}{\lambda}\right)^{\frac{k}{2}-l} \left(b - \right.$$

$$\left.\frac{1}{\lambda}\right)^l \sum_{p=0}^{\infty} (-1)^p \frac{\Gamma(l+p)}{p!\Gamma l} \lambda^p \frac{t^{-\eta p+1}}{\Gamma(-\eta p)}. \tag{47}$$

Keeping in view Eqs (45) and (47) and implementing the inverse LT on Eq. (43), the expression obtained for $\omega_1(\zeta, t)$ is as stated below

$$\omega_1(\zeta, t) = f(t) * \left(P(\zeta, t) - Q(\zeta, t)\right). \tag{48}$$

and $\omega_2(\zeta, q)$ is expressed as

$$\omega_2(\zeta, q) = \frac{G_r}{qY_0(P_rq^n - Y_2)sinh\sqrt{Y_2}} \left(qG(q)\sinh(1 - \right.$$

$$\left.\zeta)\sqrt{Y_2}\right) - \sinh(\zeta\sqrt{Y_2})\right) \tag{49}$$

The simplified form of the expression $\omega_2(\zeta, q)$ is

$$\omega_2(\zeta, q) = G_r(1 + \lambda_1)I(\zeta, q)((qG(q)R(\zeta, q) - (\zeta, q)), \tag{50}$$

where

$$I(\zeta, q) = \frac{1}{(P_rq^n(1+\lambda q^n) - (q^n+b)(1+\lambda_1))}, \tag{51}$$

and its inverse LT

$$I(\zeta, q) = -\sum_{n=0}^{\infty} \sum_{n=0}^{\infty} \frac{a_0^{n-k} b_0^k}{c_0^{n+1}} \frac{n!}{k!(n-k)!} \frac{t^{\eta(k-2n)-1}}{\Gamma_n(k-2n)}, \tag{52}$$

where $a_0 = P_r\lambda, b_0 = P_r - 1 - \lambda_1, c_0 = b(1 + \lambda_1)$.

Here,

$$R(\zeta, q) = \frac{sinh((1-\zeta)\sqrt{Y_2})}{qsinh\sqrt{Y_2}}, \tag{53}$$

$$R(\zeta, q) = \frac{sinh(\zeta\sqrt{Y_2})}{qsinh\sqrt{Y_2}}, \tag{54}$$

Inverse LT on Eqs (53) and (54) is stated below as

$$R(\zeta, t) =$$

$$\sum_{n=0}^{\infty} \sum_{k=0}^{\infty} \frac{((-Y_3)^k - (-Y_4)^k)}{n!} \sum_{l=0}^{\infty} \frac{\Gamma(\frac{k}{2}+1)}{(\frac{k}{2}-l+1)} \left(\frac{1}{\lambda}\right)^{\frac{k}{2}-m} \left(b - \right.$$

$$\left.\frac{1}{\lambda}\right)^l \sum_{p=0}^{\infty} (-1)^p \frac{\Gamma(l+p)}{p!\Gamma l} \lambda^p \frac{t^{-\eta p+1}}{\Gamma(-\eta p)}, \tag{55}$$

where

$$Y_3 = (2n + \zeta)\sqrt{1 + \lambda_1} \text{ and } Y_4 = (2n + 2 - \zeta)\sqrt{1 + \lambda_1}$$

$$S(\zeta, t) =$$

$$\sum_{n=0}^{\infty} \sum_{k=0}^{\infty} \frac{((-Y_5)^k - (-Y_6)^k)}{n!} \sum_{l=0}^{\infty} \frac{\Gamma(\frac{k}{2}+1)}{(\frac{k}{2}-l+1)} \left(\frac{1}{\lambda}\right)^{\frac{k}{2}-m} \left(b - \right.$$

$$\left.\frac{1}{\lambda}\right)^l \sum_{p=0}^{\infty} (-1)^p \frac{\Gamma(l+p)}{p!\Gamma l} \lambda^p \frac{t^{-\eta p+1}}{\Gamma(-\eta p)}, \tag{56}$$

$$Y_5 = (2n + 1 + \zeta)\sqrt{1 + \lambda_1} \text{ and } Y_6 = (2n + 1 + \zeta)\sqrt{1 + \lambda_1}$$

Applying the inverse LT in Eq. (50)

$$\omega_2(\zeta, t) = G_r(1 + \lambda_1)I(\zeta, t)$$

$$* \left(g'(t) * R(\zeta, t) - S(\zeta, t)\right), \tag{57}$$

where we get the values of $I(\zeta, t)$, $R(\zeta, t)$ and $S(\zeta, t)$ from Eq. (52), Eq. (55) and Eq. (56) respectively.

Let us consider now

$$\omega_3(\zeta, t) = \frac{G_r}{qY_0(P_rq^n - Y_2)sinh\sqrt{P_rq^n}} \left(qG(q)\sinh(1 - \right.$$

$$\left.\zeta)\sqrt{P_rq^n}\right) - \sinh(\zeta\sqrt{P_rq^n})\right) =$$

$$\frac{G_r(1+\lambda_1)}{(P_rq^n(1+\lambda q^n) - (q^n+b)(1+\lambda_1))} *$$

$$\left(\frac{qG(q)sinh(1-\zeta)\sqrt{P_rq^n} - sinh(\zeta\sqrt{P_rq^n})}{qsinh\sqrt{P_rq^n}}\right) \tag{58}$$

In simplest form $\omega_3(\zeta, q)$ is expressed as

$$\omega_3(\zeta, q) = G_r(1 + \lambda_1)I(\zeta, q)\left(q(G(q)\vartheta_1(\zeta, q) - \vartheta_2(\zeta, q))\right), \tag{59}$$

and its inverse LT expression as

$$\omega_3(\zeta, q) = G_r(1 + \lambda_1)I(\zeta, q)$$

$$* \left(g'(t) * \vartheta_1(\zeta, q) - \vartheta_2(\zeta, q)\right), \tag{60}$$

where $I(\zeta, q), \vartheta_1(\zeta, q), \vartheta_2(\zeta, q)$ are expressed in Eqs (52), (25), and (27), respectively.

Now consider,

$$\omega_4(\zeta, q) = \frac{G_c}{qY_0(S_cq^n - Y_2)sinh\sqrt{Y_2}} \left(qH(q)\sinh(1 - \right.$$

$$\left.\zeta)\sqrt{Y_2}\right) - \sinh(\zeta\sqrt{Y_2})\right) =$$

$$\frac{G_c(1+\lambda_1)}{(S_cq^n(1+\lambda q^n) - (q^n+b)(1+\lambda_1))} *$$

$$\left(\frac{qH(q)sinh(1-\zeta)\sqrt{Y_2} - sinh(\zeta\sqrt{Y_2})}{qsinh\sqrt{Y_2}}\right). \tag{61}$$

$$\omega_4(\zeta, q) = G_c(1 + \lambda_1)J(\zeta, q)\left(q(H(q)R(\zeta, q) - S(\zeta, q)\right), \tag{62}$$

where

$$J(\zeta, q) = \frac{1}{(S_cq^n(1+\lambda q^n) - (q^n+b)(1+\lambda_1))}. \tag{63}$$

Implementing the LT in EQ. (63) gives

$$J(\zeta, t) = -\sum_{n=0}^{\infty} \sum_{k=0}^{\infty} \frac{d_0^{n-k} e_0^k}{c_0^{n+1}} \frac{t^{\eta(k-2n)-1}}{\Gamma_\eta(k-2n)}, \tag{64}$$

where $d_0 = S_c\lambda, \ e_0 = S_c - 1 - \lambda_1, \ c_0 = b(1 + \lambda_1)$.

The $\omega_4(\zeta, q)$ expression takes the form

$$\omega_4(\zeta, q) = G_c(1 + \lambda_1)J(\zeta, t)$$

$$* \left(h'(t) * R(\zeta, t) - S(\zeta, t)\right), \tag{65}$$

where we get the values of $J(\zeta, t)$, $R(\zeta, t)$ and $S(\zeta, t)$ from Eqs (64), (55) and (56), respectively.

$$\omega_5(\zeta, q) = \frac{G_c}{qY_0(S_cq^n - Y_2)sinh\sqrt{S_cq^n}} \left(qH(q)\sinh(1 - \right.$$

$$\left.\zeta)\sqrt{S_cq^n}\right) - \sinh(\zeta\sqrt{S_cq^n})\right) =$$

$$\frac{G_r(1+\lambda_1)}{(S_cq^n(1+\lambda q^n) - (q^n+b)(1+\lambda_1))} *$$

$$\left(\frac{qG(q)sinh(1-\zeta)\sqrt{S_cq^n} - sinh(\zeta\sqrt{S_cq^n})}{qsinh\sqrt{P_rq^n}}\right) \tag{66}$$

Maryam Asgir, Muhammad Bilal Riaz, Ayesha Islam
Exact Analysis of Fractionalised Jeffrey Fluid in a Channel with Caputo and Caputo Fabrizio Time Derivative: A Comparative Study

DOI 10.2478/ama-2023-0068

In simplest form, we can write it as

$$\omega_5(\zeta, q) = G_c(1 + \lambda_1)J(\zeta, q)\big(q(H(q)\phi_1(\zeta, q) - \phi_2(\zeta, q)\big), \tag{67}$$

And its inverse LT

$$\omega_5(\zeta, q) = G_c(1 + \lambda_1)J(\zeta, t) \\ * \big(h'(t) * \phi_1(\zeta, t) - \phi_2(\zeta, t)\big), \tag{68}$$

where $J(\zeta, t), \phi_1(\zeta, t), \phi_2(\zeta, t)$ are obtained in Eqs (64), (33) and (35), respectively.

Introducing the expression of $\omega_1(\zeta, t),\ \omega_2(\zeta, t),\ \omega_3(\zeta, t),$ $\omega_4(\zeta, t), \omega_5(\zeta, t)$ from Eqs (48), (57), (60), (65) and (68), respectively, into Eq. (41) after implementing the LT, the exact velocity solution is achieved as

$$\omega(\zeta, t) = \omega_1(\zeta, t) + \omega_2(\zeta, t) - \omega_3(\zeta, t) + \omega_4(\zeta, t) - \omega_5(\zeta, t) \tag{69}$$

The solution obtained for velocity in Eq. (69) (with $G_c = 0$) is similar to the solution attained in literature [40].

4.2. Caputo Fabrizio formulation and solution

Replace the time deriavtive with the CF fractional derivative into Eqs (9)–(11) as,

$$^{CF}D_t^\eta \omega(\zeta, t) = \frac{1}{1+\lambda_1}(1 + \lambda\ ^{CF}D_t^\eta)\frac{\partial^2 \omega(\zeta, t)}{\partial \zeta^2} - \left(\frac{1}{K} + H_a^2\right)\omega(\zeta, t) + G_r\vartheta(\zeta, t) + G_c\Phi(\zeta, t), \tag{70}$$

$$P_r\ ^{CF}D_t^\eta \vartheta(\zeta, t) = \frac{\partial^2 \omega(\zeta, t)}{\partial \zeta^2}, \tag{71}$$

$$S_c\ ^{CF}D_t^\eta \Phi(\zeta, t) = \frac{\partial^2 \Phi(\zeta, t)}{\partial \zeta^2}, \tag{72}$$

4.2.1 Investigation of exact solution of for temperature profile

By introducing the LT into Eq. (71) we get

$$\frac{\partial^2 \bar\vartheta(\zeta, q)}{\partial \zeta^2} - \frac{P_r q z_0}{q+\gamma}\bar\vartheta(\zeta, q) = 0, \tag{73}$$

where $z_0 = \frac{1}{1-\eta}, \gamma = \eta z_0$ and $\bar\vartheta(\zeta, q)$ meets the prescribed conditions below

$$\bar\vartheta(0, q) = G(q), \bar\vartheta(1, q) = \frac{1}{q}. \tag{74}$$

The implementation of prescribed boundary conditions Eq. (74) on solving the above differential equations produce the solution

$$\bar\vartheta(\zeta, q) = qG(q)\left(\frac{\sinh\left((1-\zeta)\sqrt{\frac{P_r z_0 q}{q+\gamma}}\right)}{q \sinh\left(\sqrt{\frac{P_r z_0 q}{q+\gamma}}\right)}\right) + \\ \left(\frac{\sinh\left(\zeta\sqrt{\frac{P_r z_0 q}{q+\gamma}}\right)}{q \sinh\left(\sqrt{\frac{P_r z_0 q}{q+\gamma}}\right)}\right) = gG(q)\vartheta_1(\zeta, q) + \vartheta_2(\zeta, q). \tag{75}$$

The expression of $\vartheta_1(\zeta, t), \vartheta_2(\zeta, t)$ after employing the inverse LT on $\vartheta_1(\zeta, q), \vartheta_2(\zeta, q)$ respectively, is

$$\vartheta_1(\zeta, t) = \tag{76}$$
$$\sum_{n=0}^\infty \sum_{k=1}^\infty \frac{(-\Xi_0)^k - (-\Xi_1)^k}{k!} * \sum_{m=0}^\infty \frac{\frac{k}{2!}}{m!(\frac{k}{2}-m)!}(-1)^m * \\ \sum_{p=0}^\infty (-1)^p \frac{(m+p-1)!}{p!(m-1)!}\gamma^{-p}\frac{t^{-p}}{\Gamma(-p+1)}$$

where $\Xi_0 = (2n + \zeta)\sqrt{P_r z_0}$ and $\Xi_1 = (2n + 2 - \zeta)\sqrt{P_r z_0}$.

$$\vartheta_2(\zeta, t) = \\ \sum_{n=0}^\infty \frac{2P_r}{\pi}\int_0^\infty \left(\frac{\sin\left(\frac{2n+1+\zeta}{\sqrt{1-\eta}}x\right) - \sin\left(\frac{2n+1-\zeta}{\sqrt{1-\eta}}x\right)}{x(P_r+x^2)}\right)e^{\frac{-\eta}{1-\eta}tx^2}dx. \tag{77}$$

The inverse LT of Eq. (75) is

$$\vartheta(\zeta, t) = \int_0^t g'(t-\tau)\vartheta_1(\zeta, \tau)d\tau + \vartheta_2(\zeta, t), \tag{78}$$

where $\vartheta_1(\zeta, t)$ and $\vartheta_2(\zeta, t)$ are expressed in Eqs (77) and (78), respectively.

4.2.2 Investigation of exact solution for concentration profile

Implement the LT into Eq. (72), and on solving we get

$$\frac{\partial^2 \overline\Phi(\zeta, q)}{\partial \zeta^2} - \frac{S_c q z_0}{q+\gamma}\overline\Phi(\zeta, q) = 0, \tag{79}$$

where $z_0 = \frac{1}{1-\eta}, \gamma = \eta z_0$ and $\overline\Phi(\zeta, q)$ satisfies the prescribed conditions

$$\overline\Phi(0, q) = H(q), \overline\Phi(1, q) = \frac{1}{q} \tag{80}$$

The implementation of the prescribed boundary conditions Eq. (80) on solving the above differential equations produce the solution of concentration as

$$\overline\Phi(\zeta, q) = qH(q)\left(\frac{\sinh\left((1-\zeta)\sqrt{\frac{S_c z_0 q}{q+\gamma}}\right)}{q \sinh\left(\sqrt{\frac{S_c z_0 q}{q+\gamma}}\right)}\right) + \\ \left(\frac{\sinh\left(\zeta\sqrt{\frac{S_c z_0 q}{q+\gamma}}\right)}{q \sinh\left(\sqrt{\frac{S_c z_0 q}{q+\gamma}}\right)}\right) = gH(q)\Phi_1(\zeta, q) + \Phi_2(\zeta, q). \tag{81}$$

Employ the inverse LT on $\Phi_1(\zeta, q)$

$$\Phi_1(\zeta, q) = \tag{82}$$
$$\sum_{n=0}^\infty \sum_{k=1}^\infty \frac{(-\Xi_0)^k - (-\Xi_1)^k}{k!} * \sum_{m=0}^\infty \frac{\frac{k}{2!}}{m!(\frac{k}{2}-m)!}(-1)^m * \\ \sum_{p=0}^\infty (-1)^p \frac{(m+p-1)!}{p!(m-1)!}\gamma^{-p}\frac{t^{-p}}{\Gamma(-p+1)}$$

where $\Xi_0 = (2n + \zeta)\sqrt{S_c z_0}$ and $\Xi_1 = (2n + 2 - \zeta)\sqrt{S_c z_0}$.

Implementing the inverse LT on $\Phi_2(\zeta, q)$

$$\Phi_2(\zeta, q) = \tag{83}$$
$$\sum_{n=0}^\infty \frac{2S_c}{\pi}\int_0^\infty \left(\frac{\sin\left(\frac{2n+1+\zeta}{\sqrt{1-\eta}}x\right) - \sin\left(\frac{2n+1-\zeta}{\sqrt{1-\eta}}x\right)}{x(S_c+x^2)}\right)e^{\frac{-\eta}{1-\eta}tx^2}dx.$$

Taking inverse LT in Eq. (81), we will get the expression of $\Phi(\zeta, t)$

$$\Phi(\zeta, t) = \int_0^t h'(t - \tau)\Phi_1(\zeta, \tau)d\tau + \Phi_2(\zeta, t), \tag{84}$$

where $\Phi_1(\zeta, t)$ and $\Phi_2(\zeta, t)$ are expressed in Eqs (82) and (83), respectively.

4.2.3 Investigation of exact solution for velocity profile

Applying the LT in Eq. (70), using the LT formula for CF derivative and bearing in mind the corresponding initial condition, we get

$$\left(\frac{qz_1 + \gamma}{(1 + \lambda_1)(q + \gamma)}\right)\frac{\partial^2 \overline{\omega}(\zeta, q)}{\partial \zeta^2} - \left(\frac{qz_0}{q + \gamma} + \frac{1}{K} + H_a^2\right)\overline{\omega}(\zeta, q) = \tag{85}$$
$$-G_r \overline{\vartheta}(\zeta, q) = -G_c \overline{\Phi}(\zeta, q),$$

$$\frac{\partial^2 \overline{\omega}(\zeta, q)}{\partial \zeta^2} - \Lambda_2 \overline{\omega}(\zeta, q) = \frac{-G_r}{\Lambda_0}\overline{\vartheta}(\zeta, q) - \frac{-G_c}{\Lambda_0}\overline{\Phi}(\zeta, q), \tag{86}$$

where $z_0 = \frac{1}{1 - \eta}, z_1 = 1 + \lambda z_0, \Lambda_0 = \left(\frac{qz_1 + \gamma}{(1 + \lambda_1)(q + \gamma)}\right), \Lambda_1 = \left(\frac{qz_0}{q + \gamma} + \frac{1}{K} + H_a^2\right)$ and $\Lambda_2 = \frac{\Lambda_1}{\Lambda_0}$.

The boundary conditions after embedding the LT are

$$\overline{\omega} = (0, q) = F(q), \overline{\omega} = (1, q) = 0. \tag{87}$$

After inserting Eq. (75) into Eq. (86), the solution for Eq. (81) is obtained as

$$\overline{\omega}(\zeta, q) = \frac{F(q)}{\sinh \sqrt{\Lambda_2}}\sinh\left((1 - \zeta)\sqrt{\Lambda_2}\right)$$

$$+ \frac{G_r}{q\Lambda_0\left(\frac{Prz_0q}{q + \gamma} - \Lambda_2\right)\sinh \sqrt{\Lambda_2}}\left(qG(q)\sinh\left((1 - \zeta)\sqrt{\Lambda_2}\right) - \sinh(\zeta\sqrt{\Lambda_2}) - \right.$$

$$\frac{G_r}{q\Lambda_0\left(\frac{Prz_0q}{q + \gamma} - \Lambda_2\right)\sinh\sqrt{\frac{Prz_0q}{q + \gamma}}}\left(qG(q)\sinh\left((1 - \zeta)\sqrt{\frac{Prz_0q}{q + \gamma}}\right) - \sinh\left(\zeta\sqrt{\frac{Prz_0q}{q + \gamma}}\right)\right) +$$

$$\frac{G_c}{q\Lambda_0\left(\frac{Scz_0q}{q + \gamma} - \Lambda_2\right)\sinh\sqrt{\Lambda_2}}\left(qH(q)\sinh\left((1 - \zeta)\sqrt{\Lambda_2}\right) - \sinh(\zeta\sqrt{\Lambda_2}) - \right. \tag{88}$$

$$\frac{G_c}{q\Lambda_0\left(\frac{Scz_0q}{q + \gamma} - \Lambda_2\right)\sinh\sqrt{\frac{Scz_0q}{q + \gamma}}}\left(qH(q)\sinh\left((1 - \zeta)\sqrt{\frac{Scz_0q}{q + \gamma}}\right) - \sinh\left(\zeta\sqrt{\frac{Scz_0q}{q + \gamma}}\right)\right).$$

For suitable presentation of velocity equation, we rewrite Eq. (88) into the following simplified form

$$\overline{\omega}(\zeta, q) = \omega_1(\zeta, q) + \omega_2(\zeta, q) - \omega_3(\zeta, q) + \omega_4(\zeta, q) - \omega_5(\zeta, q), \tag{89}$$

where

$$\omega_1(\zeta, q) = \frac{F(q)}{\sinh \sqrt{\Lambda_2}}\sinh\left((1 - \zeta)\sqrt{\Lambda_2}\right) \tag{90}$$
$$= F(q)L(\zeta, q).$$

Employing the inverse LT on $L(\zeta, q)$, we arrived at

$$L(\zeta, t) = \sum_{n=0}^{\infty}\sum_{k=0}^{\infty}\frac{((-\Xi_4)^k - (-\Xi_5)^k)}{k!}(1 + \tag{91}$$
$$\lambda_1)^{\frac{k}{2}}\sum_{m=0}^{\infty}\frac{\frac{k}{2}!}{m!\left(\frac{k}{2} - m\right)!}(z_3)^{\frac{k}{2} - m}(z_4)^m$$
$$\times \sum_{p=0}^{\infty}(-1)^p\frac{(m + p - 1)!}{p!(m - 1)!}\gamma^{-(m + p)}(z_1)^p\frac{t^{-(p+1)}}{\Gamma(-p)}$$

where $b = \frac{1}{k} + H_a^2, z_0 = \frac{1}{1 - \eta}, z_1 = 1 + \lambda z_0, z_2 = z_0 + b$, $z_3 = \frac{z_2}{z_1}, z_4 = \gamma(b - z_3), \Xi_0 = (2n + \zeta)$ and $\Xi_1 = (2n + 2 - \zeta)$.

Implementing the inverse LT of Eq. (90) while bearing in mind Eq. (91), we obtain

$$\omega_1(\zeta, t) = f(t) * L(\zeta, t). \tag{92}$$

The expression of $\omega_2(\zeta, q)$ is

$$\omega_2(\zeta, q) = \frac{G_r}{q\Lambda_0\left(\frac{Prz_0q}{q + \gamma} - \Lambda_2\right)\sinh\sqrt{\Lambda_2}}\left(qG(q)\sinh\left((1 - \tag{93}\right.\right.$$
$$\zeta)\sqrt{\Lambda_2}\right) - \sinh(\zeta\sqrt{\Lambda_2})\right),$$

and in the simplest form

$$\omega_2(\zeta, q) = G_r(1 + \lambda_1)I_1(\zeta, q)\left(qG(q)R_1(\zeta, q) - \tag{94}$$
$$S_1(\zeta, q)\right)$$

where

$$I_1(\zeta, q) = \frac{1}{(P_r z_0 q(q z_1 + \gamma) - (q z_2 + b\gamma)(q + \gamma)(1 + \lambda_1))}, \tag{95}$$

And its inverse LT is

$$I_1(\zeta, t) = -\sum_{n=0}^{\infty}\sum_{k=0}^{\infty}\frac{f_0^{n-k}g_0^k}{h_0^{n+1}}\frac{n!}{k!(n-k)!}\frac{t^{\eta(k-2n)-1}}{\Gamma\eta(k-2n)}, \tag{96}$$

where $f_0 = (P_r z_0 z_1 - z_2(1 + \lambda_1))$, $g_0 = (P_r z_0 \gamma - z_2(1 + \lambda_1) - b\gamma(1 + \lambda_1)), h_0 = b\gamma^2(1 + \lambda_1)$

$$R_1(\zeta, q) = \frac{(q + \gamma)^2 \sinh\left((1 - \zeta)\sqrt{\Lambda_2}\right)}{q \sinh\sqrt{\Lambda_2}}, \tag{97}$$

$$S_1(\zeta, q) = \frac{(q + \gamma)^2 \sinh(\zeta\sqrt{\Lambda_2})}{q \sinh\sqrt{\Lambda_2}}. \tag{98}$$

Inverse LT in Eqs (97) and (98) is transformed into

$$R_1(\zeta, q) =$$
$$\sum_{\beta=0}^{2}\frac{2!}{\beta!(2-\beta)!}\sum_{n=0}^{\infty}\sum_{k=0}^{\infty}\frac{((-\Xi_4)^k - (-\Xi_5)^k)}{k!}(1 +$$
$$\lambda_1)^{\frac{k}{2}}\sum_{m=0}^{\infty}\frac{\frac{k}{2}!}{m!\left(\frac{k}{2} - m\right)!}(z_3)^{\frac{k}{2} - m}(z_4)^m \times \tag{99}$$
$$\sum_{p=0}^{\infty}(-1)^p\frac{(m + p - 1)!}{p!(m - 1)!}\gamma^{-(m + p + \beta - 2)}(z_1)^p\frac{t^{-(\beta + p)}}{\Gamma(-(\beta + p) + 1)},$$

$$S_1(\zeta, q) =$$
$$\sum_{\beta=0}^{2}\frac{2!}{\beta!(2-\beta)!}\sum_{n=0}^{\infty}\sum_{k=0}^{\infty}\frac{((-\Xi_6)^k - (-\Xi_7)^k)}{k!}(1 +$$
$$\lambda_1)^{\frac{k}{2}}\sum_{m=0}^{\infty}\frac{\frac{k}{2}!}{m!\left(\frac{k}{2} - m\right)!}(z_3)^{\frac{k}{2} - m}(z_4)^m \times \tag{100}$$
$$\sum_{p=0}^{\infty}(-1)^p\frac{(m + p - 1)!}{p!(m - 1)!}\gamma^{-(m + p + \beta - 2)}(z_1)^p\frac{t^{-(\beta + p)}}{\Gamma(-(\beta + p) + 1)},$$

Maryam Asgir, Muhammad Bilal Riaz, Ayesha Islam
Exact Analysis of Fractionalised Jeffrey Fluid in a Channel with Caputo and Caputo Fabrizio Time Derivative: A Comparative Study

DOI 10.2478/ama-2023-0068

where $b = \frac{1}{k} + H_a^2$, $z_0 = \frac{1}{1-\eta}$, $z_1 = 1 + \lambda z_0$, $z_2 = z_0 + b$, $z_3 = \frac{z_2}{z_1}$, $z_4 = \gamma(b - z_3)$, $\Xi_4 = (2n + \zeta)$ and $\Xi_5 = (2n + 2 - \zeta)$, $\Xi_6 = (2n + 1 - \zeta)$ and $\Xi_7 = (2n + 1 + \zeta)$.

The $\omega_2(\zeta, t)$ is expressed as

$$\omega_2(\zeta,t) = G_r(1 + \lambda_1)I_1(\zeta,t) * \big(g'(t) * R_1(\zeta,t) - S - 1(\zeta,t)\big) \tag{101}$$

where we get the values of $I_1(\zeta,t)$, $R_1(\zeta,t)$ and $S_1(\zeta,t)$ from Eqs (96), (99) and (100), respectively.

Consider now,

$$\omega_3(\zeta, q) = \tag{102}$$
$$\frac{G_r}{q\Lambda_0\left(\frac{P_r z_0 q}{q+\gamma} - \Lambda_2\right)\sinh\sqrt{\frac{P_r z_0 q}{q+\gamma}}}\Bigg(qG(q)\sinh\Big((1 - \zeta)\sqrt{\frac{P_r z_0 q}{q+\gamma}}\Big) - \sinh\Big(\zeta\sqrt{\frac{P_r z_0 q}{q+\gamma}}\Big)\Bigg)$$

And the abridged form

$$\omega_3(\zeta, q) = G_r(1 + \lambda_1)I_1(\zeta, q)\big(qG(q)\varphi_1(\zeta, q) - \varphi_2(\zeta, q)\big). \tag{103}$$

Taking the inverse LT in Eq. (103)

$$\omega_3(\zeta, t) = G_r(1 + \lambda_1)I_1(\zeta, t) * \big(g'(t) * \varphi_1(\zeta, t) - \varphi_2(\zeta, t)\big), \tag{104}$$

where $I_1(\zeta, t)$, is obtained in Eq. (96), and $\varphi_1(\zeta, t)$, $\varphi_2(\zeta, t)$ are obtained as below

$$\varphi_1(\zeta, q) = \sum_{\beta=0}^{2}\frac{2!}{\beta!(2-\beta)!}\sum_{n=0}^{\infty}\sum_{k=0}^{\infty}\frac{((-\Xi_0)^k - (-\Xi_1)^k)}{k!}$$
$$\sum_{m=0}^{\infty}\frac{\frac{k}{2}!}{m!(\frac{k}{2}-m)!}(-1)^m \tag{105}$$
$$\sum_{p=0}^{\infty}(-1)^p\frac{(m+p-1)!}{p!(m-1)!}\gamma^{-(\beta+p-2)}(z_1)^p\frac{t^{-(\beta+p)}}{\Gamma(-(\beta+p)+1)},$$

where $\Xi_2 = (2n + \zeta)\sqrt{P_r z_0}$ and $\Xi_3 = (2n + 2 - \zeta)\sqrt{P_r z_0}$, and

$$\varphi_1(\zeta, q) = \sum_{\beta=0}^{2}\frac{2!}{\beta!(2-\beta)!}\sum_{n=0}^{\infty}\sum_{k=0}^{\infty}\frac{((-\Xi_8)^k - (-\Xi_9)^k)}{k!}$$
$$\sum_{m=0}^{\infty}\frac{\frac{k}{2}!}{m!(\frac{k}{2}-m)!}(-1)^m \tag{106}$$
$$\times\sum_{p=0}^{\infty}(-1)^p\frac{(m+p-1)!}{p!(m-1)!}\gamma^{-(\beta+p-2)}(z_1)^p\frac{t^{-(\beta+p)}}{\Gamma(-(\beta+p)+1)},$$

where $\Xi_8 = (2n + 1 - \zeta)\sqrt{P_r z_0}$ and $\Xi_9 = (2 + 1 + \zeta)\sqrt{P_r z_0}$.

Here,

$$\omega_4(\zeta, q) = \tag{107}$$
$$\frac{G_c}{q\Lambda_0\left(\frac{S_c z_0 q}{q+\gamma} - \Lambda_2\right)\sinh\sqrt{\Lambda_2}}\Big(qH(q)\sinh\big((1 - \zeta)\sqrt{\Lambda_2}\big) - \sinh\big(\zeta\sqrt{\Lambda_2}\big)\Big),$$

which can be written in abridged form as

$$\omega_4(\zeta, q) = G_r(1 + \lambda_1)J_1(\zeta, q)\big(qG(q)R_1(\zeta, q) - S_1(\zeta, q)\big), \tag{108}$$

where

$$J_1(\zeta, q) = \frac{1}{(S_c z_0 q(q z_1 + \gamma) - (q z_2 + b\gamma)(q + \gamma)(1 + \lambda_1))} \tag{109}$$

And its inverse LT

$$J_1(\zeta, t) = -\sum_{n=0}^{\infty}\sum_{k=0}^{\infty}\frac{f_{01}^{n-k}g_{01}^k}{h_{01}^{n+1}}\frac{n!}{k!(n-k)!}\frac{t^{\eta(k-2n)-1}}{\Gamma\eta(k-2n)}, \tag{110}$$

where $f_{01} = (S_c z_0 z_1 - z_2(1 + \lambda_1))$, $g_{01} = (S_c z_0 \gamma - z_2(1 + \lambda_1) - b\gamma(1 + \lambda_1))$, $h_{01} = b\gamma^2(1 + \lambda_1)$,

The $\omega_4(\zeta, t)$ is expressed as

$$\omega_4(\zeta, t) = G_c(1 + \lambda_1)J_1(\zeta, t) * \big(h'(t) * R_1(\zeta, t) - S_2(\zeta, t)\big), \tag{111}$$

where we get the values of $J_1(\zeta, t)$, $R_1(\zeta, t)$, $S_1(\zeta, t)$ from Eqs(110), (99) and (100), respectively.

The expression for $\omega_5(\zeta, q)$ is stated below as

$$\omega_4(\zeta, q) = \tag{112}$$
$$\frac{G_c}{q\Lambda_0\left(\frac{S_c z_0 q}{q+\gamma} - \Lambda_2\right)\sinh\sqrt{\frac{S_c z_0 q}{q+\gamma}}}\Bigg(qH(q)\sinh\Big((1 - \zeta)\sqrt{\frac{S_c z_0 q}{q+\gamma}}\Big) - \sinh\Big(\zeta\sqrt{\frac{S_c z_0 q}{q+\gamma}}\Big)\Bigg).$$

For simplification,

$$\omega_5(\zeta, t) = G_c(1 + \lambda_1)J_1(\zeta, q)\big(qH(q)\psi_1(\zeta, q) - \psi_1(\zeta, q)\big), \tag{113}$$

and its inverse LT will take the form

$$(\zeta, t) = G_c(1 + \lambda_1)J_1(\zeta, t) * \big(h'(t) * \psi_1(\zeta, t) - \psi_2(\zeta, t)\big), \tag{114}$$

where

$$\psi_1(\zeta, q) = \sum_{\beta=0}^{2}\frac{2!}{\beta!(2-\beta)!}\sum_{n=0}^{\infty}\sum_{k=0}^{\infty}\frac{((-\Xi_2)^k - (-\Xi_3)^k)}{k!}$$
$$\times\sum_{m=0}^{\infty}\frac{\frac{k}{2}!}{m!(\frac{k}{2}-m)!}(-1)^m \tag{115}$$
$$\times\sum_{p=0}^{\infty}(-1)^p\frac{(m+p-1)!}{p!(m-1)!}\gamma^{-(\beta+p-2)}(z_1)^p\frac{t^{-(\beta+p)}}{\Gamma(-(\beta+p)+1)},$$

$$\psi_2(\zeta, q) = \sum_{\beta=0}^{2}\frac{2!}{\beta!(2-\beta)!}\sum_{n=0}^{\infty}\sum_{k=0}^{\infty}\frac{((-\Xi_{10})^k - (-\Xi_{11})^k)}{k!}$$
$$\times\sum_{m=0}^{\infty}\frac{\frac{k}{2}!}{m!(\frac{k}{2}-m)!}(-1)^m \tag{116}$$
$$\times\sum_{p=0}^{\infty}(-1)^p\frac{(m+p-1)!}{p!(m-1)!}\gamma^{-(\beta+p-2)}(z_1)^p\frac{t^{-(\beta+p)}}{\Gamma(-(\beta+p)+1)},$$

where $\Xi_8 = (2n + \zeta)\sqrt{S_c z_0}$ and $\Xi_{11} = (2 + 1 + \zeta)\sqrt{S_c z_0}$.

Introducing the expression of $\omega_1(\zeta, t)$, $\omega_2(\zeta, t)$, $\omega_3(\zeta, t)$, $\omega_4(\zeta, t)$, $\omega_5(\zeta, t)$ from Eqs (92), (101), (104), (111) and (114), respectively, into Eq. (89), the velocity solution is attained as

$$\omega(\zeta, t) = \omega_1(\zeta, t) + \omega_2(\zeta, t) - \omega_3(\zeta, t) + \omega_4(\zeta, t) - \omega_5(\zeta, t). \tag{117}$$

5. LIMITING CASES OF MOMENTUM EQUATION

5.1. Velocity solution for second grade fluid

5.1.1 Caputo sense

Incorporating $\lambda_1 \to 0$, the velocity solution expressed in Eq. (40) transforms into the second-grade fluid solution

$$\overline{\omega}(\zeta, q) = \frac{F(q)}{sinh\sqrt{\Omega_2}} sinh\left((1-\zeta)\sqrt{Y_2}\right) +$$
$$\frac{G_r}{q\Omega_0(P_r q^n - \Omega_2) sinh\sqrt{Y_2}}\left(qG(q)sinh(1-\zeta)\sqrt{\Omega_2}\right) -$$
$$sinh(\zeta\sqrt{\Omega_2})) -$$
$$\frac{G_r}{qY_0(P_r q^n - \Omega_2) sinh\sqrt{P_r q^n}}\left(qG(q)sinh(1-\right.$$
$$\left.\zeta)\sqrt{P_r q^n}\right) - sinh(\zeta\sqrt{P_r q^n})\right) +$$
$$\frac{G_c}{q\Omega_0(S_c q^n - \Omega_2) sinh\sqrt{Y_2}}\left(qH(q)sinh(1-\zeta)\sqrt{\Omega_2}\right) -$$
$$sinh(\zeta\sqrt{\Omega_2})) -$$
$$\frac{G_c}{q\Omega_0(S_c q^n - \Omega_2) sinh\sqrt{S_c q^n}}\left(qH(q)sinh(1-\right.$$
$$\left.\zeta)\sqrt{S_c q^n}\right) - sinh(\zeta\sqrt{S_c q^n})\right). \tag{118}$$

where $\Omega_0 = 1 + \lambda q^n, \Omega_2 = \frac{\lambda_1}{\Omega_0}$.

By taking $G_c = 0$ in Eq. (118), the solution obtained is similar to the limiting solution attained by Asgir et al. [40]. For $\eta \to 1$, and resuming $G_c = 0$, we will get the limiting result obtained by Aleem et al. [39].

5.2. Caputo Fabrizio sense

By taking $\lambda_1 \to 0$, the velocity solutions in Eq. (88) present the result of second-grade fluid

$$\overline{\omega}(\zeta, q) = \frac{F(q)}{sinh\sqrt{\varrho_2}} sinh\left((1-\zeta)\sqrt{\varrho_2}\right)$$
$$+ \frac{G_r}{q\varrho_0\left(\frac{P_r z_0 q}{q+\gamma} - \varrho_2\right) sinh\sqrt{\varrho_2}}\left(qG(q) sinh\left((1-\right.\right.$$
$$\left.\zeta)\sqrt{\varrho_2}\right) - sinh(\zeta\sqrt{\Lambda_2})\right)$$
$$\frac{G_r}{q\varrho_0\left(\frac{P_r z_0 q}{q+\gamma} - \varrho_2\right) sinh\sqrt{\frac{P_r z_0 q}{q+\gamma}}}\left(qG(q) sinh\left((1-\right.\right.$$
$$\left.\zeta)\sqrt{\frac{P_r z_0 q}{q+\gamma}}\right) - sinh\left(\zeta\sqrt{\frac{P_r z_0 q}{q+\gamma}}\right)\right)$$
$$+ \frac{G_c}{q\varrho_0\left(\frac{S_c z_0 q}{q+\gamma} - \Lambda_2\right) sinh\sqrt{\varrho_2}}\left(qH(q) sinh\left((1-\right.\right.$$
$$\left.\zeta)\sqrt{\varrho_2}\right) - sinh(\zeta\sqrt{\varrho_2})\right) -$$
$$\frac{G_c}{q\varrho_0\left(\frac{S_c z_0 q}{q+\gamma} - \Lambda_2\right) sinh\sqrt{\frac{S_c z_0 q}{q+\gamma}}}\left(qH(q) sinh\left((1-\right.\right.$$
$$\left.\zeta)\sqrt{\frac{S_c z_0 q}{q+\gamma}}\right) - sinh\left(\zeta\sqrt{\frac{S_c z_0 q}{q+\gamma}}\right)\right), \tag{119}$$

where $z_0 = \frac{1}{1-\eta}, z_1 = 1 + \lambda z_0, \varrho_0 = \left(\frac{qz_1+\gamma}{(1+\lambda_1)(q+\gamma)}\right), \Lambda_1 = \left(\frac{qz_0}{q+\lambda} + \frac{1}{k} + H_\alpha^2\right), \varrho_2 = \frac{\Lambda_1}{\varrho_0}$. For $\eta \to 1$, the results recovered are of ordinary second-grade fluid. Further taking $G_c = 0$, the results attained are similar to the limiting result of velocity [39].

5.3. Velocity solution for viscous fluid

5.3.1 Caputo sense

By introducing $\lambda \to 1, \lambda_1 \to 0$, and absence of porosity reduces the velocity solution of Jeffrey fluid into viscous fluid solution, which is stated as below

$$\overline{\omega}(\zeta, q) = \frac{F(q)}{sinh\sqrt{q_n + H_\alpha^2}} sinh\left((1-\zeta)\sqrt{q_n + H_\alpha^2}\right) +$$
$$+ \frac{G_r}{q\left(P_r q^n - (q_n + H_\alpha^2)\right) sinh\sqrt{q_n + H_\alpha^2}}\left(qG(q) sinh\left((1-\right.\right.$$
$$\left.\zeta)\sqrt{q_n + H_\alpha^2}\right) - sinh(\zeta\sqrt{q_n + H_\alpha^2})\right) -$$
$$\frac{G_r}{q\left(P_r q^n - (q_n + H_\alpha^2)\right) sinh\sqrt{P_r q^n}}\left(qH(q) sinh\left((1-\right.\right.$$
$$\left.\zeta)\sqrt{P_r q^n}\right) - sinh(\zeta\sqrt{P_r q^n})\right) +$$
$$\frac{G_c}{q\left(S_c q^n - (q_n + H_\alpha^2)\right) sinh\sqrt{q_n + H_\alpha^2}}\left(qG(q) sinh\left((1-\right.\right.$$
$$\left.\zeta)\sqrt{q_n + H_\alpha^2}\right) - sinh(\zeta\sqrt{q_n + H_\alpha^2})\right) -$$
$$\frac{G_c}{q\left(S_c q^n - (q_n + H_\alpha^2)\right) sinh\sqrt{P_r q^n}}\left(qH(q) sinh\left((1-\right.\right.$$
$$\left.\zeta)\sqrt{P_r q^n}\right) - sinh(\zeta\sqrt{P_r q^n})\right). \tag{120}$$

Further taking $G_c = 0$, the results attained are similiar to the limiting result of velocity [40]. For $\eta \to 1$, and Gc = 0, we will attain the results for ordinary viscous fluid obtained by Aleem et al. [39].

5.3.2 Caputo Fabrizio sense

By introducing $\lambda \to 0, \lambda_1 \to 0$, in Eq. (88) and the absence of porosity presents the velocity solution of viscous fluid as below

$$\overline{\omega}(\zeta, q) =$$
$$\frac{F(q)}{sinh\sqrt{\frac{qz_0}{q+\gamma} + H_\alpha^2}} sinh\left((1-\zeta)\sqrt{\frac{qz_0}{q+\gamma} + H_\alpha^2}\right) +$$
$$\frac{G_r}{q\left(\frac{P_r z_0 q}{q+\gamma} - \left(\frac{qz_0}{q+\gamma} + H_\alpha^2\right)\right) sinh\sqrt{\frac{qz_0}{q+\gamma} + H_\alpha^2}}\left(qG(q) sinh\left((1-\right.\right.$$
$$\left.\zeta)\sqrt{\frac{qz_0}{q+\gamma} + H_\alpha^2}\right) - sinh\left(\zeta\sqrt{\frac{qz_0}{q+\gamma} + H_\alpha^2}\right)\right) -$$
$$\frac{G_r}{q\left(\frac{P_r z_0 q}{q+\gamma} - \left(\frac{qz_0}{q+\gamma} + H_\alpha^2\right)\right) sinh\sqrt{\frac{P_r z_0 q}{q+\gamma}}}\left(qG(q) sinh\left((1-\right.\right.$$
$$\left.\zeta)\sqrt{P_r q^n}\right) - sinh(\zeta\sqrt{P_r q^n})\right) +$$
$$\frac{G_c}{q\left(\frac{S_c z_0 q}{q+\gamma} - \left(\frac{qz_0}{q+\gamma} + H_\alpha^2\right)\right) sinh\sqrt{\frac{qz_0}{q+\gamma} + H_\alpha^2}}\left(qG(q) sinh\left((1-\right.\right.$$
$$\left.\zeta)\sqrt{\frac{qz_0}{q+\gamma} + H_\alpha^2}\right) - sinh\left(\zeta\sqrt{\frac{qz_0}{q+\gamma} + H_\alpha^2}\right)\right) -$$
$$\frac{G_c}{q\left(\frac{S_c z_0 q}{q+\gamma} - \left(\frac{qz_0}{q+\gamma} + H_\alpha^2\right)\right) sinh\sqrt{\frac{S_c z_0 q}{q+\gamma}}}\left(qH(q) sinh\left((1-\right.\right.$$
$$\left.\zeta)\sqrt{\frac{S_c z_0 q}{q+\gamma}}\right) - sinh\left(\zeta\sqrt{\frac{S_c z_0 q}{q+\gamma}}\right)\right), \tag{121}$$

where $z_0 = \frac{1}{1-\eta}$. For $\eta \to 1$, we will attain the results for ordinary viscous fluid obtained by Aleem et al. [39].

6. GRAPHS AND DISCUSSION

The heat and mass transference study of MHD free convective flow of Jeffrey fluid bounded amidst two vertical plates via time-fractional C and CF is elaborated here. The flow phenomenon of the fluid happens owing to the moment of one plate while the other is kept constant. The dimensionless system of equations representing the fluid flow phenomenon is solved by the integral LT. The obtained results are presented in a series form. The graphical illustration is used to present the behaviour of embedded physical variables such as relaxation time, thermal Grashof number, permeability parameter, mass Grashof number, Schmidt number, Jeffrey fluid parameter Prandtl number and memory parameter on the temperature, concentration and velocity profile where the $F(q) = \frac{1}{q}, G(q) = \frac{1}{q^2}, H(q) = \frac{1}{q^2}$. Fig 2. manifests the temperature profile's fractional parameter control. As η increases, the boundary layer thickens, causing the temperature to rise. The boundary layer thickness elevates the heat of the particles. The finding for $\eta \to 1$ is easily validated because it is already existing in the literature [39]. The concentration curves rise as well due to the same reason as shown in Fig. 5. The dominance of the mass diffusivity in fluid flow outcome is a reduction of the thermal boundary layer. The thermal boundary layer reduces, resulting in a decline in temperature. These are the effects of Pr which are elaborated in Fig. 3.
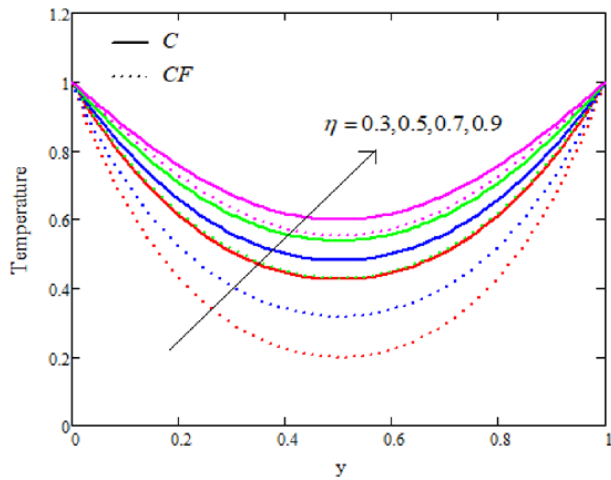
Fig. 2. Temperature plot for multiple values η with Pr = 5

The thermal boundary layer becomes thick with time, which results in an upgrade in temperature curves, as plotted in Fig. 4. We observed the similar impacts of time on the concentration profile graphed in Fig. 7. The govern of Sc on the concentration curves is depicted in Fig. 6. It is observed that the concentration descends with the rise in Sc values. Physically, this is true, because the Schmidt number increases and the concentration curves move towards the boundary, indicating the larger surface mass transfer.

The effect of the memory parameter η on fluid flow is depicted in Fig. 8. It is obvious that as η increases, so does the fluid velocity. The reason for this is that as η increases, so does the thickness of the boundary layer, resulting in velocity acceleration.
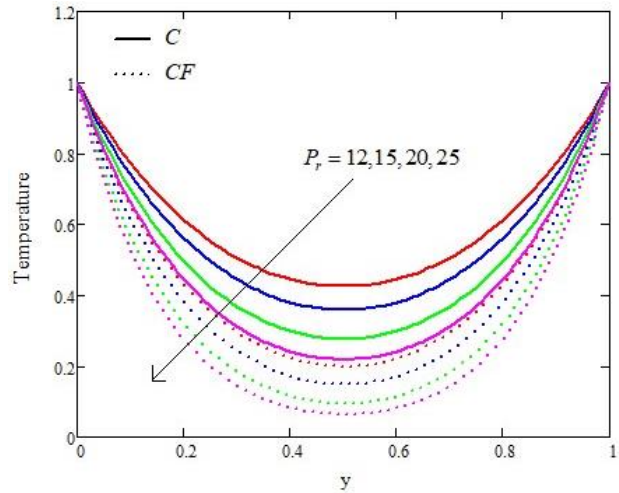

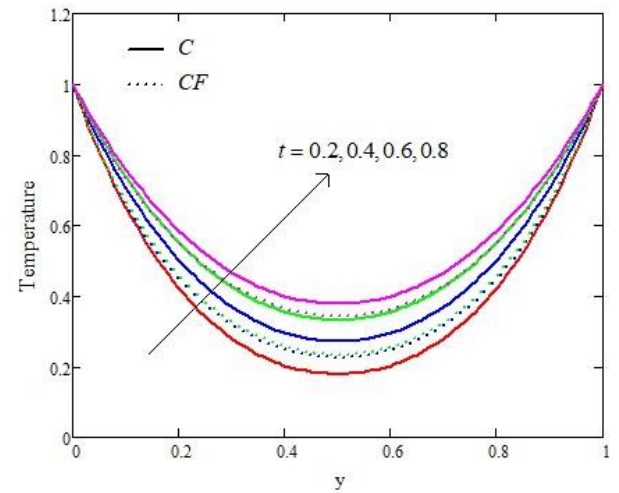**Fig. 3.** Temperature plot for multiple values of Pr with η = 0.3

Fig. 4. Temperature plot for multiple values of t with Pr = 12 and η = 0.3
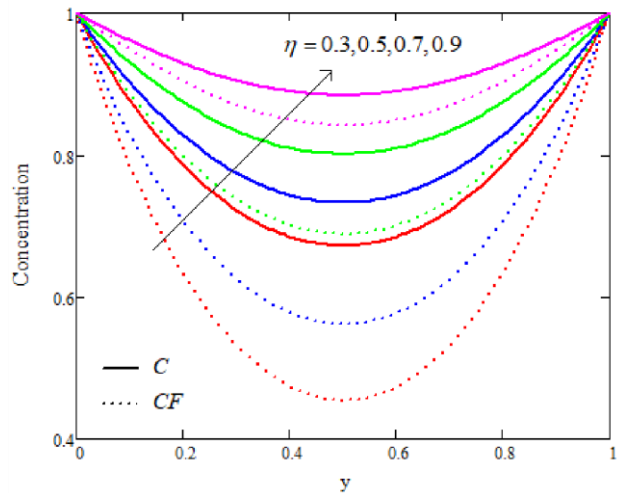

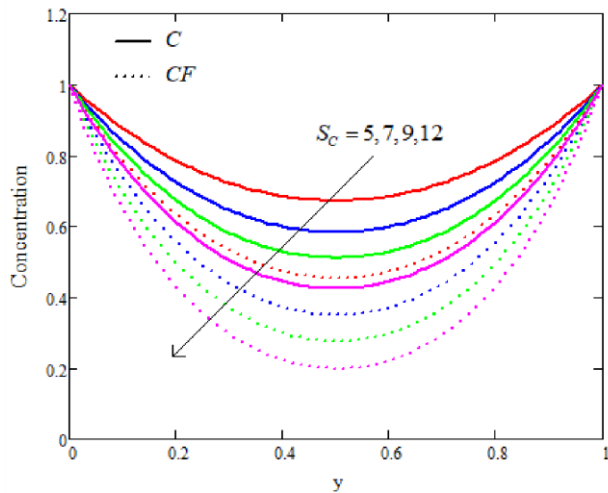**Fig. 5.** Concentration plot for multiple values η with Sc = 5.0

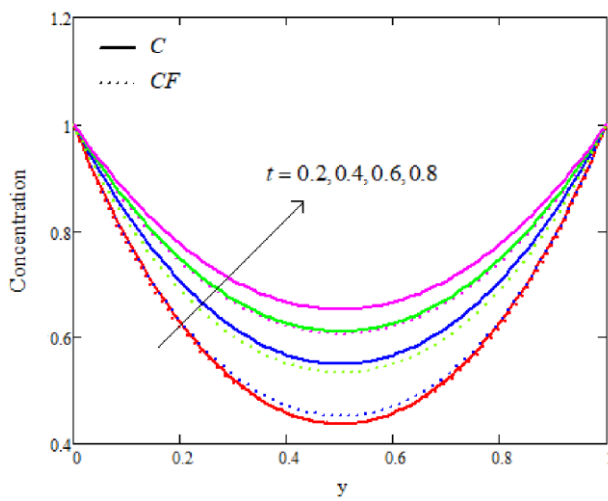**Fig. 6.** Concentration plot for multiple values of Sc with η = 0.3

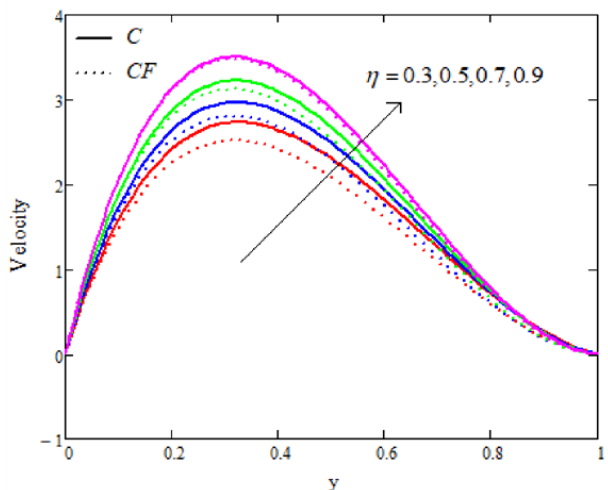**Fig. 7.** Concentration plot for multiple values of t with Sc = 5.0 and η = 0.3

Fig. 8. Velocity plot for multiple values η with Gr = 5,Gc = 8,k = 0.2, Sc = 0.5,Ha = 0.3, λ = 0.9, λ1 =1.6,Pr = 7

The Prandtl number variation influence on the fluid flow is graphed in Fig. 9. From the figure, it is noted that higher Pr values

reduce the velocity field. The thickness of the boundary layer was reduced with enhancement in the Prandtl number.

To elaborate on the effects of Gr, Fig. 10 is plotted. We observed that the fluid accelerates with the higher velocity with an ascent of thermal Grashof number Gr. Physically, increasing the value of Gr increases the buoyancy forces, which reduces the thickness of the momentum boundary layer and increases the velocity.
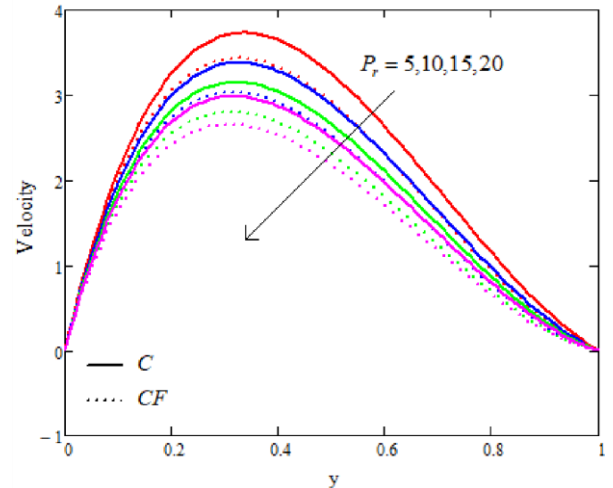

Fig. 9. Velocity plot for multiple values of $\mathrm{P_r}$, Gr = 5,Gc = 8,k = 0.2, Sc = 0.5,Ha = 0.3,λ = 0.9, λ1 =1.6, η = 0.3

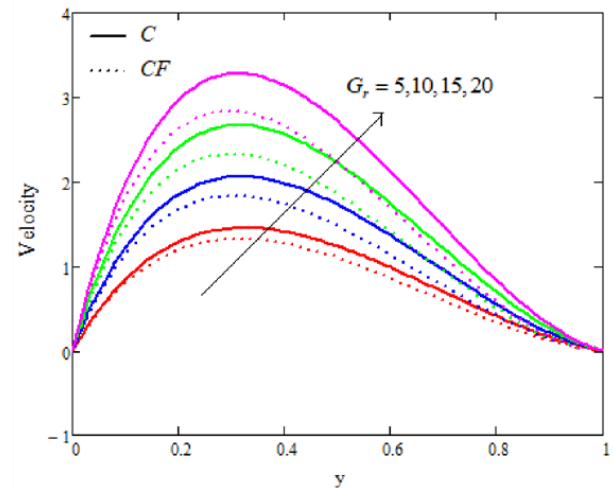**Fig. 10.** Velocity plot for multiple values of Gr with Gc = 8,k = 0.2, Sc = 0.5,Ha = 0.3,λ = 0.9, λ1 =1.6, Pr = 7,η = 0.3

The velocity curves under the effect of mass Grashof number Gc can be observed in Fig. 11. It is observed that there is a rise in velocity curves with the ascent of mass Grashof number. This is true because the concentration gradient increases the buoyancy forces, and therefore velocity accelerates.

Fig.12 elucidates the impacts of the porosity on the fluid flow. An increment in the estimation of the porosity parameter diminishes the fluid flow speed. Resistive forces bring about a decline in the speed of fluid flow. Fig 13. portrays the impacts of Sc on the fluid flow. Adding up the value of the Sc results in descending velocity curves. The point to be observed is that higher values of the Schmidt number results in more viscosity in

Maryam Asgir, Muhammad Bilal Riaz, Ayesha Islam

DOI 10.2478/ama-2023-0068

Exact Analysis of Fractionalised Jeffrey Fluid in a Channel with Caputo and Caputo Fabrizio Time Derivative: A Comparative Study

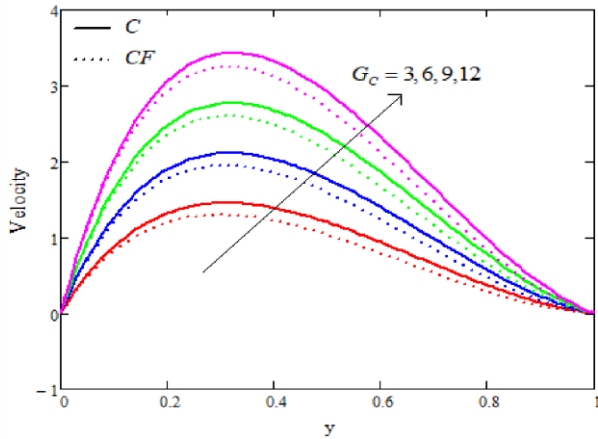fluid, causing a fall in the mass diffusion rate, and hence accordingly the fluid velocity diminishes.

Fig. 11. Velocity plot for multiple values of Gc, with $G_r = 5$, k = 0.2,Sc.=0.5,Ha = 0.3,λ = 0.9,$\lambda1$ = 1.6, $P_r = 7$, $\eta = 0.3$
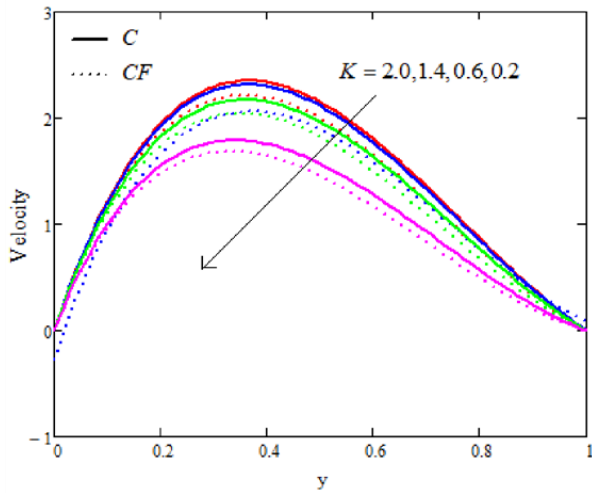

Fig. 12. Velocity plot for multiple values of K with with Gr = 5,Gc = 8, Sc = 0.5,Ha = 0.3,λ =0.9,$\lambda1$ = 1.6,Pr = 7,η = 0.3
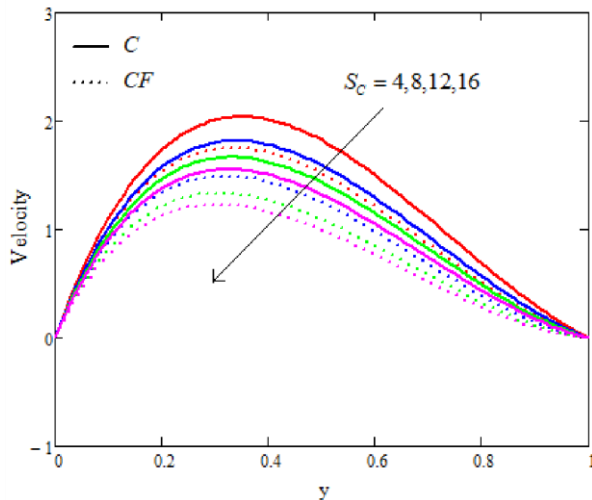

Fig. 13. Velocity plot for multiple values of S_c with $G_r = 5$, $G_c = 8$, k = 0.2, $H_a = 0.3$, $\lambda = 0.9$, $\lambda_1 = 1.6$, $P_r = 7$, $\eta = 0.3$
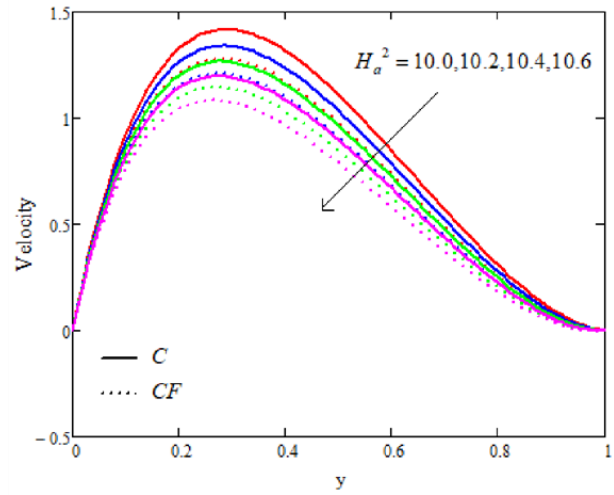

Fig. 14. Velocity plot for multiple values of Ha with Gr = 5,Gc = 8, k = 0.2,Sc = 0.5,λ = 0.9,$\lambda1$ = 1.6,Pr = 7,η = 0.3

Fig. 15. Velocity plot for multiple values of λ with $G_r = 5$, $G_c = 8$, k = 0.2, S_c 0.5, $H_a = 0.3$, $\lambda_1 = 1.6$, $P_r = 7$, $\eta = 0.3$

Fig. 16. Velocity plot for multiple values of λ_1 with $G_r = 5$, $G_c = 8$, k = 0.2, $S_c = 0.5$, $H_a = 0.3$, $\lambda = 0.9$, $P_r = 7$, $\eta = 0.3$

Fig. 17. Velocity plot for multiple values of t with $G_r = 5, G_c = 8, k = 0.2, S_c = 0.5, H_a = 0.3, \lambda = 0.9, \lambda_1 = 1.6, P_r = 7, \eta = 0.3$
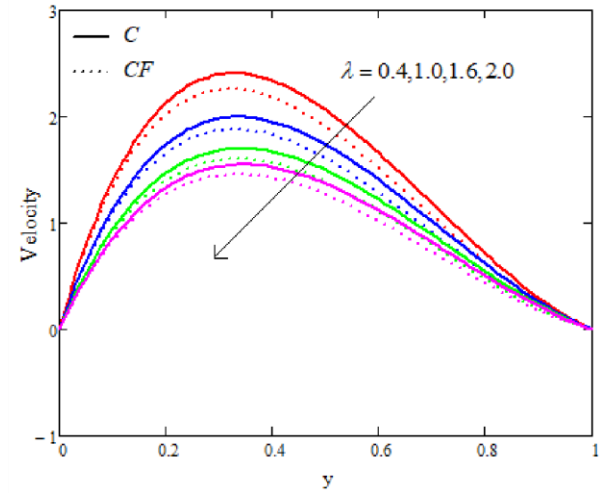

Fig. 18. Velocity plot for multiple values of y with $G_r = 5, G_c = 8, k = 0.2, S_c = 0.5, H_a = 0.3, \lambda_1 = 1.6, P_r = 7, \eta = 0.3$
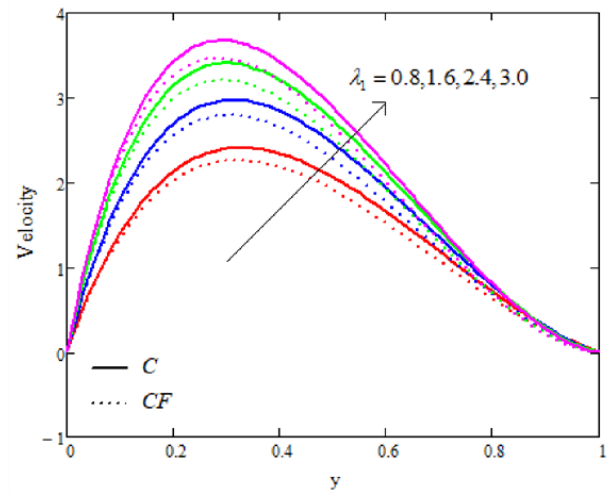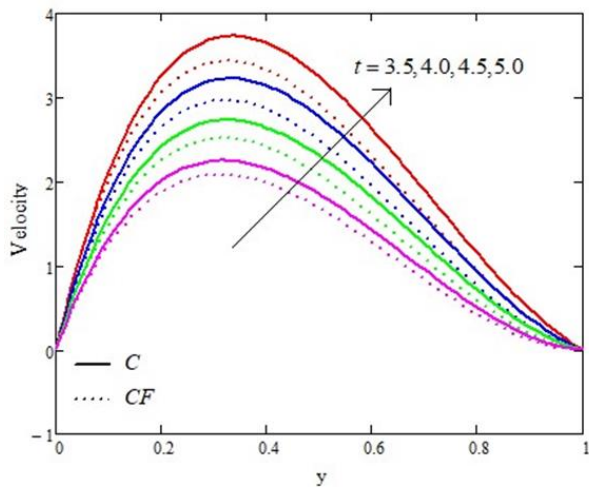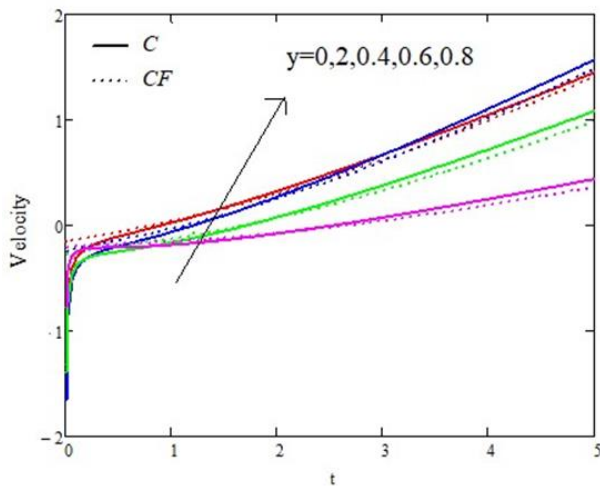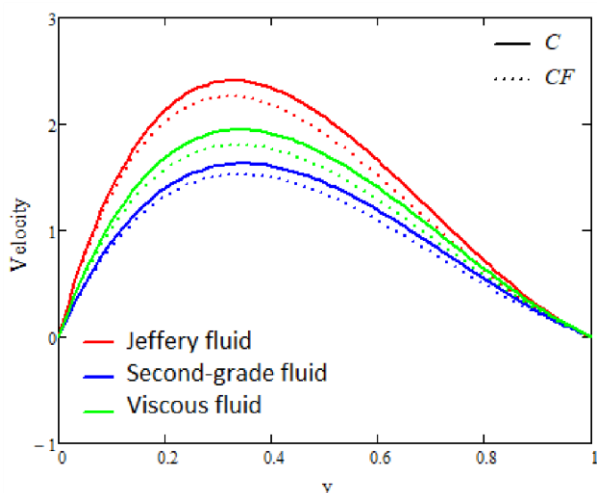

Fig. 19. Velocity plot for limiting cases

The Hartman number impacts on the velocity of the fluid, as portrayed in Fig. 14. It has been observed that an ascent in the Hartman number reduces the fluid flow. This conduct is

undeniable as transverse magnetic fields resist the flow of fluid and hence result in depreciation in the velocity field.

The governing of material parameter λ on the fluid flow is elaborated in Fig. 15. It has been observed that with the enormity of λ up, a descent in the velocity curves occurs owing to an increase in the viscous forces and elasticity of the fluid.

To visualise the impact of the rheology of fluid in the presence of Jeffrey fluid parameter λ1 on the velocity curves, Fig.16 is graphed. It has been noticed that the fluid velocity boosts up as we add up the value of λ1. From the reasoning point of view, tangential stress increases, which accelerates the fluid flow.

The velocity curves for the time variation are shown in Fig. 17. The flow of the fluid accelerates as time passes.

The velocity curves versus time are shown in Fig. 18.

In the comparison between the C and CF models, we noticed that the CF model has smaller velocity, temperature and concentration curves as compared with the C model. The limiting case's velocity profile is plotted in Fig. 19.

7. FINAL REMARKS

Caputo and Caputo Fabrizio's time-fractional approach is used to analyse the Jeffrey fluid on two parallel vertical plates immersed in a permeable medium. The exact expressions for temperature, concentration and velocity are obtained using the LT. The effect of the associated implanted parameters on velocity, temperature and concentration are detailed here using graphs. The following are the final remarks:

− Increasing the fractional parameter η increases velocity, temperature and concentration.
− Temperature curves decay with the rise in P_r and time.
− Concentration profile decays with the rise in S_c and time.
− The fluid velocity slows as the values of P_r, λ, H_a, K rise.
− The enhancement in fluid flow is observed with the increase in G_r, G_c, λ_1 and S_c values.
− The C model has a higher velocity, temperature and concentration than the CF model.
− The recovered results are of integer order derivative Jeffrey fluid for $\eta \rightarrow 1$.
− The results obtained for both $\lambda \rightarrow 0$, $\lambda_1 \rightarrow 0$ and $\eta \rightarrow 1$ are for ordinary viscous fluid.

REFERENCES

1. Dunn J E, Rajagopal K R. Fluid of differential type: critical review and thermodynamic analysis, Int J Eng Sci. 1995; 33: 689-729.
2. Rajagopal K R. Mechanics of non-Newtonian fluids, in: Galdi GP, Necas J (Eds.). Recent Developments in Theoretical Fluid Mechanics in: Pitman Res Notes Math Ser Longman Scientific and Technical. New York. 1993; 291.
3. Hayat T, Sajjad R, Asghar S. Series solution for MHD channel flow of a Jeffrey fluid. Commun Nonlin Sci Numer Simulat. 2010; 15(9): 2400-6.
4. Das K, Acharya N, Kundu P K. Thermal radiation in unsteady MHD free convection flow of Jeffrey fluid. Alex. Eng. J. 2015; 54: 815.
5. Imtiaz M, Hayat T, Alsaedi A. MHD convection flow of Jeffrey fluid due to a curved stretching surface with Homogenous Reactions. PLoS ONE 2016.
6. Jena S, Mishra S R, Dash GC, Influence of non-integer order parameter and Hartmann number on the heat and mass transfer flow

on Jeffrey fluid over an oscillating vertical plate with Caputo-Fabrizio time fractional derivatives. Int J Appl Comp Math 2016.

7. Hussain T, Shehzad S A, Hayat T, Alsaedi A, Al-Solamy F, Ramzan M. Radiative Hydromagnetic Flow of Jeffrey Nanofluid by an Exponentially Stretching Sheet. Plos One 2014; 9: 1-9.

8. Hayat T, Mustafa M. Influence of thermal radiation on the unsteady mixed convection flow of a Jeffrey fluid over a stretching sheet.

9. Z Naturforsch. 2010; 65a: 711-719.

10. Idowu A S, Jimoh A, Ahmed LO. Impact of Heat and Mass Transfer on MHD Oscillatory Flow of Jeffrey Fluid in a Porous Channel with Thermal Conductivity. Dufour and Soret. J Appl Sci Environ Manage. 2015; 19(4): 819-830.

11. Zin N A M, Khan I, Shafie S. Influence of thermal radiation on unsteady MHD free convection flow of Jeffrey fluid over a vertical plate with ramped wall temperature. Math Probl Eng. 2016; 6257071.

12. Zeeshan A, Majeed A. Heat transfer analysis of Jeffrey fluid flow over a stretching sheet with suction/injection and magnetic dipole effect. Alexandria Eng J. 2016; 55 (3): 2171-2181.

13. Agarwal V, Singh B, Nisar K S. Numerical analysis of heat transfer in magnetohydrodynamic micropolar Jeffrey fluid flow through porous medium over a stretching sheet with thermal radiation. J Therm Anal Calorim. 2022; 147: 9829–9851.

14. Bhatti MM, Zeeshan A. Analytic study of heat transfer with variable viscosity on solid particle motion in dusty Jeffrey fluid. Mod Phys Lett B. 2016; 30 (16): 1650196.

15. Turkyilmazoglu M. Unsteady convection flow of some nanofluids past a moving vertical flat plate with heat transfer. J Heat Transfer. 2014;136 (3): 031704.

16. Bagley RL, Torvik PJ. A theoretical basis for the application of fractional calculus to viscoelasticity. J Rheol. 1983;27 (3): 201-210.

17. Jamil M, Khan NA. Slip effects on fractional viscoelastic fluids. Intern. J Different Equat 2011.

18. El Kot MA, Abd Elmaboud Y. Unsteady pulsatile fractional Maxwell viscoelastic blood flow with Cattaneo heat flux through a vertical stenosed artery with body acceleration. J Therm Anal Calorim. 2022;147:4355-4368.

19. Riaz MB, Siddiqui I, Saeed ST, Atangana A. MHD Oldroyd-B Fluid with Slip Condition in view of Local and Nonlocal Kernels. J Appl Comput Mech. 2021;7(1): 116-127.

20. Alsharif M, Abdellateef AI, Abd Elmaboud Y. Electroosmotic flow of fractional Oldroyd-B fluid through a vertical microchannel filled with a homogeneous porous medium: Numerical and semianalytical solutions. Heat Transfer. 2022; 51(5): 4033-4052.

21. Khan I, Shah NA, Vieru D. Unsteady flow of generalized Casson fluid with fractional derivative due to an infinite plate. Eur Phys J Plus. 2016; 131 (6): 1-12.

22. Imran MA, Shah NA, Aleem M et al. Heat transfer analysis of fractional second-grade fluid subject to Newtonian heating with Caputo and Caputo-Fabrizio fractional derivatives: A comparison. Eur Phys J Plus. 2017; 132: 340-358.

23. Abdellateef I, Alshehri HM, Abd Elmaboud Y. Electro-osmotic flow of fractional second-grade fluid with fractional Cattaneo heat flux through a vertical microchannel. Heat Transfer. 2021; 50(7): 6628-6644.

24. Alsharif AM, Abd Elmaboud Y. Electroosmotic flow of generalized fractional second grade fluid with fractional Cattaneo model through a vertical annulus. Chinese Journal of Physics. 2022; 77: 1015-1028.

25. Saqib M, Ali F, Khan I, Sheikh NA, Jan SAA. Exact solutions for free convection flow of generalized Jeffrey fluid: a Caputo-Fabrizio fractional model. Alexandria Engineering Journal. 2018; 57(3): 18491858.

26. Shehzad SA, Hayat T, Alhuthali MS, Asghar S. MHD three-dimensional flow of Jeffrey fluid with Newtonian heating. J Cent South Univ. 2014; 21: 1428-1433.

27. Hayat T, Sajjad R, Asghar S. Series solution for MHD channel flow of a Jeffrey fluid. Commun Nonlin Sci Numer Simulat. 2010; 15(9): 2400-6.

28. Farman M, Besbes H, Nisar KS, Omri M. Analysis and dynamical transmission of Covid-19 model by using Caputo-Fabrizio derivative. Alexandria Engineering Journal. 2023; 66: 597-606.

29. Liu Y, Zheng L, Zhang X. Unsteady MHD Couette flow of a generalized Oldroyd-B fluid with fractional derivative. Comput Math Appl. 2011; 61: 443-450.

30. Hilfer R. Applications of Fractional Calculus in Physics. World Scientific Press. Singapore 2000.

31. Tan W, Pan W, Xu M. A note on unsteady flows of a viscoelastic fluid with the fractional Maxwell model between two parallel plates. Internat J Non-Linear Mech. 2003;38: 645-650.

32. Wang S, Xu M. Exact solution on unsteady Couette flow of generalized Maxwell fluid with fractional derivatives. Acta Mech. 2006;187: 1-4.

33. Qi HT, Jin H. Unsteady rotating flows of viscoelastic fluid with the fractional Maxwell model between coaxial cylinders. Acta Mech Sin. 2006; 22: 301-305.

34. Siddique I, Sajid Z. Exact solutions for the unsteady axial flow of non-Newtonian fluids through a circular cylinder. Commun Nonlinear Sci Numer Simul. 2011; 16: 226-238.

35. Vieru D, Fetecau C, Fetecau C. Time-fractional free convection flow near a vertical plate with Newtonian heating and mass diffusion. Therm Sci. 2015; 19 (1): S85–S98.

36. Iftikhar N, Baleanu D, Riaz MB, Husnine SM. Heat and Mass Transfer of Natural Convective Flow with Slanted Magnetic Field via Fractional Operators. J Appl Comput Mech. 2021; 7(1): 189-212.

37. Iftikhar N, Saeed ST, Riaz MB. Fractional study on heat and mass transfer of MHD Oldroyd-B fluid with ramped velocity and temperature. Computational Methods for Differential Equations 2021. 2021: 1-28.

38. Dharmendar Reddy Y, Shankar Goud B, Nisar KS, Alshahrani B, Mahmoud M, Park C. Heat absorption/generation effect on MHD heat transfer fluid flow along a stretching cylinder with a porous medium. Alexandria Engineering Journal. 2023; 64: 659-666.

39. Zafar A, Awrejcewicz J, Mazur O, Riaz MB. Study of composite fractional relaxation differential equation using fractional operators with and without singular kernels and special functions. Advances in Difference Equations 2021. 2021: 87.

40. Aleem M, Asjad MI, Ahmadian A, Massimiano Ferrara MS. Heat transfer analysis of channel flow of MHD Jeffrey fluid subject to generalized boundary conditions. Eur Phys J Plus. 2020; 135:26.

41. Asgir M, Abualnaja KM, Zafar AA, Riaz MB, Abbas M. Special function form exact solutions for Jeffrey fluid: An application of power law kernel (submitted).

42. Butt AR, Abdullah M, Raza N, Imran MA. Influence of non-integer order parameter and Hartmann number on the heat and mass transfer flow of a Jeffrey fluid over an oscillating vertical plate via Caputo Fabrizio. Euro Phys J Plus. 2017; 132(10): 4-14.

43. Imran MA, Aleem M, Chowdhury MSR, Hussnain A. Analysis of mathematical model of fractional viscous fluid through a vertical rectangular channel. Chin J Phys. 2019; 61: 336-50.

Maryam Asgir: iD https://orcid.org/0009-0006-0654-4836

Muhammad Bilal Riaz: iD https://orcid.org/0000-0001-5153-297X

Ayesha Islam: iD https://orcid.org/0000-0003-0372-5261

NUMERICAL ANALYSIS OF THE BOILING HEAT TRANSFER COEFFICIENT
IN THE FLOW IN MINI-CHANNELS

Beata MACIEJEWSKA* , **Sylwia HOŻEJOWSKA*** , **Mirosław GRABOWSKI**** , **Mieczysław E. PONIEWSKI****

*Faculty of Management and Computer Modelling, Department of Mathematics and Physics,
Kielce University of Technology, Al.1000-lecia P.P. 7, 25-314 Kielce, Poland
**Institute of Mechanical Engineering, Warsaw University of Technology,
Płock Campus, ul. Łukasiewicza 17, 09-400 Płock, Poland

beatam@tu.kielce.pl, ztpsf@tu.kielce.pl, Miroslaw.Grabowski@pw.edu.pl, Mieczyslaw.Poniewski@pw.edu.pl

Abstract: This paper deals with boiling heat transfer in the flow of water through an asymmetrically heated horizontal rectangular mini-channel. The mini-channel was made by gluing three transparent glass plates and a copper block. Through the glass window, the variable along the length of the mini-channel two-phase flow structures were recorded to determine local values of the void fraction. Four resistance heaters were attached to the copper block, powered by direct current, generating the heat initiating the flow boiling inside the channel. During the experiment, the following were measured: water volumetric flow rate, inlet pressure with pressure drop, inlet and outlet water temperature, copper block temperatures at three points inside its body, voltage and current supplied to the heaters. Stationary and laminar fluid flow with low Reynolds numbers were assumed in the mathematical model of heat transfer in selected elements of the measuring module. The temperature distributions in the copper block and flowing water were described by the appropriate energy equations: the Laplace equation for the copper block and the Fourier–Kirchhoff equation with parabolic fluid velocity for the flowing water. These equations were supplemented with a set of boundary conditions based on measurement data; moreover, data from experimental studies were the basis for numerical calculations and their verification. Two-dimensional temperature distributions of the copper block and water were calculated with the Trefftz method (TM). The main objective of this study was to determine the heat transfer coefficient on the contact surface of the copper block and water, which was calculated from the Robin boundary condition. The results of the calculations were compared with the results of numerical simulations performed using the Simcenter STAR-CCM+ software, obtaining consistent values. Computational fluid dynamics (CFD) simulations were verified based on experimental data including void fraction and temperature measurements of the copper block and flowing water.

Key words: flow boiling, void fraction, heat transfer coefficient, Simcenter STAR-CCM+, CFD, Trefftz method

1. INTRODUCTION. BRIEF STATE OF THE ART

Boiling heat transfer in mini-channel flow has been the subject of extensive experimental and numerical research presented in the literature [1–11]. Due to the complexity of the process, the development of comprehensive correlations and/or flow boiling models based solely on experimental data is not possible. The use of numerical simulation in the modelling thermal and flow phenomena allows estimating the approximate values of physical parameters (e.g. temperature or pressure) and examining their impact on the studied phenomenon [8–11]. Numerical simulation also reduces the time needed for time-consuming and costly experimental investigation. However, it should be noted that the results of numerical simulations should always be verified based on the results of the experiment.

Experimental studies of flows in mini- and micro-channels focus on boiling flow and, to a lesser extent, condensation. Flow modelling with change of fluid phase is hampered by the fact that these flows are described on a macroscopic scale as stationary, but the formation, growth, coagulation and collapse of vapour bubbles generate local non-stationary changes in temperature,

pressure and flow velocity. Complex two-phase boiling flow models require numerous simplifying assumptions or hard-to-measure experimental data. For this reason, numerous models of specific boiling flow cases have been developed, such as the three-zone model for the case of flow of elongated bubbles [12,13] or the model for annular flow [9], both of which are the characteristic flows for mini- and micro-channels. The Lagrangian–Eulerian framework with finite element method (FEM) requires a laborious and complicated numerical procedure for a one-fluid model and thus has limited applicability [14].

The briefly described state of modelling and numerical simulation indicates the necessity for invention of a general and specific model of flow boiling in mini-channels as well as corresponding computation methods. The most common methods used in flow boiling in mini-channels include correlation equations, the Galerkin FEM, volume of fluid (VOF) method, lattice Boltzmann methods (LBM), the Trefftz method (TM) and the recently rapidly developing computational fluid dynamics (CFD) methods. The description of the current experimental and numerical approaches to the analysis of heat transfer in mini- and micro-channels can be found in the literature [5,15–18]. A particularly important parameter for the description of flow boiling is the local value of the void fraction, which causes the search for various non-intrusive methods of its measurement. In these methods, it is important that the measur-

Beata Maciejewska, Sylwia Hożejowska, Mirosław Grabowski, Mieczysław, E. Poniewski
Numerical Analysis of the Boiling Heat Transfer Coefficient in the Flow in Mini-Channels

DOI 10.2478/ama-2023-0069

ing transducer does not disturb the flow and does not affect the observed two-phase structure. Methods that meet this condition are usually based on the use of changes in certain physical parameters of the flowing fluid related to the void fraction, e.g. change in the dielectric constant of the two-phase mixture (capacitance method [19–21]), change in the acoustic properties of the two-phase mixture for ultrasonic wave propagation [22] and optical methods based on image analysis, which are often used in experimental studies of two-phase flows in mini-channels [18]. An extended overview of experimental techniques and correlations for the void fraction can be found in the literature [23].

In the presented experimental research, the new approach concerning high-speed filming with a high-resolution camera, specific photographic data reduction and experimental errors analysis of the observed two-phase boiling flow structures in a horizontal, rectangular mini-channel [3] was applied. This technique allowed simultaneous boiling two-phase flow visualisation and local void fraction measurement.

In the paper, the results were obtained using the TM and numerical simulation performed in the CFD environment. The choice of methods results from the main goal of the article, which is to formulate and solve a mathematical model concerning the heat transfer problem in flow boiling in mini-channels.

The TM, compared to traditional numerical methods, offers advantages in terms of computational efficiency and accuracy. By utilising Trefftz functions, which are solutions to the governing equations, the method can provide highly accurate results, with fewer computational resources. The TM is a meshless method that allows for stable solutions to inverse heat transfer problems and does not require advanced software. Numerical simulations performed using CFD codes enable predictions and analysis of temperature distributions of heaters elements and working fluid in exchanges. This allows to gain deeper insights into the physics of the system and identify any heat transfer inefficiencies.

In the paper, the results of numerical simulations were compared with the results of the TM. Overall, the Trefftz and Simcenter STAR-CCM+ results are coincident. In the future, the TM can be used to validate, together with experimental data, the results of numerical simulations carried out on commercial CFD codes.

2. EXPERIMENTAL APPARATUS AND PROCEDURE

2.1. Experimental apparatus

The diagram of the experimental apparatus is shown in Fig. 1. The mini-channel, which is the basic element of the apparatus, was created by gluing three transparent glass plates and a rectangular milled copper block, as shown in Fig. 1b. The copper block forms the structural basis for the mini-channel and acts as a thermal buffer, ensuring equalisation of the temperature field. One of the surfaces of the block is the heating surface in the mini-channel (Fig. 1b). Heat is generated by four flat heating resistors placed on the outer surface of the copper block opposite the heating surface in the mini-channel.

The heating resistors were powered by a TDK Lambda GEN 50–30 high-current DC power supply. Optiwhite glass was chosen as the construction material for the walls of the mini-channels. It is colourless, contains a limited amount of iron and has a high light transmission factor. To illuminate the channel, a proprietary illumi-

nator system based on Citizen CL-L233-HC13L1-C LED elements was used. LOCTITE® SI 5145 adhesive was used to glue the mini-channel glass and copper elements. The dimensions of the mini-channel are as follows: length 180 mm, width 4 mm and depth 1.5 mm, with a cross-section of 6 mm2. The hydraulic diameter of the mini-channel is 2.18 mm, as shown in Fig.1b. Five thermocouples were placed in the mini-channel module, one at the inlet, one at the outlet of the mini-channel and three inside the copper heating block (Fig. 1b). Two pressure sensors were placed at the inlet and outlet of the channel. The flow of distilled water was generated by a precision gear pump and reached a maximum values of 1.5 × 10−7 m3/s. The flow in the mini-channel was laminar, where Re = 198. Flows at low Reynolds numbers are quite often used in miniature cooling systems for electronic devices.
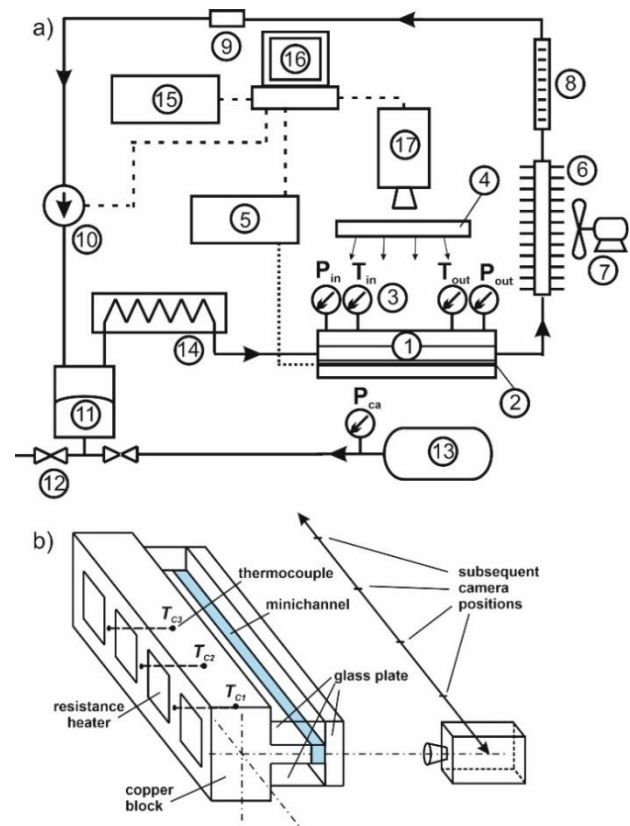

Fig. 1. (a) Scheme of the experimental apparatus: 1 – measurement module with a mini-channel, 2 – copper heating block, 3 – temperature and pressure sensors [Czaki K-type, TP-201; Kobold, 0–2.5 bar], 4 – LED lighting, 5 – DC power supply [TDK Lambda], 6 – cooler, 7 – fan, 8 – rotameter [Heinrichs], 9 – filter, 10 – precision gear pump [Tuthill Concord DGS 38 PP], 11 – pressure control, 12 – compressed air valves, 13 – compressed air tank, 14 – preheater, 15 – control and measurement module [NI cDAQ-9178 chassis], 16 – computer controlling the experiment with a LabView script, 17 – high-speed video camera [Phantom 711, Vision Research], Pca – compressed air pressure sensor; Tin, Pin temperature, pressure at the inlet to the channel, Tout, Pout temperature, pressure at the outlet of the channel, (b) General view of the mini-channel: TC1, TC2 i TC3 thermocouples located inside the copper heating block

Figs. 2 and 3 show the view of the test stand and the measurement module with a mini-channel, respectively.
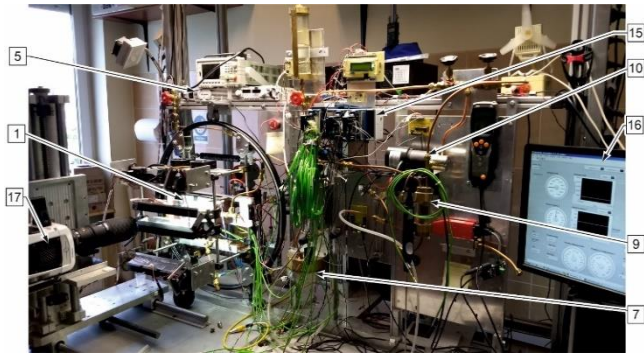
Fig. 2. View of the experimental setup, markings as in Fig. 1

Fig. 3. View of the measuring module with mini-channels, markings:
1a – mini-channel, 18 – radiator of the LED illuminator,
other markings as in Fig. 1.

2.2. Experimental procedure

The measurement procedure used for the experiments performed at the stand (Fig. 1) is as follows:
(a) Pumping the fluid through the mini-channel at the set volumetric flow rate, inlet temperature and pressure.
(b) Two-stage heating of the fluid up to the boiling point by using a preheater, followed by a heating copper block for the mini-channel.
(c) Recording of the basic thermal and flow parameters: water volumetric flow rate, water inlet and outlet temperatures, inlet pressure, pressure drop along the length of the mini-channel, power supply to the heater and temperature in three points of the copper heater. A single measurement had the following course: within 6–7 s, all experimental parameters were read and saved to a computer disk.
(d) Filming two-phase flow structures with a high-speed video camera and saving the recorded file to a computer disk.

Images of two-phase flow structures recorded by a high-speed camera were used to determine the local void fraction in the channel, as mentioned in papers [3,7]. This was achieved by a specially developed procedure based on image analysis on the MatLab environment.

3. MATHEMATICAL MODEL AND CALCULATION METHODS

This paper study proposes two approaches to determine the heat transfer coefficient between a copper heating surface and distilled water flowing in a mini-channel. In the first approach, it was assumed that the temperature distribution of the copper block

satisfies the Laplace equation, and the water temperature satisfies the corresponding the energy equation with one component of the velocity vector (with other components equal to zero) parallel to the direction of fluid flow. The given energy equations have been supplemented with an appropriate set of resulting boundary conditions from measurement data. The semi-analytical TM [24] was used to determine the two-dimensional temperature distributions of the copper block and water. The idea behind the TM is to approximate the unknown solution of a partial differential equation with a linear combination of functions (these are the Trefftz functions) that satisfy the equation exactly. Knowing the boundary conditions allows determining the coefficients of a linear combination based on the least squares method. The approximation obtained in this way is a continuous and differentiable function that satisfies the governing equation in an exact manner and the boundary conditions in an approximate manner. In the presented approach, the knowledge of the temperature distribution of the copper block and water allows determining the heat transfer coefficient at the copper block surface–water interface from the Robin boundary condition. A wide range of applications of the TM for solving direct and inverse engineering problems can be found in articles and monographs, e.g. [25–30].

In the second approach, as in [31], Simcenter STAR-CCM+ software was used to analyse the heat transfer in the measurement module. The geometrical dimensions of the heating copper block and the physical parameters of both the material of the block and the flowing fluid were used in the numerical calculations, as well as the spatial orientation of the entire measurement module and the thermal and flow parameters recorded during the experiment.

It is important to note that the TM and CFD simulations have advantages and limitations, and the choice between the two methods depends on the specific problem at hand, the available resources and the desired accuracy and scope of the solution. Tab. 1 shows the differences between the Simcenter STAR-CCM+ simulation and the TM.

Tab. 1. Differences between the Simcenter STAR-CCM+ simulation and the TM

Differences	CFD simulation	TM
Need meshing	+	-
Solution satisfies the governing equation	Approximately	Exactly
Used to solve non-linear equations	+	– *)
Domain	No limitations on shape	Simple shape **)
Computer	Requires large processing power	Does not require large processing power and advanced software

*Combination of the TM with other methods (e.g. FEM, Picard method) enables solving non-linear equations.
**Geometrically complex domain can be divided into simple subdomains.

3.1. Trefftz method

The model given below is a simplified version of the model described in [7], where it was assumed that the measurement mod-

Beata Maciejewska, Sylwia Hożejowska, Mirosław Grabowski, Mieczysław, E. Poniewski
Numerical Analysis of the Boiling Heat Transfer Coefficient in the Flow in Mini-Channels

DOI 10.2478/ama-2023-0069

ule is in a steady state and the heat transfer process in the copper block and water is carried out in two directions: x (referring to the length of the block and the mini-channel) and perpendicular to it, y (referring to the height of the block and the depth of the mini-channel δM). As in [7], assuming that the physical phenomena occurring on the side edges of the module do not significantly affect the thermodynamics of the process taking place in the central part of the module, further considerations concerned only the central part of the measurement module, i.e. the section along its length. A laminar flow with one velocity component v(y) with a parabolic profile fulfilling the condition was assumed in the channel:

$$\frac{1}{\delta_M} \int_0^{\delta_M} v(y) dy = v_{\text{ave}} \tag{1}$$

where δ_M is the mini-channel depth, $v(y)$ is the parabolic water velocity and v_{ave} is the average speed of water in the mini-channel based on the known volume flow.

The model assumes that the temperature of the copper block and water satisfies the Laplace equation and the Fourier–Kirchhoff equation, respectively, in the appropriate forms:

- For a copper block in the domain,
$D_C = \{(x,y) \in R^2 : 0 < x < L, 0 < y < \delta_C\}$

$$\nabla^2 T_C = 0 \tag{2}$$

- For water in the domain,
$D_f = \{(x,y) \in R^2 : 0 < x < L, \delta_C < y < \delta_C + \delta_M\}$

$$\lambda_f \nabla^2 T_f = v(y) c_p \rho_f \frac{\partial T_f}{\partial x} \tag{3}$$

where T_C is the cooper block temperature, δ_C is the cooper block depth, L is the length of the measurement module, T_f is liquid (water temperature), λ_f is the water thermal conductivity, ρ_f is the water density and c_p is the water specific heat. For Eqs (2) and (3), the appropriate Dirichlet and Neumann boundary conditions were adopted. Following boundary conditions were assumed for Eq. (2):

- the temperature of the block T_{Ck} is known from the measurements in its three inner points (x_k, δ_{mp}) (Fig. 1b)

$$T_C(x_k, \delta_{mp}) = T_{Ck} \text{ for } k = 1,2 \tag{4}$$

- its outer wall and walls perpendicular to the mini-channel are insulated

$$\frac{\partial T_C(x,0)}{\partial y} = 0 \tag{5}$$

$$\frac{\partial T_C(0,y)}{\partial x} = 0 \tag{6}$$

$$\frac{\partial T_C(L,y)}{\partial x} = 0 \tag{7}$$

- heat exchange takes place on the contact surface with the resistors, i.e. for $x \epsilon D$, where $D = \langle 2.5\ mm; 41.5\ mm \rangle \cup \langle 47.5\ mm; 86.5\ mm \rangle \cup \langle 93.5\ mm; 132.5\ mm \rangle \cup \langle 139.5\ mm; 178.5\ mm \rangle$

$$\lambda_C \frac{\partial T_C(x,0)}{\partial y} = -q \tag{8}$$

where q is the heat flux and λ_C is the cooper thermal conductivity.

The following assumptions constitute a set of boundary conditions for Eq. (3):

- ideal thermal contact between the copper block and the water

$$T_C(x, \delta_C) = T_f(x, \delta_C) \tag{9}$$

$$\lambda_C \frac{\partial T_C(x,\delta_C)}{\partial y} = \lambda_f \frac{\partial T_f(x,\delta_C)}{\partial y} \tag{10}$$

- the knowledge of water temperature at the entrance and exit to/from the mini-channel

$$T_f(0,y) = T_{f,in} \tag{11}$$

$$T_f(L,y) = T_{f,out} \tag{12}$$

where $T_{f,in}$ is the water temperature at the inlet to the mini-channel and $T_{f,out}$ is the water temperature at the outlet from the mini-channel.

The system of differential equations defined in this way together with the boundary conditions leads to the solution of two inverse Cauchy-type problems [25,32] in two different regions (copper block and mini-channel) with different shapes and physical parameters. To determine the two-dimensional temperature distributions of the copper block and water, the TM described in detail in [28,29] was used. The knowledge of temperature distribution in both areas allows determining the heat transfer coefficient of on their contact surface from the Robin boundary condition:

$$\alpha(x) = \frac{-\lambda_C \frac{\partial T_C}{\partial y}(1-\varphi(x))}{T_C - T_{l,\text{ave}}} \tag{13}$$

where $T_{f,\text{ave}}$ is the reference water temperature and φ is the local void fraction.

Reference water temperature $T_{f,\text{ave}}$ was calculated as the average water temperature in the mini-channel, and the local void fraction φ was approximated by the logistic curve in further calculations.

3.2. Simcenter STAR-CCM+ software

To verify the calculation results obtained by using the TM, the temperature distribution of the copper block and water and the value of the heat transfer coefficient were calculated using Simcenter STAR-CCM+ software (version 2020.2.1 (15.04.010-R8)).

The calculations assume that (i) the fluid flow is incompressible with a known constant flow rate, (ii) the temperature of the fluid at the inlet to the mini-channel and its overpressure at the outlet are known, (iii) the temperature of the copper block at three measurement points is known (Fig. 1b), (iv) there is no heat losses to the surroundings, (v) the heat flux delivered to the resistors is known and (vi) the material properties do not depend on temperature.

A PC with an Intel Core i9 CPU (24 cores), clocked at 3.50 GHz and 256 GB of RAM, was used for the calculations. The polyhedral computational grid in the entire module was created from 7,573,690 cells (the grid in the mini-channel consisted of 340,198 cells), as shown in Fig. 4. The material parameters used in the calculations are presented in Tab. 2.

Numerical calculations were performed using the multiphase VOF model found in the literature [33]. In this approach, the issues of heat transfer and fluid flow are described by the equations of mass, momentum and energy balances and the void fraction in a two-phase mixture. The problem formulated in this way is solved by the finite volume method (FVM) [34], which consists in discretising the integral form of given equations to a system of algebraic equations. Values of functions in nodes located in the centres of

control areas equivalent to the cells of the calculation grid are sought.

Tab. 2. Material parameters of the measurement module

Element of the measuring module			
Material parameter	Cooper block	Heater	Distilled water
Density [kg/m³]	8,940.0	7,832.0	997.561
Dynamic viscosity [Pa/s]	-	-	0.00088871
Specific heat [J/kg/K]	386.0	434.0	4,181.72
Thermal conductivity [W/m/K]	398.0	63.9	0.620271
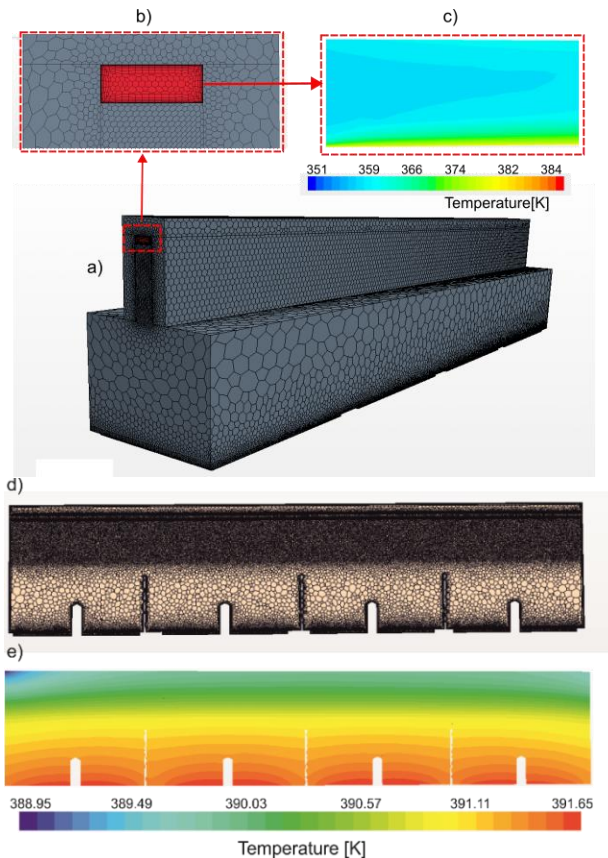
Fig.4. (a) Calculation grid applied to the mini-channel with the heating block, (b) enlargement of the cross-section at the entrance to the mini-channel, (c) water temperature at a distance of 0.0045 m from the inlet to the mini-channel, (d) middle cross-section of the mini-channel with the heating block along their length, (e) heating block temperature in the middle cross-section

Systematic refining of the grid size is important for computer simulations.

The grid convergence method (GCI) [35,36], based on the Richardson extrapolation (RE) [37,38], was used to examine and evaluate the quality of the adopted computational grid. According to the procedure for estimation of discretisation error described in the literature [36] and recommended by the Fluids Engineering Division of the American Society of Mechanical Engineers (ASME), the grid convergence index for the 3D grid has the following form:

$$GCI_{ij} = \frac{1.25 e_{ij}}{r_{ij}{}^p - 1} \tag{14}$$

where

$$e_{ij} = \left| \frac{\phi_i - \phi_j}{\phi_i} \right| \tag{15}$$

while ϕ_k denotes the solution on the k th grid.

The grid refinement factor r in Eq. (14) was calculated according to the following formula:

$$r_{ij} = \frac{h_i}{h_j} \text{ for } h_j < h_i \tag{16}$$

while the order p of the method is the solution of the following equation:

$$p - \frac{\left| ln\left| \frac{\varepsilon_{32}}{\varepsilon_{21}} \right| + ln\left(\frac{r_{21}{}^p - \text{sgn}\left(\frac{\varepsilon_{32}}{\varepsilon_{21}} \right)}{r_{32}{}^p - \text{sgn}\left(\frac{\varepsilon_{32}}{\varepsilon_{21}} \right)} \right) \right|}{\ln(r_{21})} = 0 \tag{17}$$

where representative grid size h for the 3D grid was calculated from the following formula:

$$h = \left[\frac{1}{N} \sum_{i=1}^{N} (\Delta V_i) \right]^{1/3} \tag{18}$$

and V_i is the volume of the ith cell and N is the total number of cells used for the computations, while

$$\varepsilon_{ij} = \phi_i - \phi_j \tag{19}$$

where ϕ_k is defined as in Eq. (15).

Calculations should be carried out for at least three different grids such that the grid refinement factor r should be >1.3 [36]. Additional extrapolated values can be taken from:

$$\phi_{ij}^{ext} = \frac{r_{ij}{}^p \phi_j - \phi_i}{r_{ij}{}^p - 1} \tag{20}$$

and

$$e_{ij}^{ext} = \left| \frac{\phi_{ij}^{ext} - \phi_j}{\phi_{ij}^{ext}} \right| . \tag{21}$$

The aim of the calculation was the numerical uncertainty GCI_{21} in the fine-grid solution, which is the basis for generating the results presented in the article. Tab. 3 illustrates results of this calculation procedure for three selected grids.

Tab. 3. Values of parameters in calculations of discretisation error

Parameter	Experiment 1 $q = 7.80$ kW/m²	Experiment 2 $q = 21.90$ kW/m²	Experiment 3 $q = 26.52$ kW/m²
N_1 N_2 N_3	7,573,690 2,837,607 1,251,945	7,573,690 2,837,607 1,251,945	7,573,690 2,837,607 1,251,945
r_{21}	1.39	1.39	1.39
r_{32}	1.31	1.31	1.31
ϕ_1	381.59 K	390.42 K	382.43 K
ϕ_2	381.69 K	390.77 K	382.30 K
ϕ_3	381.83 K	391.30 K	382.26 K
p	1.4	2	2.9
ϕ_{21}^{ext}	381.40 K	390.04 K	382.51 K
e_{21}	0.10%	0.30%	0.12%
e_{32}	0.12%	0.44%	0.03%
e_{21}^{ext}	0.17%	0.32%	0.07%
GCI_{21}	0.21%	0.40%	0.09%

Eq. (14) is interpreted as an uncertainty estimate of discretisation error [39], whereas Eqs (15) and (21) express the value of the approximate relative error. For the calculation of a more conservative estimate uncertainty of the discretisation error, authors of Report INL/EXT-06-11789 TRN: US0800104 [40] suggest the following formula:

$$\delta = \frac{1}{4}(e_{21} + e_{32} + e_{21}^{ext} + GCI_{21}) \qquad (22)$$

The confidence interval (at a confidence level $(1 - \alpha) * 100\%$, here $\alpha = 0.05$) of the estimate of the discretisation error was defined as follows:

$$\left(max(0, \delta - s\, t_{\alpha/2}), \delta + s\, t_{\alpha/2}\right) \qquad (23)$$

where s is the estimate of the standard deviation of all the values calculated from Eqs (14), (15) and (21), and $t_{\alpha/2}$ is calculated from T-distribution. For $\alpha = 0.05$ (confidence level is equal to 95%) and the T-distribution with 3 degrees of freedom, the value of the coverage factor $t_{\alpha/2}$ is equal to 3.182.
Values of parameters lead to obtain the confidence interval defined by Eq. (23), as given in Tab. 4.

Tab. 4. Values of parameters in calculations of the estimate of the numerical uncertainty

Parameter	Experiment 1 $q = 7.80$ kW/m²	Experiment 2 $q = 21.90$ kW/m²	Experiment 3 $q = 26.52$ kW/m²
δ	0.0015	0.0037	0.0008
s	0.0005	0.0007	0.0003
$s\, t_{\alpha/2}$	0.0016	0.0022	0.0011

As can be seen from Tab. 4, expanded uncertainty (at the confidence level of 95%) of the discretisation error for the three selected grids in presented experiments varies from 0.19% to 0.59%.

4. RESULTS

The values of other experimental parameters used in the calculations along with their measurement errors are presented in Tabs. 2 and 5.

Tab. 5. Values of experimental parameters and their measurement errors

Parameter	Variation range of the parameter	Experimental error
Inlet pressure [kPa]	5.33–26.33	1.25
Pressure drop [Pa]	20.25–108.17	3.75
Inlet temperature [K]	352–362	0.5
Outlet temperature [K]	374–382	0.5
Average inlet subcooling [K]	17.10	0.5
Copper block temperature at the measuring points [K]	T_{C1}:382.03–391.10 T_{C2}:382.92–391.96 T_{C3}:382.89–391.45	0.5
Ambient temperature [K]	294	0.5

Heat flux [kW/m²]	7.80–26.52	6%
Mass flux [kg/m²s]	11–111.9	7.8%

Fig. 5 lists the values of the experimentally determined void fraction, its approximation with the logistic curve and the results obtained from the simulations performed in STAR-CCM+.
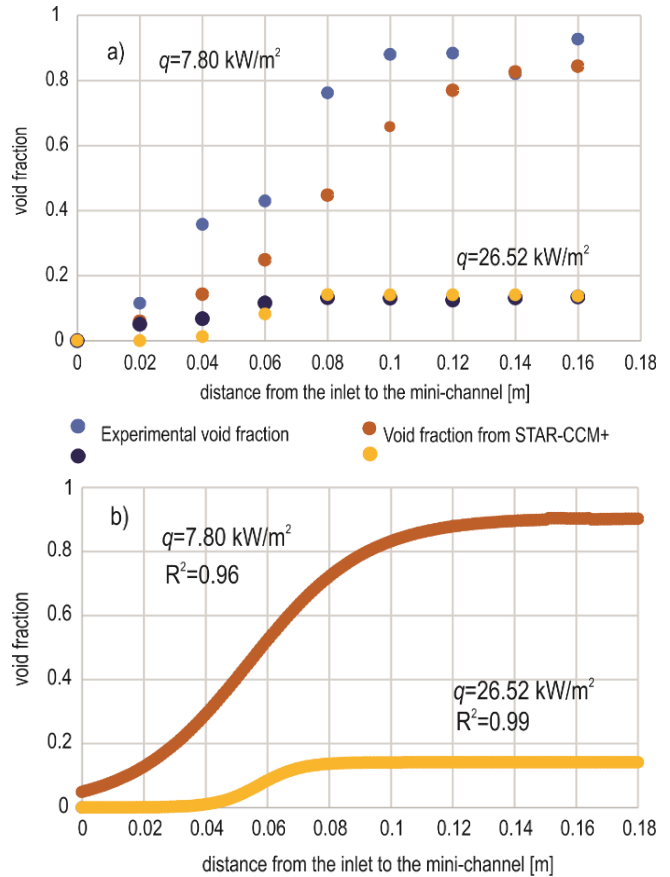

Fig. 5. (a) Experimental void fraction obtained from calculations using the STAR-CCM+ program, (b) Void fraction approximation with the logistic curve; experimental data: heat flux q = 7.80 kW/m2 and vave = 0.011 m/s, heat flux q = 26.52 kW/m2 and vave = 0.023 m/s

The maximum absolute differences (MAD) are calculated using the following formula:

$$MAD = max|f - g| \qquad (24)$$

where f, g are functions.
The MAD between the experimental void fraction and the void fraction calculated using the STAR-CCM+ program ranged from 0.12 to 0.31, and the largest differences occurred for the smallest heat fluxes (q = 7.80 kW/(m2 K)) and in the middle part of the mini-channel. The logistic curve approximates the void fraction very well, where the smallest coefficient of determination R^2 was 0.95. There is an increase in the void fraction with the increase in the distance from the inlet to the mini-channel, with slightly higher values for the void fraction approximated by the logistic curve than that obtained from the CFD program. The MAD between the values of both functions (i.e. the logistic curve and the void frac-

tion obtained by STAR-CCM+) do not exceed 0.34, and the largest differences occur in the middle part of the mini-channel.

Fig. 6 shows the temperature of the copper block measured in three points (marked in Fig. 1b) with the temperature distributions obtained by using the TM and STAR-CCM+.
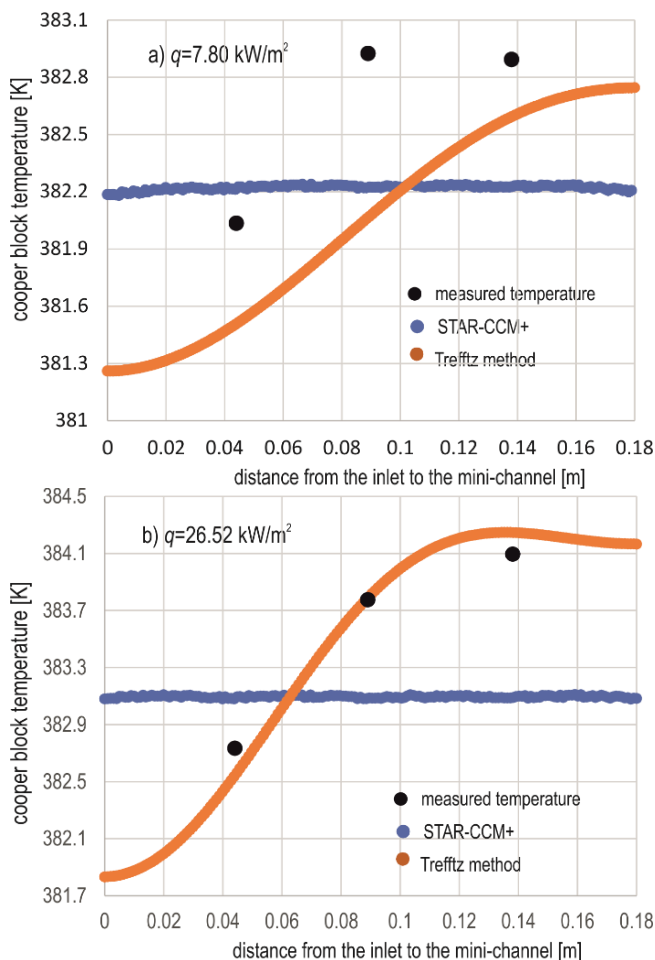

Fig. 6. Temperature of the copper block measured in three points and the temperature obtained by using the TM and STAR-CCM+ program; experimental data: (a) heat flux q = 7.80 kW/m2, (b) heat flux q = 21.90 kW/m2

To compare the measured and computed temperatures of the copper block, the maximum average relative difference (MARD) calculated from the formula are used:

$$\text{MARD} = \max\left(\frac{\|f-g\|}{\|f\|}, \frac{\|f-g\|}{\|g\|}\right) \qquad (25)$$

where $\| \ \|$ denoted L^2 norm.

The MARD and MAD for considered results are presented in Tab. 6.

Fig. 7 shows the course of water temperature variability along the flow axis obtained by the TM and numerical simulations performed in STAR-CCM+ for various heat fluxes. The water temperature for both numerical approaches has similar values; the MAD between the results range from 5.33 K to 9.17 K (the largest difference is for heat flux q = 21.90 kW/m²). The MARD do not exceed 1%.

Tab. 6. MARD and MAD values.

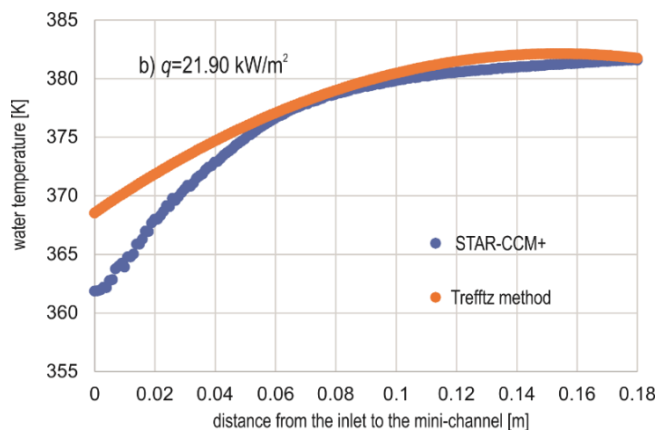| Compared results	MARD [%]	MAD [K]
The cooper block temperature measurements and results obtained by STAR-CCM+	0.14–0.26	0.56–1.01
The cooper block temperature measurements and results obtained by the TM	0.03–0.22	0.1–0.86
Temperature of the cooper block obtained by the TM and STAR-CCM+	0.09–0.33	0.89-–1.25

Fig. 7. Water temperature distribution along the flow axis obtained by the TM and STAR-CCM+ program; experimental data: (a) heat flux q = 7.80 kW/m2 and vave = 0.011 m/s, (b) heat flux q = 21.90 kW/m2 and vave= 0.011 m/s. TM, Trefftz method
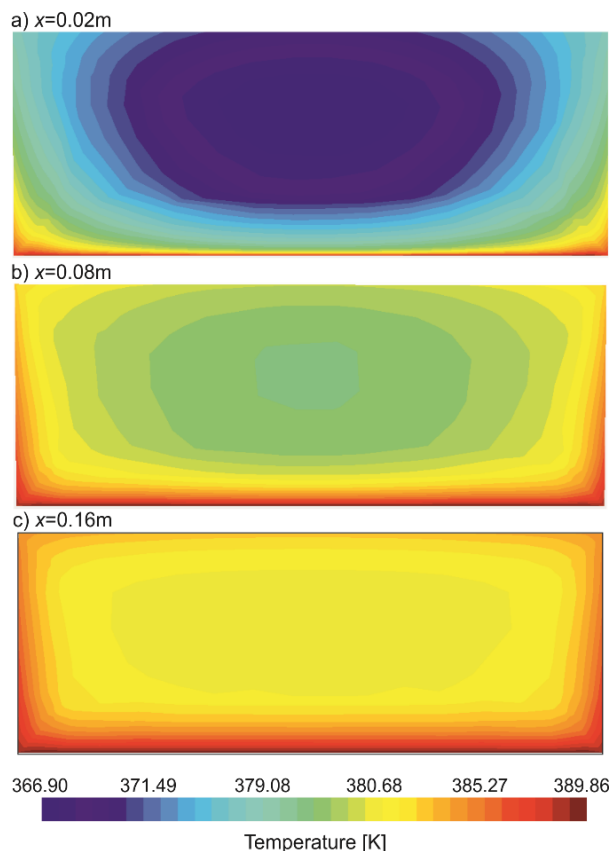

Fig. 8. Temperature distribution of fluid in three cross-sections perpendicular to the flow direction: (a) x = 0.02 m, (b) x = 0.08 m, (c) x = 0.16 m and heat flux q = 21.90 kW/m2
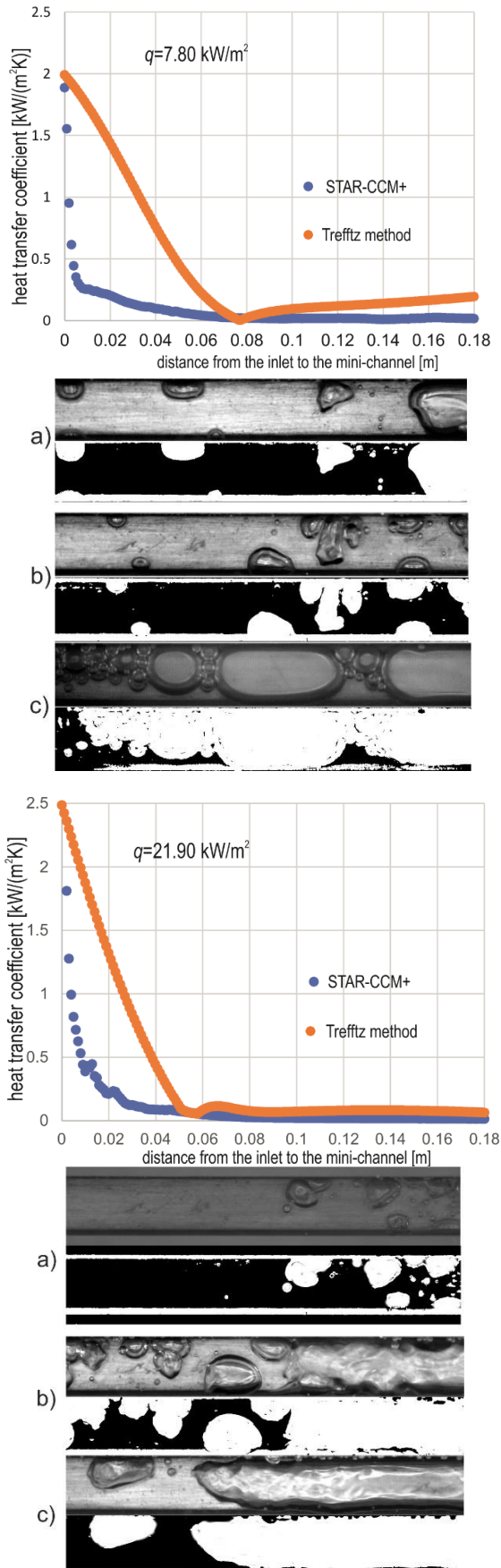
Fig. 9. Heat transfer coefficient obtained by the TM and STAR-CCM+ program. Below the graph, there are photos of two-phase structures and phase contours for the distance from the beginning of the channel: (a) 0.04 m, (b) 0.1 m, (c) 0.16 m. TM, Trefftz method

Fig. 8 shows temperature distributions in selected cross-sections ($x = 0.02$ m, $x = 0.08$ m, $x = 0.16$ m) of the fluid flow in the mini-channel. Temperature fields are determined based on a model of a homogeneous two-phase mixture. The actual course of boiling deviates from this strong assumption, and clustered phase structures of liquid and vapour are observed. However, from the point of view of the averaged parameters, it is assumed that both approaches are equivalent. The model of a homogeneous two-phase mixture allows a good reflection of the temperature field in the cross-section of the fluid flow, which is well correlated with the probability of the appearance of vapour bubbles in the real flow.

The dependence of the heat transfer coefficient as a function of distance from the inlet to the mini-channel is shown in Fig. 9, with a visible decrease in the growing distance. It is the effect of the increasing void fraction in the mini-channel (Fig. 5). The heat transfer coefficient calculated using CFD software "quickly" decreases compared to the coefficient calculated using the TM. The greatest differences between the values of heat transfer coefficients can be noticed in the initial section of the mini-channel, with the average difference between them reaching 1.6 kW/(m² K). The largest differences between the results are achieved for the lowest heat flux.

The effectiveness of the adopted computational grid was examined and assessed using the grid convergence method (GCI). Calculations were carried out for three different grids, with the grid refinement factor >1.3. The values of the numerical uncertainty GCI_{21} in the fine-grid solution range from 0.09% to 0.40% (see Tab.3). As can be seen from Tab. 4, expanded uncertainty (at a confidence level of 95%) of the discretisation error for the three selected grids in presented experiments does not exceed 0.6%.

5. CONCLUSIONS

The article describes the study of saturated boiling during the flow of distilled water through an asymmetrically heated mini-channel.

The results of experiments were the basis for numerical calculations. To solve the heat transfer problem, two numerical approaches were used: one approach was based on the Trefftz functions and the other based on the Simcenter STAR-CCM+ program. Inverse heat transfer problem was solved using the TM, while a direct heat transfer problem was solved using the Simcenter STAR-CCM+ program.

The following conclusions can be drawn from the experiments and the analysis of the results obtained using the TM and the simulation in CFD software:

- The results of CFD simulations are consistent with the results obtained by using the TM and the results of the experiment. The obtained MAD are at a low level, which allows validation of the CFD model and the calculations by the TM.
- In selected experiments presented in this article, the value of the heat transfer coefficient determined by using the TM is higher than the heat transfer coefficient obtained from CFD simulations. The most significant differences were observed near the mini-channel inlet, and the average difference did not exceed 1.6 kW/(m² K).
- Regardless of the method used for determining the heat transfer coefficient, the coefficient decreased with the increase in the distance from the inlet to the mini-channel, which was accompanied by an increase in the void fraction local value.

– Expanded uncertainty (at a confidence level of 95%) of the discretisation error for three selected grids in the presented experiments does not exceed 0.6%

The advantage of CFD software lies in the ability to obtain a solution in domains with complex shapes and comprehensive analysis of results with their visualisation. It is worth noting that STAR CCM+ software requires discretisation of the studied domain, which leads to some simplifications and inaccuracies. The TM can bypass this problem by solving differential equations in the whole domain without meshing, which helps avoid discretisation errors. Additionally, the TM enables flexible incorporation of boundary conditions to the error functional, thus leading to a better representation of real conditions.

The planned experimental studies are aimed at time-dependent and non-adiabatic flows in mini-channels and modification of the two-dimensional model and the TM. It is also planned to use CFD software in research, which will allow reducing the experimental part in favour of numerical simulations. However, it should be kept in mind that the results of numerical simulations should always be verified by the results of the experiment.

REFERENCES

1. Kandlikar SG. History, advances, and challenges in liquid flow and flow boiling heat transfer in microchannels: a critical review. J Heat Transf ASME. 2012;134(3):Article Number: 034001.
2. Kharangate C, O`Neill LE, Mudawar I. Effects of two-phase inlet quality, mass velocity, flow orienta-tion, and heating perimeter on flow boiling in a rectangular channel: Part 1 – Two-phase flow and heat transfer results. Int J Heat Mass Transf. 2016;103:1261–1279.
3. Płaczkowski K, Grabowski M, Poniewski ME. Novel twofold use of photographic technique for simultaneous flow boiling image recording and void fraction computation in a minichannel experiment. Energies. 2021;14:4478.
4. Amalfi RL, Vakili-Farahani F, Thome JR. Flow boiling and frictional pressure gradients in plate heat exchangers. Part 2: Comparison of literature methods to database and new prediction methods. Int J Refrig. 2016;61:185–203.
5. Cheng L, Xia G. Fundamental issues, mechanisms and models of flow boiling heat transfer in microscale channels. Int J Heat Mass Transf. 2017;108:97–127.
6. Layssac T, Lips S, Revellin R. Effect of inclination on heat transfer coefficient during flow boiling in a mini-channel. Int J Heat Mass Transf. 2019;132:508–18.
7. Grabowski M, Hozejowska S, Maciejewska B, Placzkowski K, Poniewski ME. Application of the 2-D Trefftz Method for Identification of Flow Boiling Heat Transfer Coefficient in a Rectangular MiniChannel. Energies. 2020;13:3973. https://doi.org/10.3390/en13153973.
8. Tentner A, Merzari E, Vegendla P. Computational fluid dynamics modeling of two-phase boiling flow and critical heat flux. In: 2nd Int Conf on Nuclear Engineering ICONE22. Prague; 2014. p. 1–9.
9. Guo Z, Fletcher DF, Haynes BS. Numerical simulation of annular flow hydrodynamics in microchannels. Comput Fluids. 2016;133:90–102.
10. Colombo M, Fairweather M. Accuracy of Eulerian–Eulerian, two-fluid CFD boiling models of subcooled boiling flows. Int J Heat Mass Transf. 2016;103:28–44.
11. Li Z, Pan J, Peng H, Chen D, Lu W, Wu H. Numerical study on subcooled flow boiling in narrow rectangular channel based on OpenFOAM. Prog Nucl Energy. 2022;154(104451. https://doi.org/10.1016/j.pnucene.2022.104451).
12. Thome JR, Dupont V, Jacobi AM. Heat transfer model for evaporation in microchannels . Part I : presentation of the model. Int J Heat Mass Transf. 2004;47:3375–85.
13. Dupont V, Thome JR, Jacobi AM. Heat transfer model for evaporation in microchannels . Part II : comparison with the database. Int J Heat Mass Transf. 2004;47:3387–401.
14. Anjos G, Mangiavacchi N, Borhani N, Thome JR. 3D ALE finite-element method for two-phase flows with phase change. Heat Transf Eng. 2014;35(5):537–547.
15. Çebi A, Celen A, Donmez A, Karakoyun Y, Celen P, Cellek MS, Taner T, Wongwises S. No Title. J Therm Eng. 2018;4(3):2037–74.
16. Elahi M, Soudagar M, Kalam M., Sajid MU, Afzal A, Banapurmath RN, Akram N, Mane SD, Saleel CA. Thermal analyses of minichannels and use of mathematical and numerical models. Numer Heat Transf Part A Appl. 2020;77(5):1–41.
17. Guo Z, Fletcher DF, Haynes BS. A review of computational modelling of flow boiling in microchannels. J Comput Multiph Flows. 2014;6(2):79–110.
18. Gupta R, Fletcher DF, Haynes BS. Taylor flow in microchannels: a review of experimental and computational work. J Comput Multiph Flows. 2010;2(1):1–31.
19. Qian H, Hrnjak P. Design and calibration of capacitive sensors for measuring void fraction in vertical headers of microchannel heat exchangers. Int J Refrig. 2021;129:Pages 224-236.
20. Libert N, Morales REM, Silva MJ. Capacitive measuring system for two-phase flow monitoring. Part 1: Hardware design and evaluation. Flow Meas Instrum. 2016;47:90–99.
21. Libert N, Morales REM, Silva MJ. Capacitive measuring system for two-phase flow monitoring. Part 2: Simulation-based calibration. Flow Meas Instrum. 2016;50:102–111.
22. Cavaro M. A void fraction characterization by low frequency acoustic velocity measurements in microbubble clouds. Phys Procedia. 2015;70:496 – 500.
23. Gardenghi AR, Filho ES, Chagas DG, Scagnolatto G, Oliveira RM, Tibiriça CB. Overview of void fraction measurement techniques, databases and correlations for two-phase flow in small diameter channels. Fluids. 2020;5(216):1–26.
24. Trefftz E. Ein Gegenstück zum Ritzschen Verfahren, Zurich, Switzerland, Sep. 12-17. In: Proc Int Kongress für Technische Mechanik. Zürich; 1926. p. 131–7.
25. Ciałkowski M, Olejnik A, Joachimiak M, Grysa K, Frąckowiak A. Cauchy type nonlinear inverse problem in a two-layer area. Int J Numer Methods Heat Fluid Flow. 2022;32(1):313-331. https:// doi.org/10.1108/HFF-09-2020–0584.
26. Maciag A, Pawińska A. The solution of nonlinear direct and inverse problems for beam by means of the Trefftz functions. Eur J Mech - A/Solids. 2022;92:104476. https:// doi.org/10.1016/j.euromechsol.202.
27. Grysa K, Maciejewska B. Trefftz functions for non-stationary problems. J Theor Appl Mech. 2013;51(2):251–64.
28. Hożejowski L, Hożejowska S. Trefftz method in an inverse problem of two-phase flow boiling in a minichannel. Eng Anal Bound Elem. 2019;98:27-34. https:// doi.org/10.1016/J.ENGANABOUND.2018.
29. Liu CS. A modified collocation Trefftz method for the inverse Cauchy problem of Laplace equation. Eng Anal Bound Elem. 2008;32(9):778-785. https:// doi.org/10.1016/j.enganabound.20.
30. Qin QH. The Trefftz Finite and Boundary Element Method. Southampton: WIT Press; 2000.
31. Piasecka M, Piasecki A, Dadas N. Experimental Study and CFD Modeling of Fluid Flow and Heat Transfer Characteristics in a Mini-channel Heat Sink Using Simcenter STAR-CCM+ Software. Energies. 2022;15(536):1-20. https:// doi.org/10.3390/en15020536.
32. Belgacem F Ben, Fekih H El. On Cauchy's problem: I. A variational Steklov–Poincaré theory. Inverse Probl. 2005;21(6):1915-1936. https:// doi.org/10.1088/0266-5611/21/6.
33. Hirt C., Nichols B. Volume of fluid (VOF) method for the dynamics of free boundaries. J Comput Phys. 1981;39(1):201-225. https:// doi.org/10.1016/0021-9991(81)901.
34. Eymard R, Gallouët T, Herbin R. Finite volume methods. Handb Numer Anal. 2000;7:713-1018. https:// doi.org/10.1016/S1570-8659(00)0.

35. Roache PJ. Perspective: A Method for Uniform Reporting of Grid Refinement Studies. J Fluids Eng ASME. 1994;116(3):405–13.
36. Celik IB, Ghia U, Roache PJ, Freitas CJ. Procedure for Estimation and Reporting of Uncertainty Due to Discretization in CFD Applications. J Fluids Eng ASME. 2008;130(7):1–4.
37. Richardson LF. The Approximate Arithmetical Solution by Finite Differences of Physical Problems Involving Differential Equations, With an Application to the Stresses in a Masonary Dam. Philos Trans R Soc A. 1911;210:307–357.
38. Richardson LF. The Deferred Approach to the Limit. Philos Trans R Soc A. 1927;226:299–361.
39. Roache PJ. Quantification of Uncertainty in Computational Fluid Dynamics. Annu Rev Fluid Mech. 1997;29:123–60.
40. Johnson RW, Schultz RR, Roache PJ, Celik IB, Pointer WD, Hassan YA. Processes and Procedures for Application of CFD to Nuclear Reactor Safety Analysis. U.S. Department of Energy Office of Scientific and Technical Information. 2006.

Beata Maciejewska: https://orcid.org/0000-0002-4692-7560

Sylwia Hożejowska: https://orcid.org/0000-0003-2558-5132

Mirosław Grabowski: https://orcid.org/0000-0001-5057-4158

Mieczysław E. Poniewski: https://orcid.org/0000-0003-2458-6299

A NEW APPROACH TO DESIGNING CONTROL OF DISSOLVED OXYGEN AND AERATION SYSTEM IN SEQUENCING BATCH REACTOR BY APPLIED BACKSTEPPING CONTROL ALGORITHM

Michał KOLANKOWSKI*, Michał BANACH*, Robert PIOTROWSKI*,**, Tomasz UJAZDOWSKI*

*Faculty of Electrical and Control Engineering, Gdańsk University of Technology,
G. Narutowicza 11/12, 80-233 Gdańsk, Poland
**Digital Technologies Center, Gdańsk University of Technology,
G. Narutowicza 11/12, 80-233 Gdańsk, Poland

s176294@student.pg.edu.pl, s176230@student.pg.edu.pl, robert.piotrowski@pg.edu.pl, tomasz.ujazdowski@pg.edu.pl

Abstract: The wastewater treatment plant (WWTP) is a complex system due to its non-linearity, time-variance and multiple time scales in its dynamics among others. The most important control parameter in a WWTP is the dissolved oxygen (DO) concentration. The tracking problem of the DO concentration is one of the most fundamental issues in biological wastewater treatment. Proper control of DO concentration is necessary to achieve adequate biological conditions for microorganisms in the WWTP. Aeration is an important process to achieve those conditions, but it is expensive. It was performed using an aeration system, which includes blowers, pipelines and diffusers. This paper presents a new approach to designing a non-linear control system for controlling DO concentration using an adaptive backstepping algorithm. A model of biological processes and aeration system were applied in designing the control system. Simulation tests of the control system were performed and very good results on control were obtained. The proposed solution has proved to be effective and computationally efficient.

Keywords: aeration system, backstepping control algorithm, dissolved oxygen, non-linear system, wastewater treatment plant, SBR

1. INTRODUCTION

The growth of global population and rising urbanization have contributed to diminishing clean water supply and irreversibly damaging many ecosystems. Therefore, uncontrolled disposal of wastewater and waste, which relies solely on the self-purifying properties of natural ecosystems, is not acceptable. The scientific and technical development allows to create better solutions in the field of wastewater treatment and reduces the negative effect on the environment, health and quality of people's lives [1].

In this paper, a municipal, biological, batch-type (sequencing batch reactor [SBR]) wastewater treatment plant (WWTP) with fine-bubble compressed air aeration is applied. The biological processes occurring in a WWTP are complex dynamic, non-linear, time-variant processes with many interactions and varying time constants. Thus, it is justified to apply modern control algorithms to such a system. The main goal of developing new control methods for a WWTP is to improve pollution indices and maintain acceptable pollutant concentrations in the effluent, according to the water-law permit. Moreover, the objective is to improve the efficiency, i.e. reduce the operational costs of a WWTP, in particular, the cost of pumping air through the aeration system [2].

One of the most important factors that have an impact on the biological wastewater treatment process is dissolved oxygen (DO) concentration. The population and activity of waste-treating microorganisms vary depending on this factor. The demanded DO concentration is guaranteed through the wastewater aeration

process. Additionally, it is used for mixing the activated sludge and raw wastewater. However, the aeration process generates the highest power consumption out of all the elements of the treatment process, and thus the highest operational costs of a WWTP [3]. Therefore, an efficient DO concentration and aeration system control allows to reduce these costs.

The history of designing control algorithms for biological processes in the activated sludge process dates back to the 1970s and 1980s. The examples of early DO concentration control algorithms are a self-tuning, robust controller [4] and an adaptive controller with an online estimation of oxygen transfer and respiration rates [5]. With the advancement of digital technology and increasing possibilities for automatic control algorithm implementation, more advanced control methods were developed, e.g., model predictive control (MPC). This method was used in the literature [6], where instead of generating a reachable reference trajectory, process performance was optimised using the economic objective function. In the literature [7], the authors proposed a two-level hierarchical control system with the supervisory layer (MPC and Fuzzy) designating the setpoint of the DO concentration based on the ammonia composition and the lower layer controller (proportional-integral [PI]) dealing with DO concentration. Another fuzzy controller in the supervisory layer, which calculates the setpoint of DO concentration and adapts parameters of the lower control layer, was presented in the literature [8]. Fuzzy logic may also be applied in direct DO concentration control, e.g., using a fuzzy-proportional-integral-derivative (PID) control strategy [9]. In the literature [10], an adaptive PID controller with a radial basis

function network for parameter adaptation was used to control the DO concentration.

Designing model-based control (MPC) requires not only knowledge of the system and the design of utility models but also significant computational resources. Another challenge is the non-linear nature of the DO and aeration system equations, and in the literature, one often encounters the use of approaches dedicated to solving linear problems, which can have negative effects on system robustness. Fuzzy control solutions have many advantages; however, their development requires substantial expert knowledge about the system and the formulation of a set of rules. Furthermore, despite the popularity of fuzzy control in academic research, it has limited practical implementations in various fields [11]. Another drawback of algorithms that require significant expert knowledge (MPC and Fuzzy) is the social concerns of operators and technologists regarding new technologies. On the other hand, popular PID controllers with fixed parameters are simple algorithms designed for linear problems. They remain popular, especially with additional modifications for parameter adaptation. However, in practice, most controllers of this type operate in basic versions with suboptimal settings or settings determined by engineering methods, prioritizing system stability without considering the quality.

The proposed adaptive backstepping algorithm is dedicated to non-linear problems, ensuring stability in the Lyapunov sense. Furthermore, due to its form, it can be easily implemented on programmable logic controllers (PLCs). An additional advantage is the algorithm's adaptation capabilities, which are important in the context of differences between simulation systems and real-world systems where significant disturbances occur.

Aeration is the most important and most expensive activity in WWTP [12]. From a control point of view, this system is dynamic and highly non-linear. Controlling this process using a PID controller with fixed parameters, over a wide operating range, can be inefficient and ineffective. Therefore, a new approach to designing a non-linear control system for DO concentration control using an adaptive backstepping algorithm is proposed.

The control method considered in this paper is applied in many different fields of technology. The adaptive backstepping method was used in the literature [13] to control a dual-arm of a humanoid robot based on fuzzy approximation. In literature [14], a double-star induction machine control system was designed using the backstepping method. The backstepping approach was applied for reference value tracking of flux and speed and for uncertainty compensation.

The remainder of this paper is organised as follows. Section 2 includes the description of the case-study SBR system and its model, as well as the model of DO concentration and the description of the considered aeration system. The designed control system and its elements, followed by the synthesis of the backstepping controller are presented in Section 3. The simulation results are presented and discussed in Section 4. The paper concludes in Section 5.

2. DESCRIPTION AND MODELLING OF THE CONTROL PLANT

2.1. Sequencing batch reactor

The process of wastewater treatment is divided into physical, biological and chemical methods. This paper concerns only biological methods. In biological treatment, the pollutants are transformed or decomposed by microorganisms. The main objective of biological treatment is to remove or reduce the biodegradable organic matter, nitrogen and phosphorus compounds that are contained in wastewater to an acceptable level, according to the water-law permit [1].
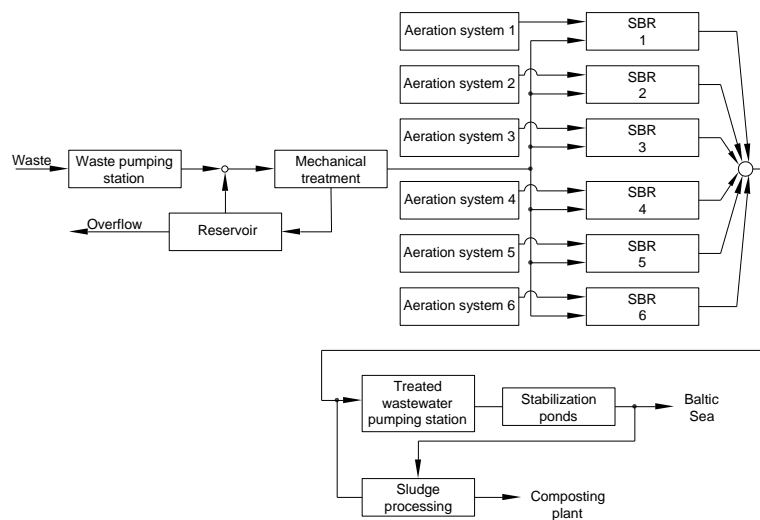

Fig. 1. Scheme of the Swarzewo WWTP

One of the most common biological wastewater treatment methods is the activated sludge method, which is considered in the paper. The activated sludge is a suspension of flocs, which is mainly composed of anaerobic heterotrophic bacteria and other organisms, such as protozoa, rotifera and fungi, as well as mineral particles. Wastewater treatment is based on the mineralization of

organic pollutants present in the effluent by the microorganisms of the activated sludge in controlled conditions. Because of this process, the microorganisms acquire the energy that is necessary for them to live. Additionally, mineral compounds of carbon, nitrogen, phosphorus and sulphur are formed and the biomass grows.

The WWTP in Swarzewo is a biological-chemical-mechanical

system, which means that the treatment process consists of several stages. The first stage of mechanical primary treatment involves the retention of solid contaminants on grids, screens, grit chambers and sand separators. In the secondary stage, which is a biological treatment, the activated sludge method is applied. Then the sludge is separated from the treated wastewater in the sedimentation process. The process may be supported by using chemical reagents.

The biological part of the WWTP in Swarzewo consists of six independent SBRs. The technological scheme of the plant is shown in Fig. 1.

In this paper, the SBR 2 (see Fig. 1) and its aeration system are considered. The reactor's capacity is 5,000 m3. A single SBR cycle includes the following phases: filling, biological reactions (aerobic and anaerobic), sedimentation, decantation and idling. At the end of the treatment process, the treated wastewater is discharged into the Baltic Sea. The excess sludge is removed, further processed, and finally may be used for the fertilization of crops.

In the modelling of biological processes occurring in an SBR, a widely used model Activated Sludge Model No. 2d (ASM2d) was applied [14]. It is an extension of previous models: ASM1 and ASM2. It is one of the most popular descriptions of the activated sludge process. ASM2d consists of 21 biological processes and 19 state variables, 8 of which describe soluble fractions and 11 particulate fractions. The values of those parameters are equal to their default values at 20°C [15]. The model was implemented in the Simba environment, applying data and parameters of the WWTP in Swarzewo [16].

2.2. DO concentration

The DO concentration is one of the most important variables in the control of biological processes. In this paper, the model proposed in the literature [17] was applied:

$$\frac{d\mathrm{DO}(t)}{dt} = k_L a\left(Q_{\mathrm{air,ref}}(t)\right) \cdot \left(\mathrm{DO}_{\mathrm{sat}}(t) - \mathrm{DO}(t)\right) +$$
$$- \frac{\mathrm{DO}(t)}{K_{\mathrm{DO}} + \mathrm{DO}(t)} \cdot R(t) \tag{1}$$

$$k_L a\left(Q_{\mathrm{air,ref}}(t)\right) = \alpha \cdot Q_{\mathrm{air,ref}}(t) \tag{2}$$

where kLa (·) – oxygen transfer function into sewage through aeration system; Qair,ref – reference trajectory of airflow to SBR [m3/h]; DOsat = 8.63736 – dissolved oxygen saturation concentration [g O2/m3]; KDO= 2 – Monod constant [g O2/m3]; R – respiration [g O2/m3 h]; α = 0.0016 – oxygen transfer coefficient [1/m3].

2.3. Aeration system

During the aerobic phase, the wastewater is aerated by the aeration system (blowers, pipes and diffusers). This is the most expensive process in the WWTP. The scheme of the aeration system is presented in Fig. 2.

The first component is the blower Aerzen AT 150-1.0S with a power of 11 5kW. It is connected via the main pipeline with a diameter of 0.4 m and a length of 62.7 m, and then separate pipes to two diffuser systems, which are located in the SBR. Disk membrane diffusers ABS PIK 300 manufactured by Sulzer were used in the system. The working flow range of a single diffuser is 1.5–

8.0 m3/h, which means that it opens, when a pressure of 2 kPa is exceeded. The size of the obtained air bubbles is 1–3 mm. Diffuser systems 1 and 2 consist of 616 and 600 diffusers, respectively.
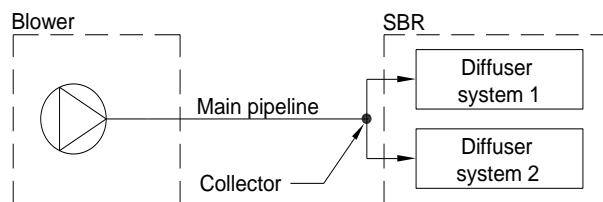

Fig. 2. Structure of the aeration system in the Swarzewo WWTP

Modelling the aeration system in an analogy to an electrical system, based on phenomena characteristic of fluid mechanics, has a long history [18]. In this model, the airflow is analogous to the amperage and the pressure drop is analogous to the voltage in the electrical circuit. The remaining elements are presented as resistors, capacitors, current and voltage sources. Based on the electrical diagrams, a mathematical model was derived. The aeration system was assumed to be a static element compared to the SBR model. The aeration system dynamics are measured in seconds; thus they are much faster compared to the SBR dynamics (minutes and hours). Hence, the aeration system's dynamics can be omitted when designing the control system. The scheme of the aeration system's model is presented in Fig. 3.
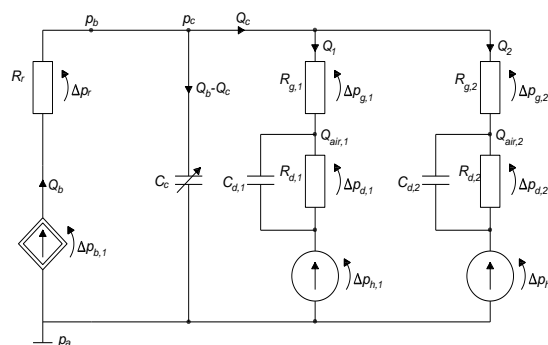

Fig. 3. Aeration system model

Airflow, represented by Q in Fig.3, is an analogy to electric current. Air pressure drop Δp is analogous to voltage drop in electrical systems. The blower was approached, analogically to current sources, as elements with non-linear characteristics of airflow Q_b [m3/h], which is a function of pressure drop on the blower Δp_b [Pa] and its rotational speed nb [rpm]. Airflow resistance at the connection point of the blower to the main pipeline was modelled by the resistance Rr. The variable resistance Cc was used to model the capacitance of the main pipeline. The two branches of the circuit at the right-hand side of the scheme are a model of two diffuser systems. Resistances $R_{g,j}$ correspond to the airflow resistance of a pipeline leading to each diffuser system. Capacitances $C_{d,j}$ correspond to the capacitances of those pipelines, while resistances $R_{d,j}$ – to airflow resistance of diffusers. The pressure drop $\Delta p_{h,j}$, which occurs in the SBR caused by the aeration system, was modelled as a voltage source.

The characteristic of the blower is further described in Section 3. The pressure drop on the blower is described by the following equation:

$$\Delta p_{b,i} = p_b - p_a \tag{3}$$

where p_b — pressure at the output of the blower [Pa]; $p_a = 1.014 \cdot 10^5$ — atmospheric pressure [Pa].

The resistance R_r, which is a function of the airflow Q_b, is given by:

$$R_r(Q_b) = \frac{\Delta p_r}{Q_b} \tag{4}$$

where Δp_r – pressure drop on the resistance R_r related to the connection point of the blower to the main pipeline [Pa].

Pressure in the main pipeline, its dynamics, and the values describing – the capacitance C_c and the volume of the main pipeline it are as follows:

$$\Delta p_c = \Delta p_{b,i} - \Delta p_r + p_a = p_b - \Delta p_r; i \in \{1,2\} \tag{5}$$

$$\frac{dp_c}{dt} = \frac{1}{C_c}(Q_b - Q_c) \tag{6}$$

$$C_c = k_c V_c p_c; V_c = \frac{1}{4}\pi d_c^2 l_c \tag{7}$$

where p_c – pressure in the main pipeline [Pa]; C_c – air capacitance in the main pipeline [m3]; Q_c – airflow in the main pipeline [m3/h]; k_c – conversion coefficient [m2s4/kg2]; V_c – volume of the main pipeline [m3]; d_c – diameter of the main pipeline [m]; l_c – length of the main pipeline [m].

The values of the parameters k_c, d_c and l_c were determined based on the geometry of the main pipeline. The formulas describing the capacitance of each diffuser system $C_{d,j}$ and volume of each branch of the aeration system $V_{d,j}$ take the following form:

$$C_{d,j} = k_{d,j} V_{d,j} p_{d,j}; V_{d,j} = \frac{1}{4}\pi d_{d,j}^2 l_{d,j}; j \in \{1,2\} \tag{8}$$

where $p_{d,j}$ – pressure in the pipeline in the j-th branch [Pa]; $C_{d,j}$ – air capacitance of the pipeline in the j-th branch [m3]; $k_{d,j}$ – conversion coefficient in the j-th branch [m2s4/kg2]; $V_{d,j}$ – volume of the pipeline in the j-th branch [m3]; $d_{d,j}$ – diameter of the pipeline in the j-th branch [m]; $l_{d,j}$ – length of the pipeline in the j-th branch [m].

The values of the parameters $k_{d,j}$, $d_{d,j}$ and $l_{d,j}$ were determined based on the geometry of the main pipeline.

The resistance $R_{g,j}$, which is a function of the airflow Q_j in the j-th branch, is described by:

$$R_{g,j}(Q_j) = \frac{\Delta p_{g,j}}{Q_j} \tag{9}$$

where $\Delta p_{g,j}$ – pressure drop on the resistance $R_{g,j}$ related to the pipeline of the j-th branch [Pa].

The inflow of air to the diffusers in the branch j $Q_{air,j}$ is as follows:

$$Q_{air,j} = \begin{cases} w_j \frac{\Delta p_{d,j} - \Delta p_{d,j}^{\text{open}}}{R_{d,j}} \text{ dla } \Delta p_{d,j} \geq \Delta p_{d,j}^{\text{open}} \\ 0 \text{ dla } \Delta p_{d,j} < \Delta p_{d,j}^{\text{open}} \end{cases} j \in \{1,2\} \tag{10}$$

where w_j – number of diffusers in the j-th branch [-]; $\Delta p_{d,j}^{\text{open}}$ – pressure drop across the pipeline of the j-th branch, necessary to open the diffuser [Pa].

The value of the parameter w_j was determined based on the documentation of the WWTP. The value of $\Delta p_{d,j}^{\text{open}}$ was determined based on diffusers' characteristics.

The inflow of air to diffusers has the following dynamics:

$$R_{d,j} C_{d,j} \frac{dQ_{\text{air},j}}{dt} + Q_{\text{air},j} = Q_j ; j \in \{1,2\} \tag{11}$$

The pressure drop across the j-th branch is described by:

$$\Delta p_{h,j} = \rho g h_j ; j \in \{1,2\} \tag{12}$$

where ρ – density of wastewater in the reactor [kg/m3]; g – standard gravity [m/s2]; h_j – immersion depth of diffusers in the reactor in the j-th branch [m].

The total value of the airflow Q_c inflowing to the system consisting of two diffuser branches is the sum of airflows in each branch of the system:

$$Q_c = \sum_{j\in\{1,2\}} Q_j \tag{13}$$

The influence of temperature on the pressure in the main pipeline was modelled as:

$$p_c = p_b \frac{T_2}{T_1} \tag{14}$$

where T_1 – temperature of the pumped air at the input of the main pipeline [˚C]; T_2 – temperature of the pumped air at the output of the pipeline [˚C].

Airflow in each branch of the aeration system is related to the air temperature:

$$Q_1 = \frac{T_3}{T_2}(p_c - \Delta p_{d,1}) \cdot \frac{1}{R_{g,1}}; Q_2 = \frac{T_4}{T_2}(p_c - \Delta p_{d,2}) \cdot \frac{1}{R_{g,2}} \tag{15}$$

where T_3 – temperature of the pumped air in the first branch of the system [˚C]; T_4 – temperature of the pumped air in the second branch of the system [˚C].

For the identification of the aeration system, a simplification of the model was performed. Because the values of parameters $R_{g,1}$ and $R_{g,2}$ are small and similar with each other, and the number of diffusers in each is similar, two diffuser systems were reduced to one. The scheme of the simplified model is presented in Fig. 4.
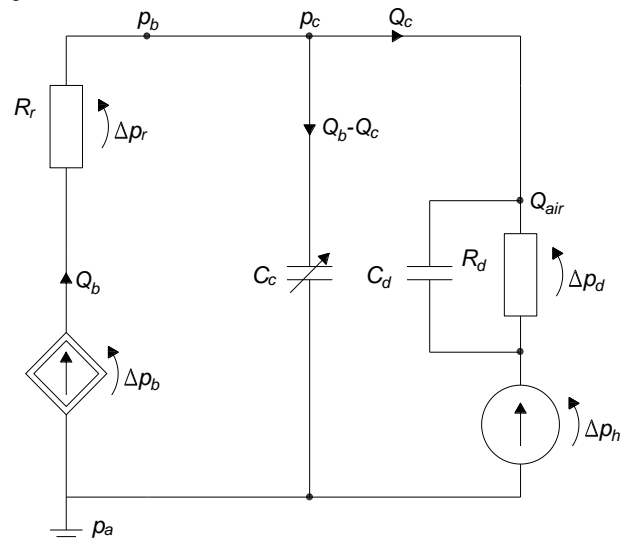

Fig. 4. Simplified aeration system model.

The parameters of the equivalent branch are as follows:

$$C_d = C_{d,1} + C_{d,2} \tag{16}$$

$$Q_{\text{air}} = Q_{\text{air},1} + Q_{\text{air},2} = a_d \cdot (k_1 \Delta p_{d,1} + k_2 \Delta p_{d,2}) \tag{17}$$

$$\Delta p_{d,1} = \Delta p_{d,2} = \Delta p_d \tag{18}$$

where ad – slope of the diffuser's characteristic [-]; k1, k2 – number of diffusers in the first branch and the second branch, respectively [-].

Given Eqs (17) and (18):

$$Q_{air} = a_d \cdot (k_1 + k_2) \cdot \Delta p_d \tag{19}$$

The equivalent airflow resistance Rd is

$$\frac{1}{R_d} = \frac{1}{R_{d,1}} + \frac{1}{R_{d,2}} = \frac{Q_{\text{air}}}{\Delta p_d} = a_d \cdot (k_1 + k_2) \tag{20}$$

The final form of the simplified model of the aeration system consists of the model of the blower, Eqs (6) and (7) and equations:

$$\frac{d\Delta p_d}{dt} = \frac{Q_b}{C_c + C_d} - \frac{\Delta p_d}{R_d(C_c + C_d)} \tag{21}$$

$$C_d = \frac{1000 \cdot V_d}{R_m \cdot T_d}; \quad V_d = \frac{1}{4}\pi d_d^2 l_d \tag{22}$$

where Rm – gas constant [J·m–3·K-1].

The aeration system model was implemented in the Matlab environment and verified based on the results of the simulation tests. The results were compared with data from the case study WWTP in Swarzewo. Because the results were satisfactory, the model was applied to the considered control system.

3. CONTROL SYSTEM DESIGN

The biological wastewater treatment processes in an SBR are non-linear complex processes. Therefore, designing a control system for it is not a trivial research task. However, it may be approached by decomposing the system into subsystems with different time constants. Then it is possible to apply a hierarchical control system with an upper-level controller (supervisory controller) and a lower-level controller (see Fig. 5).
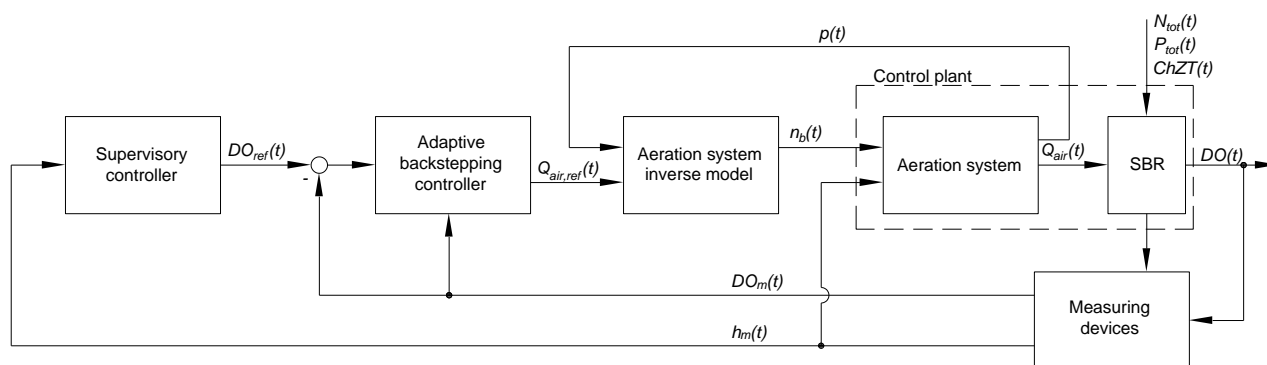

Fig. 5. Scheme of the novel control system

The supervisory controller is responsible for specific phase order in the SBR and the predefined duration of each phase. The input variable of the supervisory controller is the level of wastewater in the reactor h(t). Based on it, the duration of the filling phases is determined. In the filling phases, the reactor is filled to a specified level. The output of the controller is the state vector, which determines the state (on/off) of the following utilities or stages of the SBR work cycle: pumps responsible for the inflow of wastewater to the SBR, stirrers, blowers, decantation and excess sludge pumps. The order of the phases applied in the supervisory controller is given in Table 1.

Tab. 1. Phases in the SBR's cycle in the supervisory controller

No.	1	2	3	4	5	6	7	8	9	10	11	12
Phase	First anaerobic	First anaerobic/ filling	First aerobic	Second anaerobic	Second anaerobic/ filling	Second aerobic	Third anaerobic	Third anaerobic/ filling	Third aerobic	Sedimentation	Decantation	Excess sludge removal

Based on the phase of the SBR cycle, the supervisory controller generates a control signal, which is the reference value of the DO concentration DOref(t).

An inverse model of the aeration system was derived to find the control variables of the aeration system. In order to acquire the inverse model, the model described in the literature [19] was used. The output variable of the inverse model is nb(t) – which is a relative (to the characteristic velocity) rotational speed. The input variables of the inverse model are the reference value of airflow Qair,ref(t), which is calculated by the DO concentration controller and the pressure present in the aeration system p(t).

The nb(t) is determined based on the matrix of characteristic velocities, the matrix of blower characteristic airflows and the matrix of blower characteristic pressures.

Limitations, such as modelling the overheat and the surge of the blower, were included in the inverse model. The equations of the limitations are:

$$p_1(t) = 0.0094 \cdot Q_{\text{air,ref}}(t) + 0.8792 \tag{23}$$

$$p_2(t) = 0.0205 \cdot Q_{\text{air,ref}}(t) - 36.1888 \tag{24}$$

$$p_3(t) = 0.0094 \cdot Q_{\text{air,ref}}(t) - 12.6264 \tag{25}$$

where p1(t), p2(t) and p3(t) are pressure limit functions.

The overheat limitation is active if the pressure in the aeration system $p(t)<p1(t)$ or if $p(t)<p2(t)$. The surge limitation is active if $p(t)>p3(t)$.

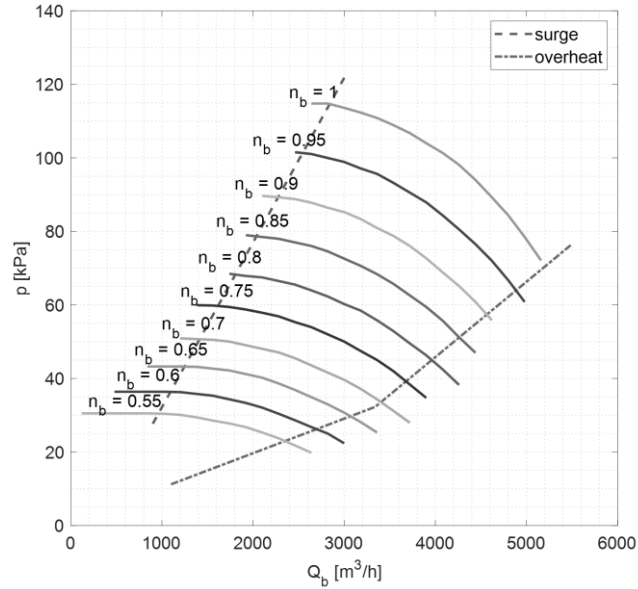By considering the limitations, the characteristics of the blower were obtained (see Fig 6).

Fig. 6. Characteristics of the blower

The model of DO concentration (1)–(2) is a parametric, dynamic, non-linear, deterministic and continuous lumped-parameter model. The parameter R(t) introduces uncertainty and time invariance to the model, thus significantly complicating the task of designing a controller for the process. The scheme of the DO concentration control system is shown in Fig. 5.
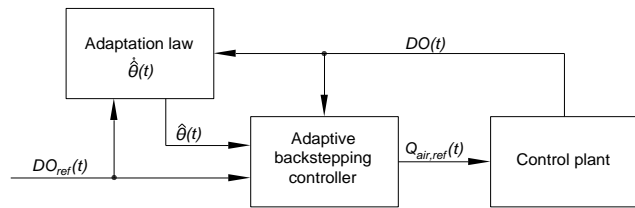

Fig. 5. Scheme of DO concentration control system

In the role of the DO controller, the adaptive backstepping algorithm was applied. It is a recursive method, which allows to achieve a globally stable control system for non-linear dynamic systems, as it ensures a solution for control and tracking problems. The method is based on a mathematical model and is used primarily for cascade systems. At every step of the design process, a stable control law is achieved based on the Lyapunov function theorem. The classical backstepping method is used for designing a static feedback loop. However, if there are uncertainties in the system, which can be written as unknown, variable parameters, it is justifiable to use adaptive backstepping. It allows to design a dynamic feedback loop [20].

The disturbances in this control system are the total nitrogen $N_{tot}(t)$, the total phosphorus $P_{tot}(t)$ and the chemical oxygen demand COD(t).

The control variable is the reference value of airflow: $u(t) = Q_{air,ref}(t)$. The unknown parameter is respiration: $\theta(t) = R(t)$.

As the first step of the backstepping procedure, the control error variable ec(t) was defined as a deviation of the control variable from its reference value:

$$e_c(t) = DO(t) - DO_{ref}(t) \qquad (26)$$

where ec(t) – control error.

The derivative of the control error was obtained:

$$\frac{de_c(t)}{dt} = \frac{dDO(t)}{dt} - \frac{dDO_{ref}(t)}{dt} = -\frac{DO(t)}{DO(t)+K_{DO}} \cdot \theta(t) + \alpha \cdot \left(DO_{sat} - DO(t)\right) \cdot u(t) - \frac{dDO_{ref}(t)}{dt} \qquad (27)$$

where $\theta(t)$ – unknown parameter [g O2/m3 h].

The following control law was proposed:

$$u(t) = \frac{1}{\alpha(DO_{sat}-DO(t))} \left(ke_c(t) - \frac{DO(t)}{DO(t)+K_{DO}}\theta(t) - \frac{dDO_{ref}(t)}{dt}\right) \qquad (28)$$

where k – controller parameter [1/h], k>0.

The parameter $\theta(t)$ is unknown, thus it was substituted with its estimated value $\hat{\theta}(t)$. Given this change, the control law Eq. (8) takes the form:

$$u(t) = \frac{1}{\alpha(DO_{sat}-DO(t))} \left(ke_c(t) - \frac{DO(t)}{DO(t)+K_{DO}}\hat{\theta}(t) - \frac{dDO_{ref}(t)}{dt}\right) \qquad (29)$$

Given Eqs (7) and (9), the following equation was obtained:

$$\frac{de_c(t)}{dt} = -ke_c(t) - \frac{DO(t)}{DO(t)+K_{DO}} \cdot (\theta(t) - \hat{\theta}(t)) \qquad (30)$$

Lyapunov function was proposed:

$$V(e_c) = \frac{1}{2}e_c{}^2(t) + \frac{1}{2\gamma} \cdot (\theta(t) - \hat{\theta}(t))^2 \qquad (31)$$

where γ – adaptation mechanism parameter [-].

Its derivative is:

$$\frac{dV(e_c)}{dt} = e_c(t) \cdot \frac{de_c(t)}{dt} + \frac{1}{\gamma} \cdot (\theta(t) - \hat{\theta}(t)) \cdot \hat{\theta}(t) \qquad (32)$$

Substituting $\frac{de_c(t)}{dt}$ in Eq. (32) with Eq. (28):

$$\frac{dV(e_c)}{dt} = -ke_c{}^2(t) - (e_c(t) \cdot \frac{DO(t)}{DO(t)+K_{DO}} + \frac{1}{\gamma} \cdot \frac{d\hat{\theta}(t)}{dt}) \cdot \left(\theta(t) - \hat{\theta}(t)\right) \qquad (33)$$

The following adaptation law was proposed:

$$\frac{d\hat{\theta}(t)}{dt} = -\gamma \cdot e_c(t) \cdot \frac{DO(t)}{DO(t)+K_{DO}} \qquad (34)$$

Finally:

$$\frac{dV(e_c)}{dt} = -ke_c{}^2(t) < 0 \qquad (35)$$

Hence, the Lyapunov function's derivative is negative definite, thus it guarantees asymptotic convergence of the control error ec(t) to zero.

4. RESULTS AND DISCUSSION

The simulation results of the control system designed in Section 3 are shown in Fig. 7. Full work cycle of the SBR is presented. The cycle includes three aerobic phases with a predetermined duration. During these phases, the aeration system and the DO controller are activated. Outside aerobic phases, the DO controller is turned off, which means that the control signal Qair,ref(t) (Fig. 7b) is set as zero.

DO(t) was compared with its reference trajectory in Fig. 7a. Due to the time variance of the control plant and the influence of disturbances, the trajectory of DO(t) in each aerobic phase differs. The achieved rise time of DO(t) was within the range of 3.73–4.23 min and it was satisfactory. The shortest rise time was achieved for the second aerobic phase and it was approximately 3.73 min. The longest rise time was achieved for the third aerobic phase and it was approximately 4.23 min. Following the overshoot at the beginning of each aerobic phase, DO(t) is maintained within an acceptable control error value, as the control error does not exceed 2.5% of the reference value. The 'noise' in the DO(t) signal in a steady state is a result of the aeration system's action. The control signal Qair,ref(t) (Fig. 7b) assumes negative values, although it is not physically achievable. However, in the aeration system inverse model, the negative values of Qair,ref(t) are set as zero; thus it does not affect the functioning of the control system. The trajectory of Qair(t), which is the output of the aeration system, is shown in Fig. 7c. The values assumed by Qair(t) are as expected, which shows that the control system has been designed correctly.
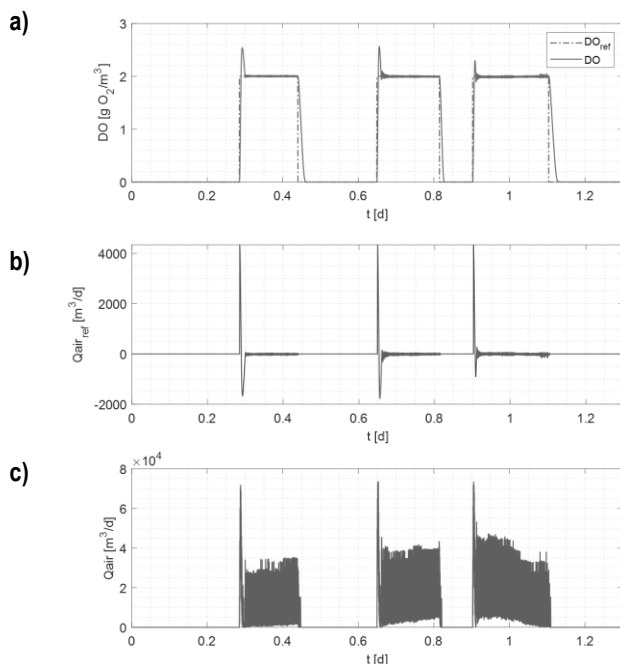

Fig. 7. Control results for constant DOref trajectory; a) dissolved oxygen; b) reference airflow trajectory; c) airflow rate

An analysis of the algorithm for a variable DO trajectory was also carried out (Fig. 8). It was assumed that in the first phase the wastewater is under-oxygenated therefore an increased DO reference value was used, while in the third phase, the DO value was reduced, due to the pre-oxygenation in the previous phases.

Overall, the obtained results highlight the successful implementation of the DO control strategy. The control system demonstrated its capability to achieve high-quality control performance for both variable and constant setpoint trajectories, ensuring the desired DO levels are maintained with accuracy and stability. These findings contribute to the understanding of the effectiveness of the control algorithm in practical applications and provide valuable insights for future process optimisation and control improvements.
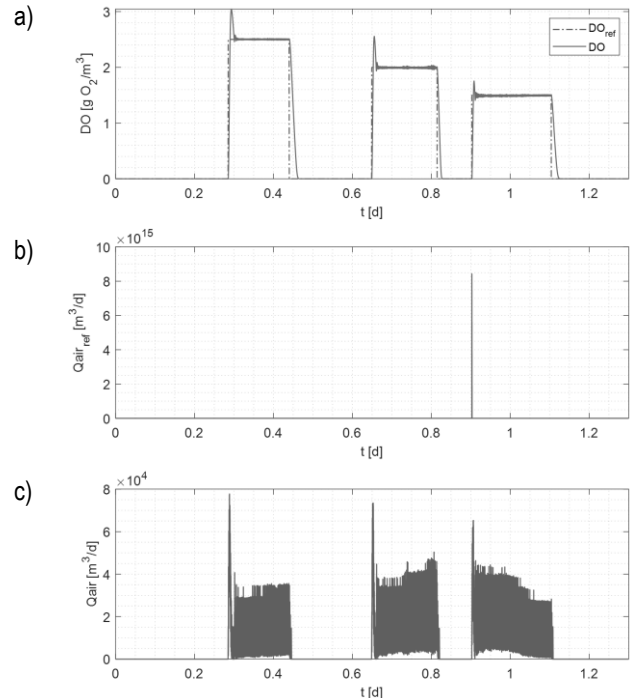

Fig. 8. Control results for variable DOref trajectory; a) dissolved oxygen; b) reference airflow trajectory; c) airflow rate

Rapid attainment of the desired DO value is crucial in maintaining the proper duration of the phase. Microorganisms rapidly consume the supplied oxygen, making the speed of reaching the setpoint more important in the context of reactor conditions than the occurrence of overshoot.

5. CONCLUSIONS

In this paper, a novel approach to designing a controller tracking the reference trajectory of DO concentration was presented. A hierarchical control system with an adaptive backstepping controller as the lower-level controller was designed. Simulation tests of the control system were performed based on real data from the Swarzewo WWTP and the properties and performance of the control system were assessed. A good tracking performance was achieved. The results obtained for the fixed and variable DO reference trajectory are satisfactory. The control error does not exceed 2.5% of the reference value, and a near-zero steady-state deviation was obtained for each oxygen phase in both cases. Furthermore, in addition to good control performance, the presented algorithm has low computational complexity and adaptability to ensure control robustness.

The next step of this research will be designing and implementing an optimal supervisory controller, which allows to achieve an appropriate quality of cleared wastewater while maintaining minimal operational costs of the WWTP.

REFERENCES

1. Riffat R, Husnain T. Fundamentals of Wastewater Treatment and Engineering. 2nd ed. London: CRC Press; 2022.
2. Khan AH, Rudayni HA, Chaudhary AA, Imran M, Vambol S. Modern use of modified Sequencing Batch Reactor in wastewater Treatment. EQ [Internet]. 2022 Jul. 11 [cited 2023 Jan. 25];33(4):1-23.
3. Pittoors E, Guo Y, Van Hulle SWH. Modeling Dissolved Oxygen Concentration for Optimizing Aeration Systems and Reducing Oxygen Consumption in Activated Sludge Processes: A Review. Chemical Engineering Communications. 2014;201(8): 983-1002.
4. Olsson G, Rundqwist L, Eriksson L, Hall L. Self-Tuning Control of the Dissolved Oxygen Concentration in Activated Sludge Systems. Instrumentation and Control of Water and Wastewater Treatment and Transport Systems: Proceedings of the 4th IAWPRC Workshop Held in Houston and Denver, U.S.A., 27 April – 4 May 1985. Pergamon Press Ltd. 1985:473-480.
5. Holmberg U. Adaptive Dissolved Oxygen Control and On-Line Estimation of Oxygen Transfer and Respiration Rates. Department of Automatic Control. Lund Institute of Technology; 1987.
6. Nejjari F, Khoury B, PuigV, Quevedo J, PascualJ, de Campos S. Economic Linear Parameter Varying Model Predictive Control of the Aeration System of a Wastewater Treatment Plant. Sensors. 2022;22(16):6008.
7. Sheik AG, Seepana MM, Ambati SR. Supervisory control configurations design for nitrogen and phosphorus removal in wastewater treatment plants. Water Environ Res. 2021;93(8):1289-1302.
8. Piotrowski R. Supervisory fuzzy control system for biological processes in sequencing wastewater batch reactor. Urban Water Journal. 2020;17:325-32.
9. Man Y, Shen WH, Chen XQ, Long Z, Corriou, JP. Dissolved oxygen control strategies for the industrial sequencing batch reactor of the wastewater treatment process in the papermaking industry. Environmental Science-Water Research & Technology. 2018;4(5):654–662.
10. Du X, Wang J, Jegatheesan V, Shi G. Dissolved Oxygen Control in Activated Sludge Process Using a Neural Network-Based Adaptive PID Algorithm. Applied Sciences. 2018;8(2):261.
11. Nguyen A, Taniguchi T, Eciolaza L, Campos V, Palhares R, Sugeno M. Fuzzy Control Systems: Past, Present and Future. IEEE Computational Intelligence Magazine. 2019; 14(1): 56-68.
12. Khatri N, Khatri KK, Sharma A. Enhanced Energy Saving in Wastewater Treatment Plant using Dissolved Oxygen Control and Hydrocyclone. Environmental Technology & Innovation. 2020; 18: 100678.
13. Bai K, Jiang G, Jiang G, Liu Z.Based on fuzzy-approximation adaptive backstepping control method for dual-arm of humanoid robot with trajectory tracking. International Journal of Advanced Robotic Systems.2019;16(3).
14. Chaabane H, Djalal Eddine K, Salim C. Sensorless back stepping control using a Luenberger observer for double-star induction motor. Archives of Electrical Engineering. 2019;69(1):101-116.
15. Henze M, Gujer W, Mino T, Matsuo T, Wentzel MC, Marais GVR, Van Loosdrecht MC. Activated sludge model no. 2d, ASM2d. Water science and technology. 1999;39(1):165-182.
16. IFAK Technology, Simba. user's Guide. https://www.ifak.eu/en/produkte/simba. Accessed: 2023-01-10.
17. Olsson G, Newell R. Wastewater treatment systems. Modelling, diagnosis and control. London: IWA Publishing; 1999.
18. Piotrowski R, Brdyś MA, Konarczak K, Duzinkiewicz K, Chotkowski W. Hierarchical dissolved oxygen control for activated sludge processes. Control Engineering Practice. 2008;16(1):114-131.
19. Piotrowski R, Ujazdowski T. Model of aeration system at biological wastewater treatment plant for control design purposes. Proc. of the 20th Polish Control Conference – KKA'2020. October 14-29, 2020, Łódź, Poland, (in:) Bartoszewicz A., Kabziński J., Kacprzyk J. (eds). Advanced, Contemporary Control. Advances in Intelligent Systems and Computing. Springer; 2020;1196:349-359.
20. Witkowska A, Tomera M, Śmierzchalski R. A Backstepping Approach to Ship Course Control. International Journal of Applied Mathematics and Computer Science. 2007;17(1):73-85.

Michał Kolankowski: https://orcid.org/0000-0003-4528-3449

Michał Banach: https://orcid.org/0000-0002-7501-0436

Robert Piotrowski: https://orcid.org/0000-0002-8660-300X

Tomasz Ujazdowski: https://orcid.org/0000-0001-6679-2985